UNIVERSITY OF THESSALY – SCHOOL OF ENGINEERING

DEPARTMENT OF MECHANICAL ENGINEERING

Experimental and computational investigation of the thermal and electrical performance of a new building integrated photovoltaic concept

Olympia Zogou, Dipl.-Ing., MSc
Thesis Supervisor: Assoc.-Professor Herricos Stapountzis

Volos, July 2011

τα Μέλη της Επταμελούς Εξεταστικής Επιτροπής:

Πρώτος Εξεταστής (Επιβλέπων)	Δρ. Ε. Σταπουντζής Αναπληρωτής Καθηγητής, Τμήμα Μηχανολόγων Μηχανικών, Πανεπιστήμιο Θεσσαλίας
Δεύτερος Εξεταστής	Δρ. Π. Τσιακάρας Αναπληρωτής Καθηγητής, Τμήμα Μηχανολόγων Μηχανικών, Πανεπιστήμιο Θεσσαλίας
Τρίτος Εξεταστής	Δρ. Κ. Παπαδημητρίου Καθηγητής, Τμήμα Μηχανολόγων Μηχανικών, Πανεπιστήμιο Θεσσαλίας
Τέταρτος Εξεταστής	Δρ. Ν. Πελεκάσης Αναπληρωτής Καθηγητής, Τμήμα Μηχανολόγων Μηχανικών, Πανεπιστήμιο Θεσσαλίας
Πέμπτος Εξεταστής	Δρ. Ι. Αικατερινάρης Καθηγητής Πανεπιστήμιο Πατρών
Έκτος Εξεταστής	Δρ. Α. Λιακόπουλος Καθηγητής, Τμήμα Πολιτικλών Μηχανικών, Πανεπιστήμιο Θεσσαλίας
Έβδομος Εξεταστής	Δρ. Γ. Λυμπερόπουλος Καθηγητής, Τμήμα Μηχανολόγων, Μηχανικών, Πανεπιστήμιο Θεσσαλίας

AKNOWLEDGEMENTS

I would like to express my special thanks to my advisor Prof. Herricos Stapountzis for his invaluable support in every aspect of this work and all things that he taught me in the class and the Lab, starting from my student years in Aristotle University Thessaloniki. For the confidence he showed to me in the assignment of this thesis and for keeping my morale high in every difficulty we found in the course of this work.

I wish to extend my sincere thanks to the other members of my supervising committee, namely, Prof. Panagiotis Tsiakaras and Prof. Costas Papadimitriou, for their valuable advice, support, help and motivation during the last 5 years.

Further, special thanks are due to Professors N. Pelekasis, J. Ekaterinaris and A. Liakopoulos, members of the examination board, for their valuable comments on the thesis manuscript, mainly regarding the Fluid Mechanical part and especially the CFD and heat transfer computations, as well as to Prof. G. Liberopoulos for fruitful discussions and motivation on the economic analysis of the proposed concept.

From the personnel of the Laboratory of Thermodynamics & Thermal Engines, special thanks are due to my colleague, PhD candidate Mr. Dimitris Tziourtzioumis, for his help and support in experimental and computational aspects of this work, as well as our perfect cooperation all these years in the Lab. Further, I wish to extend my thanks to my friend and former collaborator in LTTE, Dr.-Ing. George Pontikakis, manager, EXTHERM S.A., for his valuable advice and support in the testing device. Also, to the graduating engineer Ms. Afroditi Salpiggidou, for her assistance in the carrying out of the demanding hot-wire anemometry experiments, in the frame of her Diploma Thesis in the Lab.

We would like to express our thanks to Kyocera Solar Europe s.r.o. for supplying free of charge the PV panels for the testing devices. Special thanks are due to the family friend, Dr.-Ing. Georgios Georgiadis, Research & Development Dept. Manager, Kyocera Solar Europe s.r.o., for his help with valuable advice in many experimental aspects of this work and the fruitful discussions we had on photovoltaic technology and future.

Finally, I would like to this PhD Thesis to my two children, Antiopi-Malvina and George and to my husband, Tassos Stamatelos, for their patience and support during the last difficult years.

ΥΠΟΛΟΓΙΣΤΙΚΗ ΚΑΙ ΠΕΙΡΑΜΑΤΙΚΗ ΜΕΛΕΤΗ ΘΕΡΜΙΚΗΣ ΚΑΙ ΗΛΕΚΤΡΙΚΗΣ ΑΠΟΔΟΣΗΣ ΕΝΕΡΓΕΙΑΚΟΥ ΣΥΣΤΗΜΑΤΟΣ ΚΤΙΡΙΟΥ ΜΕ ΕΞΥΠΝΑ ΑΕΡΙΖΟΜΕΝΑ ΦΩΤΟΒΟΛΤΑΪΚΑ ΠΑΝΕΛ

Experimental and computational investigation of the thermal and electrical performance of a new building integrated photovoltaic concept

Επιβλέπων Καθηγητής : Δρ. Ερρίκος. Σταπουντζής, Αναπληρωτής Καθηγητής, Μηχανικής Ρευστών, Μηχ. Συμπιεστών & Ασυμπίεστων Ρευστών, Εφ. Υδροδυναμικής, Θεωρίας & Κατασκευής Υδροδυναμικών Μηχανών

ABSTRACT

A new concept of integrating PV modules to the south-facing walls of a building is developed. The feasibility of the concept is studied by means of experiment, CFD computations and building energy simulation. An air gap between the backsheet of the modules and the building wall is employed for circulating outdoor air to cool the modules, keeping their efficiency high. The heated air is exploited by the HVAC and service water system, thus improving building energy efficiency.

Experimental data in real world operating conditions are critical to support the design optimization of the concept and layout. A testing device was designed for this purpose and subjected to indoor and outdoor testing. Three operating modes are tested: natural convection (no fan), and forced convection cooling by means of two different capacity axial fans.

The transient electrical and thermal behavior of the device was recorded outdoors, for several hours during a number of days in summer and autumn. Further investigation of the air flow and velocity fluctuation field was carried out by means of indoor measurements in the above mentioned flow modes.

The flow and heat transfer investigation of the device was supported by CFD modeling that also helped to the determination of more accurate wall heat transfer correlations. Based on reasonable assumptions and exploiting the indoor and outdoor measurements' results, average convection coefficients were estimated to the order of 4 W/m^2K for natural convection (no fan), 10 W/m^2K for the low capacity

fan and 10.6 W/m^2K for the higher capacity fan. The existing average Nu/ Re or Nu/ Ra number correlations were improved after they have been found to underestimate Nu by a factor of 2 in the specific flow regime.

The heat transfer correlations were used to improve the respective sub model of the TRNSYS building energy simulation, which was employed in the computation of the overall effect on the energy performance of the modules, by means of the electricity produced by the PV panels, the heating energy gains and their overall effects on the energy rating of the building.

The annually produced electricity is calculated at the order of 750 kWh/ kW_p. The respective thermal energy gain for space heating in winter amounts to 310 kWh/kWp. An additional annual thermal energy gain at the order of 210 kWh/ kW_p was calculated for service water heating during the summer. For comparison, the respective electrical energy produced by rooftop installation of south-facing modules at optimal slope in the same location, amounts to 1200 kWh/ kW_p approximately, with no further exploitable thermal gains.

The results of this study show that the selection of flow rate and duct dimensions are affecting significant to the performance of the PV facade. According to the building energy simulation, measurable improvements in the thermal gains of the building can be succeeded by an improved design of the backsheet (enhancing heat transfer by micro-fins, modified backsheet material etc.). It should be noted that up to now, the design of the backsheet has not received the attention it deserves by the photovoltaic design engineers and manufacturers.

The profitability of the investment for a vertical placement of the modules in the proposed BIPV arrangement was compared to the standard rooftop installation by means of the return on investment after 20 and 25 years. As expected, the roof-mounted photovoltaic installation remains the most economically profitable. If the investors sell the electricity to the utility company at a rate of 0.55 Euro /kWh then the return on investment for 20 and 25 years of operation for the BIPV with improved backsheet corresponds to 9.0 % and 12.3 % respectively calculated for the vertical placement of the modules in the building.

The contribution of the proposed concept to the building's energy performance rating becomes significant whenever the building heating (and cooling) loads are minimized by adequate insulation and shading, as well as an energy efficient ventilation system design.

TABLE OF CONTENTS

LIST OF FIGURES

LIST OF TABLES

NOMENCLATURE

A	area [m^2]
AM	Air Mass
c_p	heat capacity [kJ/kg K]
d	the depth between the plates defining the flow [m]
D_h	hydraulic diameter [m]
g	gravity acceleration [m^2/s]
G_T	radiation intensity [W/m^2]
GDF	glass double façade
Gr	Grashoff number
g-value	solar gain factor at 0^o incidence angle
h	heat transfer coefficient, air-to-channel wall [W/m^2K]
H	height of channel [m]
I_0	reverse leakage current
I_{sc}	short-circuit current
I_{ph}	photon current
I_{Pmax}	current at maximum Power Point
k	thermal conductivity [W/m K]
m	mass flowrate [kg/s]
Nu	Nusselt number of the fluid in the channel
P	Power [W]
Pr	Prandtl number for the fluid in the duct
Q	heat flowrate [W]
R	resistance [Ohm]
Ra	Rayleigh number of the fluid in the channel
Re	$\mathrm{Re} = \frac{4\mathrm{m}}{\pi\mu\mathrm{D_h}}$ Reynolds number (channel)
R_{sol}	solar reflectivity of the glazing layer
R_{vis}	visible spectrum reflectance of the glazing layer
St	Stanton number
T	temperature [K]
TMY	typical Meteorological Year
u’	RMS velocity fluctuation
U	velocity [m/s]
U*	heat transmission coefficient – central window area [W/m^2K]
U**	heat transmission coefficient – including frame [W/m^2K]
u’	RMS velocity fluctuation
V_{oc}	Open-circuit voltage
V_{max}	voltage at maximum Power Point

GREEK SYMBOLS

α	thermal diffusivity [m^2/s]
α_s	solar altitude angle
α_{sl}	the slope of the duct (vertical = 90^o)
β	volumetric coefficient of expansion [T^{-1}]
$\boldsymbol{\gamma_s}$	solar azimuth angle
$\boldsymbol{\gamma}$	surface azimuth angle
δ	declination angle ($-23.45^o<\delta<23.45^o$)
Δp	pressure drop, pressure head [Pa]
ΔT	temperature difference
ε_1	infrared (long wave) emissivity of glazing layer
Θ	dimensionless temperature
$\boldsymbol{\vartheta}$	angle of incidence
θ_z	zenith angle
λ	thermal Conductivity of glass [W/m K]
μ	dynamic Viscosity [Pa s] [kg/ms]
ν	kinematic viscosity [m^2/s]
ρ	density (kg/m^3)
τ	time response
τ_{ir}	infrared (long wave) transmissivity of glazing layer
τ_{sol}	solar transmissivity of the glazing layer
τ_{vis}	visible transmittance of the glazing layer
ϕ	latitude
ω	hour angle

SUBSCRIPTS

air	air flowing in the duct
a	ambient
w	wall
el	electrical

ABBREVIATIONS

AC	Alternating Current
ANSI	American National Standards Institute
AWG	American wire gauge
ASTM	American Society for Testing and Materials
BIPVT	building integrated photovoltaic/thermal
CEN	Comité Européen de Normalization
DC	Direct Current
EN	European Norm
EVA	Ethylene Vinyl Acetate
PFA	a fluorocarbon polymer used for insulation of electrical wires
PSD	power Spectral Density
PV	photovoltaic
PV/T	photovoltaic/thermal collector
MPP	maximum Power Point
NOCT	normal operating cell temperature
NPV	net present value
NCF	net cash flow
SOC	standard operating conditions
STC	standard operating conditions
TCI	investment capital

CHAPTER

1

1 INTRODUCTION

1.1 PRINCIPLES OF PV ENERGY

Greece is a country with plenty of sunshine. The total solar radiation on a horizontal surface is around 1400 kWh / m^2 year in the north (e.g. Thessaloniki) and may reach 1700 kWh / m^2 year in certain parts of the south (e.g. Crete). This potential is increasingly exploited for the production of domestic hot water and electricity, thus reducing the consumption of fossil fuels and electricity and their respective CO_2 emissions. During the last decade, the idea of additionally exploiting the rejected heat of the photovoltaic modules is gaining attention. One example is the so-called PV/T collectors (photovoltaic/thermal) [1], the expansion of which was further promoted by the adoption of the Directive 2002/91/EC [2]. This Directive and the series of standards issued to support its implementation**,** established a common calculation methodology for the integrated energy performance of buildings and laid down the requirements of minimum standards on the energy performance to new buildings and to renovated existing buildings, taking into account the positive influence of active solar systems and other heating and electricity systems based on renewable energy sources. Although rooftop installation is the most common mode of PV application in buildings, vertical installation in the form of south or west facing double façades is gaining attention.

Photovoltaic cells (see Figure 1-1 and Figure 1-2) collect *solar energy* and partially convert it to electricity. This process requires, first a material in which the absorption of light raises an electron to a higher energy state, and second, the transfer of this higher energy electron from the solar cell into an external circuit. The electron then dissipates its energy in the external circuit and returns to the solar cell. A variety of

materials and processes can potentially satisfy the requirements for photovoltaic energy conversion, but in practice nearly all photovoltaic energy conversion uses semiconductor materials in the form of a *p*-*n* junction.

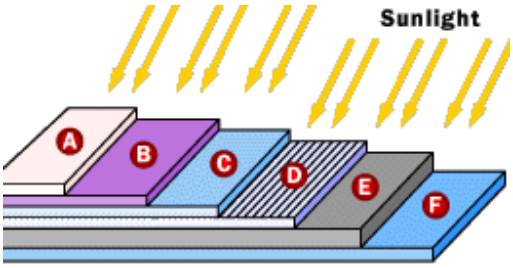

A = Glass cover **B** = Anti-reflective coating **C** = Contact grid
D = N-type Silicon **E =** P-type silicon **F =** Back contact

Figure 1-1 Basic structure of a generic silicon PV cell, adapted from [3]

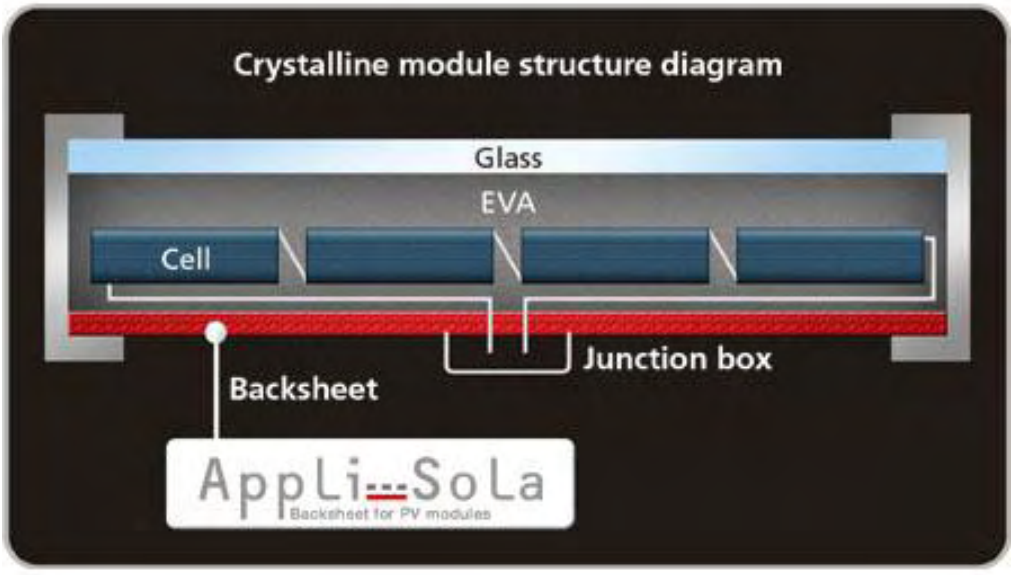

Figure 1-2 Crystalline module structure diagram (adapted from [4]).

PV modules work best when their absorbing surface is oriented perpendicular to the Sun's rays (the power density will always be at its maximum when the PV module is perpendicular to the sun). Adjustment of static-mounted PV modules can result in 10 to 40% power output increase.

Sunlight is a form of electromagnetic radiation and the visible light is a small subset of the electromagnetic spectrum (Figure 1-3). Light may be viewed as consisting of "packets" or particles of energy, called photons. A photon is characterized by either a wavelength, denoted by λ or equivalently energy, denoted by *E* (Figure 1-4). There

is an inverse relationship between the energy of a photon (*E*) and the wavelength of the light (λ) given by the equation:

$$\mathbf{E} = \frac{\mathbf{hc}}{\boldsymbol{\lambda}} \qquad \textbf{(1.1)}$$

where:

h = 6.626 * 10^{-34} J·s (Planck's constant)
c = 2.998 × 10^{8} m/s (speed of light in vacuum)

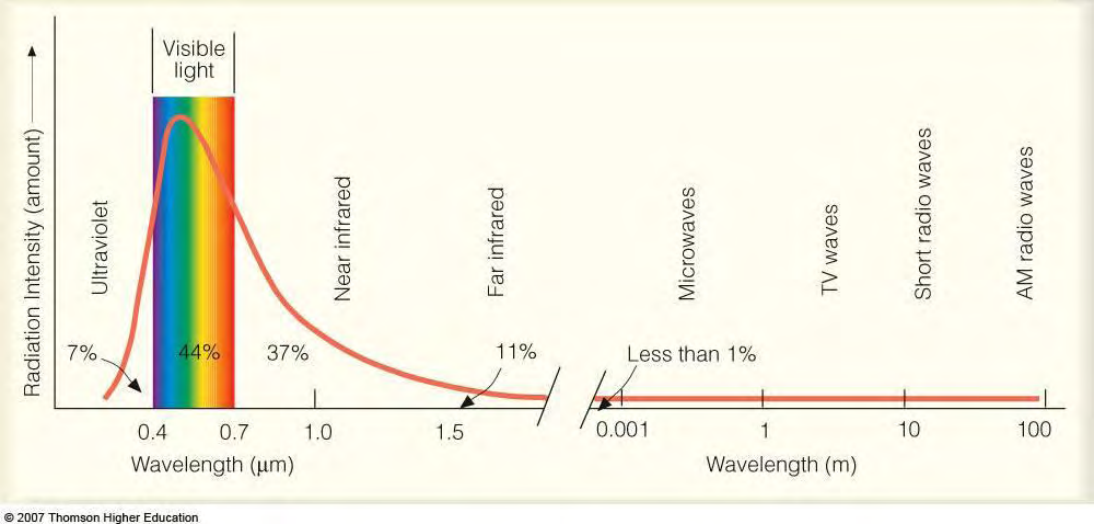

Figure 1-3 Percentages of incoming solar radiation in each wavelength band (adapted from [5]).

It must be mentioned here that only the most energetic photons with $\boldsymbol{\lambda} \leq \frac{\mathbf{hc}}{\mathbf{E_G}}$ contribute to the electricity generation, where $\mathbf{E_G}$ is the semiconductor band gap (the energy needed to release one conduction electron). In a silicon crystal this corresponds to the photon energy of electromagnetic waves with a wavelength of 1120 nm or 1.12 microns. While the solar radiation incident on the Earth's atmosphere is relatively constant, the radiation at the Earth's surface varies widely due to atmospheric effects (Figure 1-5), which are related to:

- reduction in solar radiation due to absorption, scattering and reflection in the atmosphere
- a change in the spectral content of the solar radiation due to greater absorption or scattering of some wavelengths (Figure 1-5)
- the introduction of a diffuse or indirect component into the solar radiation
- local variations in the atmosphere (water vapor, clouds and pollution)
- the season of the year and the time of the day. Solar time is used for all sun angle relationships (ANNEX I).

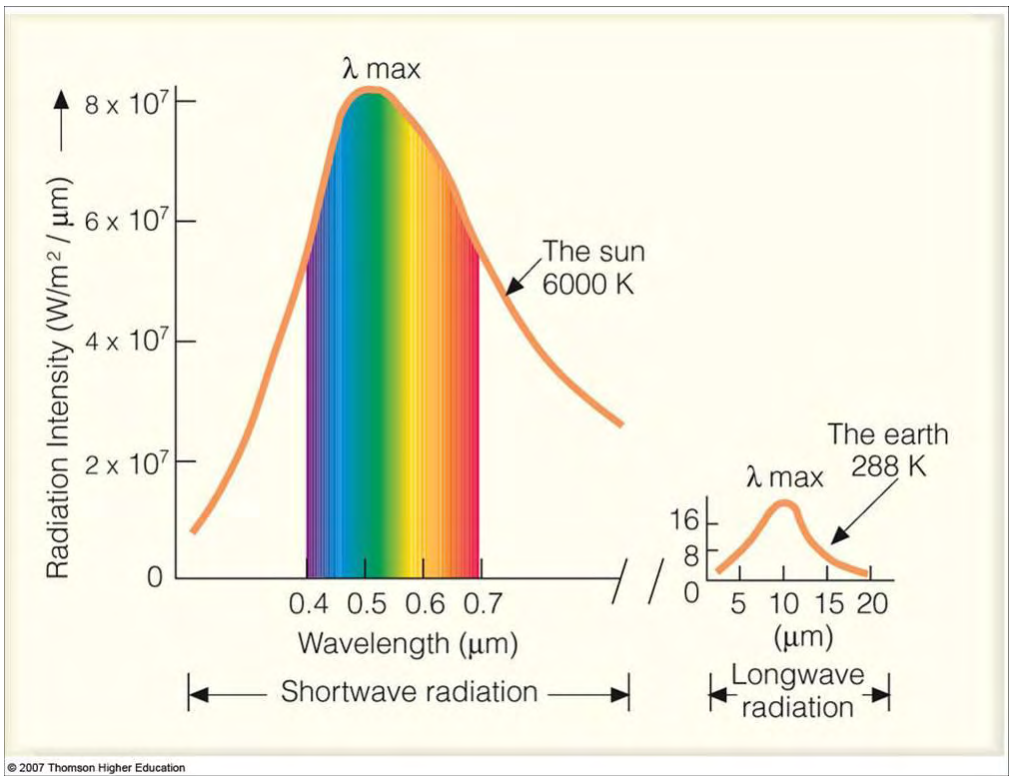

Figure 1-4 Main wavelength bands of solar radiation compared to the earth's radiation (adapted from [5]).

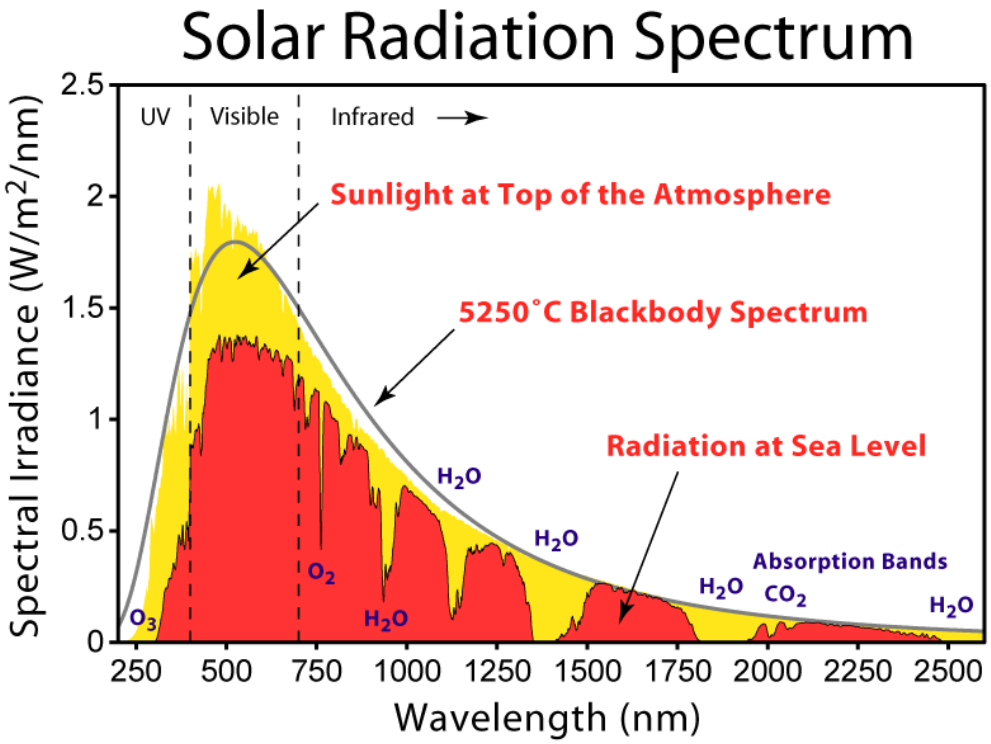

Figure 1-5 Solar irradiance outside the earth's atmosphere, denoted by Air Mass=0, and at sea level, for Air Mass=1.5 (adapted from [5]).

1.2 EFFICIENCY OF A PV MODULE

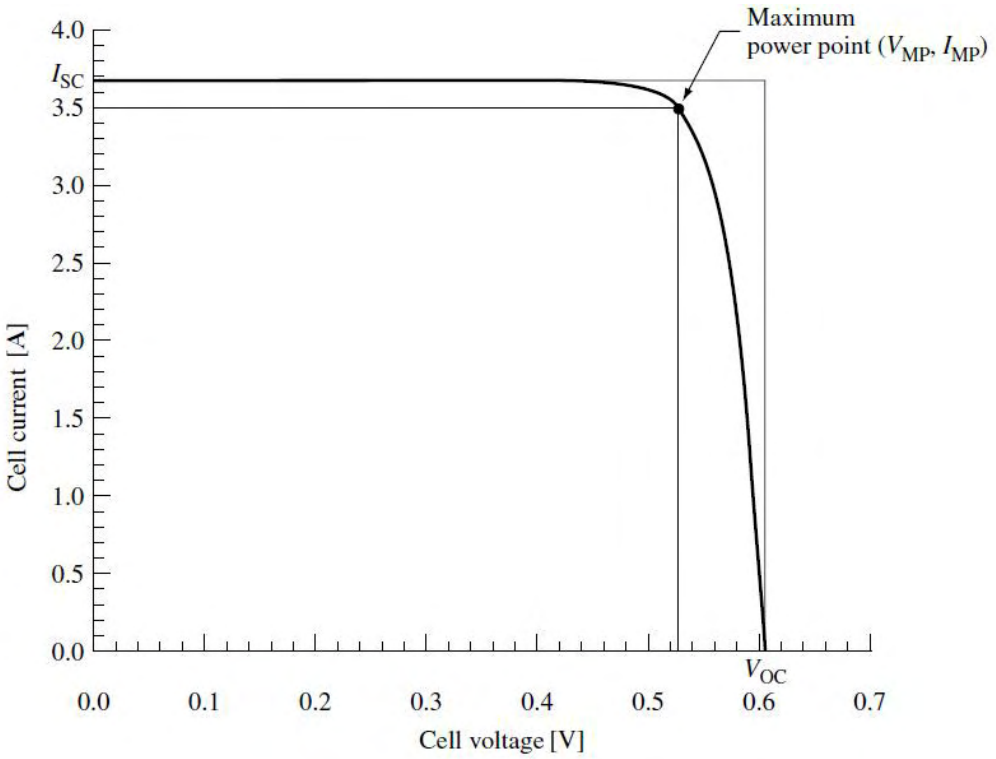

Figure 1-6 Current-Voltage characteristic of a silicon solar cell, adapted from [6]

The efficiency of a solar cell is defined as the ratio of electrical power produced to the incoming solar radiation:

$$n = \frac{P_{el\,max}}{P_{in}} \quad \textbf{(1.2)}$$

It is dependent on the incoming solar radiation intensity:

$$P_{in} = G_T * A \quad \textbf{(1.3)}$$

And the maximum electric power produced by the module [7]:

$$P_{max} = I_{Pmax} U_T \ln \frac{I_{Ph} - I_{Pmax} + I_0}{I_0} - I_{Pmax}^2 R_{PV} \quad \textbf{(1.4)}$$

where:

P_{max} max output Power
I_0 reverse leakage current
I_{Pmax} current at maximum Power Point
I_{ph} photon current
G_T radiation intensity

1.3 FACTORS AFFECTING OUTPUT OF PHOTOVOLTAIC MODULES

1.3.1 STANDARD TEST CONDITIONS

Solar modules produce direct current (DC) electricity, which is rated by manufacturers under Standard Test Conditions (STC). These conditions are easily created in a factory environment allowing consistent comparisons of products, but need to be modified to estimate output under common outdoor operating conditions. STC are: solar cell temperature = 25 ^{o}C, solar irradiance = 1000 W/m^{2} (often referred to as peak sunlight intensity, comparable to clear summer noon time intensity), and solar spectrum as filtered by passing through 1.5 AM (Air Mass) thickness of the atmosphere (ASTM). A particular solar module with rated output 100 W under STC, is understood to have a production tolerance of +/-5% of the rating.

1.3.2 ORIENTATION AND ELEVATION OF MODULES

The amount of irradiance depends on the latitude. A PV module will deliver maximum power when oriented perpendicular to the sun rays (see ANNEX II, Figure A. 4). This can only be achieved in tracking systems, but in most applications the modules are installed in a fixed position. Then the best time averaged irradiation has to be chosen as a compromise. In Central Europe the following boundary conditions are recommended: Orientation toward the south, but a deviation of 10^{0} to 15^{0} degrees does not appreciably reduce output. Inclination should be 30^{0} –42^{0} from horizontal for an optimized output over the whole year. If output is to be optimized for spring, fall, and winter, the inclination should be increased to 45^{0}– 60^{0}. Other geographic locations require different optimization rules. For the inclination β, in dependence on geographic latitude, the following rule for optimized yearly yield applies:

β = geographical latitude ± 10% [8] **(1.5)**

At 52^{0} north good results (>90%) can be achieved by orienting the modules between southeast and southwest, with system angles between 30^{0} and 50^{0} from the horizontal. Orientations between east and southeast, and between southwest and west, are fairly reasonable with system angles between 10^{0} and 30^{0} from horizontal. The irradiance will be reduced by around 15% of the maximum.

It is important to mention the weak sensitivity of the annual energy production to the inclination angle. A value of 0.2% loss for each degree of deviation from the optimum value is a rough approximation. This is also true with azimuthal orientation, where only a 0.08% loss occurs for each degree of deviation from the south. This means that many existing surfaces (roofs, car parks, etc.) are suitable for PV modules integration, even if their orientation differs considerably from the optimum [6] .

Table 1: Orientation factors for various roof pitches and directions [9]

	Flat	4:12	7:12	12:12	21:12	Vertical
South	0.89	0.97	1.00	0.97	0.89	0.58
SSE,SSW	0.89	0.97	0.99	0.96	0.88	0.59
SE, SW	0.89	0.95	0.96	0.93	0.85	0.60
ESE,WSW	0.89	0.92	0.91	0.87	0.79	0.57
E, W	0.89	0.88	0.84	0.78	0.70	0.52

1.3.3 MISMATCH AND WIRING LOSSES

The maximum power output of the total PV array is always less than the sum of the maximum output of the individual modules. This difference is a result of slight inconsistencies in performance from one module to the next and is called module mismatch and amounts to at least a 2% loss in system power. Power is also lost to resistance in the system wiring. These losses should be kept to a minimum, but it is difficult to keep them below 3% for the system. A reasonable reduction factor for these losses is 95%.

1.3.4 MODULE TEMPERATURE

Module output power reduces as module temperature increases. When operating on a roof, a solar module will heat up substantially, reaching inner temperatures of 50 - 75 ^{o}C. For crystalline modules, a typical temperature reduction factor recommended by the CEC (Commission for Environmental Cooperation) is 89%. For silicon solar cells the decrease at P_{max} with temperature being in conformity with the results of Van Dyke [10], is 0.65 %/K , whereas according to the theory, the electric output power of crystalline PV cells decreases by 0.4%/K of the temperature increase [11]. Thus, the changes of the output parameters: I, U, and P_{max} shows the influence of temperature as one of the two most important effects to be considered when using PV modules: irradiance and temperature. The solar irradiance role is well

understood and accounted when PV systems are designed, but the temperature effect is often neglected [12].

Module efficiency decreases as the temperature increases for mono and poly silicon cells but not for amorphous silicon cells. In many non-BIPV applications, modules are mounted on free standing frames with ambient air on both sides, allowing for cooling on both sides. In contrast, some BIPV applications install the modules in close contact to building material like roofs or wall insulation. The lack of circulating air increases the module temperature. Relative losses of >5% are possible. A good design criterion for mono or poly silicon applications is to allow as much cooling as possible by providing for air flow behind the module and minimizing the effect of insulation. This is not an issue for amorphous silicon modules [13].

1.3.5 DIRT AND DUST

Dirt and dust can accumulate on the solar module surface, blocking some of the sunlight and reducing output. Much of Greece has a rainy season and a dry season. Although typical dirt and dust are cleaned off during every rainy season, it is more realistic to estimate system output taking into account the reduction due to the dust buildup in the dry season. A typical annual dust reduction factor to use is 93%.

1.3.6 DC TO AC CONVERSION LOSSES

The dc power generated by the solar module must be converted into common household ac power using an inverter. Some power is lost in the conversion process, and there are additional losses in the wires from the rooftop array down to the inverter and out to the house panel. Modern inverters used in residential PV power systems have to peak at efficiencies of 92-96% indicated by their manufacturers, but these are measured under well-controlled factory conditions. Actual field conditions usually result in overall dc-to-ac conversion efficiencies of about 88-92%, with 90% a reasonable compromise. So a nominal “100-Watt module” output, when reduced by factors of production tolerance, heat, dust, wiring, AC conversion, and other losses will translate roughly to 68 Watts of AC power delivered by the house panel during the middle of a cloudless day (100 W x 0.95 x 0.89 x 0.93 x 0.95 x 0.90 = 68 W).

1.4 AIM OF THIS STUDY

Glazed double façade in the form of a PV-hybrid façade can be regarded as an architectural design concept suited to prestige buildings. In comparison with other high-quality façade types, the price is within the same range as that of ceramic-façades, which are often used on bank or insurance company buildings. In comparison to a representative granite façade, the PV-façade is more economical. The idea of combining photovoltaic and solar thermal collectors (PVT collectors) to provide electrical and heat energy is becoming increasingly popular. Although PVTs are not as prevalent as solar thermal systems, the integration of photovoltaic and solar thermal collectors into the walls or roofing structure of a building is another opportunity. Typically, commercially available PV modules are only able to convert 6–18% of the incident radiation falling on them to electrical energy, with the remainder lost by reflection or as heat (Bazilian et al.[14]). Van Helden et al. [15] noted that PV collector's absorb 80% of the incident solar radiation but convert only a small portion of this to electrical energy, the remainder being dissipated as thermal energy. Furthermore, they noted that the temperatures reached by PV cells are higher than the ambient temperature and that the efficiency of PVT is greater than the combined sum of separate PV and thermal collectors [16].

Advances in PV-technology allow today to use PV-modules for several additional purposes on a building, for example as a sky-light, a wall-cladding or a window-pane. In order for the PV-System to become an integral part of an overall concept of a building, a close collaboration among architects, civil and mechanical engineers will be necessary. Such collaboration is still missing [17]. Most of the experiments reported in the European literature were conducted at indoor facilities using artificial radiation sources [18] and, in general, small scale test façades [5], [19]. There exist relatively few buildings with double-skin façades and there is still little operation experience on their energy performance [1–9]. Results are conflicting regarding their actual energy saving potential (annual energy savings from negative to above 50% are reported in the literature). For instance, Wong et al. [20] found significant cooling energy savings resulting from the façade's ability to shield the building from solar gains and extract heat with natural airflow even on east and west- facing façades, while Gertis [11] claimed that existing Double Skin Facades simulations are not satisfactory [21].

The present study aims at further improving our knowledge and knowhow on the installation of optimized BIPV systems in buildings. This aim is accomplished by means of the following specific objectives:

- To define a novel ventilated PV façade concept integrated in the building's HVAC system in winter and service water heating system in summer.
- To design, construct and test a device considered as the building block of the proposed BIPV concept.

Testing of the device includes:

  - *Indoor testing by means of flow visualization and hot wire anemometry measurements in buoyancy flow conditions (natural convection) and forced recirculation conditions (forced convection).*
  - *Outdoor testing of the device in real insolation conditions in three modes of PV cooling system operation (natural convection cooling, forced recirculation cooling with low capacity and high capacity fan).*

- To perform CFD modeling of the device based on the validation from indoor and outdoor measurement results.
- To extract improved wall heat transfer coefficient correlations for the specific concept based on the experiments and CFD computations. To study possible improvements in heat transfer by design improvements of the backsheet.
- To perform building energy simulation for a full year on an hourly basis, of the proposed concept applied on a specific office building.
- To perform an economic analysis of the concept and its improved design, taking into account the renewable electricity and heat production of the building, which increase overall building's energy efficiency.

1.5 THESIS OUTLINE

The structure of this thesis is as follows (see Figure 1-7): A proposed ventilated façade concept is described in chapter 3, following an Introduction and a literature review on double skin façades and air flow and heat transfer inside the façade ducts.

Part A (Chapters 4, 5, 6), presents and discusses the results from the experimental and computational study of the basic building block of the proposed concept.

Part B (Chapters 7, 8 and 9) presents and discusses the results from the building energy simulation and economic analysis of the proposed concept applied to a small office building.

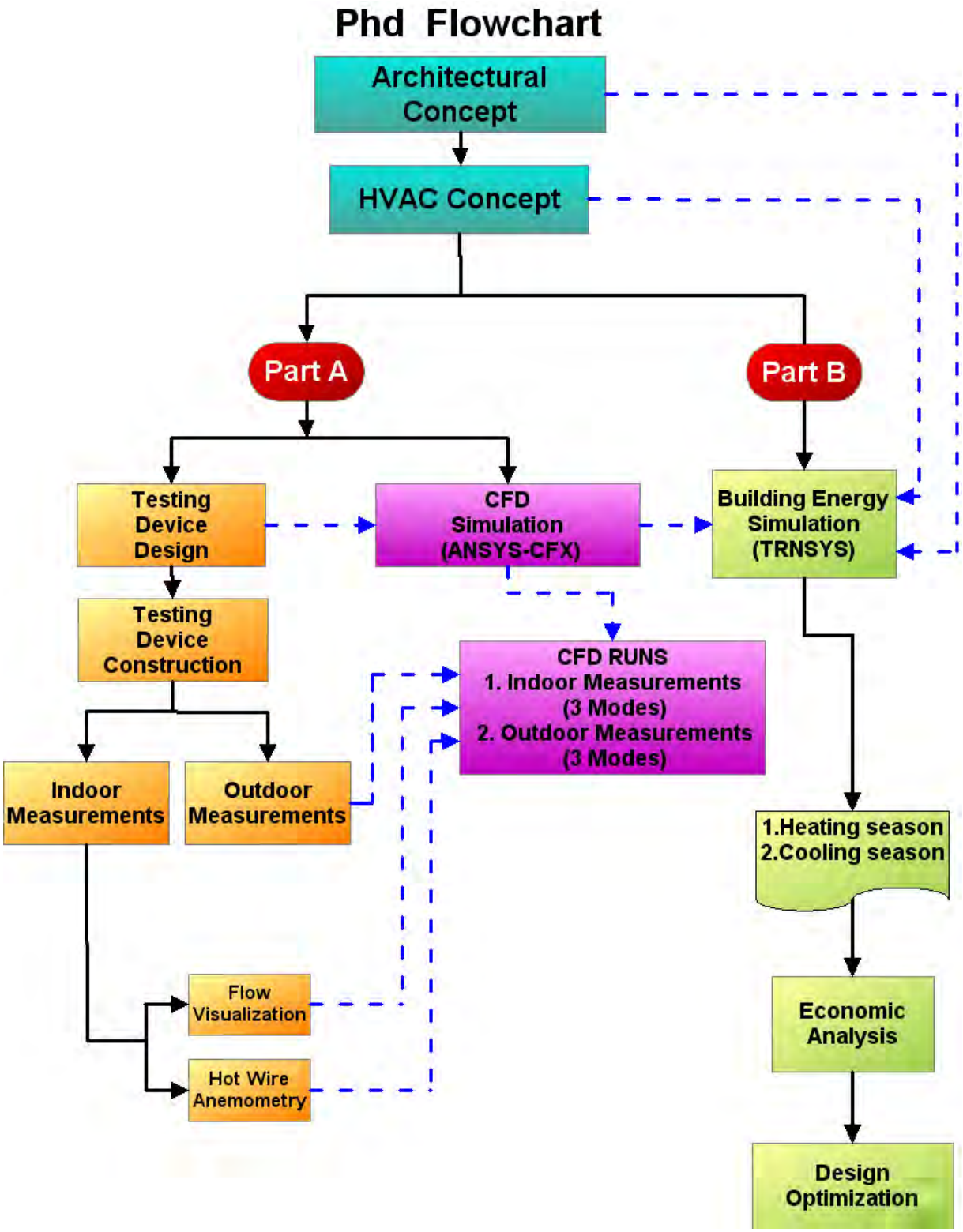

Figure 1-7 Flowchart of this thesis

1.6 NOVEL FEATURES OF THIS THESIS

- Proposal of an improved building concept to exploit BIPV in HVAC system.
- Specially designed test rig for testing the building block of the concept.
- Transient experiments of the module in real insolation conditions.
- Combination of hot-wire anemometry measurements with 3D CFD computations in the study of the air flow field and the determination of heat transfer coefficients.
- Improved building energy simulation of the concept.
- Proposed design optimization of the backsheet to improve energy efficiency of the concept.

CHAPTER

2

2 LITERATURE REVIEW

This chapter offers a survey of relevant literature. A brief summary of the chapter's organization is presented in the following paragraphs. We start with a brief presentation of the concept of double skin façades in architecture.

Next we focus on applications with PV modules forming an independent external layer. In most of these applications the PV panels are freely fixed on the outer shell of the building, thus allowing atmospheric air to cool the backsheet of the modules.

In section 2.3 we focused on double façades where the PV module forms the outer part of a building cell and the backsheet of the module is cooled by buoyancy air flow, where the air could be introduced from outdoors or indoors of the building.

In section 2.4, we concentrate on the concept of ventilated PV façade, where the PV modules' cooling efficiency is strengthened by forced convection, and the heated air by this process is exploited for heating or cooling of the building.

2.1 PV IN ARCHITECTURE

PV panels are usually placed on the roof and seldom on south-facing building walls. PV cells convert sunlight into electricity (with typical efficiencies of 6–15%) with the remainder of the solar energy being converted into heat. The roof top modules are placed at a distance from the roof to allow rejection of the heat that is not transformed to electricity. During the last decade, the idea of exploiting also the rejected heat of the photovoltaic modules is gaining attention. At the project "Haus der Zukunft" in Schmidling (near Linz, Austria), this residual heat is also used for

direct heating of the building (see Figure 2-1 and Figure 2-2 below). An air cavity has been created underneath the PV modules, through which warm air (heated by PV modules) is exhausted. The solar system based on air collectors and thermal storage provides almost half of the required energy needed for heating. Heated air is leading through hypocausts (hollow brick ducts in concrete) into the massive ground floor and thus heats the floor (to 25°C). When irradiation is low, two heat pumps (an air-air heat pump or a ground-coupled heat pump) will produce the necessary heat. [22]

Figure 2-1 "House of the future" in Schmidling in Austria

Figure 2-2 The hybrid collector provides warm air to the heating system in the house of future

Figure 2-3 PV system integrated in a façade (adapted from [23])

Façades are basically constructed using in situ bricklaying or concrete constructions, prefab elements or structural metal façades that are mounted in place. Concrete constructions form the structural layer and are covered with insulation and a protective cladding [24]. This cladding can be wood, metal sheets, panels, glass or PV modules. For luxury office buildings, which often have expensive cladding, cladding with PV modules is not more expensive than other commonly used materials, for example, natural stone and expensive special glass. These cladding costs around \$1000/m^2, which is comparable to the cost of the PV module today [25].

Structural glazing or structural façades are constructed using highly developed profile systems, which can be filled with all types of sheeting, such as glass or frameless PV modules (Figure 2-3). Façades are very suitable for all types of sunshades, louvers and canopies [26]. There is a logical combination between shading a building in summer and producing electricity at the same time. Architects recognize this and many examples of PV shading systems can be seen around the world. A canopy (entrance protection) on the sunny side of a building is a good place for BIPV systems (Figure 2-4) thus providing shade, protection from rain, as well as electricity. Solar shading with PV modules as part of a vertical louver system on the west façade of the SBIC office building in Tokyo is shown in Figure 2-5. The transparent vertical louvers, with a total capacity of 20.1 kWp, were manufactured by Atlantis Switzerland.

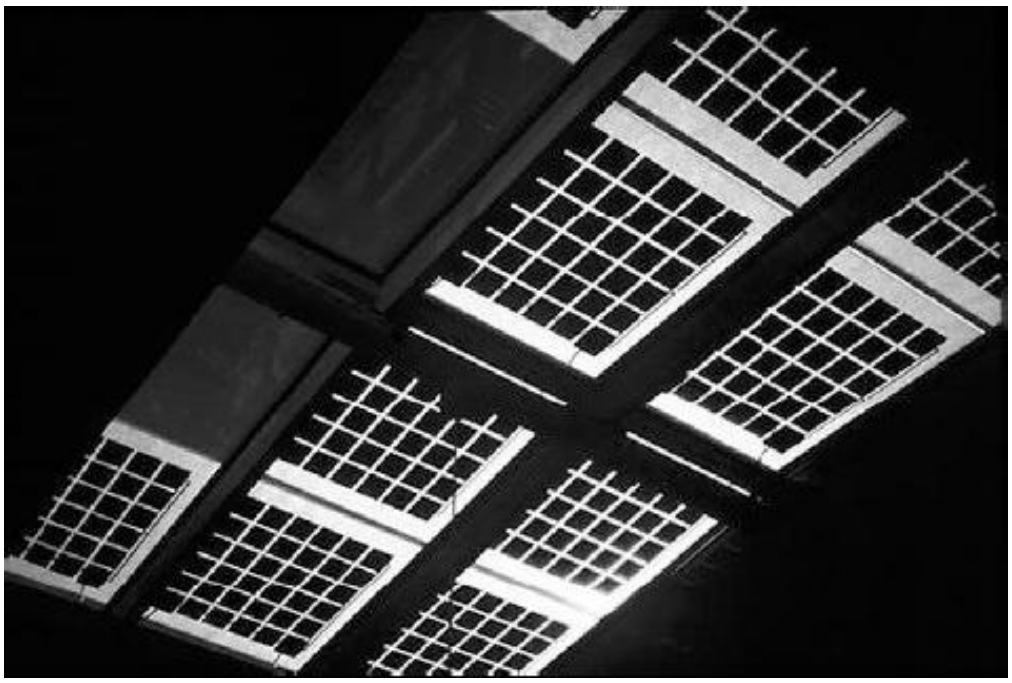

Figure 2-4 Thoreau Center in San Francisco (adapted from [25]).

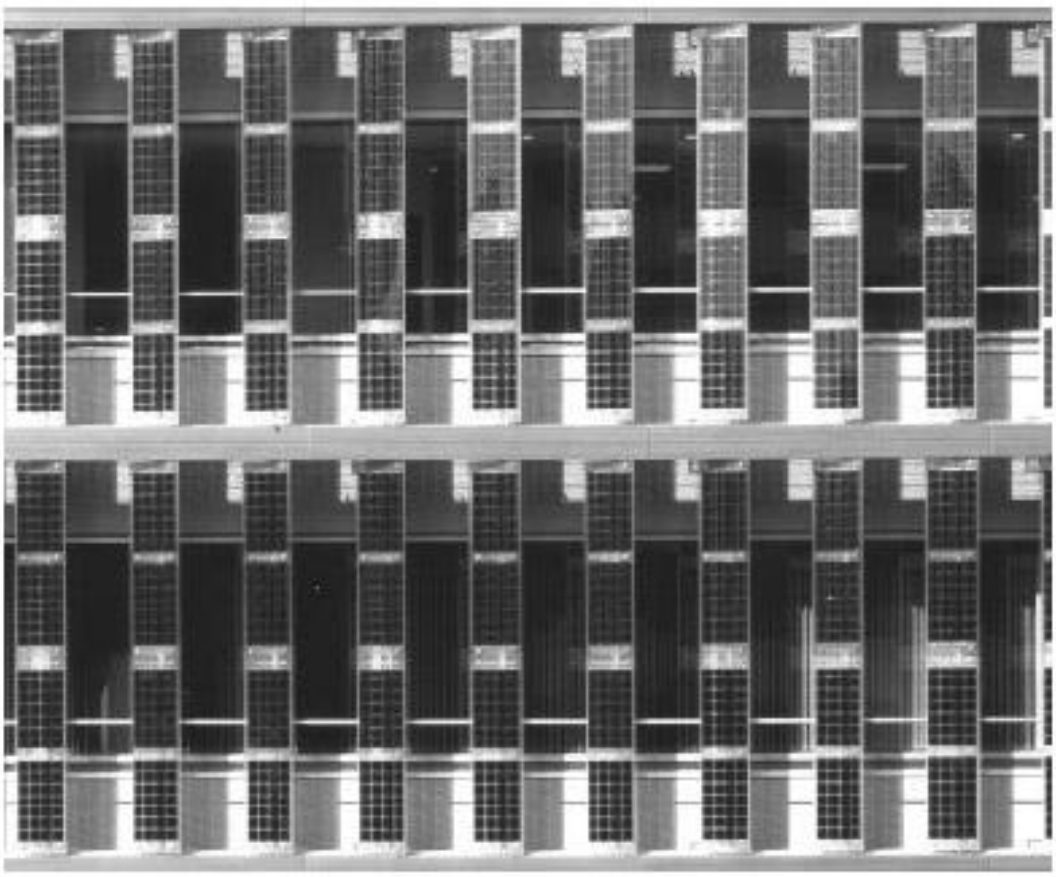

Figure 2-5 PV modules as part of a vertical louver system on the west façade of the SBIC office building in Tokyo, Japan [27].

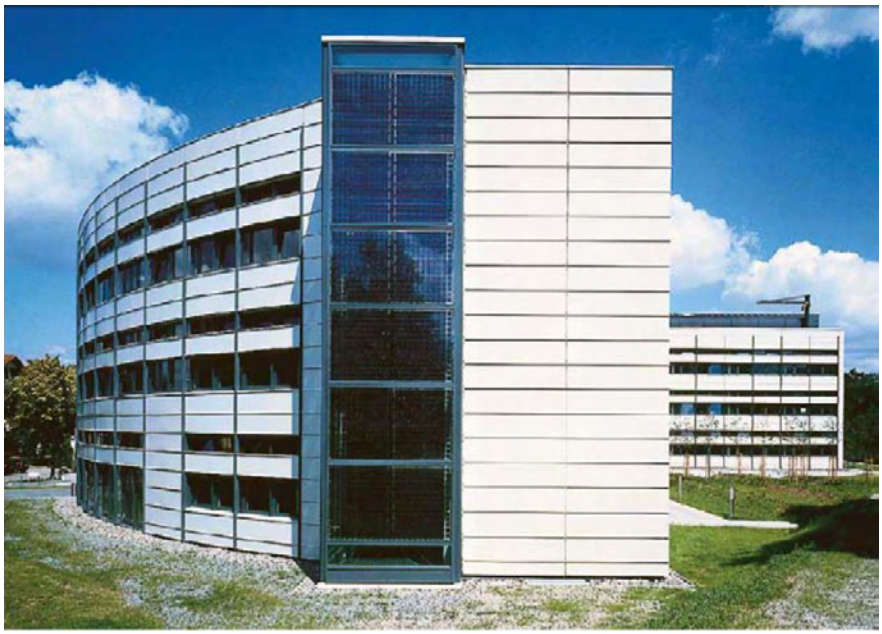

Figure 2-6 The PV façade at the office building of the Fraunhofer ISE, Freiburg.(adapted from [8])

Figure 2-7 ATERSA ventilated façade.

ATERSA and TAU Cerámica have finished installing a patented Ventilated Façade integrating solar power photovoltaic modules connected to a 6 kWp electricity grid at the headquarters of TAU Cerámica, located in Castellón de la Plana. The installation consists of a new ventilated façade system integrated with a ceramic coating, where ceramics are complemented by using photovoltaic modules of exactly the sameSize

The assembly procedure is very simple, both in new and finished buildings, as the photovoltaic modules are placed just like the ceramic units (the tiles just have to be replaced by the photovoltaic modules). Once the perimetric profile of the module has been modified to the same size as the ceramic unit, these are arranged to stay perfectly flush on the active side with the ceramic tile. The result is an attractive

combination of modules and ceramic plates, where design and functionality merge together in one concept.

2.2 DOUBLE SKIN FAÇADES

Double skin façade appeared in late 1849 [28]. At first, the construction of double skin façade began based on aesthetic standards. However, after some time passed, the overheating of glass building, leaded to search for solution in order to face heating and cooling issues.

Jean-Baptiste Jobard, director of the industrial Museum in Brussels (1950), described an early version of a mechanically ventilated multiple skin façade. He mentions how hot air in the winter should be circulated between two glazing's, while in summer it should be cold air. The evolution of Double Skin Façades is described in several books, reports and articles (see for example references [28-31]).

Double skin façade is an arrangement with a glass skin in front of the actual building façade. A double glazed façade system usually consists of a single outer pane, an intermediate enclosed air space and an inner window.

A brief overview of the several types is given by Gertis [32], Lang [33], Zollner [34] , Lee [35] and Fux [30].

Oesterle et al.,[36] categorize the Double Skin Façades, mostly by considering the type (geometry) of the cavity. Very similar is the approach of Saelens [28] and E. Lee et al. [37] in *"High Performance Commercial Building Façades"*. These types are listed below:

- Box window type: In this case horizontal and vertical partitioning divide the façade in smaller size and independent boxes.
- Shaft box type: In this case, a set of box window elements are placed in the façade. These elements are connected via vertical shafts situated in the façade, ensuring an increased stack effect.
- Corridor façade: Horizontal partitioning is realized for acoustical, fire security and ventilation purposes.

Gertis [32] studied double façades taking into consideration physical parameters (such as acoustic performance, fluid and thermal characteristics, energy efficiency, light penetration and fire protection). He concluded that double glazed façades - except for special cases - are unsuitable for the northern European climate. Moreover, they are much too expensive.

Zöllner et al. [34], [38] described the experiments performed in an outdoor double-skin façade test. In their conclusions, the authors stated that solar radiation induced mixed convection fluid flow in double skin façades, depending strongly on the height of the box window, the distance between external and internal façade and the height of the air inlet and outlet. Due to the circulatory motion of the flow, the highest temperatures occur in the core of the air gap. Turbulent mixed convection in air gaps with a distance of S< 0.6m, analyzed using the ‘‘channel model’’ for the computation of the average Nusselt number as a function of the average Archimedes number, whereas the ‘‘plate model’’ has to be employed for situations within an air gap of distances of S > 0.6 m.

Gratia and de Herde [19] studied, for eight standard days (week days), the thermal behavior of a building with and without double-skin. Simulations were realized with TAS software. Case study analysis shows that, for this building, the use of a double-skin façade decreases the heating loads and increases the cooling loads. Moreover, if the double-skin is sunny, the air temperature increases very quickly. This air can be used as ventilation air of the shaded zones. During the summer, when the sun is shining, it is difficult to apply the strategy of day natural ventilation. Indeed, cross day ventilation by extraction through the double-skin is delicate and is a function of the wind orientation and of the building wind protection. Moreover, the hot air layer prevents the natural cooling of the building. Even, if the double-skin is largely ventilated, the air temperature is always some degrees higher than the outside temperature. On the other hand, when the sky is cloudy (or during the night) the cross-ventilation is totally effective, even if the direction of air flow is reversed. Indeed, it is not important since the double-skin temperature is nearly the same with the outside temperature. In any case, these results cannot be generalized for other configurations of double-skin façades and cannot provide sufficient guidelines for the technical design of a double-skin. If the double-skin is oriented towards the South and is not ventilated, temperature in this one would reach 47 ^{o}C if there are no shading devices, temperature would reach 52 ^{o}C if south windows are equipped with shading devices. Indeed, the greenhouse effect is increased due to the blinds [39].

Hien et al. [40] investigated the combined effects of double glazed façade with a ventilation system on the energy consumption, thermal comfort and condensation aspects and compared them to single glazed façade system for a typical office building in Singapore. TAS and CFD software was utilized to calculate energy consumption, thermal comfort and condensation for a single glazed façade building as well as a double glazed façade building. The simulation results showed that double glazed façade with natural ventilation was capable of minimizing energy consumption as well as to enhancing the thermal comfort.

Balocco applied non-dimensional analysis in the context of naturally ventilated façade. The method presented in [41] can be used to analyze and compare thermal energy performance of different façade systems like solar chimneys for example. The results can be useful for building designers to have an indication of heat flux throughout the wall as a function of simple parameters without modeling fluid flow and heat transfer by CFD or complex numerical simulation programs with reference to experimental validation. The proposed method can be applied to all naturally ventilated façade typology.

Yılmaz and Cetintas [42]¸studied the basic thermal performance of double skin façade in Constantinople. For the selected urban case, single skin façade's heat loss is 40% higher than the respective double skin façade's. Different glass types, different transparency ratios and component's different thermal properties would give different results. The introduced method was developed to be used for thermal evaluation of double skin façade's during the design process of new office buildings, as well as for energy efficient renovation of existing office buildings. Their method does not include the cost analysis calculations.

Fux [30] investigated by means of indoor measurements and CFD computations, the convective heat transfer rate in both internal sides of a double façade system.

Hamza [43] in his study adopts a quantitative analytical methodology to test and refute the hypothesis on the efficiency of double skin façades as a façade technology suitable for reducing air-conditioning loads in hot arid climates. Transparent double skin façades are predicted to increase cooling loads in office buildings in hot arid areas when compared to a single skin façade with reflective glazing. However, such a disadvantage may be neglected if the double skin façades are to be used in cases where protection from the environment is needed to preserve front view of historic building.

Höseggen et al. [44], used a planned office building in the city-center of Trondheim, Norway, as a case study for considering whether a double-skin should be applied to the east façade in order to reduce the heating demand, thus making the double-skin façade a costs-saving investment. The building is modeled both with and without a double-skin façade with the building energy simulation program ESP-r [45]. The simulation results indicate that the energy demand for heating is roughly about 20% higher for the single-skin façade with the basic window solution than to the double-skin alternative. This study shows, contrary to some other studies on this subject, that application of a double-skin façade decreases the heating energy demand, without significantly increasing the number of hours with excessive temperatures. Moreover, using the cavity of the double-skin as a pre-heater for the air supply, further savings may be achieved. However, from an economic point of view, the energy savings will not balance that the additional costs the double-skin façade construction implies.

Manz [46, 47] investigated heat transfer by natural convection of air layers within vertical, rectangular cavities with a predefined aspect ratio. The study focused on tall, vertical cavities in building elements such as insulating glazing units, double skin façades, doors, façade-integrated solar collectors and transparent insulation panels. Using as a starting point the results of previous studies that date back to the fifties [48], he performed CFD computations with a revised k-ε turbulence model for cavities with aspect ratios (height/depth) of 20, 40 and 80, and Rayleigh numbers between 1000 and 10^6. His results compare well with previous experimental and theoretical results in the laminar and turbulent flow regimes. Except for one calculation, no calculated Nusselt number deviates more than 20% from the empirical correlations. Deviation is even less than 10% for an aspect ratio of 20. This study improved the starting position for future applications of the code to more complex cases of façade elements, where less or even no experimental data are available in literature. Selkowitz [49] suggests that for a single air space, the minimum conductance is typically reached with an air space thickness of 0.6 to 0.2 cm. Once the boundary layer regime has been reached, further increases in air space thickness show little or no decrease in air space conductance.

2.3 DOUBLE SKIN FAÇADES WITH INTEGRATED PHOTOVOLTAIC PANELS

The first installation of building-integrated photovoltaic (BIPV) was realized in 1991 in Aachen, Germany [50] (Figure 2-8). The photovoltaic elements were integrated into a curtain wall façade with isolating glass. Today, photovoltaic modules for building integration (BIPV) are produced as a standard building product, fitting into

standard façade and roof structures these elements creating a whole new market. Since then, building integration is one of the fastest growing market segments in photovoltaics, and several other large-scale projects are under construction or in the planning phase.

Clarke et al [50] in their study from a combined experimental/simulation analysis of a PV façade have indicated:

(i) An operational electric efficiency less than the peak published data: 12% compared to 15%.

(ii) That the utilization of thermal energy significantly increases the system efficiency.

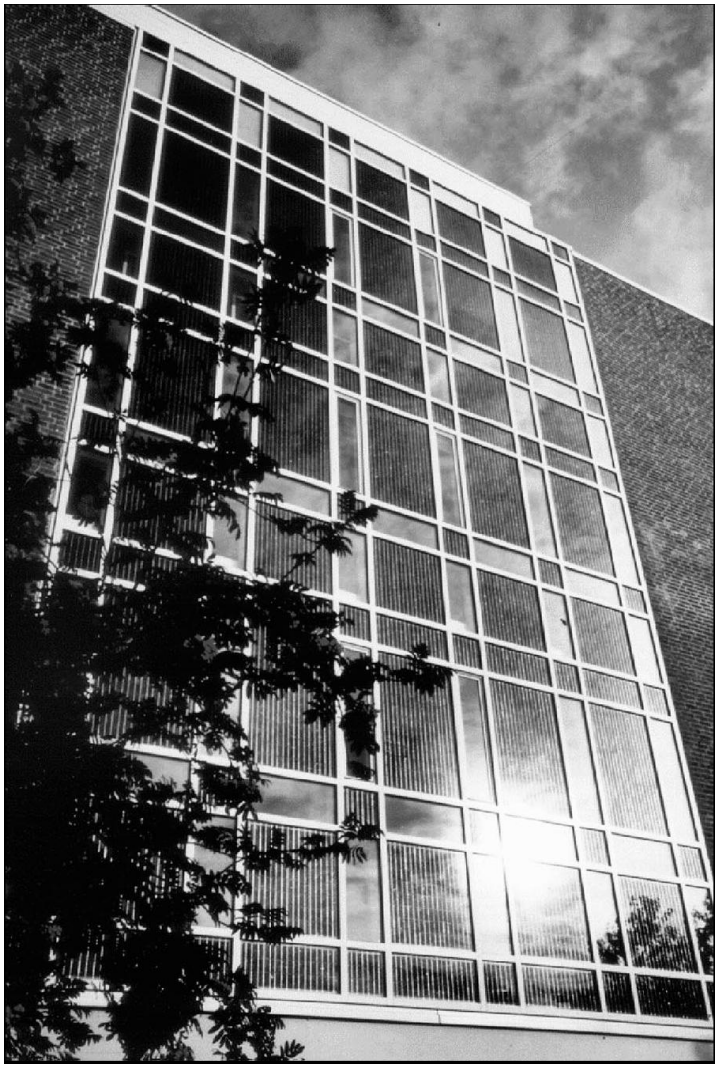

Figure 2-8 PV-façade with isolating glass (Utility company Aachen, Germany) adapted from [50]

Bazilian et al. [14] investigated thermographically a residential-scale building with an integrated photovoltaic (BIPV) cogeneration system. An Infra-Red (IR) thermographic analysis was conducted on a BIPV roofing element to graphically and numerical investigate its heat transfer properties. The system is being used to test the feasibility of a heat recovery unit that will utilize the waste heat from the back of the array while cooling the PV cells. The interior of the BIPV array was found to be distinctly hotter than the surrounding roofing on a clear sunny day. This will impact both the building envelope and the PV cell thermal performance. It will also provide a graphical representation to view the nature of BIPV systems that use typical PV module construction or architectural glass–glass construction. The thermographic images help to calibrate the numerical models being written for the cogeneration system by deriving surface emissivity. Data from on-site temperature transducers were also validated. An impetus for removal of heat off of the back of BIPV modules was shown. They conclude that thermographic investigation is a useful tool for examining various components under normal system operation.

Davis et al. [13] developed a new technique to compute the operating temperature of cells within building integrated photovoltaic modules using a one dimensional transient heat transfer model. The resulting predictions are compared to measured BIPV cell temperatures for two single crystalline BIPV panels (one insulated panel and a second uninsulated panel). Finally, their results are compared to predictions using the nominal operating cell temperature (NOCT technique).

Chow et.al [51] investigated Building-integrated photovoltaic and thermal applications in a subtropical hotel building. They present numerical analysis via the ESP-r building energy simulation software [45]. The results showed that, effective cooling of a PV panel can increase the electricity output of solar cells. This can be important for PV installations in warm climatic regions. The effectiveness of cooling by means of a natural ventilating air stream has been studied numerically based on two cooling options with an air gap between the PV panels and the external façade: (i) an open air gap with mixed convective heat transfer (PV/C), and (ii) a solar chimney with a buoyancy-induced vertical flow (PV/T). Their simulation results were compared and further evaluated by comparing with additional simulation results of the conventional BIPV option and the bare external façade without PV features as a base case. The results indicate that appears to be no significant difference in electricity output comparing the three PV options. This is because the indoor space with 24-h temperature control provides continuous cooling of the solar cells through the external façade, and hence increases the outputs of BIPV as well as PV/T, during the morning period without direct solar radiation. Therefore the weather conditions and the operating mode of the building will have a determining effect on the PV

productivity. In terms of annual electricity output, PV/C is marginally the best and BIPV the worst. In terms of the effectiveness in space heat gain reduction, the PV/C and PV/T options appear superior to the BIPV option. Hence they are preferable than BIPV for applications in the subtropical climate. The choice between PV/C and PV/T will depend on whether the collected heat energy in the PV/T option is useful or not. Without a ready use for the heat energy, PV/C appears to be the proper choice because of its simple design, its greater effectiveness in reducing the space cooling energy consumption, and the resulting small improvement in the PV cooling performance.

The summer performance of single and double façades with sun shading systems was analyzed both experimentally and by computer simulation by Eicker et al [52]. It was shown that externally shaded single façades and internal gap shaded double façades can effectively reduce the total energy transmittance to a building in summer. The highest energetic priority is always the reduction of short wave solar irradiance, which is the dominant energy flow. With measured g-values as low as 7% with even slightly open blinds, this condition can be fulfilled by both single and double façades. Secondary heat flows only play a role, if no shading system is used and are otherwise negligible. If the façade is used for providing fresh air to the room with air exchange rate below two per hour, additional cooling loads of 2 - 5 $kWhm^{-2}$room occur compared to ambient air ventilation (for blind absorption coefficient of 10 and 30%, respectively). All results were obtained for moderate German summer climate conditions, where even in summer ambient temperatures are not always above room temperature. In climates with higher ambient air temperatures, summer ventilation through a double façade will increase room cooling loads even more and cannot be recommended. Also secondary heat fluxes will obviously be higher, but should not be significant, as long as a shading system is used.

Anderson et al. [16] studied the design of a novel building integrated photovoltaic/thermal (BIPVT) solar collector. The PV is directly integrated into the roof of a building. From the results presented it has been shown that there are a number of parameters such as the fin efficiency, the thermal conductivity between the PV cells and their supporting structure that can be varied in the design of a BIPVT collector to maximize performance. The fact that the collector base material made a little difference to the thermal efficiency of the BIPVT suggests that lower cost materials, such as steel, could be utilized for these systems. The disadvantage of using steel is that the electrical efficiency would be decreased marginally.

Seng et.al [53] examined economic, environmental and technical analysis of building integrated photovoltaic systems in Malaysia. Under the current regulatory and commercial frameworks, the owners of PV systems are not able to make any financial return on their investment of the PV systems even after the government has provided a subsidy of up to 70% of the PV capital. Therefore, the current size of PV market is very small; only about 470 kW is owned by a small number of domestic customers. Therefore, it may be necessary for the government and the utility companies to consider offering a higher tariff of PV electricity to the PV owners in order to promote PV installations. The government or utility company can save RM 10.26 million of natural gas and avoid a total greenhouse emission of 35,140 tones over the lifespan of 2MWp PV systems. The PV owners can create additional income streams by selling CERs to developed countries in addition to the reduction of their maximum demand charges every month. The utility companies can avoid or defer the needs of upgrading their networks with minimum concern for the voltage rise issues. One of the possible challenges faced by the PV sectors is that the price of PV modules may still be high even after First Solar has been established. Another challenge is that the yearly yield (kWh) of existing PV systems is diminishing every year. One of the possible reasons could be the growth of air pollutants in the atmosphere of major cities that reduces the intensity of the solar radiation on the ground.

The results in terms of wall temperatures show that the effect of increasing the channel spacing is to reduce, on an average base, the working temperatures for all the studied cases. It was also observed a typical temperature profile during uniform heating on a single wall configuration at the higher spacing (d = 0.16 and 0.1), where the wall temperature reaches a maximum at vertical positions of about 0.8m. At the shortest separating distances (d = 0.05 and 0.03), the above temperature profiles show an almost monotonic trend. Local Nusselt values were expressed in terms of the vertical coordinate for the uniform heating case while, in the other cases, they were evaluated according to the local distance from the leading edge heated zone. Comparisons with literature correlations were finally performed with reference to the wall average Nusselt numbers, and it was demonstrated that uniform heating correlations can be successfully employed provided that a proper dimensionless wall distance is applied for any particular heating mode considered.

Gan [54] employed CFD to assess the effect of the size of air gap between PV modules and the building envelope on the PV performance in terms of cell temperature for a range of roof pitches and panel lengths and to determine the minimum air gap that is required to minimize PV overheating. To reduce possible overheating of PV modules and hot spots near the top of modules he suggested a

minimum air gap of 0.12–0.15 m for multiple module installation and 0.14–0.16 m for single module installation depending on roof pitches.

2.4 AIR FLOW IN PHOTOVOLTAIC FACADES

Sandberg and Moshfegh [55] analyzed numerical the mass flow rate, velocity, temperature rise and location of neutral height (location where the pressure in the air gap is equal to the ambient pressure) in air gaps behind solar cells located on vertical façades. The flow was assumed to be turbulent or laminar and behave as bulk flow, i.e. the velocity and temperature are assumed to be uniform across the air gap and only a function of the height channel. For turbulent flow and constrained flow, i.e. the flow is controlled by the losses at the inlet and outlet. The mass flow rate, velocity and volumetric flow rate follow a power-law relation with the effective heat input raised to an exponent equal 1/3. The temperature increase between the inlet and the outlet is proportional to the heat input raised to 2/3.Laminar flow might occur in very narrow air gaps. At the laminar flow, for special cases, there is a simple relation between the heat input and flow variables. For a given heat input, the maximum flow rate is obtained by increasing the height of the air gap until a balance between friction and buoyancy is obtained. Experiments were conducted with air gaps with an aspect ratio from 28 to 108. With both ends open and with an opening area equal to the area of the air gap the agreement was between10% and 20%. Better agreement was obtained for higher aspect ratios. This discrepancy between theory and measurement scan partly be attributed to experimental difficulties. The theoretical predictions require more parameters to be determined, which increases the uncertainties in the theoretical predictions. Therefore, measurements with higher accuracy are required to provide better estimates of the true error.

A procedure for modeling double façades made of glass layers with a ventilated mid-pane shading device —comprising a spectral optical and a computational fluid dynamic (CFD) model—is described by Manz [56]. The simulation results are compared with data derived from an experimental investigation of a single-story glass double façade (GDF) with free convection, incorporated in an outdoor test facility. It is shown that, for a given set of layers, total solar energy transmittance can easily vary by a factor greater than five. Hence, for reliable prediction of the total solar energy transmittance of a designed façade, models are needed that factor in all the relevant parameters. A spectral optical model (is needed where properties depend strongly on wave length) combined with a CFD model that includes

convection, conduction and radiation, is therefore, recommended for analyzing and optimizing glass double façades. With a well-designed GDF element with free convection, the secondary internal heat transfer factor can be reduced to values below 2%. Total solar energy transmittance values lower than 10%—recommended for highly glazed building can be readily achieved with such façades.

However, use of these models even for GDF with free convection only is questionable. This is because gaps between cavities, airflows through shading devices, etc. cannot be modeled using a simplistic approach. There circulations that frequently occur in real façade cavities are inherently impossible to model using a piston-flow approach.

For multistory buildings with a GDF, an increase, both in temperatures in the façade cavities and in total solar energy transmittance g is observed as a function of height. In other words, any external thermal coupling between the stories will mean that the whole façade has to be analyzed. The temperature increase as a function of height might be reduced by wind. Here, however, a construction where inlet and outlet openings are not vertically aligned but staggered horizontally is advantageous. To preserve the same inlet and outlet opening areas—given the reduction in the horizontal direction—the vertical dimension of the opening must be increased. A three-dimensional flow pattern is then obtained inside the façade cavities. It was observed in the experimental investigations that short-term wind fluctuations can reverse the direction of air flow in the façade cavities by 180 ◦ and increase the air change rate. Yet, provided they are limited to short periods, such changed airflow patterns are likely to have only a minor impact on energy flows. A windless situation should be assumed as a worst-case scenario for overheating. Measured and calculated temperature distributions showed that the maximum air temperature in a façade cavity occurs near the top, where electric motors for the shading devices are usually located. Depending on the quality of the optical and thermal design of the construction and the façade orientation, air temperatures of more than 80 ◦ C may occur on days with high solar irradiation and high outside temperatures. This has to be considered when choosing and locating electric motors for the shading devices.

Pappas and Zhai [21] briefly reviewed the primary parameters for a double skin façade (DSF) design. This research has developed an iterative modeling process with integrated CFD and building energy simulation program (BESP) to analyze the thermal performance of double skin façade with buoyancy-driven airflow. The model was validated using measured data from Dirk Saelens taken at the Vliet Test Cell in Leuven, Belgium, and errors are calculated with root mean differences for air flow

rate prediction of 2.7 m^3/h (or 9%), and 2.0 ^0C (or 15%) for temperature stratification. The study investigated the energy performance and potential fluential factors of such a DSF. The modeling process was used to develop correlations for cavity air flow rate, air temperature stratification, and interior convection coefficient that can provide a more accurate energy analysis of a DSF with buoyancy-driven airflow within an annual building energy simulation program than is currently possible. The correlations are established only for DSFs with solely buoyancy-driven airflow.

Fossa et al [57] studied the natural convection in an open channel in order to investigate the physical mechanisms which influence the thermal behavior of a double-skin photovoltaic (PV) façade. To this aim, a series of vertical heaters is cooled by natural convection of air flowing between two parallel walls. Different heating configurations are analyzed, including the uniform heating mode and two different configurations of non-uniform, alternate heating. The experimental procedure allows the wall surface temperature, local heat transfer coefficient and local and average Nusselt numbers to be inferred.

Sarhaddi et al [58] developed an analytical model to investigate the thermal and electrical performance of a solar photovoltaic thermal (PV/T) air collector. Some corrections are done on heat loss coefficients in order to improve the thermal model.

Infield et al [59] investigated different approaches to estimate thermal performance of ventilated photovoltaic (PV) façades. Heat loss and radiation gain factors (U and g values respectively) has been employed to take account of the energy transfer to the façade ventilation air. Four terms describing ventilation gains and transmission losses in terms of irradiance and temperature components are defined, which characterize the performance of the façade in total. Steady state analysis has been applied in order to express the above parameters in terms of the detailed heat transfer process within the façade. This approach has been applied to the ventilated PV façade of the public library at Mataro, Spain. Monthly U and g values have been derived and the associated thermal energy gains calculated for various climates. An even simpler approach, based on solar collector thermal analysis has been presented which, for the case of Mataro, compares reasonably well with the more sophisticated approach. Summer and winter energy yield calculations carried out on this basis have been compared to the four parameter approach. The Mataro building is marginally less energy efficient than had it been constructed with a conventional windowed south wall. The building does, however, have other

advantages in terms of the quality of the interior space, the contribution of natural light, and the aesthetically pleasing integration of PV. Moreover, the ventilated façade ensures that the PV modules do not reach high temperatures (generally below 45^{o}C) with the well-known associated improvements in performance.

Balocco [60] provide a steady state calculation model to simulate and study the energy performance of a ventilated façade and it can be used to compare different typologies façade systems. Results show that it is possible to obtain a sensible solar cooling effect when the air cavity width of the chimney is wider than 7 cm.

Mei et.al [61] studied the thermal performance of a specific type of ventilated PV façade, consisting of a PV panel, an air gap and an inner double glazing. A dynamic thermal model based on TRNSYS developed, for a building with an integrated ventilated PV façade/solar air collector system. The building model developed has been validated against experimental data from a 6.5 m high PV façade on the Mataro Library near Barcelona. Based on the developed building model, the heating and cooling loads for the building, in different European locations, have been estimated. From both measurement and simulation, it can be seen that the PV façade outlet air temperature reaches around 50 ^{o}C in summer and 40 ^{o}C in winter. Twelve percent of heating energy can be saved using the pre-heated ventilation of the air for the building location in Barcelona in winter season. For Stuttgart and Loughborough, only 2% heating energy can be saved, although of course the design was not made within these locations in mind. Indeed it is clear that for such northern latitude, a far higher proportion of solar air collector area would be appropriate.

Manz et al [62] developed a procedure for modeling glass double façades (GDFs) comprising a spectral optical and a computational fluid dynamic model. Simulated results are compared with data derived from an experimental investigation of two mechanically ventilated GDFs built in an outdoor test facility. It is shown that simple models assuming piston- flows can lead to inaccurate results. Hence, a combination of experiment and simulation is considered the most reliable approach for analyzing GDFs. Boundary conditions have to be carefully set in CFD simulations because they affect the total solar energy gain of the room and the temperature of the inner pane. Piston-flow models are not recommended for analyzing mechanically ventilated GDFs.

Liao et al [63] studied the heat transfer and fluid flow in a building-integrated photovoltaic-thermal system intended for single story applications with a two-dimensional CFD model. The realizable k-e model is used to simulate the turbulent flow and convective heat transfer in the cavity, including buoyancy effect and long-

wave radiation between boundary surfaces is also modeled. Although the main case of interest in this paper is forced convection with fan-induced airflow, at low pressure differentials, there is a buoyancy-induced velocity peak near the PV surface. The heat transfer coefficients were predicted for the two cavity surfaces, and the convective coefficient was determined through a combination of CFD simulations and experimental measurements that provided boundary conditions; the convective coefficients were generally higher than expected by other correlations due to leading-edge effects and the turbulent nature of the flow. Experimental measurements of the velocity profiles in the BIPV system cavity using a particle image velocimetry system were in good agreement with CFD model predictions. The heat transfer coefficients calculated can be utilized in simpler models to facilitate the design of BIPV/T systems. Correlations have been developed for the convective heat transfer coefficients and as a function of commonly used dimensionless numbers.

Infield et al [64] proved that the parameters $U_{transmission}$, $U_{ventilation}$, $g_{transmission}$ and $g_{ventilation}$ can be used to adequately characterize the thermal performance of partially transparent ventilated PV façades. Using these parameters it is straightforward to calculate the heating and cooling loads due to the façade. As such they provided a useful tool for building engineers and architects in the design of building integrated multifunctional photovoltaic-solar air façades. The approach has been demonstrated for the calculation of both winter heating and summer cooling loads. In addition, the significant heat gains to the ventilation air in summer, which offer the potential for active solar cooling of such buildings, can be straight forwardly calculated using the presented methodology. Future work is needed to validate further, both the heat transfer parameterization and the methodology for annual energy balance calculations.

Yun et al. [65] investigated the complex interrelationship between a ventilated PV façade and the overall energy performance of a building. They analyzed a theoretical ventilated photovoltaic (PV) façade, which functions as a pre-heating device in winter and a natural ventilation system in summer and reduces PV module temperatures. The interrelationship between an optimum proportion of a transparent window (and an opaque PV module) to the total façade area, and the variables relevant to the energy performance were assessed. The design parameters under consideration have been categorized according to climate, building characteristics, façade configurations and PV system elements. One outcome of this investigation is a new index, effectiveness of a PV Façade (PVEF), that has been developed to evaluate the overall energy performance of a PV façade with regard to the proportion of useful daylight that may displace the use of electric lighting, and

the electricity generated by the PV modules to the heating and cooling energy consumption within a building. The optimum window ratio is strongly influenced by heat gains from artificial lighting. The use se of the shading device leads to the 10% increase in an optimum window ratio. Only a small increase in annual PV output is achieved by allowing air to flow along the back of the PV modules. Another finding of this study is that the position of the outlet from an air gap is crucial for the successful operation of a ventilated PV façade. Locating the air outlet in a region of wind-induced negative pressure is a good solution to enhance the natural ventilation within a building with a ventilated PV façade.

Solanki et al [66] report on the design, fabrication and performance assessment of a PV/T solar air heater. A simplified 1-D thermal model of the device was developed, based on the energy balance equations. The test method developed is proposed as a standard indoor test procedure for thermal and electrical testing of PV/T collectors connected in series. Typical electrical efficiency figures of the order of 10% and thermal efficiency of the order of 35% are reported for the specific design of PV/T collector for various climatic conditions. Sarhaddi et al [58] developed an analytical model to investigate the thermal and electrical performance of a solar photovoltaic thermal (PV/T) air collector. Some corrections are done on heat loss coefficients in order to improve the thermal model. The results of numerical simulation are in agreement with the outdoor test results of Joshi et al [67].

Agrawal and Tiwari [68] report on the installation of a building integrated photovoltaic thermal (BIPVT) system as the roof top of a building to produce thermal energy for space heating. A one-dimensional transient model was employed to select an appropriate BIPVT system suitable for cold climatic conditions of India. The glazed BIPVT system, fitted with optimal slope on the rooftop with an effective area of 65 m^2, annually produces a net electrical exergy of 16 MWh and a net thermal energy of 1.5 MWh.

Skoplaki and Palyvos [69] reviewed most of the correlations found in the literature which link cell temperature with standard weather variables and material/ system-dependent properties, in an effort to support the modeling and design process.

Table 2-1 Literature Review

Author	Year	Reference		
Clarke, J.A.,	**1996**	**[70]**	**He investigated the practical operational efficiencies that might**	**PV**

			be delivered from BIPV/T façades. The results from laboratory experiments and computer simulations are presented.	
A.Zöllner et. al	**2002**	**[38]**	**Experimental study performed in an outdoor test stand to investigate was to determine the time and local averaged overall heat transfer coefficients for solar radiation augmented turbulent mixed convection flows in transparent vertical channels.**	**Windows**
Saelens D.,	**2002**	**[28]**	**At the Vliet test building of the Laboratory of Building Physics in Leuven, Belgium, three façade systems have been built:** **(a) a classical cladding system with external shading device,** **(b) a mechanically ventilated multiple-skin façade and** **(c) a naturally ventilated multiple-skin façade** **(Figure 3.1). The envelopes face south-west. The cells, in which the envelope systems were built, measure 1.2 m wide by 2.7 m high by 0.5 m deep**	**Windows**
Heinrich Manz	**2003**	**[62]**	**A procedure for modeling such façades—comprising a spectral optical and a computational fluid dynamic (CFD) model—is described and simulation results are compared with data derived from an experimental investigation of a**	**Windows**

			single-story glass double façade (GDF) with free convection, incorporated in an outdoor test facility	
Liao, L. Athienitis, A. K. et. al	**2005**	**[63]**	**Numerical and Experimental Study of Heat Transfer in a BIPV-Thermal System**	**PV**
M.Fossa et. al	**2008**	**[57]**	**Experimental study on natural convection in an open channel**	**The test section consists of two parallel vertical walls, covered by a series of thin metal heaters, separated by a constant distance a. In the gap between the plane walls, an air flow is induced by natural convection.**
U. Eicker, et.al	**2008**	**[52]**	**The work quantifies the thermal performance of single and double façades under summer conditions using laboratory and full scale building experiments.**	**Solar simulator and windows**

Although numerous investigations appeared in the literature regarding PV/T collectors during the recent years, there is room for additional experimental research work, to improve our understanding of different design concepts and layouts, in different climatic conditions. In the present work, the building block of a proposed, improved BIPVT concept already presented in [71], was subjected to outdoor testing in Volos, Greece, to assess its transient electrical and thermal performance.

2.5 FLOW AND HEAT TRANSFER IN TALL VERTICAL CAVITIES AND CHANNELS

Turbulence can be characterized in terms of its production processes, the most important ones being shear and buoyancy. The physics and consequences of these processes are best studied in simple flow geometries to avoid other disturbing influences, as for example two parallel infinite walls [72]. In this idealized case all flow statistics depend only on the coordinate perpendicular to the wall and are independent of the other two directions. As regards orientation, the most familiar case is when gravity is perpendicular to the walls (Rayleigh-Benard convection). The other possibility, which is of interest in our case, is with gravity parallel to the wall. A natural convection flow results in this geometry when the two walls are kept at a different temperature. For small temperature differences the flow is laminar and beyond a certain critical value the flow becomes turbulent. This case has been relatively little studied, in comparison with the case between horizontal walls [72]. The problem is also interesting from a fundamental point of view, because, in contrast to the Rayleigh-Benard convection, a mean flow develops which complicates the turbulence dynamics due to the additional effect of turbulence production by shear. Moreover, the turbulence production by shear occurs in the same direction here as the buoyant production. In most other flows where both buoyant and shear production play a role, the two processes usually act in different directions. The homogeneity in two directions ensures that no disturbing top/ bottom, or sidewall effects are present [73]. Versteegh and Nieuwstadt have studied the details of turbulence in this flow by means of DNS, showing details in the form of the budget of turbulent quantities, such as Reynolds-stress components, heat fluxes and temperature variances. In principle one should also be able to obtain these second-order statistics from experiments; however, it is still a very difficult task to measure Reynolds stresses, fluxes and their budgets, especially in regions near the wall, while this wall region is important for the behaviour of the entire flow. Although LDV measurements allowed measuring stresses to a certain extent, until now the most reliable sources of Reynolds budgets' terms are DNS techniques. But even with the help of DNS data, the calculation of second-order statistics involving all components such as production, transport and dissipation, is very elaborate (see Mansour et al [74] for a channel flow). Another advantage of DNS is that it allows us to compute terms which cannot be observed experimentally, as for example the pressure-strain term. Information on these budgets can, for instance, be used for the development of advanced turbulence models. In natural convection flows one frequently finds large-scale flow motions, which are usually interpreted as remnants of the flow structures that appear during the onset of turbulence, i.e. as a result of linear instability of the laminar flow. A DNS was performed in [75] for the case of a

natural convection flow between two differentially heated vertical walls for a range of Rayleigh numbers ($5.4 \times 10^5 < Ra < 5.0 \times 10^6$). The simulation data were successfully compared with experimental data of Dafa' Alla and Betts [76]. Given the numerical data, Versteegh and Nieuwstadt considered the scaling behaviour of the mean temperature, the mean velocity profile and of the profiles of various turbulence statistics. Point of departure was the approach proposed by George and Capp [77] who have formulated scaling relationships valid, respectively, in the near-wall inner layer and in the outer layer in the centre region of the channel. Under the assumption of a turbulent flow, each variable can be subdivided in a mean flow (overbar) and a fluctuation (prime). The mean flow in the channel under the influence of the temperature difference ΔT is stationary and homogeneous in the *y*- and *z*-direction. Consequently, all turbulence statistics are functions of the coordinate *x* only. From the governing equations, Versteegh and Nieuwstadt [72] extracted the equations for the mean flow as follows:

$$\mathbf{0} = g\beta\ T - T_r\ + \frac{\theta}{\theta x}(-u'w' + \nu\frac{\theta w}{\theta x}) \quad \textbf{(2.1)}$$

$$\mathbf{0} = \frac{\theta}{\theta x}(-u'T' + \kappa\frac{\theta T}{\theta x}) \quad \textbf{(2.2)}$$

In order to find a parameter that can characterize the production of turbulence by buoyancy, the same authors integrated the above equation for the mean temperature:

$$f_t = (-u'T' + \frac{\theta T}{\theta x}) \quad \textbf{(2.3)}$$

where f_t is the horizontal temperature flux (>0) which is representative for the heat lux lowing from the left-hand to the right-hand wall. This equation implies that this horizontal temperature flux consists of a turbulence- and a molecular- contribution and that it is independent of x. Consequently, f_t *is* a parameter which is relevant everywhere in the flow and for this reason the authors selected f_t as a characteristic scaling parameter (the same proposed by George and Capp [77]). In the same work [72], the authors performed a very useful analysis of the DNS results, especially as regards the Reynolds stresses, where they found that similarly as with the mean velocity profile, the Reynolds stress is a strong function of the Rayleigh number. However, the most interesting result is the behaviour of the Reynolds stress near the wall, which appears to become negative only very close to the wall, but to change to a positive value near $x \approx 0.015$. On the other hand the mean velocity gradient was computed to change sign near $x \approx 0.7$. If one assumes for the moment that the gradient transfer hypothesis for the Reynolds stress holds, that is:

$$-\overline{u'w'} = K\frac{\theta T}{\theta x} \quad \textbf{(2.4)}$$

The near-wall behaviour mentioned above of the Reynolds stress and of the mean velocity profile, implies that the exchange coefficient *K* must be negative for ~0.015 < *x* < ~0.7. From a physical point of view the concept of an exchange coefficient which implies transport down the gradient, only makes sense when the exchange coefficient is larger than zero. The conclusion therefore is that the gradient transfer hypothesis cannot be valid in this near-wall region. Thus, all modeling approaches for this flow which are based on a gradient-transfer hypothesis, are fundamentally incorrect.

Finally, Versteegh and Nieuwstadt [72] concluded with matching of the scaling relationships in the overlap between the inner and outer region leads to explicit expressions which can be used as wall functions in computational procedures. Their matching expression agreed excellently with the DNS data which confirmed the consistency of the outer- and inner-layer scaling approach of the temperature. They also showed a very good fit to the data in terms of a power law given by

$$Nu = 0.071H^{1/3} \quad \textbf{(2.5)}$$

which is an expression frequently used as a heat transfer law in practice.

In another study, Versteegh [75] had performed this linear stability analysis and obtained the flow mode connected to the most unstable eigenvalue. In [73], Versteegh and Nieuwstadt computed the budgets for this linear instability mode. From a comparison with the turbulent budgets a first estimate can be made as to how much the turbulence budgets are influenced by large-scale flow motions that occur in transitional flow. On the subject of stability in natural convection in vertical slots and channels, many studies have already been published, following thepioneering work of Batchelor [48], which was the first to give rough estimates for the critical Rayleigh number. Later experimental data by Elder [78] gave insight in the flow patterns that occur in a flow with viscous fluids. Since then, computer power gradually became available at increasing rates and several numerical studies about linear stability were published [79], [80], [81].

The experiments of Betts and Bokhari [82] aimed to investigate the natural convection of air in a tall differentially heated rectangular cavity (2.18 m high by 0.076 m wide by 0.52 m in depth). The experimental test rig was an improved version of the one employed in [76], modified by fitting partially conducting top and

bottom walls and outer guard channels, to provide boundary conditions which avoid sharp changes in temperature gradient and other problems associated with insufficient insulation of "adiabatic" walls. They were performed with temperature differentials between the vertical plates of 19.6°C and 39.9°C, giving Rayleigh numbers 0.86 x 10^6 and 1.43 x 10^6 respectively (turbulent flow in the core of the cavity and small property variations with temperature). Mean and turbulent temperature and velocity variations within the cavity were measured, together with heat fluxes and turbulent shear stresses. The temperature and flow fields were found to be closely 2-dimensional, except close to the front and back walls, and anti-symmetric across the diagonal. The results provide a benchmark for testing of turbulence models in this low Re number flow (http://ercoftac.mech.surrey.ac.uk/).

The flow through a vertical, differentially heated cavity induced by buoyancy alone may be analytically studied based on a number of simplifications. The heated wall of the channel may be considered to receive a uniform constant heat flux while the opposing wall may be kept adiabatic. Air may be assumed to be drawn into the channel at the inlet under the ambient conditions of p_1, T_1, and the heated air discharged into the quiescent ambient air at the outlet (no thermal mixing of inlet and outlet). All transport processes may be considered to take place at steady state and as two-dimensional. Air with Pr = 0.7 and constant properties except density may be assumed, and density changes only with temperature (ideal gas law). Thermal radiation is neglected for simplification. It is expected that the flow will start as laminar in the inlet region of the channel undergoing transition and becoming fully turbulent downstream, depending upon the thermal and geometric parameters. A completely turbulent flow assumption could be taken due to the lack of transition criteria. A certain level of turbulence exists at the channel inlet. The time averaged continuity, momentum and energy equations along with turbulence model equations can be written as follows, following [83]:

Continuity equation

$$\frac{\partial(\overline{\rho}\,\overline{u})}{\partial x}+\frac{\partial(\overline{\rho}\,\overline{u})}{\partial y}=0 \qquad (2.6)$$

x component of momentum equation

$$(\overline{\rho}\,\overline{u})\frac{\partial\,\overline{u}}{\partial x}+\ \overline{\rho}\,\overline{u}\ \frac{\partial\,\overline{u}}{\partial y}=-\frac{\partial\,\overline{p_m}}{\partial x}+\ \overline{\rho}-\rho_\infty\ \rho+\frac{\partial}{\partial x}\ (\mu+\mu_t)\frac{\partial\,\overline{u}}{\partial x}\ +\frac{\partial}{\partial y}\ (\mu+\mu_t)\frac{\partial\,\overline{u}}{\partial y} \qquad (2.7)$$

y component of momentum equation

$$(\overline{\rho}\,\overline{u})\frac{\partial \overline{v}}{\partial x} + \overline{\rho}\,\overline{u}\,\frac{\partial \overline{v}}{\partial y} = -\frac{\partial \overline{p_m}}{\partial x} + \overline{\rho} - \rho_\infty\ \rho + \frac{\partial}{\partial x}\ (\mu + \mu_t)\frac{\partial \overline{v}}{\partial x} + \frac{\partial}{\partial y}\ (\mu + \mu_t)\frac{\partial \overline{v}}{\partial y} \quad \textbf{(2.8)}$$

Energy equation

$$c_p(\overline{\rho}\,\overline{u})\frac{\partial \overline{T}}{\partial x} + c_p(\overline{\rho}\,\overline{u})\frac{\partial \overline{T}}{\partial y} = \frac{\partial}{\partial x}\ (\lambda + \frac{c_p\mu_t}{\sigma_t})\frac{\partial \overline{T}}{\partial x} + \frac{\partial}{\partial y}\ (\lambda + \frac{c_p\mu_t}{\sigma_t})\frac{\partial \overline{T}}{\partial y} \quad \textbf{(2.9)}$$

LRN k-ε turbulent model equations

$$(\overline{\rho}\,\overline{u})\frac{\partial k}{\partial x} + \overline{\rho}\,\overline{v}\,\frac{\partial k}{\partial y} = \frac{\partial}{\partial x}\ \mu + \frac{\mu_t}{\sigma_t}\frac{\partial k}{\partial x} + \frac{\partial}{\partial y}\ \mu + \frac{\mu_t}{\sigma_t}\frac{\partial k}{\partial y} + (P + G - \overline{\rho}\,\varepsilon) \quad \textbf{(2.10)}$$

$$(\overline{\rho}\,\overline{u})\frac{\partial \varepsilon}{\partial x} + \overline{\rho}\,\overline{v}\,\frac{\partial \varepsilon}{\partial y} = \frac{\partial}{\partial x}\ \mu + \frac{\mu_t}{\sigma_t}\frac{\partial \varepsilon}{\partial x} + \frac{\partial}{\partial y}\ \mu + \frac{\mu_t}{\sigma_t}\frac{\partial \varepsilon}{\partial y} + \frac{\varepsilon}{k}(C_{\varepsilon 1}f_1 P + C_{\varepsilon 1}f_1 G - C_{\varepsilon 2}f_2\overline{\rho}\,\varepsilon) \quad \textbf{(2.11)}$$

Where

$$\mu_t = \overline{\rho}\,C_\mu f_\mu \frac{k^2}{\varepsilon} \quad \textbf{(2.12)}$$

$$P = \mu_t\ 2(+\ \overline{\rho}\,\overline{v}\ \frac{\partial \varepsilon}{\partial y} = \frac{\partial}{\partial x}\ \mu + \frac{\mu_t}{\sigma_t}\frac{\partial \varepsilon}{\partial x} + \frac{\partial}{\partial y}\ \mu + \frac{\mu_t}{\sigma_t}\frac{\partial \varepsilon}{\partial y} + \frac{\varepsilon}{k}(C_{\varepsilon 1}f_1 P + C_{\varepsilon 1}f_1 G - C_{\varepsilon 2}f_2\overline{\rho}\,\varepsilon) \quad \textbf{(2.13)}$$

$$G = \beta\ \frac{\mu_t}{\sigma_t}\frac{\partial \overline{T}}{\partial x}g \quad \textbf{(2.14)}$$

The turbulent natural convection boundary layer next to a heated vertical surface has been extensively studied in the past. George and Capp [77], [84] analyzed the boundary layer by classical scaling arguments and showed that the fully developed turbulent boundary layer must be treated in two parts: an outer region consisting of most of the boundary layer in which viscous and conduction terms are negligible and an inner region in which the mean convection terms are negligible. The inner layer is identified as a constant heat flux layer. A similarity analysis yields universal profiles for velocity and temperature in the outer and constant. An asymptotic matching of these profiles in an intermediate layer (the buoyant sub-layer) as

$$H_\delta = g\beta F_0\ \delta^4/\alpha^3 \to \infty \quad \textbf{(2.15)}$$

yields analytical expressions for the buoyant sub-layer profiles as:

$$\frac{T - T_W}{T_1} = K_2\ \frac{y}{n}^{-1/3} + A(Pr) \quad \textbf{(2.16)}$$

$$\frac{U}{U_1} = K_1\ \frac{y}{n}^{1/3} + B(Pr) \quad \textbf{(2.17)}$$

Where K1, K2 are universal constants and A(Pr), B(Pr) are universal functions of Prandtl number.

Asymptotic heat transfer and friction laws are obtained as:

$$\mathbf{Nu_{x=}}\ \mathbf{C'(Pr)H_x^{*1/4}},\ \frac{\tau_W}{\rho U_1^2} = \mathbf{C_f(Pr)} \qquad \textbf{(2.18)}$$

Where C'_H (Pr) is simply related to A (Pr). Finally, conductive and thermo-viscous sub-layers characterized by a linear variation of velocity and temperature are shown to exist at the wall. All predictions agree with experimental evidence.

Tieszen et al [85] presented results from two-dimensional calculations using the υ^2 – f and a k – ε model, compared with experimental data available for two geometries, the vertical flat plate and the 5:1 height: width box with a constant temperature hot and cold side wall. The results show that the υ^2–f model is at least as good as a k–ε model with a two-layer wall treatment. The nature of buoyancy/ turbulence coupling was discussed and three different treatments of it were compared. All three treatments showed little effect on the heat transfer in fully turbulent conditions but the generalized gradient diffusion hypothesis can make a large difference in the location of transition with the υ^2–f model. The υ^2–f model compared well with the vertical flat plate data without changes. However, in the hot-wall, cold-wall box, it had a delayed transition with respect to the data and significantly under-predicted the heat transfer. With the addition of the generalized gradient diffusion term to the model, the transition occurred near that in the data and the overall heat transfer comparisons were excellent. Since a coefficient was set in the generalized gradient diffusion term, substantially more comparisons are needed to establish whether or not it is generally useful in transitionally buoyant flows. The nature of buoyancy/turbulence interactions is not well known. Hence, the ability to model it is not universally agreed upon. Of the three levels of treatment of the buoyant production term tested, none produced any large effect (outside of the location of transition) on the heat transfer. It is not clear whether this outcome means that buoyancy has little effect, or a more sophisticated model is required to delineate the effects. Certainly the good agreement between the models and the test results indicate that if the effect is large, it is being masked by other modeled terms.

Di Piazza and Ciofalo [86], studied computationally free convection at low-Prandtl numbers in a volumetrically heated rectangular enclosure of aspect ratio 4, having adiabatic top and bottom walls and isothermal side walls. They solved the two-dimensional continuity and momentum equations, coupled with the energy

transport equation under the Boussinesq approximation, by using a finite-volume technique based on the SIMPLEC pressure-velocity coupling algorithm [87].

Albets-Chico et al. [88] focused on the simulation of turbulent natural convection flows by means of two-equation eddy-viscosity models. To check the scope of applicability, precision, and numerical issues related to these models under natural convection, three different buoyancy-driven cavities were studied: a tall cavity with a 30:1 aspect ratio, a cavity with a 5:1 aspect ratio and a 4:1 aspect ratio cavity. All cases were solved under moderate and/or transitional Rayleigh numbers (2.43 x 10^{10}, 5 x 10^{10}, and 1 x 10^{10}, respectively) and all simulations were compared to experimental or DNS data available in literature. These different situations allowed a good checking of the applicability of two-equation eddy-viscosity models in buoyancy-driven flows, based on computational effort/precision criteria and the associated physics. Turbulent natural convection prediction by means of two-equation turbulence models was shown to be associated with physical and numerical limitations of the models. However, they are generally acceptable tools for different Rayleigh numbers and aspect ratio cavities, taking into account that, depending on the case, specific models should be used.

The above research works always focused on smooth vertical surfaces. However, extended surfaces with roughness or fins, are known to enhance heat transfer. Experiments conducted to measure the local heat transfer on an endwall with pin fin array are reported in [89]. Heat transfer behavior was examined for the cases of a single pin, a single row, in-line and staggered arrays having six streamwise rows. Thermosensitive liquid crystal film was used to measure the local heat transfer coefficient on the endwall. Local heat transfer on the endwall having a single row of pin fin was affected by flow acceleration between the pin fins rather than the horseshoe vortex around the pin fin. Therefore, the average Nu number exhibited a good correlation to the Re number Re_{max}, which was based on the average velocity of the minimum flow area, regardless of the pin fin spacing. For in-line and staggered arrays, the average Nu numbers correlated with Re_{max} decreased with the reduction of the pin fin spacing. An optical technique for measuring local heat transfer coefficients by use of thermochromic liquid crystals in enhanced heat transfer channels is discussed in [90]. The 2-D temperature distribution was visualized in colour and observed by a CCD videocamera and further processed. The hue can be directly related to surface temperature through a linear relationship, determined by means of calibration experiments. If a uniform heat flux condition is applied to the test surface, the pattern of the heat transfer coefficient can be obtained. This optical technique was applied to the study of forced convection heat transfer characteristics

in a rectangular channel with rib turbulators mounted on one of the surfaces. Continuous and broken parallel ribs, deployed normal to the main direction of air flow, were considered, for different values of the geometric parameters. The range of variation of the Reynolds number, based on the hydraulic diameter of the channel, was 8000–35,000.

2.6 HEAT TRANSFER IN A BIPV COOLING DUCT

A new building integration concept have been proposed in [91]. The configuration is schematically presented in Figure 2.9. A wide rectangular duct is formed between the backside of the PV modules and the external wall of the building behind them. The duct is closed also in its narrow sides, thus allowing the transport of air in the duct by the combined effect of buoyancy, fans and regulated dampers. As the air is moving upwards, its temperature is raised by its thermal interaction with the backsheet of the PV modules.

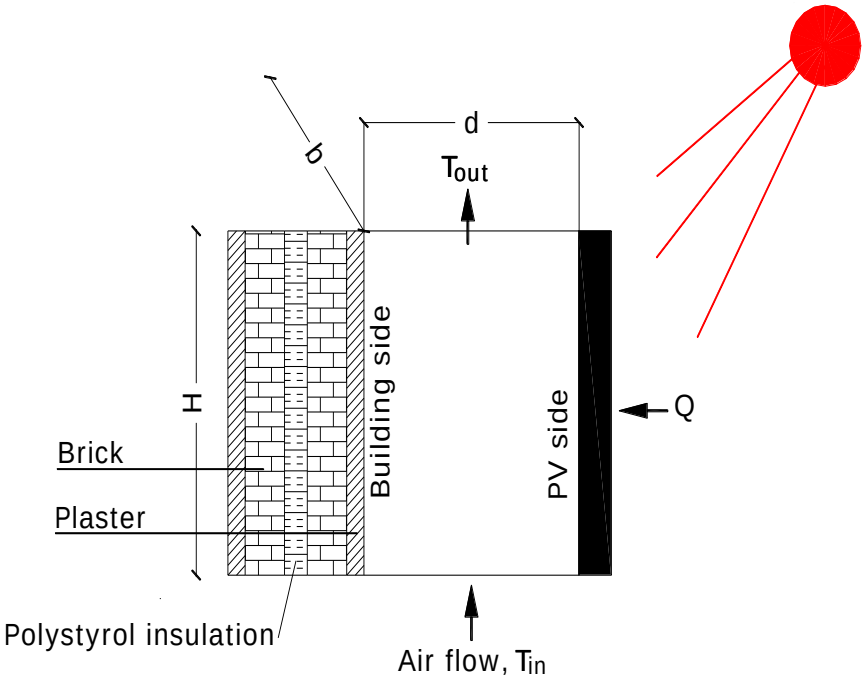

Figure 2-9 Heat transfer in the rectangular duct behind the PV modules

In the case of unobstructed buoyancy flow, a part of the solar radiation heat absorbed by the PV module is transferred by natural convection to the air in the duct behind the module and the heated air flows upwards. If the building wall forming the opposite part of the duct is at a lower temperature than the air in the duct, then a

part of the heat flow is directed towards the building interior. If we ignore the less important phenomena (conduction to building wall, radiative exchange with the building shell), the system's performance is governed

(i) by the kinetic relation for the convection heat transfer to the duct air:

$$\mathbf{Q = h * A * (T_W - T_{air})} \quad \textbf{(2.19)}$$

where h is the convection heat transfer coefficient from the duct wall to air, T_w the temperature of heated surface and A the heat transfer area and

(ii) by the energy balance of the duct flow:

$$\mathbf{Q = h * A * (T_W - T_{air})} \quad \textbf{(2.20)}$$

In the natural convection case, the air flow rate is determined by the static pressure head from the buoyancy effect:

$$\mathbf{\Delta p = H * g * (\rho_{air} - \rho_a)} \quad \textbf{(2.21)}$$

where Δp is the buoyancy pressure head in the channel [Pa] (ρ_{air} the mean density of air in the duct, ρ_a the ambient air density [kg/m^3]), along with the friction pressure drop due to the buoyancy flow. For typical values of the exit air temperature, the static pressure head is of the order of 5-10 Pa and the resulting buoyancy flow rates for the specific cross section of the duct range between 0.2 – 0.5 m^3/s [92]. The convection coefficient may be estimated by a typical Nu (Gr,Pr) relationship[91]. Of course, the real world situation in the duct is significantly more complex, due to the important role of radiation. The energy balance of the specific BIPVT concept is presented in Figure 2-10 and relies on algorithms supplied by the classic book of Duffie and Beckman [93].

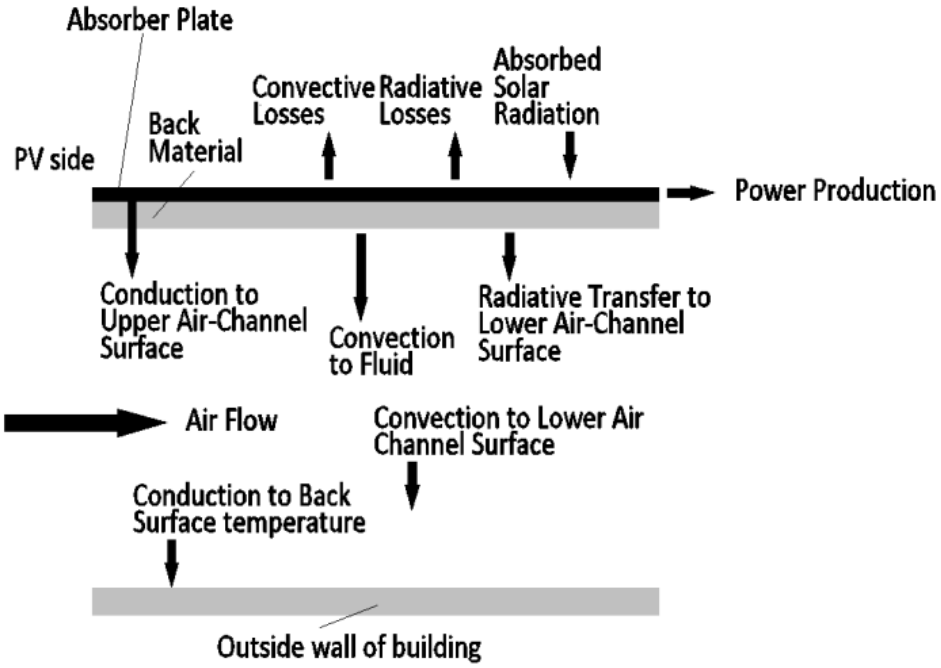

Figure 2-10 Energy balance components on the PV module, adapted from [94]

A typical energy balance of the system, as quantified based on the building energy simulation of chapter 6 is presented in Figure 2-11. According to this figure, following the initial loss of about 20% due to reflection, an average 11% of the solar radiation incident on the vertical BIPV panels is transformed to electricity. Another 18% is transformed to useful thermal energy (for space heating in winter and service water heating in summer). Convective and radiative losses, mainly from the front side of the panels, adding to a total of 51%, close the energy balance of the BIPV installation.

A detailed description of energy balance will be given in Chapter 6.2.

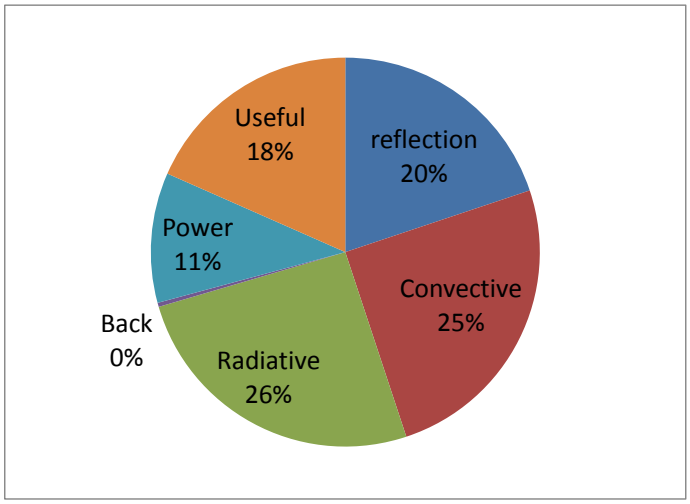

Figure 2-11 Typical energy balance of a building integrated PV system.

2.7 EXISTING CORRELATIONS FOR HEAT CONVECTION IN A DUCT

Convection heat transfer can be classified according to the nature of the flow. We speak of forced convection when the flow is caused by external means, such as by a fan or pump. In contrast, for free (or natural) convection the flow is induced by buoyancy forces, which arise from density differences caused by temperature variation in the fluid. Both modes may coexist in building's façade.

In heat transfer at a boundary (surface) within a fluid, the Nusselt number is the ratio of convective to conductive heat transfer across the boundary and is given by the follow expression:

$$\mathbf{Nu} = \mathbf{h}\frac{\mathbf{L}}{\mathbf{k}} \qquad \textbf{(2.22)}$$

where :

- L : the characteristic length
- k: the heat conductivity of the air
- h: the convective heat transfer coefficient

The Rayleigh number is a dimensionless number and is given by the following expression:

$$\mathbf{Ra} = \mathbf{g\beta\Delta TL^3/v\alpha} \qquad \textbf{(2.23)}$$

where :

- g : gravitational constant
- β : volumetric coefficient of expansion (for ideal gas β = 1/T)
- ΔT : temperature difference between plates
- v: kinematic viscosity
- α: thermal diffusivity
- L: characteristic length.

2.7.1 FREE (OR NATURAL) CONVECTION

Free convection heat transfer data usually correlated of two or three dimensionless parameters:

- Nusselt Number (Nu)
- Rayleigh Number (Ra) and
- Prandtl Number (Pr)

where :

$$\mathbf{Pr} = \frac{\nu}{\alpha} \tag{2.24}$$

The free convection flows that are induced within the enclosure depend strongly on the angle of tilt; however, regardless of tilt angle, the results are correlated using a Rayleigh number and average Nusselt number that are defined based on the separation distance, *L*:

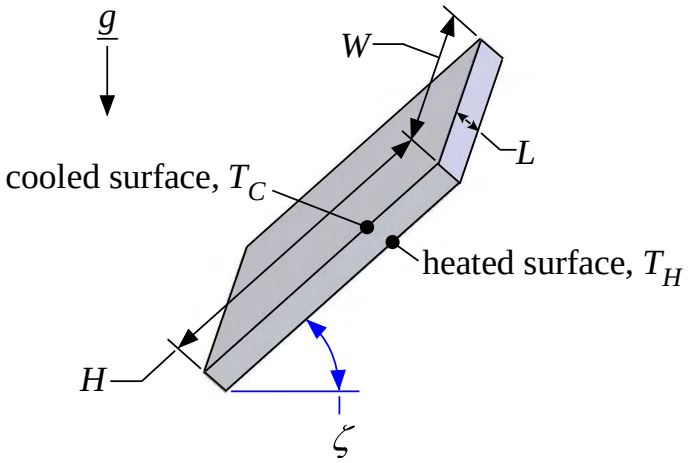

At a tilt angle of $\alpha = \pi/2$ radian (vertical), the fluid adjacent to the heated wall tends to rise until it reaches the top of the cavity and comes into contact with the cooled wall. If the Rayleigh number is less than a critical value of $Ra_{L,crit} \approx 1000$, then the buoyancy force is insufficient to overcome the viscous force and the fluid remains stagnant. In this limit, the free convection problem reduces to a conduction problem.

Above the critical Rayleigh number, the Nusselt number has been correlated by Hollands et al. [95] according to:

$$\mathbf{Nu} = \mathbf{1} + \mathbf{1.44}\left(\mathbf{1} - \frac{\mathbf{1708\ \sin^{1.6}\ 1.8\alpha_{sl}}}{\mathbf{Racos\ \alpha_{sl}}}\right)\left(\mathbf{1} - \frac{\mathbf{1708}}{\mathbf{Ra\cos\ \alpha_{sl}}}\right) + \left(\left(\frac{\mathbf{Ra\cos\ \alpha_{sl}}}{\mathbf{5830}}\right)^{\mathbf{1/3}} - \mathbf{1}\right) \tag{2.25}$$

The equation will reduce to 1 when $Ra_L < Ra_{L,crit}$.

The above equation is used in TRNSYS code for the analytical solution of Type 568 see chapter 6.2

For tilt angles between the critical angle and vertical ($75^0<\alpha<90^0$ or 1.22 radian $<\alpha<\pi/2$ radian), Ayyaswamy and Catton [96] recommend:

$$\mathbf{Nu} = \mathbf{Nu}_{\mathbf{L,a=\pi/2[\sin\ \alpha\ ]^{0.25}}} \quad \textbf{(2.26)}$$

For natural convection within two parallel plates Bar-Cohen and Rohsenow [97] recommended two formulas for Nu calculation. For isothermal and isoflux condition, respectively, the correlations are of the form

$$\mathbf{Nu} = \left[\frac{576}{\mathbf{Ra}^2} + \frac{2.87}{\mathbf{Ra}^{0.5}}\right]^{-0.5} \quad \textbf{(2.27)}$$

$$\mathbf{Nu} = \left[\frac{48}{\mathbf{Ra}} + \frac{2.51}{\mathbf{Ra}^{2\ 5}}\right]^{-0.5} \quad \textbf{(2.28)}$$

In 1998 Rohsenow et al. [98] recommended a new formula for the Nu calculation.

$$\mathbf{Nu} = (\mathbf{Nu}_{\mathbf{fd}}^{-1.9} + \mathbf{Nu}_{\mathbf{plate}}^{-1.9})^{-1/1\cdot 9} \quad \textbf{(2.29)}$$

where :

$$\mathbf{Nu}_{\mathbf{fd}} = \frac{\mathbf{Ra}}{24} \qquad \mathbf{Nu}_{\mathbf{plate}} = 1.32\ \mathbf{C}_1\mathbf{Ra}^{1/4} \quad \textbf{(2.30)}$$

$$\mathbf{C}_1 = \frac{0.671}{(1+(0.492/Pr)^{9/16})^{4/9}} \quad \textbf{(2.31)}$$

Sparrow et al. [99, 100] analyzed data, which was based on the heat flux for two parallel wall, the one heated and the other adiabatic. The data ranged from Ra = 200 to Ra = 80000 and had the best correlation with the follow expression

$$\mathbf{Nu} = 0.667\ \mathbf{Ra}^{0.229} \quad \textbf{(2.32)}$$

2.7.2 FORCED CONVECTION

In order to select the appropriate correlation, it is necessary to classify the salient features of the flow. The most critical classification is the flow condition, which is determined by the Reynolds number based on the hydraulic diameter (D_h):

$$\mathbf{Re}_{\mathbf{Dh}} = \frac{\rho\ \mathbf{u}_{\mathbf{m}}\ \mathbf{D}_{\mathbf{h}}}{\mu} \quad \textbf{(2.33)}$$

the hydraulic diameter is defined according to:

$$\mathbf{D_h = \frac{A_C}{per}} \quad \textbf{(2.34)}$$

where A_c is the cross-sectional area of the duct and *per* is the wetted perimeter. The flow will be laminar if the Reynolds number based on the hydraulic diameter is less than approximately 2300, otherwise it will be turbulent.

2.7.2.1 LAMINAR FLOW IN RECTANGULAR DUCTS

Shah and London [101] provide the local Nusselt number for a laminar, hydrodynamically and thermally fully developed flow in a rectangular duct that is exposed to a uniform heat flux and uniform wall temperature. The constant temperature result is correlated by:

$$\boldsymbol{Nu_{Dh} = 7.541(1 - 2.610AR + 4.970AR^2 - 5.119AR^3 + 2.702AR^{34} - 0.548AR^5)} \quad \textbf{(2.35)}$$

The constant heat flux result is correlated by:

$$\mathbf{Nu_{Dh} = 8.235\ (1 - 2.042AR + 3.085AR^2 - 2.477AR^3 + 1.058AR^{34} - 0.186AR^5)} \quad \textbf{(2.36)}$$

where *AR* is the aspect ratio of the duct (the ratio of the minimum to the maximum dimensions).

Duffie and Beckman [93] present the local Nusselt number for laminar flow between two plates with one side insulated and the other subjected to a constant hat flux obtained by Heaton et al. [102]. The results have been correlated in the form of equation 5.2 with the constants given in

$$\mathbf{Nu = Nu_\infty + \frac{a\ \left(\frac{RePrD_h}{L}\right)^m}{1 + b\ \left(\frac{RePrD_h}{L}\right)^n}} \quad \textbf{(2.37)}$$

Table 2-2 Constants for Equation 5.2 for calculation of local Nu for infinite Flat plates, one side insulated and constant heat flux on the other side.

Pr number	a	B	m	N
0.7	0.00190	0.00563	1.71	1.17
10	0.00041	0.00156	2.12	1.59
∞	0.00021	0.00060	2.24	1.77
$Nu_\infty = 5.4$				

For case of parallel plates with constant temperature on one side and insulated on the other side, Mercel et al. [103] obtained the average Nusselt number in the form of equation for 0.1 < Pr < 10

$$\mathbf{Nu} = \mathbf{4.9} + \frac{\mathbf{0.0606}\,((\mathbf{RePrD_h/L})^{\mathbf{1.2}}}{\mathbf{1+0.0909(RePrD_h/L)^{0.7}Pr^{0.17}}} \quad \textbf{(2.38)}$$

2.7.2.2 TURBULENT FLOW IN RECTANGULAR DUCTS

A turbulent flow is not affected by the duct shape or boundary conditions, but it is sensitive to the scale of the surface roughness (ε). The Nusselt number for fully developed turbulent flow is provided by Gnielinski (eq. 2.41), who modified the correlation of Petukhov [104] (eq. 2.39), to obtain values that agree with data for smaller Reynolds number:

$$\mathbf{Nu_{Dh,fd}} = \frac{(\frac{\mathbf{f_{fd}}}{\mathbf{8}})\mathbf{Re_{Dh}\,Pr}}{\mathbf{1+12.7(Pr^{\frac{2}{3}}-1)}\,\sqrt{\frac{\mathbf{f_{fd}}}{\mathbf{8}}}}\,(\mathbf{1}+\frac{\mathbf{d}}{\mathbf{H}}^{\mathbf{2/3}}) \quad \textbf{(2.39)}$$

where :

$$\mathbf{f_{fd}} = \mathbf{0.184/Re_{Dh}}^{\mathbf{0.2}} \quad \textbf{(2.40)}$$

for 0.5 < Pr < 2000

and 2300 < Re_{Dh} < 5*10^6

f_{fd} is the fully developed friction factor. The effect of roughness on the Nusselt number in Eq. (2.39) is included through its effect on the friction factor.

$$\mathbf{Nu_{Dh,fd}} = \frac{(\frac{\mathbf{f_{fd}}}{\mathbf{8}})\ \mathbf{Re_{Dh}-1000}\ \ \mathbf{Pr}}{\mathbf{1+12.7(Pr^{2\ 3}-1)}\,\sqrt{\frac{\mathbf{f_{fd}}}{\mathbf{8}}}}\,(\frac{\mathbf{d}}{\mathbf{H}}^{\mathbf{2/3}}) \quad \textbf{(2.41)}$$

where :

$$\mathbf{f_{fd}} = \mathbf{1/(1.82\ \log Re_{Dh} - 1.64)^2} \quad \textbf{(2.42)}$$

The average Nusselt number can be approximately computed according to (Kakaç et al. [105]):

$$\mathbf{Nu_{Dh}} \approx \mathbf{Nu_{Dh,fd}}\left(\mathbf{1} + \mathbf{C}\ \frac{\mathbf{x}}{\mathbf{D_h}}^{\ \mathbf{-m}}\right) \quad \textbf{(2.43)}$$

where reasonable values of the constants C and m are 1.0 and 0.7.

When a mixed convection regime occurs, heat exchange laws become complicated. *Hatton* et al. [106] suggested an explicit correlation based on a vectorial addition of the forced and natural Reynolds numbers

$$\mathbf{Nu_f} = (\mathbf{0.384} + \mathbf{0.581Re_{eff}^{0.439}})(\frac{\mathbf{T_f}}{\mathbf{T_a}})^{\mathbf{0.154}} \quad \textbf{(2.44)}$$

$$\mathbf{Re_{eff}^{0.439}} = \mathbf{Re_f^2}\left(\mathbf{1} + \mathbf{2.06}\ \frac{\mathbf{Ra^{0.418}}}{\mathbf{Re_f}}\mathbf{cos\theta_z} + \mathbf{1.06}\ \frac{\mathbf{Ra^{0.836}}}{\mathbf{Re^2{}_f}}\mathbf{cos\theta_z}\right) \quad \textbf{(2.45)}$$

where Ra is the Rayleigh number, Ra = Gr Pr, and θ_z is the angle from the vertically upward direction of the of the forcing flow.

2.7.3 CORRELATIONS FOR AN ASYMMETRICALLY HEATED, VERTICAL PARALLEL PLATE CHANNEL

Natural convection in vertical parallel-plate channels may take place under laminar or turbulent flow regimes depending on the geometrical size and thermal parameters. Laminar natural convection in vertical parallel-plate channels has been the focus of extensive investigation, using experiments, analytical, and numerical methods, to study a wide range of geometrical and thermo-physical aspects of the problem such as the edge effects, interactive convection and radiation, channel aspect ratio, effect of channel wall conductivity etc. [107] [108]. On the other hand, a limited number of studies exist on the turbulent natural convection in asymmetrically heated vertical parallel-plate channels. The most cited experimental work is that of Miyamoto et al., [109], which considered uniform wall heat flux heating mode and presented correlating equation for heat transfer applicable at the fully turbulent region of the channel. Fraser et al. [110] conducted turbulent natural convection velocity profile measurements in an asymmetrically heated vertical channel. La Pica et al. [111] reported the results of an experimental study on an asymmetrically heated vertical parallel-plate channel with horizontal inlet and outlet. They considered uniform wall heat flux and presented correlations for average Nu and Re numbers based on the average inlet velocity and channel width. Fedorov and Viskanta [107] studied turbulent natural convection in a vertical parallel plate channel numerically, considering both uniform wall heat flux and uniform wall

temperature. They presented correlations for average heat transfer and produced scaling relations for induced mass flow rates and average heat transfer. Yilmaz and Fraser [108] presented a detailed experimental and numerical study on turbulent natural convection of air in an asymmetrically heated vertical parallel-plate channel formed by a uniform wall temperature heated wall and an opposing glass wall. Velocity and temperature flow field measurements were carried out and subsequently, turbulent natural convection in the channel was numerically computed, considering three different LRN k–ε turbulence models. For a selected case, experimental and numerical velocity, temperature and turbulent kinetic energy profiles along the channel were presented, to indicate how the flow develops and how accurately the flow field can be predicted by numerical techniques. Correlations for the induced flow rate and average heat transfer rate were also presented.

When we study solar air heaters it is necessary to know the forced convection heat transfer coefficient between two plates. For air and fully developed turbulent flow with one side heated and the other side insulated Duffie and Beckman [93] presents the equation derived from the data of Kays and Crawford [112].

$$\mathbf{Nu = 0.0158Re^{0.8}} \qquad \textbf{(2.46)}$$

Where, the characteristic length is the hydraulic diameter *(twice the plate spacing).*

In our building energy simulation studies (Part B of this thesis), for free convection we employed equation 2.20 and for forced convection (Re>2300) equation 6.9 [113]. We corrected these correlations in order to become more accurate for the specific flow regime, based on the combination of test results and CFD computations of chapters 4-5.

2.8 DESIGN AND ROLE OF THE BACKSHEET

Although the front side of the Photovoltaic module (see Figure 2-12 and Figure 2-13), being the most important part of the device, has received most of the attention and development effort, the backsheet of the module (see Figure 2-14) deserves its own attention, because of its important role in heat exchange for cooling the photovoltaic panel.

Typical photovoltaic modules consist of:

- a glass sheet or a flexible transparent front sheet (polymer)

- solar cells
- encapsulant (Figure 2-13)
- protective backsheet (Figure 2-14)
- a protective seal which covers the edges of the module and
- a perimeter frame made of aluminum which covers the seal

These components are bonding together under heat and pressure.

The front sheet, the encapsulant and the backsheet are designed to protect the array of solar cells from the weather and the mechanical load.

The protective backsheet apart from protecting the solar cells, are intended to improve the lifecycle and the efficiency of photovoltaic module and thus reducing the cost per watt of the photovoltaic electricity.

The front sheet and the encapsulant must be transparent in light transmission, the backsheet has high opacity and reflectivity for functional purposes [115].

Light and thin solar cell modules are desirable for many reasons, including weight reduction, especially for Architectural applications (Building integrated PV).

One way to manufacture light and thin solar cells is to incorporate light and thin backsheets.

Additionally, the backsheet should provide [116-131]:

- high moisture resistance to prevent permeation of moisture vapor and water, which can cause rusting in photovoltaic elements, wire and electrodes and solar cells.
- electrical isolation,
- mechanical protection,
- adherence to the enqapsulant layers and
- ability to attach output leads.

Protective backsheets are usually laminates. The laminate consists of a films structure (Figure 2-15 and Figure 2-16)

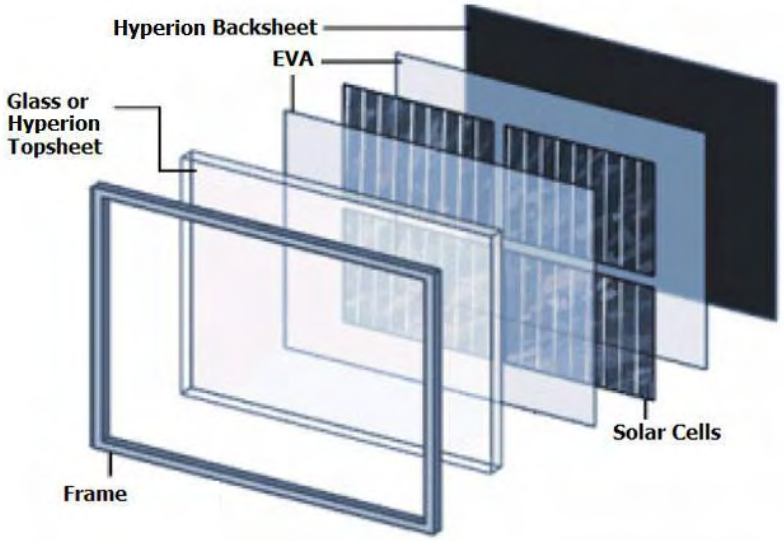

Figure 2-12 Photovoltaic module structure adapted from [114]

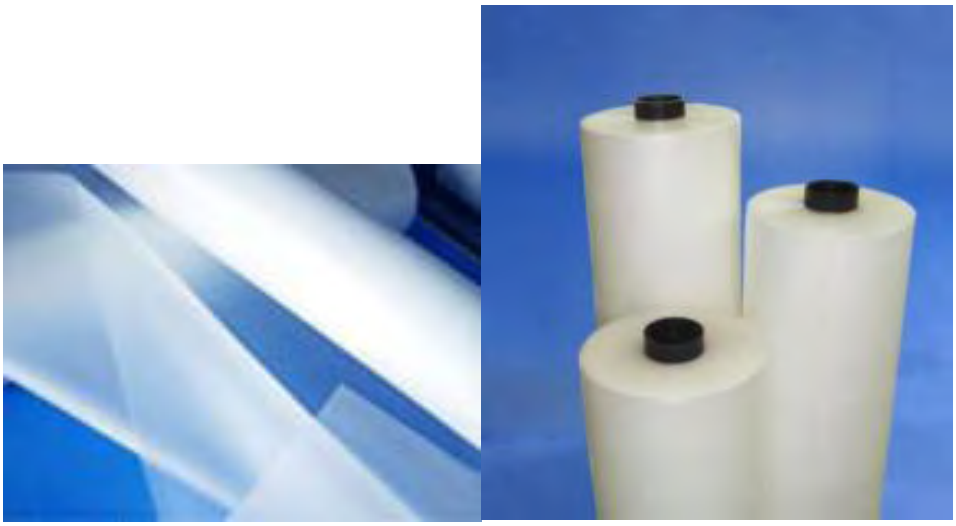

Figure 2-13 EVA Film for Encapsulating Solar Module [132]

Figure 2-14 Backsheet for Encapsulating Solar Module [132]

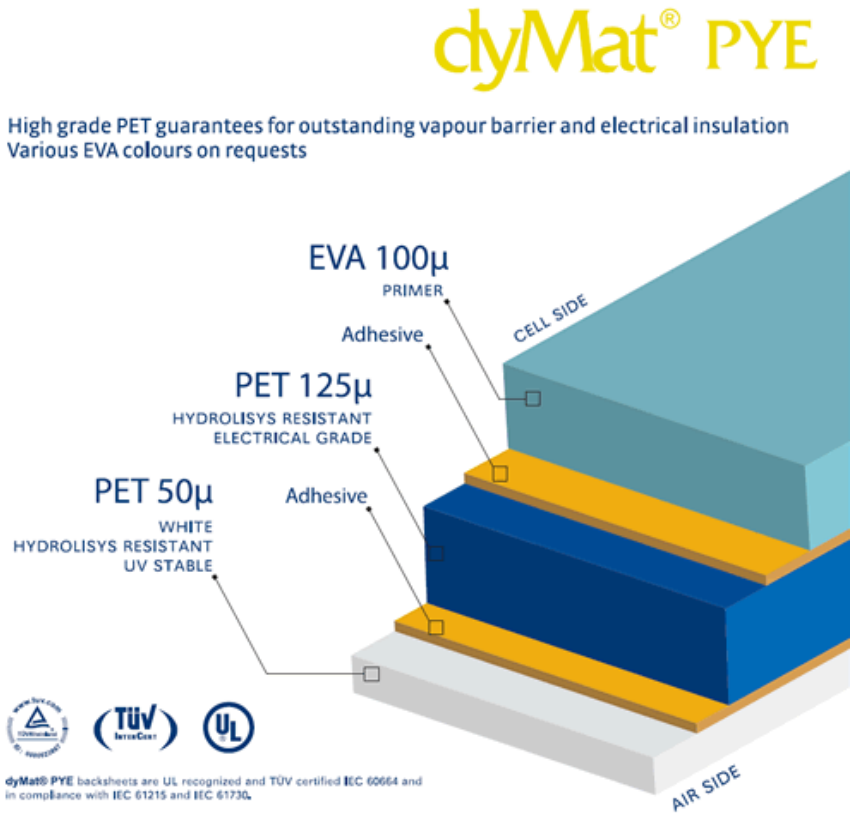

Figure 2-15 Backsheets structure - adapted from [133]

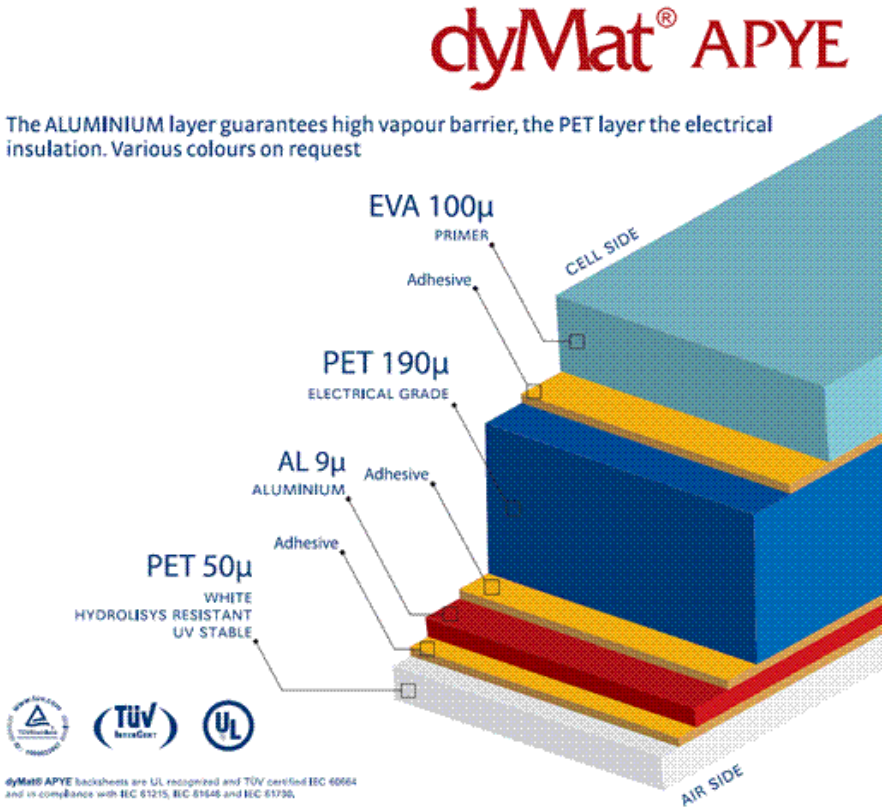

Figure 2-16 Typical backsheet's structure (adapted from [133]).

CHAPTER

3

3 PROPOSED ARCHITECTURAL AND HVAC CONCEPT

In Greece, the residential and nonresidential buildings are traditionally concrete constructions. During the last two decades, metal constructions with glazed façades have become popular especially for commercial buildings.

Moreover, expensive metal, natural stone, marble, ceramic (Figure 3-1, Figure 3-2) and granite as well as special glass is increasingly popular for aesthetic and energy efficiency reasons. The most expensive claddings cost around 1000 €/m^2, which is comparable to the cost of high efficiency PV modules.

PV modules in buildings are usually placed on the roof and sometimes also on south-facing building walls (Figure 3-3). The last year BIPV have been incorporating in various parts of the buildings Figure 3-4. They are providing electrical energy to cover a part of the building's needs. The roof-top modules are placed at a distance from the roof to allow rejection of the absorbed solar radiation that is not transformed to electricity.

During the last decade, the idea of additionally exploiting the rejected heat of the photovoltaic modules is gaining attention [134]. To this end, the PV modules must be placed in South- or SW-facing external building walls in the form of a double façade, where an air channel is to be formed behind the modules to cool them and exploit the heating energy gained by the air.

An architectural and HVAC integration concept is proposed in this chapter to better exploit the capabilities of building integrated PV modules in the above direction.

Figure 3-1 Photo of a two-story house with double façade of ceramic tiles (adapted from [135]).

Figure 3-2 The facing tile is a single-skin cladding product which is easy and economical to install, with a lightweight system resting on horizontal rails (adapted from [135]).

Figure 3-3 South facing walls of a two-story house are fitted with solar modules.

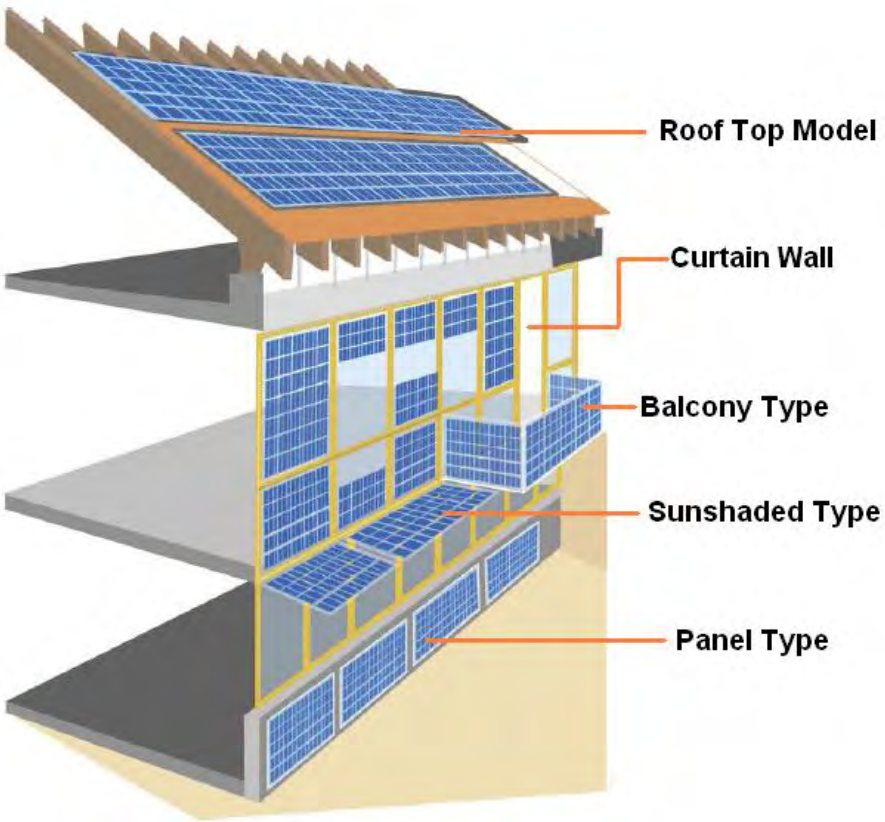

Figure 3-4 BIPV for various applications, (adapted from [136]).

3.1 ARCHITECTURAL CONCEPT

In this work, we investigate the feasibility of incorporating PV modules in the south façade of an office building (see for example a South elevation view of the building in Figure 3-5 and a schematic N-S section of the building in Figure 3-6) to exploit both

the electricity produced and heat rejected by the module in increasing the building's energy efficiency.

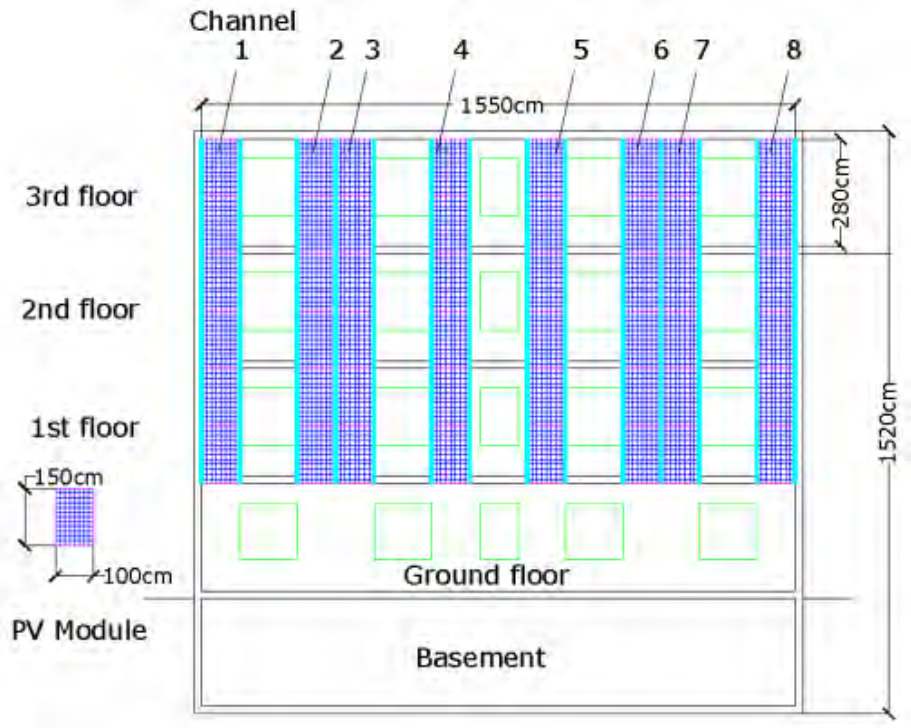

Figure 3-5 South elevation of a building with integrated PV panels (to be employed in the simulations).

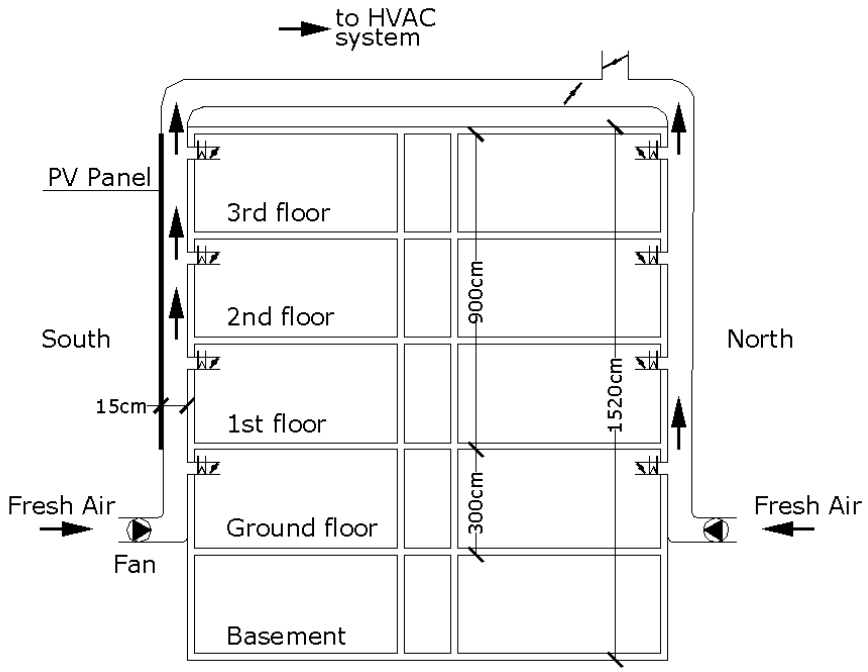

Figure 3-6 Principle of operation of PV cooling duct – interfacing with HVAC system (N-S section view)

In the example building concept of Figure 3-5, several bands of 6 modules each are vertically placed at a 0.15 m distance from the long south- facing wall (see **Figure 2-9**). Each band creates a duct behind it, with dimensions of 9 m x 0.15 m x 1 m (aspect ratio H/d = 9/0.15 = 60). Each duct is employed to supply ventilation air to a number of nearby office compartments of the building (Figure 3-6) [71]. Small fans are employed to supply the air to the spaces. The air is heated as it passes by the backside of the PV modules. The upward flow produced by the buoyancy effects, can easily satisfy the cooling of the PV panels. On the other hand, the flow rate is more than adequate for the ventilation needs of the nearby spaces of the building. Sizing and control of the proposed system to satisfy both purposes is essential to its economic viability as will be demonstrated below.

A detailed computation of the transient thermal behavior of the building on an hourly basis is required to support system's design. Such a computation can be supported by one of the in-use certified building energy simulation programs, such as TRNSYS, DOE-2 or ENERGYPLUS [137]. The hour-by-hour computation allows for sufficient accuracy in the calculation of solar gains that contribute significantly to the energy consumption for cooling, and also affect heating energy consumption. Moreover, the hourly base calculation is required for the study of the performance of the PV modules integrated on the south façade of the building and the thermal and flow behavior of the associated air duct, which deserves to be studied in detail based on the discussion of the next section.

3.2 HVAC CONCEPT FOR AIR DISTRIBUTION AND EXPLOITATION

The typical office building of Figure 3-5 is employed as a case study. Eight vertical bands of PV modules with the characteristics of Table 6-1 are installed on the south façade of the building, that is, a total of 48 PV modules with an area of about 72 m^2 and a total rated power of 9.84 kW. An air flow rate of 110 m^3/ h (133 kg/h) in each of the 8 ducts (Figure 3-7) is adequate to cover the ventilation needs of several spaces. It will be tested if this flow rate sufficiently cools the PV panels. An increased air flow of 330 m^3/ h (400 kg/h) is also comparatively assessed.

The specific concept of decentralized fresh air ventilation system is a modern concept that is increasingly applied in double façade system in large buildings (Figure 3-8) [138]. Usual applications of this concept do not employ PV panels, but simple claddings (Figure 3-8, upper left and right). The HVAC components for the ventilation system (fans and heat exchangers), are conveniently packaged inside the double façade (Figure 3-8, lower center and right).

Figure 3-7 Typical connection of fan and takeoffs for space heating to the main duct receiving heated air from one of the 8 ducts behind a band of 6 PV modules.

3.3 SERVICE WATER HEATING DURING SUMMER

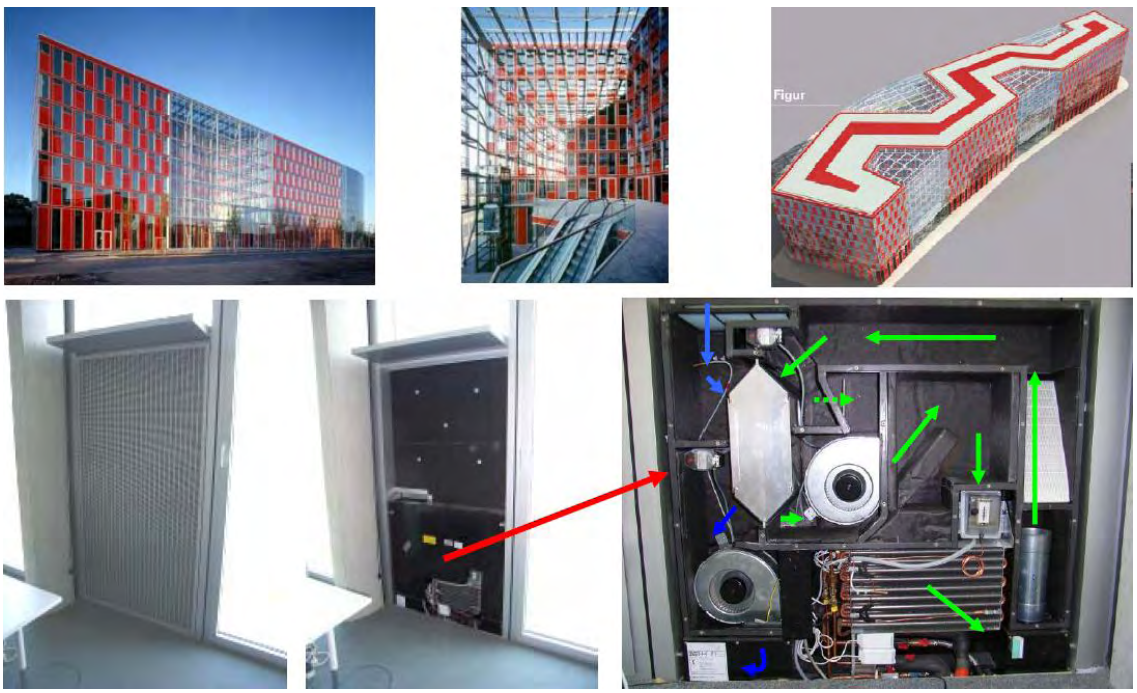

Figure 3-8 Decentralised fresh air ventilation system in double facade: integration of fans and heat exchangers in the facade. (Adapted from [138]).

During the sunny summer days, the outdoor air driven through the ducts is heated to high temperatures. Due to the small size and height of the system, the air temperature does not exceed 60 ^{o}C (Figure 6-17). Since heating is not required, the high air enthalpy can be alternatively exploited for producing domestic hot water. In the proposed concept, this is done by means of a tank-type air to water heat exchanger or an air source heat pump water heater (Figure 3-9).

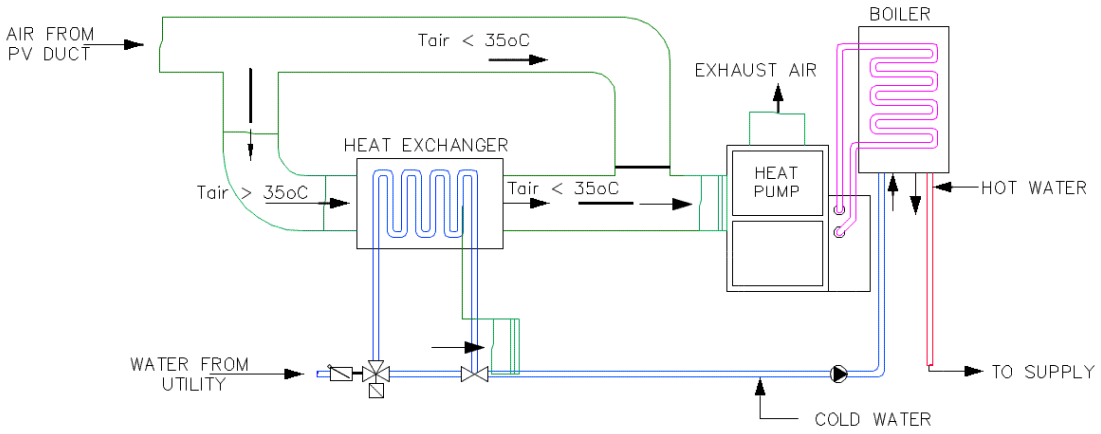

Figure 3-9 Service water heating by hot air during summer.

PART A: Study of the basic building block of the concept

CHAPTER

4

4 EXPERIMENTAL [1]

4.1 EXPERIMENTAL METHOD AND PROCEDURE

4.1.1 BASIC TESTING DEVICE

The basic building block of the concept is a vertically placed PV panel, in front of a south- or west-facing wall, with an air-gap in-between. The feasibility of the concept and its performance when installed on a reference building was computationally assessed by means of TRNSYS building energy simulation software presented in section 8.

An experimental device was designed to test the transient thermal and electrical behavior of the basic building element of the double façade concept, in order to improve modeling accuracy and design optimization. The device is schematically presented in Figure 4-1 [139] and photographs of its front and back side are shown in Figure 4-2.

The experimental façade arrangement consists basically of two vertical parallel plates, the photovoltaic panel and a panel made of 5 mm plexiglass, each with the dimension of 1.50 m x 0.99 m. Both plates are integrated in a double window-type

1 A part of this chapter has been published as: article in press: Zogou O, Stapountzis H, Experimental validation of an improved concept of building integrated photovoltaic panels, Renewable Energy (2011), doi:10.1016/j.renene.2011.05.034

aluminum frame with a cavity in-between. The distance between the two plates is set to 150 mm.

Thus, a rectangular duct with an aspect ratio of 6.6 (0.99/0.15 = 6.6) is formed. The bottom of the duct is open to allow the outdoor cooling air to enter (first passing through a honeycomb flow homogenization grid) and flow upwards with free or forced convection. The top of the duct (outlet) is fitted to a tapered outlet hood leading to a circular outlet with a diameter of 125 mm, where two axial fans of different capacities can be optionally fitted to investigate the effects of forced convection in the duct.

The main dimension, technical data and Electrical characteristics of the PV module used for experiments are present in section 4.1.2 (see Figure 4-4, Figure 4-5 and Table 4-5).

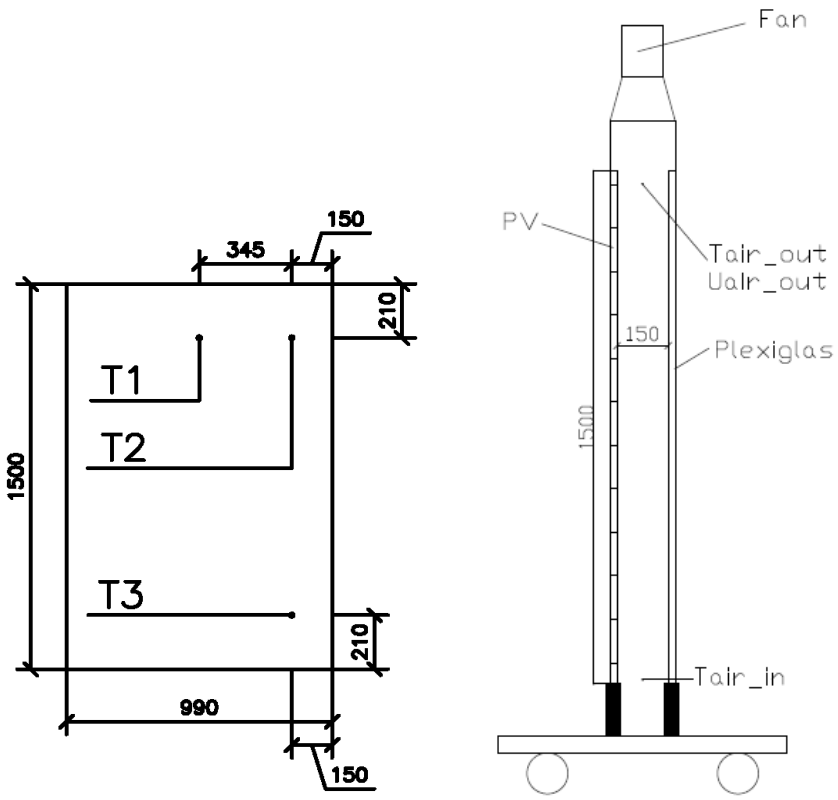

Figure 4-1 Thermocouples' (T) and anemometer's (U) locations at the backsheet of the PV panel (distances in mm) and longitudinal cross section.

Five temperatures are measured using K- type thermocouples (5TC-TTK-30-36): the air inlet and outlet temperature (Tair_in and Tair_out in Figure 4-1) and three

surface temperatures on the backsheet of the PV panel (T1, T2, T3 in Figure 4-1). The technical data of thermocouples are presented in Table 4-1. Solar radiation reaching the *vertical* panel surface is measured with a pyranometer (CMP 3 - Kipp & Zonen) (Table 4-2). A typical air velocity near the outlet section is measured by an anemometer (TSI Air Velocity Transducer Model 8455-300) (Table 4-3). An electronic load (ARRAY ELECTRONIC 3711A) (Table 4-4) is employed to dissipate the electricity produced and measure the electric power, current, voltage and load resistance. Measurements are recorded with a time step of 2 s with a NI-USB 6212 data acquisition device. The LabVIEW code employed in the data acquisition and recording, also controls the resistance of the electronic load by means of a PID controller module, to keep output voltage in the range 23.5 - 25V, thus keeping PV voltage and power output close to the maximum power point (MPP) [140].

Table 4-1 Technical data of thermocouples

Model No. ANSI Color Code	AWG Gage	Diameter mm (in)	Insulation	Time constant (s)
5TC-TT-K 30-36	30	0.25 (0.010")	PFA	0.2

Table 4-2 Technical data of Pyranometer

Spectral range		310 to 2800nm
Response time	@95%	<18s
Non linearity	0 – 1000 W/m^2	<2.5%
Temperature dependence of sensitivity	-40 ^{o}C to 40 ^{o}C -40 ^{o}C to 80 ^{o}C	<5% <10%

Table 4-3 Technical data of TSI Air Velocity Transducer

Range	0.051 to 5 m/s
Accuracy	±2% of reading at 18 to28°C +0.5% of full scale
Response time	0.2 seconds

Table 4-4 Technical data of Electronic Load

Input Voltage		0-360V DC
Input Current:		0-30A DC
Input Power		**0-300 W**
Voltage Accuracy	0.000-3.999 V 4.00-35.99 V 36.0-360.0 V	0.2%+3 mV 0.2%+30 mV 2%+300 mV
Current Accuracy	0.000-2.999A: 0.2%+3mA 3.00-30.00A: 0.2%+30mA	
Minimum Resolution Voltage		1 mV, Current 1 mA

The PV module is tested outdoors in real insolation conditions (Figure 4-2), at the University Campus in Pedion Areos, Volos, Greece (Lat 39.3604, Long 22.9299).

Figure 4-2 Photos of the front and backsheet of the test device.

4.1.2 SELECTION OF SOLAR MODULES

Figure 4-3 Detail view of Kyocera multicrystal photovoltaic module KD 205 GH – 2P

Kyocera KD 205 GH – 2P high efficiency polycrystalline photovoltaic modules was acquired for the comparative study. The dimensions of the modules are presented in the following figure.

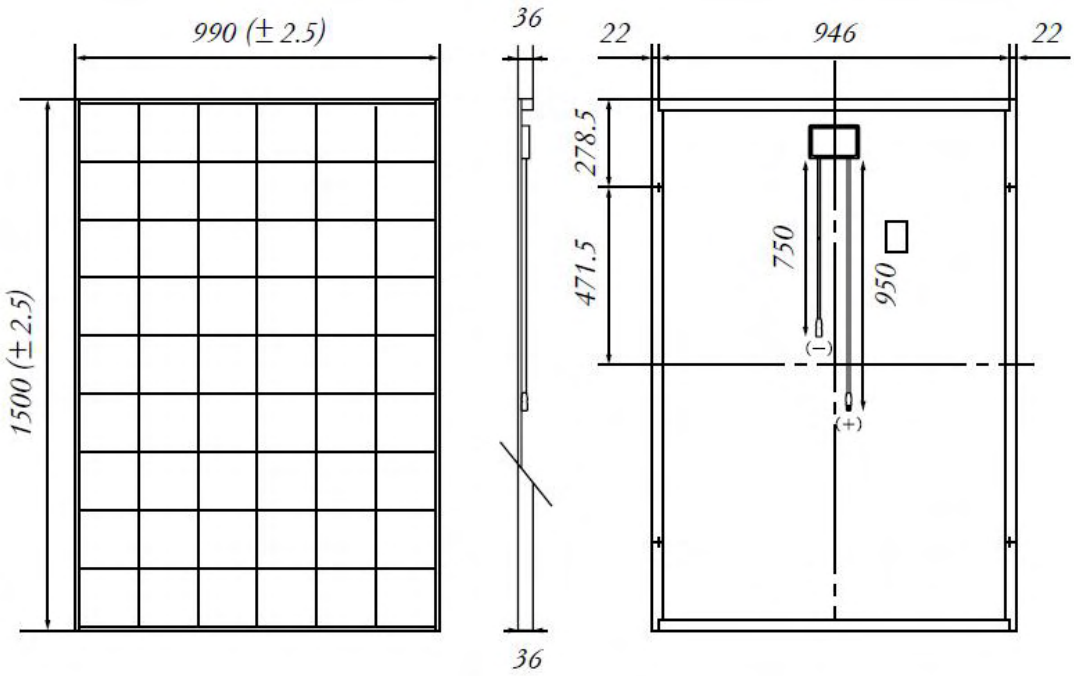

Figure 4-4 Main dimensions of the modules

The main technical data for the KD-205 GH-2P modules are summarized below:

Table 4-5 Technical data of PV panel

PV Module Type		KD205GH-2P	
Cell Technology		Multicrystalline, 54 cells per module	
Performance at 1000 W/m^2(Standard Test Conditions:Air Mass 1.5 , cell temp. 25 ^{o}C)			
Maximum Power		[W]	205
Maximum Power Voltage		[V]	26.6
Maximum Power Current		[A]	7.71
Open Circuit Voltage (V_{oc})		[V]	33.2
Short Circuit Current (I_{sc})		[A]	8.36
At 800 W/m^2(Normal Conditions: AM 1.5, wind speed 1 m/s, ambient temp. 20 ^{o}C)			
Maximum Power		[W]	145
Maximum Power Voltage		[V]	23.5
Maximum Power Current		[A]	6.17
Open Circuit Voltage (V_{oc})		[V]	29.9
Short Circuit Current (I_{sc})		[A]	6.82
NOCT		[°C]	49
Power Tolerance		[141]	+5/-5
Temperature Coefficient of V_{oc}		[V/°C]	-1.20x10^{-1}
Temperature Coefficient of I_{sc}		[A/°C]	5.02x10^{-3}
Temperature Coefficient of Max. Power		[W/°C]	-9.43x10^{-1}
Reduction of Efficiency (from 1000 to 200 W/m^2)		[141]	6.0
Length	[mm]	1500 (±2.5)	
Width	[mm]	990 (±2.5)	
Weight	[kg]	18.5	

Electrical characteristics are presented in the following figure:

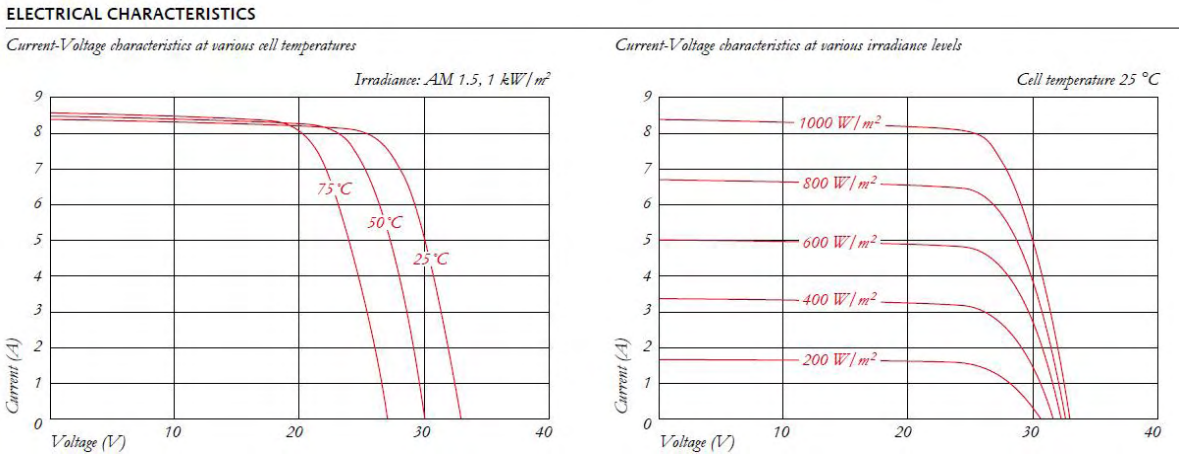

Figure 4-5 Electrical characteristics of the Kyocera KD-205 GH-2P module.

4.1.3 TEST RIG DESIGN DETAILS

A duct is constructed behind the solar module, to take off the heat produced by the cells operation, thus cooling the module and keeping a high efficiency in electricity production.

Dimensioning of the duct is as follows:

The width of the solar module is 990 mm.

A duct depth of 150 mm is considered as adequate, leading to an aspect ratio of the duct of 6.5 (38 in. x 6 in.). This would correspond to an equivalent circular duct of about 14 in. diameter (ASHRAE Table). According to the friction diagram of Figure 4-8, this duct could carry an air flow rate of 225 cfm (380 m^3/h), with an extremely low friction loss of about 0.01 in. w.g./100 ft. (or 1 Pa/m), with a mean air velocity of 1.5 m/s.

The design of the duct fitting to the take-off section is presented in the following figures:

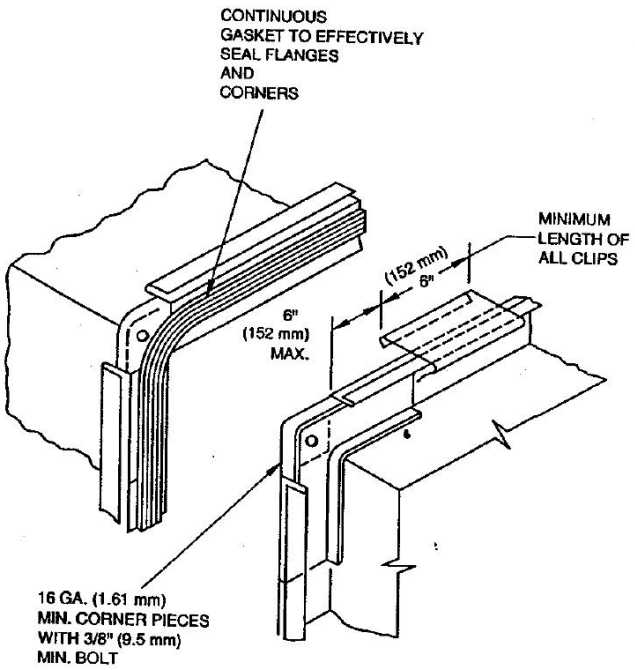

Figure 4-6 Flange connection of the duct and exit section.

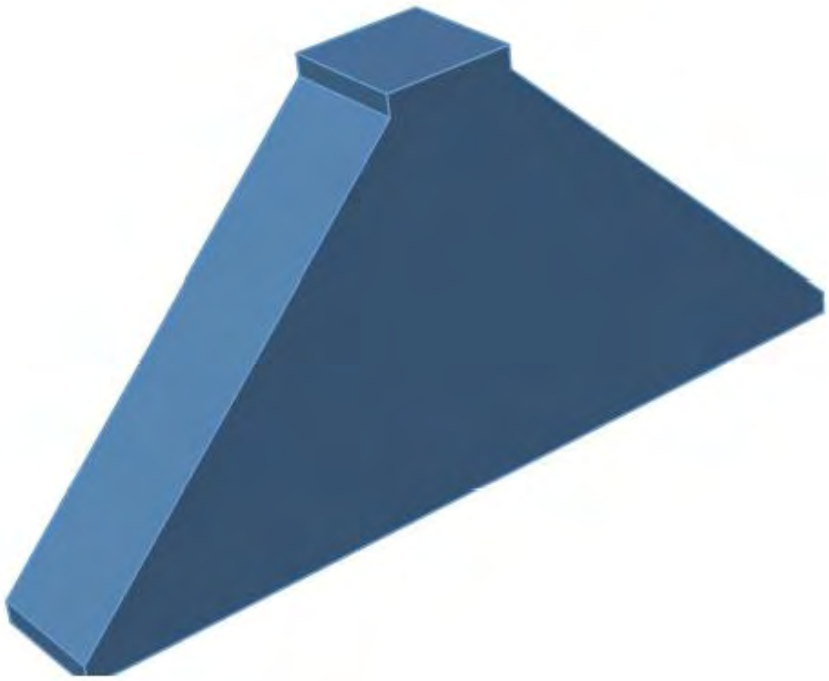

Figure 4-7 Design of the duct take-off section.

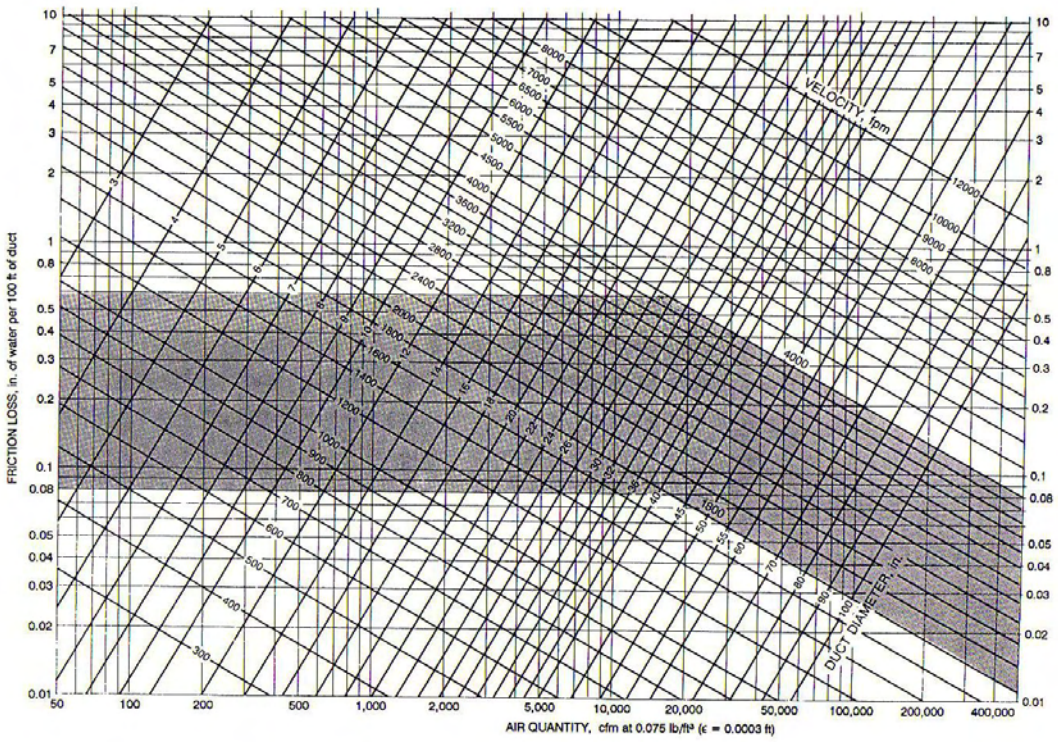

Fig. 9-2 Friction Chart for Round Duct (ρ = 0.075 lb_m/ft^3 and e= 0.0003 ft)

Figure 4-8 Friction chart for Round duct (ρ = 1.2 kg/m^3, ε = 0.0009)

In practice, less air flow rate is necessary for cooling the module.

We assume that the cell is placed in a vertical position facing south in March 21, 39.22^{o} latitude, and an average incidence angle of the order of 45^{o} would be observed around the solar noon. With favorable atmospheric conditions (clear sky), about 1 kW/m^{2} of solar radiation intensity would fall on a surface perpendicular to the sun's rays.

This would give in our case (Table 4-5):

1000 W/m^{2} sin (45^{o})(1.5m*0.99m) = 1000 W/m^{2} ($\frac{\overline{2}}{2}$) (1.5m*0.99m) =1050 W.

An approximate energy balance for this heat flux radiated to the solar module is as follows:

Absorbed by the module surface: 0.9 *1050 W = 945 W

Transformed to electricity (see technical data sheet of Kyocera KD 205 in Table 4-5 and Figure 4-5)

0.14* 945 W = 129 W

Heat rejected from both faces of the module

945 W – 129 W = 816 W

That is, from the back face of the module, it would be necessary to take off about 400 – 500 W of rejected heat.

This heat would be taken by convection from the ambient air entering the duct from below, with an indicative inlet temperature of about 20 ^{0}C.

An air flow rate of about 180 m^{3}/h, or 0.05 m^{3}/s, would suffice for this case, since it could take off the rejected heat of 500 W with a relatively small increase of the air temperature ΔT = 10 ^{0}C

500 W = 0.05 m^{3}/s *1.06 kJ/kg K ΔT

In order to interface with the building HVAC system, we design a converging part from the 990 x 150 duct to a circular duct of 125 mm diameter that could accommodate the flow rate from a longer duct, cooling 4 modules in series.

In our experimental case we employ just one module, thus we connect a contraction fitting to 125 mm diameter duct, where we can fit an axial fan of about 110 m^3/h nominal flow rate (main technical data in Table 4-6, left side of Figure 4-9). This fan would easily accommodate the required flow rate of 180 m^3/h with a mean velocity of 5 m/s at the 125 mm circular exit duct.

The optimization is supported by experimental data of the PV panel exposed to the outlet conditions but in different ventilations rates for the air flow in the gap.

Of course, the same 990 x 150 mm duct could accommodate higher air flow rates, in case of a higher construction of up to 6 solar modules placed one above the other, to cover the external shell of an office building, as already discussed in the architectural concept of chapter 3.

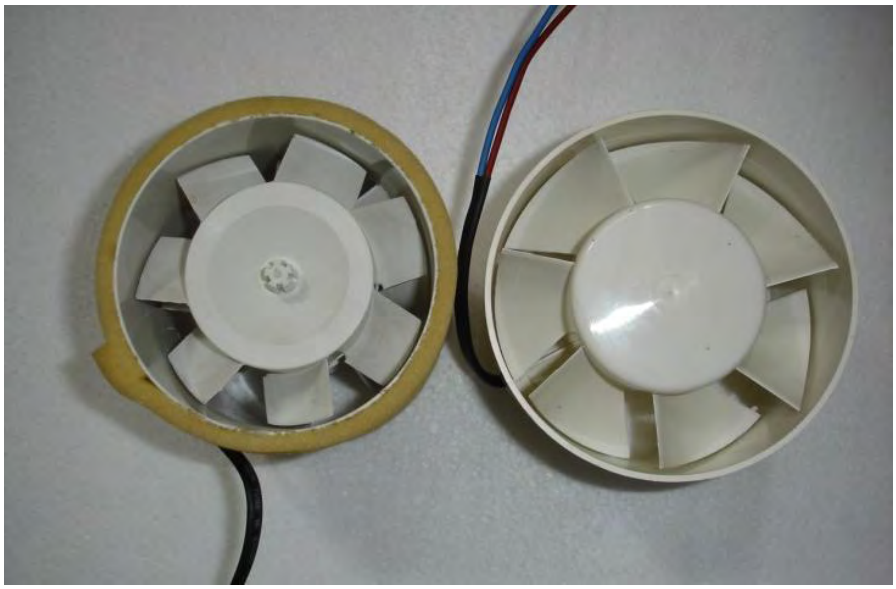

Figure 4-9 Photo of the lower and higher capacity axial fans fitted to the exit duct (20 W each).

Table 4-6 Technical data of the two axial fans

Type	Nominal flowrate [m3/h]	Nominal static pressure [Pa]	Power consumption [W]	Total efficiency[-]
AC shaded pole induction motor	110	49	20	0.075
AC shaded pole induction motor	190	49	20	0.13

4.1.5 TEST PROCEDURE AND METHODOLOGY

In principle, a steady-state free- or forced- convection coefficient could be estimated by a typical Nu (Gr, Pr) or Nu (Re, Pr) relationship [91]. However, the real world situation in the duct is quite complex, due to the important role of radiation and the transient phenomena involved, requiring an experimental approach. Further, it would be interesting to record incoming solar radiation and its daily and seasonal variation in the specific place. For the above reason, the PV module was first subjected to a series of outdoor tests in real insolation conditions (Figure 4-2), at the University Campus in Pedion Areos, Volos, Greece (Lat 39.3604 N, Long 22.9299 E). The panel was oriented south or west, and schedules made up as a combination of the following operation modes:

- Mode 1: no fan (cooling with natural convection).
- Mode 2: lower capacity fan installed (nominal flow rate 110 m^3/h).
- Mode 3: higher capacity fan installed (nominal flow rate 190 m^3/h).

Each outdoor experiment lasted for several hours during the same day. Sunny days were mainly selected for the experiments. Sometimes, a decrease in the incoming solar radiation is observable in the recordings, due to cloud formation.

A second series of measurements was carried out indoors to better understand the flow field in the three operating modes. These were flow visualization measurements. A third series of measurements was carried out indoors to better quantify the flow field in the three operating modes. These were hot wire anemometry measurements. Details and results of all three sets of measurements are presented in the following sections.

4.2 OUTDOOR MEASUREMENTS WITH THE TESTING DEVICE

4.2.1 SOLAR RADIATION MEASUREMENTS

The measurement of incoming solar radiation is usually done on a horizontal surface, according to the operation principles of the pyranometer [142]. Here we decided to place the pyranometer in a vertical position, in the upper left corner of the PV panel (see photo in Figure 4-2) [139]. Recordings of the variation of solar radiation measured by the pyranometer placed on the vertical, south-facing panel surface are shown in Figure 4-10 for several hours (local time) during seven days: 7, 14, 15, 16,

21 June and 12, 16, 21 July, that is, close to the summer solstice. At midday (12:00 – 16:00), the incoming radiation to the vertical plane with clear sky varies between 250 – 380 W/m^2.

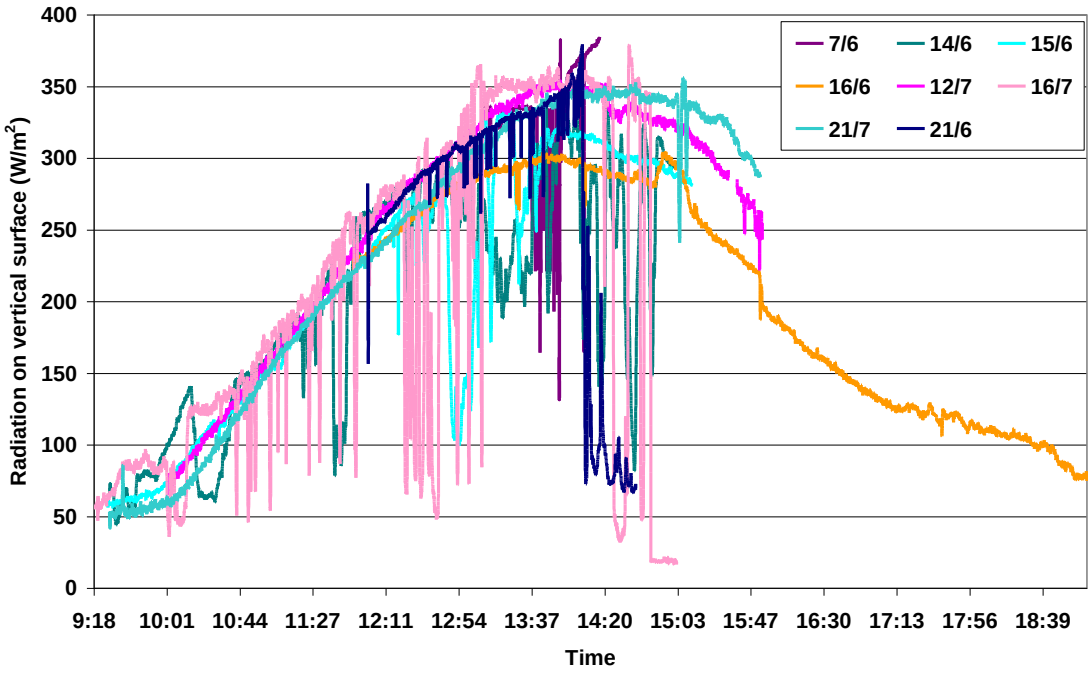

Figure 4-10 Daily variation of total radiation falling on the vertical south-facing surface during several days in June – July 2010 (Lat 39.3604, Long 22.9299) (local time)

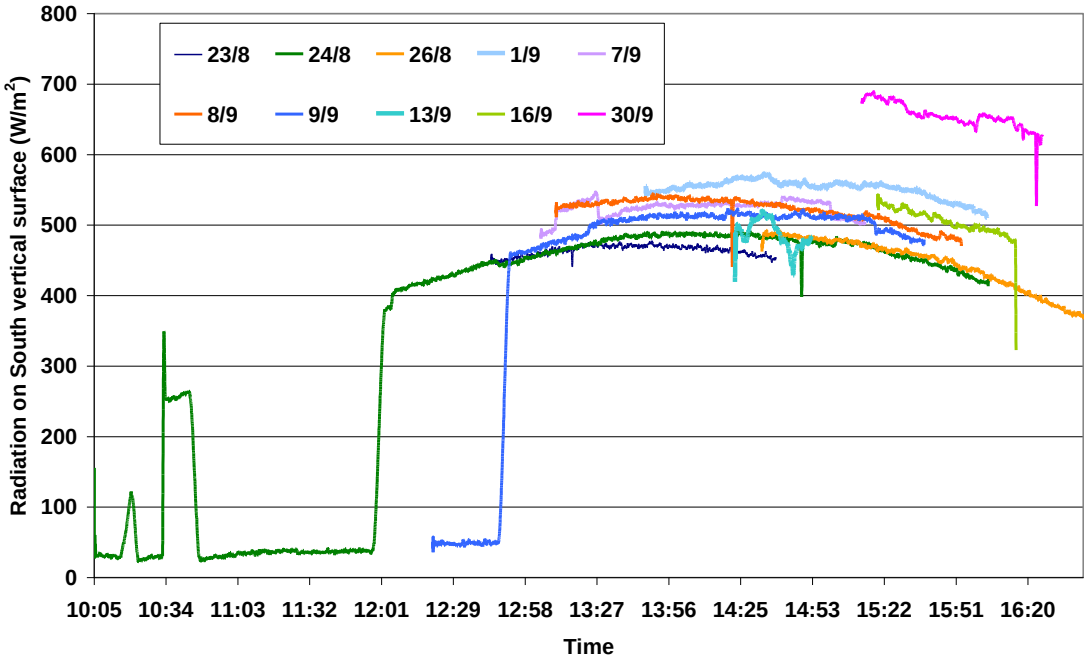

Figure 4-11 Daily variation of total radiation falling on the vertical south-facing surface during several days in August – September 2010 (Lat 39.3604, Long 22.9299) (local time)

Similarly, recordings of the variation of solar radiation falling on the vertical, south-facing panel surface are shown in Figure 4-11 for several hours during the following days: 23, 24,26 of August, 1,7,8,9,13,16 and 30 September 2010 (that is, close to the Autumnal equinox).

At midday (12:00 – 16:00), the incoming radiation to the vertical plane with clear sky varies between 400 – 570 W/m^2. As expected, the radiation intensity increases as the sun's height angle (α_s) decreases, moving from the summer solstice to the autumnal equinox. This is observed by a comparison of Figure 4-10 and Figure 4-11. That is, in August and September we have significantly higher incoming solar radiation intensity on the vertical, south-facing plane, than in June and July. This tendency is continuing as we move closer to the winter solstice.

4.2.2 FLOW AND HEAT TRANSFER MEASUREMENTS

In this section we concentrate on the results of the measurement of transient flow and heat transfer characteristics during the days mentioned above [139]. That is, we examine the evolution of air and panel temperatures during the day, as function of the radiation and meteorological conditions prevailing, as well as the mode of cooling applied.

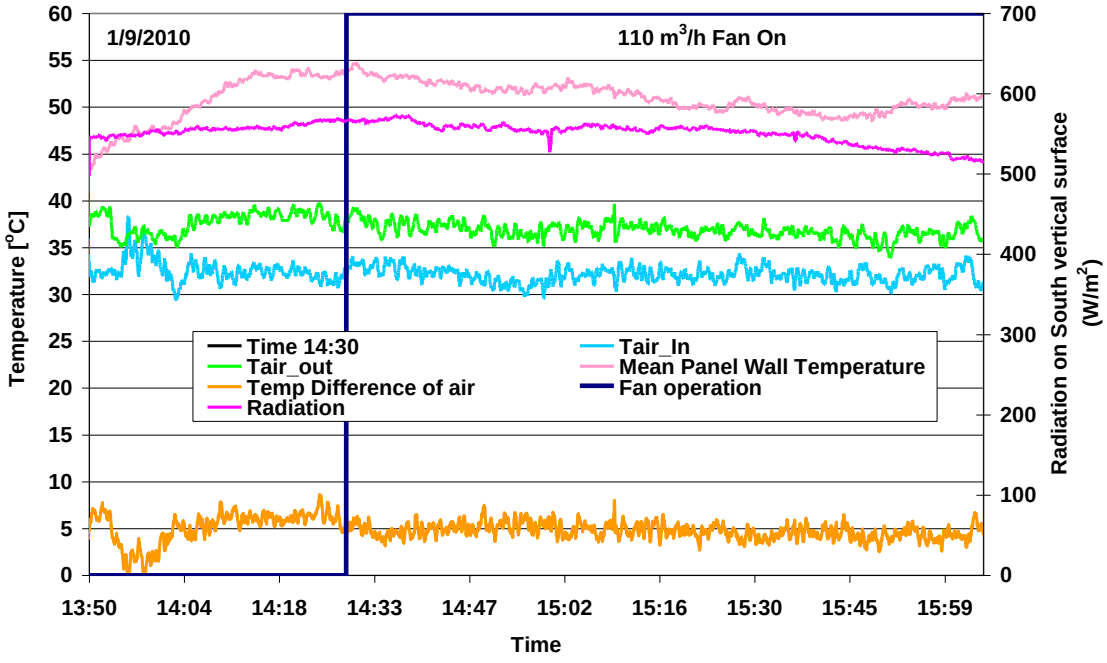

Figure 4-12 Recording of the performance on 1/9/2010. At 14:31 the fan is switched ON (nominal flow rate: 110 m^3/h)

First, a recording of the transient thermal performance of the device during several hours in September 1st is presented in Figure 4-12. The noisy temperature recordings are due to the lack of a thermocouple signal conditioning device before the data acquisition card. The test device is placed outside the northwest side of our Department building. For this reason, the device starts to be radiated by the sun at about 13:50, where the recording of Figure 4-12 begins.

For this reason, the first part of the diagram (from 13:50 to 14:17) shows the transient phenomenon of heating of the device by the sun. This is depicted both in the sharp increase of the average panel temperature and the fluctuations of inlet and outlet air temperatures at the specific measurement points (along the centerline of the device). During this period the fan is switched off and the cell temperatures (cooling by natural convection) stabilize at around 54 ^{o}C (average radiation 560 W/m^2). The temperature increase of air passing through the duct stabilizes at about 7.0 ^{o}C. Such an increase seems not so important but we must take into account that we test a small building block of the system – just 1.5 m height of double façade. At 14:30 the low capacity fan, with a nominal flow rate of 110 m^3/h, is switched on. Now the cooling is performed by forced convection, the average cell temperatures vary between 48.5 ^{o}C and 54.7 ^{o}C (average radiation 550 W/m^2) and the temperature increase of air passing through the duct reaches 8.0 ^{o}C.

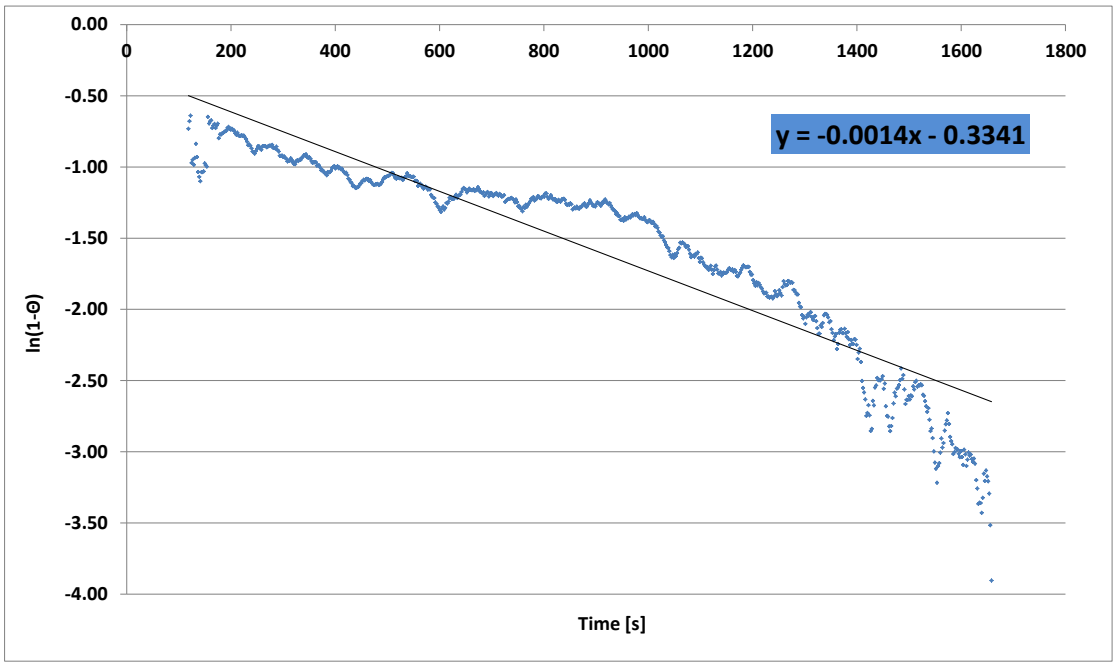

Figure 4-13 Calculation of time constant for the thermal response of the PV panel

The recorded data of the first part of Figure 4-12 can be used in the determination of the time constant of panel temperature response, assuming a first order response. A dimensionless panel temperature is defined as follows:

$$\Theta = \frac{T - T_0}{T_\infty - T_0} \quad (4.1)$$

Assuming a first order response, Θ is depending on time according to the following relation :

$$\Theta = 1 - e^{-t/\tau} \quad (4.2)$$

where τ is the time constant, calculated by linear regression on the temperature response data (Figure 4-13).

The time constant of the photovoltaic module is 714s ≈ 12min.

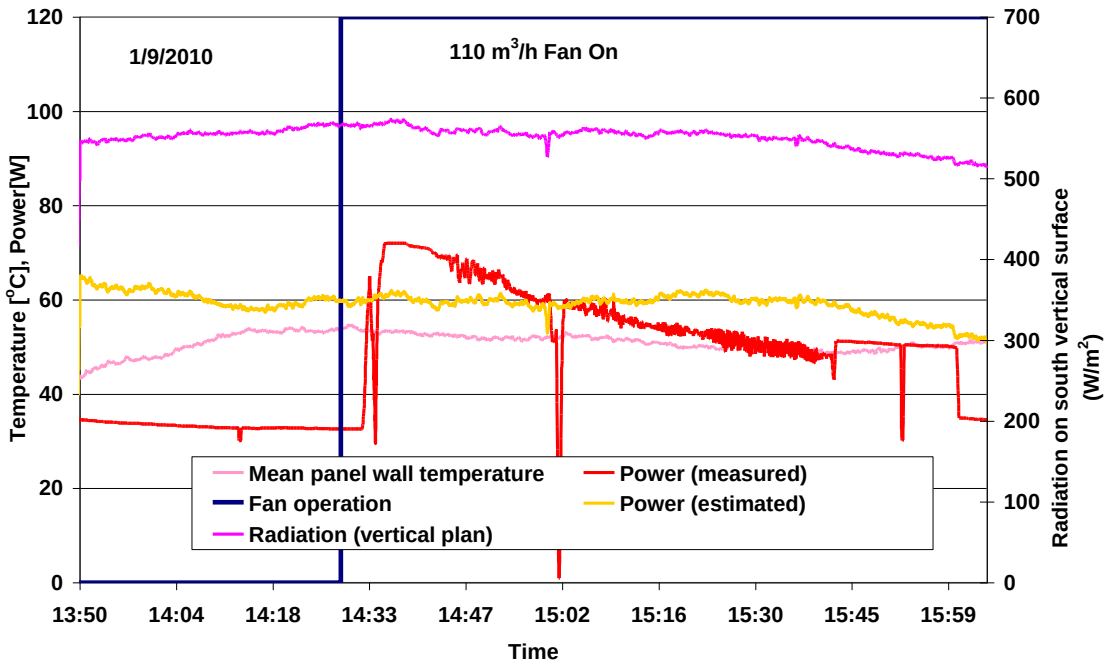

Figure 4-14 Solar radiation, power generated and average cell temperature variation during 2 hours in September 1st, 2010

In Figure 4-14, the electric power produced by the panel is compared to the theoretical efficiency that would correspond to the same level of insolation, with the reference air mass. During the first 40 minutes, the efficiency of the unit is reduced because of a failure of the electric load control system to accurately match the MPP point. Afterwards, at about 14:33, the MPP point is reached and initially, the measured performance is higher than the theoretical one. As the sun goes down

during the afternoon, the measured efficiency is slightly dropping compared to the theoretical one. This is in line with the results of other researchers [143], and could be partly attributed to the increase of air mass as the sun's height decreases during the afternoon [144, 145].

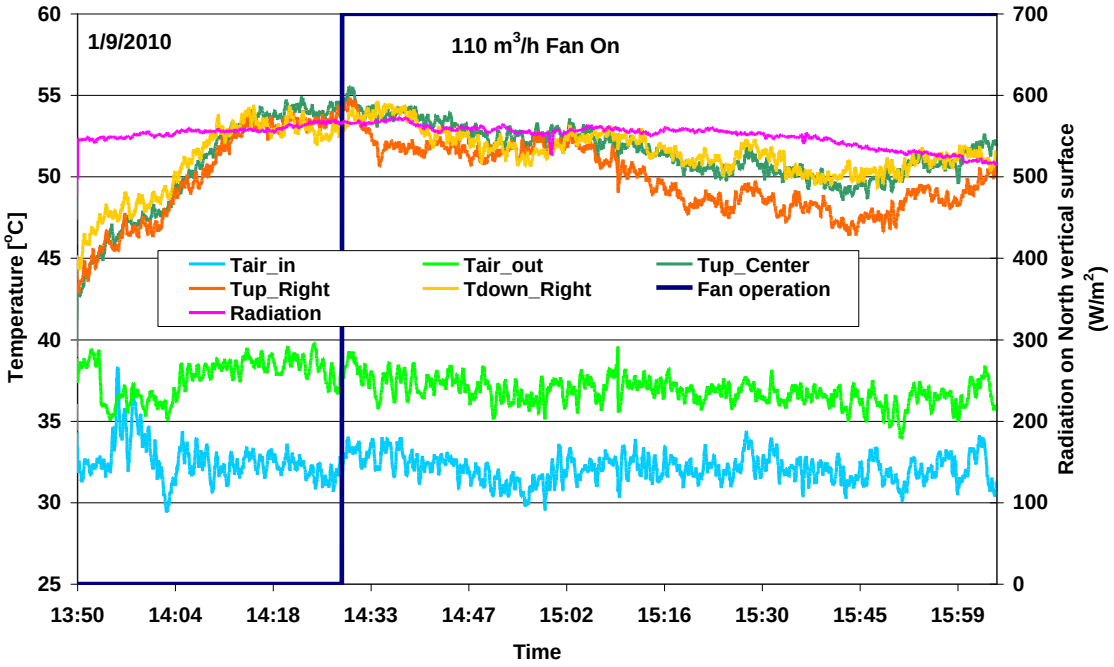

Figure 4-15 Variation of air inlet, outlet and selected back panel wall temperatures (September 1st, 2010)

Next we focus of the thermal behavior of the testing device. Figure 4-15 presents the variation of the air inlet and outlet temperatures, along with the three characteristic panel temperatures monitored by the data acquisition system. It can also be observed that the panel temperatures are decreasing after 15:00, possibly due to the effect of increased cooling by use of the fan. But this needs further investigation.

A summary of the observed behavior in the form of average values is shown in **Table 4-7**.

In order to better understand the heat transfer behavior of the panel, a local convection coefficient can be defined for the shaded part of the panel with dimensions 200 x 500 mm (see Figure 4.15), according to the expression below:

$$\mathbf{Q = mc_p \Delta T} \quad \textbf{(4.1)}$$

$$\mathbf{Q = h_{local} A (T_w - T_{air})} \quad \textbf{(4.2)}$$

$$\mathbf{h_{local} = Q\ \ A(T_w - T_{air})} \qquad \textbf{(4.3)}$$

Table 4-7 Summary of results in the various operation modes (September 1st, 2010)

Time average values:	T_panel (oC)	Tair_out (oC)	Tair_In (oC)	ΔT air (oC)	Power (W)	Radiation (W/m2)	Power/ Radiation
Mode 1	50.3	37.9	32.2	5.7	33.0	558	0.040
Mode 2	51.1	36.8	32.1	4.7	54.0	550	0.066

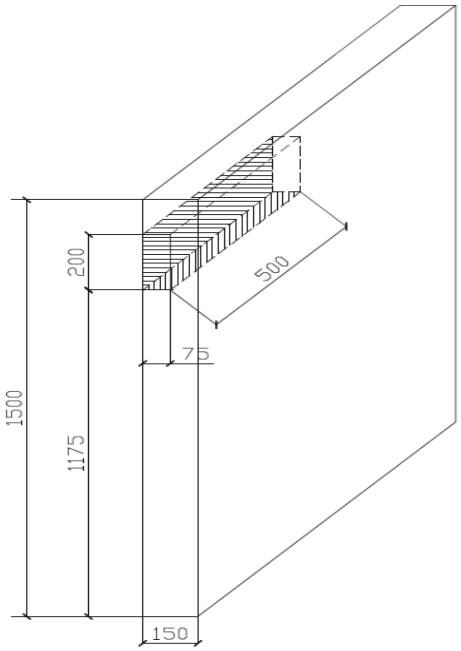

Figure 4-16 Definition of local convection coefficient at a specific measurement point (distances in mm)

The specific part of the panel is the upper right part as seen from the back side. It is selected because of the fact that the data acquisition system is recording enough local data for this part, e.g. air velocity, panel wall temperature. However, we do not record local data regarding air temperature at this section. Instead, we measure air temperature at the same height, at the centerline of the device. If we make a simplifying assumption that 20% of the incoming solar radiation is transmitted to the cooling air to the back of the panel (see energy balance at the introduction section), and assume that the air temperature does not change significantly at the same horizontal section, then we can solve equation (4.3) to calculate an approximate value for the local heat transfer coefficient.

The resulting variation of the calculated local convection coefficient is presented in Figure 4.17, along with the variation of air velocity measured at a characteristic point at the upper right part of the cavity as we look at it from the back side (see Figure 4-2). A small decrease in local air velocity is observed, along with an increase in convection coefficient with the shift to forced convection following switching on the fan. Thus, the installation of the specific capacity fan does not seem to increase the air flow through the cavity under the specific insolation and weather conditions.

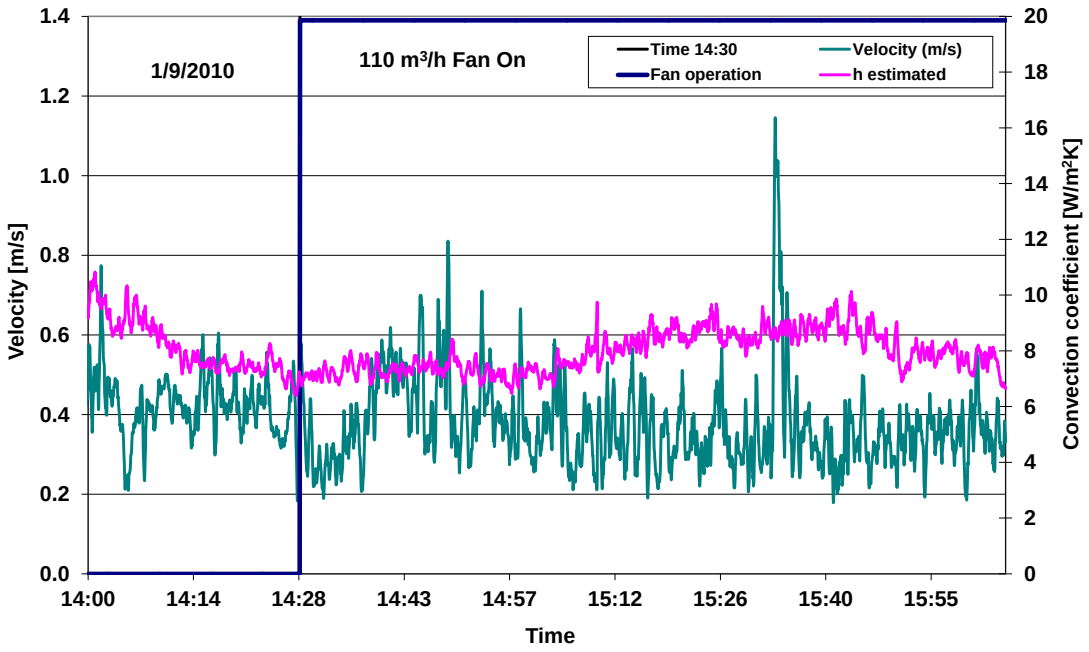

Figure 4-17 Variation of local air velocity at the measurement point and calculated variation of estimated local convection coefficient (September 1st, 2010)

Another example of the transient response of the system is presented in Figure 4-18, which corresponds to several hours of September 8th, 2010. In this test, two fans of different capacity are alternatively tested, so, all three modes of operation are present.

In the period from 13:11 to 13:43, the fan remains switched off. The panel temperature is steadily increasing during the first 20 minutes (transient heating-up of the panel after placed outdoors under the sun). Average cell temperature increased stabilizes at about 58°C with average radiation levels on vertical surface 530 W/m^2. During the same heat-up period, the inlet air temperature steadily increases and stabilizes at about 38°C. The air temperature increase through the duct fluctuates very much during the heat-up period, with a time scale of the order of a few minutes and stabilizes in the range 10 -12°C. Obviously, there exist large eddies in the cavity during the heat-up period.

At 13:43 the high capacity (190m^3/h) fan is switched ON. The outlet air temperature is observed to significantly decrease, presumably due to an increase in the air flow rate. On the other hand, the air inlet temperature at the specific measurement point is seen to decrease slightly. Again, this can only be explained by the changing mode of air circulation at the inlet section (the specific point of measurement of the inlet temperature is already "inside" the device).

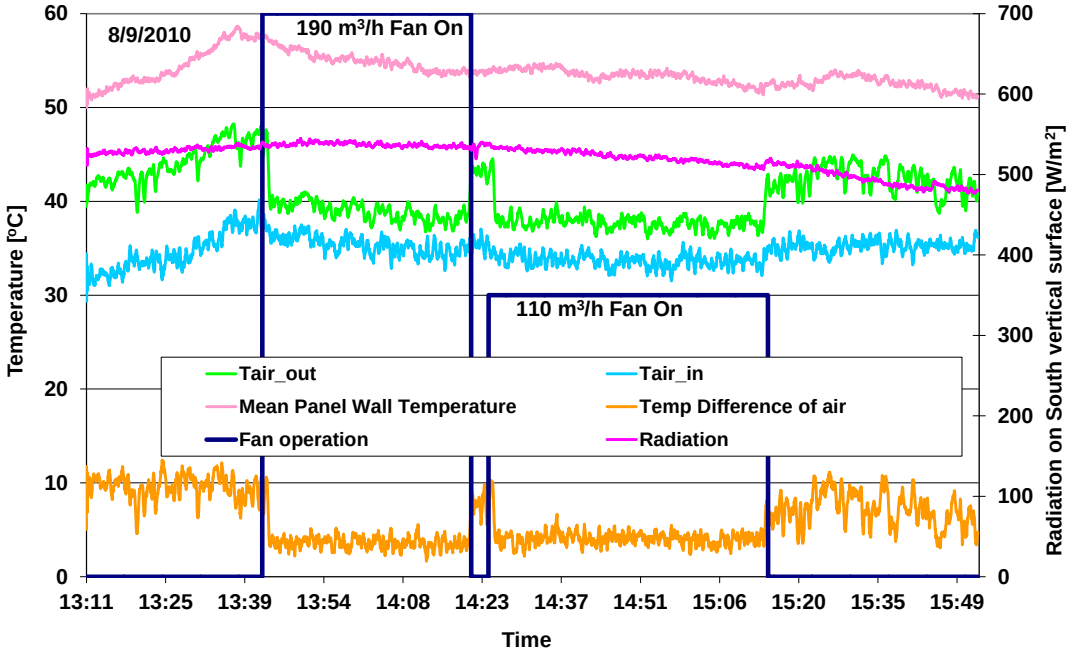

Figure 4-18 Recording of the performance on 8/9/2010. At 13:43 the Fan is switched ON (nominal flow rate: 190 m^3/h). Fan switched OFF at 14:21, Fan switched ON again at 14:24, with a lower nominal flow rate (110 m^3/h). Fan switched OFF at 15:15

As expected, the air temperature increase through the duct is reduced (higher flow rate). The fan is switched OFF at 14:21. The lower capacity fan (110m^3/h) is installed and switched ON at 14:24. Again, the whole flow field is seen to be affected. Inlet air temperature is seen to slightly decrease. As expected, the air temperature increase through the duct is increased (lower flow rate). The fan is switched OFF at 15:15.

This diagram is indicative of the complex nature of the transient operation of the test device and the different time scales existing in the various modes of operation. The most important observation that can be made here is that the inlet-outlet air temperature difference is not significantly changing between the lower and the higher capacity fan. This observation is in agreement with the results of the CFD computations of Chapter 5.

A summary of the observed behavior in the form of average values is shown in Table 4-8. Obviously, the flow field inside the cavity deserves more in-depth study for

better understanding of the phenomena involved that would allow system design optimization.

Table 4-8 Summary of results in the various operation modes (September 8th, 2010)

Time average values:	T_panel (°C)	Tair_out (°C)	Tair_In (°C)	ΔT air (°C)	Power (W)	Radiation (W/m^2)	Power/ Radiation
Mode 1	55.5	44.2	34.6	9.0	72.0	530	0.091
Mode 3	55.0	39.2	35.4	3.8	68.6	537	0.086
Mode 2	53.4	37.8	33.7	4.1	57.2	522	0.074
Mode 1	52.5	42.4	35.2	7.2	44.9	495	0.061

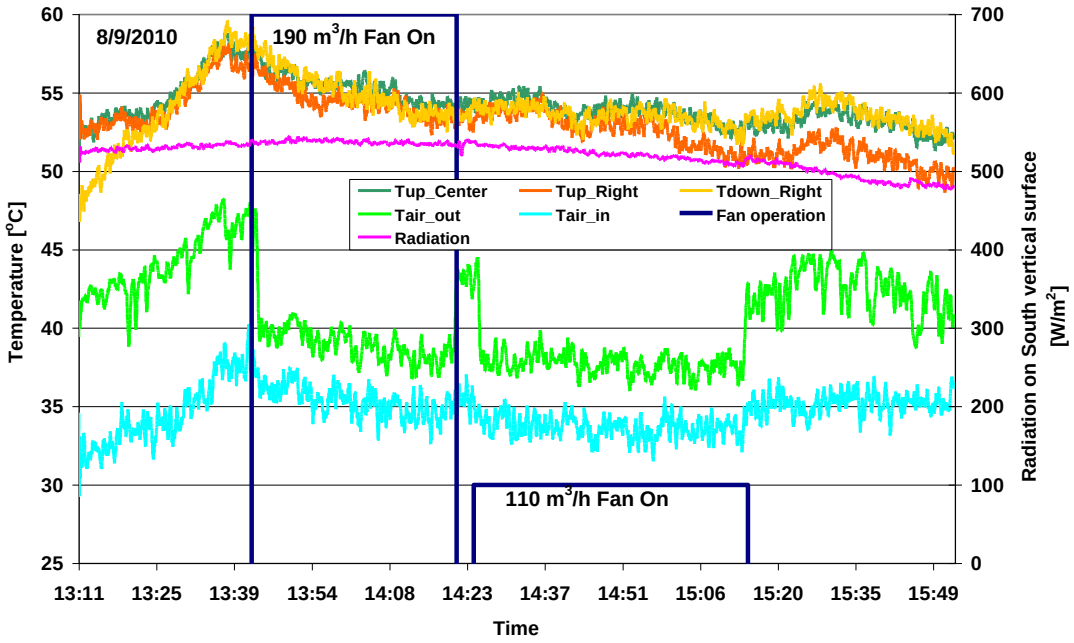

Figure 4-19 Variation of air inlet, outlet and selected PV panel back wall temperatures (September 8th, 2010)

Next we focus of the thermal behavior of the testing device. Figure 4-19 presents the variation of the air inlet and outlet temperatures, along with the three characteristic panel temperatures monitored by the data acquisition system. The panel temperatures are decreasing after 15:30, possibly due to the decrease in solar radiation. This is further investigated below.

As regards the panel's efficiency (Figure 4-20), it is measured above the estimated values (manufacturer's data) from 13:11 until 15:06. Afterwards, it stays in

agreement with estimated efficiency, except for some intervals with failing load control.

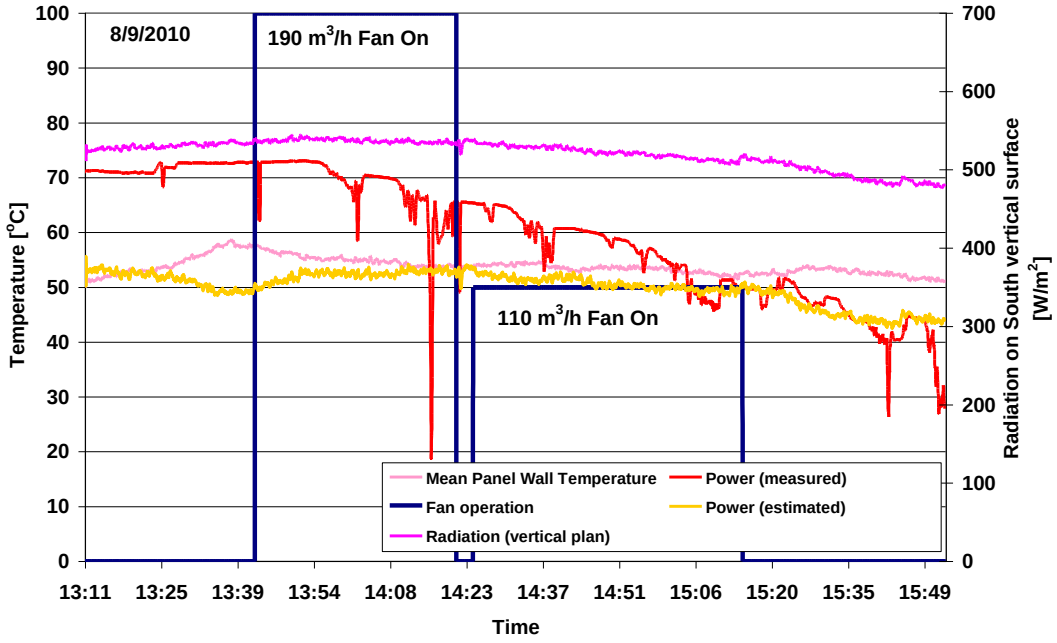

Figure 4-20 Solar radiation, power generated and average cell temperature variation during 2 hours in September 8th, 2010.

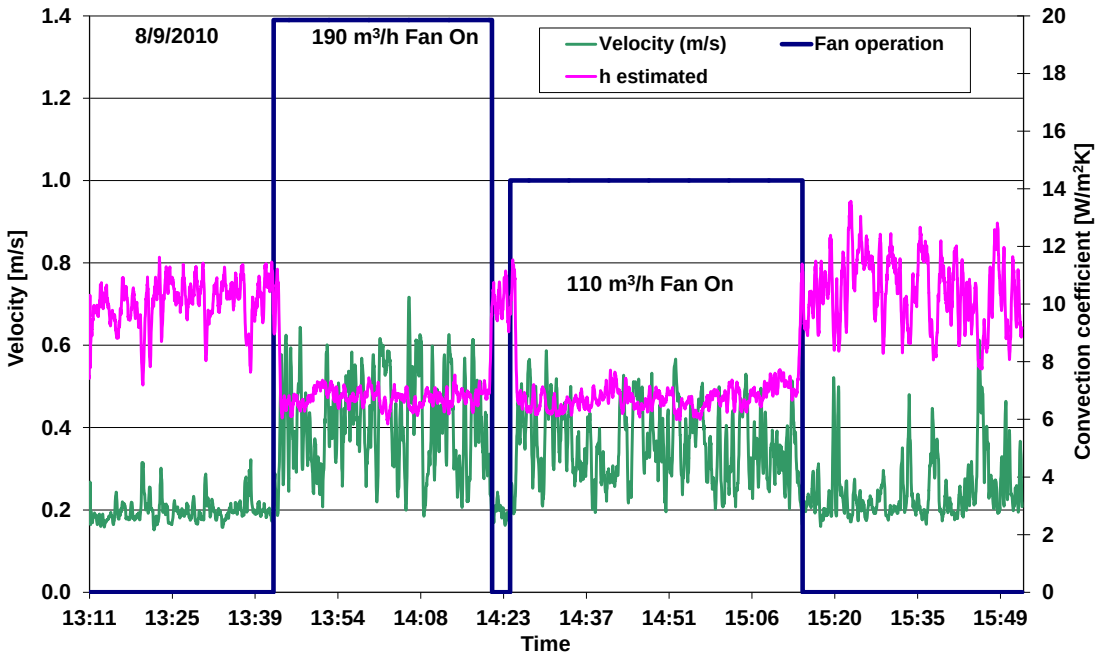

Figure 4-21 Variation of local air velocity at the measurement point and calculated variation of convection coefficient (September 8th, 2010)

The resulting variation of the calculated local convection coefficient is presented in Figure 4.21, along with the variation of the air velocity measured at the upper right part of the cavity (see Figure 4-2). It is interesting that a decrease in the estimated convection coefficient is observed with the shift to forced convection following switching on the high capacity fan. This is associated with a respective increase in air velocity, a reduction in outlet air temperature and a reduction in mean panel temperature for equal radiation levels. That is, overall the installation of the high capacity fan leads to an increase in air flow through the cavity and overall heat transfer rate between panel wall and cooling air. The same is true now also for the lower capacity fan, although the increase in overall heat transfer is lower in this case.

Another example of the transient response of the system is presented in Figure 4-22, recorded on September 30, 2010.

In the period from 15:13 to 15:34, the high capacity fan was switched on, (nominal air flow rate: 190 m^3/h). The panel temperature fluctuated between 45.6^{o}C – 48.6^{o}C (average panel temperature 47.3^{o}C) and the radiation varied between 656 W/m^2 and 690 W/m^2 (average radiation on vertical surface 675 W/m^2). At the same period, the temperature increase of air from inlet to outlet was in the range 2.9 - 5.7^{o}C.

From 15:35 to 15:39 the fan was switched off. Afterwards, the low capacity fan was switched on (nominal flow rate of 110m^3/h) from 15:39 to 16:00. In the period from 15:39 to 16:00 (see also Figure 4-22) the PV panel temperature varied between 46.7^{o}C – 49.8^{o}C (average cell temperature 48.5^{o}C) and the radiation varied between 632 W/m^2 and 663 W/m^2 (average radiation on the vertical surface 650 W/m^2). During the same period, the temperature increase of duct air was measured in the range 3.4 – 7.2^{o}C.

From 16:00 to 16:22 the fan was switched off. As shown in Figure 4-22 the average cell temperature was 49.6^{o}C, with instantaneous values varying between 47.7^{o}C – 51.3^{o}C and the radiation varied between 621 W/m^2 and 658 W/m^2 (average: 648 W/m^2). During the same period, a significant increase and fluctuation of air temperature increase through the duct is observed, in the range 3.9 -11.5^{o}C. Table 4-9 summarizes the average panel temperature and air temperature difference along with the power produced and incoming solar radiation for the three modes of operation.

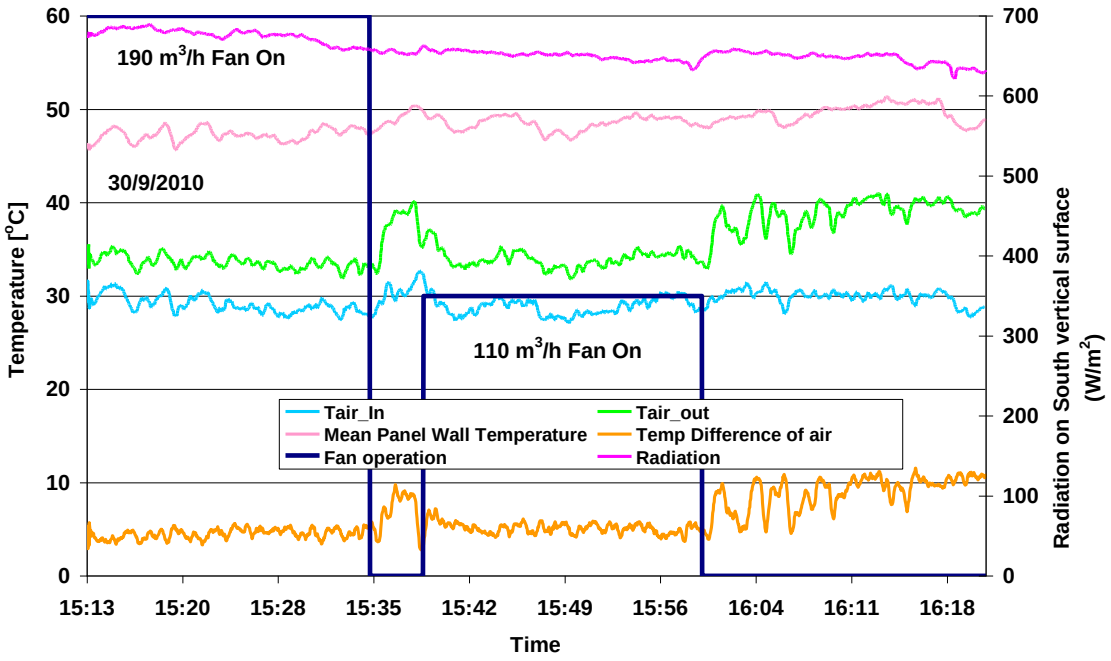

Figure 4-22 Recording of the performance on 30/9/2010 (vertical surface)

Table 4-9 Summary of results in the various operation modes (September 30th, 2010)

Time average values:	T_panel (°C)	Tair_out (°C)	Tair_In (°C)	ΔT air (°C)	Power (W)	Radiation (W/m²)	Power/ Radiation
Mode 3	47.3	33.6	29.1	4.5	85.5	676	0.085
Mode 2	48.5	34.0	28.9	5.1	73.8	650	0.076
Mode 1	49.6	38.8	29.9	8.9	74.7	648	0.078

Table 4-9 presents the variation of the air inlet and outlet temperatures, along with the three characteristic panel temperatures monitored by the data acquisition system.

As observed in Figure 4.23, in the period of 15:13 until 15:21 the produced electricity of tested PV is higher than the theoretical calculated using the coefficients from Table 4.1 (manufacturer's data: Temperature Coefficient of Max Power [-9.43*10-1 W/°C] and Reduction of Efficiency [6% from 1000 W/m2 to 200 W/m2]). As the sun goes down during the afternoon, the measured efficiency is slightly dropping compared to the estimated one. In certain periods the load controller is failing and an abrupt drop in the produced power is apparent (e.g. 15:45-15:52 etc.)

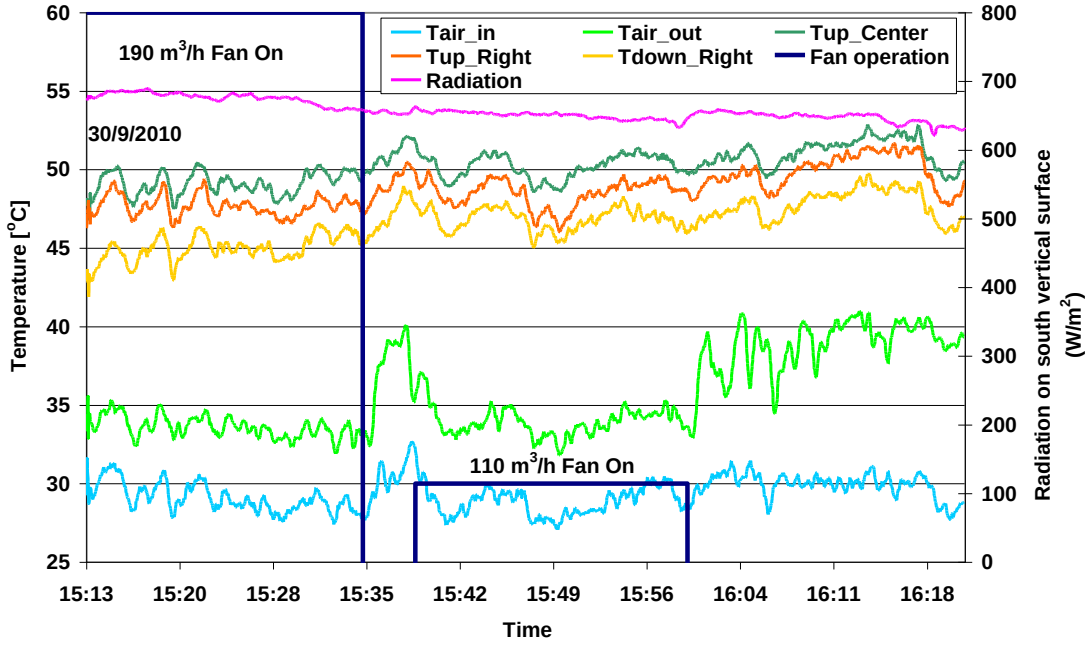

Figure 4-23 Variation of air inlet, outlet and selected back panel wall temperatures (September 30th, 2010)

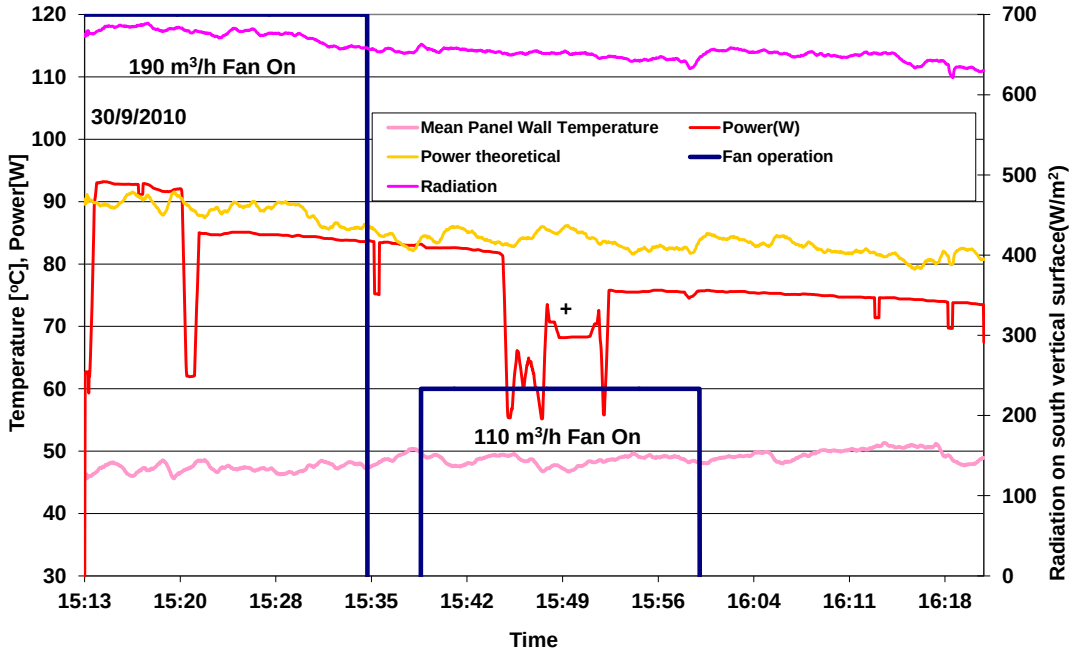

Figure 4-24 Variation of electricity output during the experiment on 30/9/2010

In order to further investigate the thermal behavior of the device, we proceed to the calculation of an approximate local convection coefficient between panel walls and cooling air (Figure 4.25). Again, we observe that switching on the high capacity fan results in an increase of air velocity at the measurement point, along with a very high fluctuation in air velocity. Also, a small decrease in the approximate local convection

coefficient is observed with forced convection, both with the low and the high capacity fan. This is in line with what is known from the specialized literature for very low air velocities [91]. On the other hand, the overall heat transfer rate is higher with forced convection, the panel temperatures are kept lower and the exit air temperature is reduced compared to the natural convection mode.

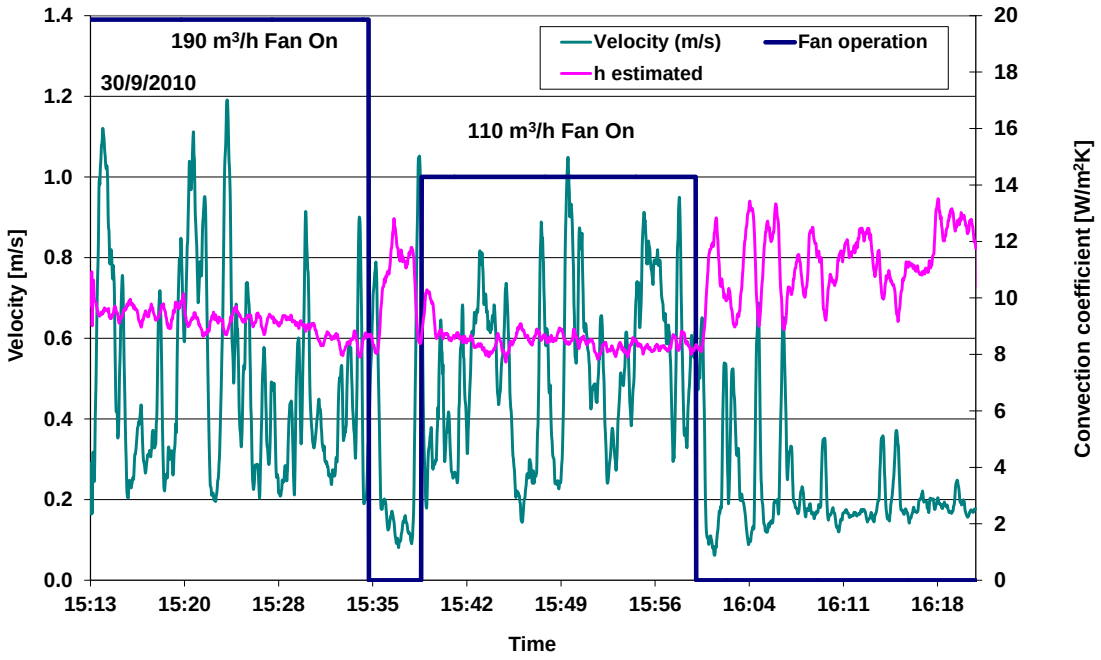

Figure 4-25 Variation of local air velocity at the measurement point and calculated variation of convection coefficient (September 30th, 2010)

As regards the PV panel's efficiency, the experiments show a clear correlation with the panel temperature that is in line with the manufacturer's characteristics. On the other hand, the deterioration of panel efficiency with the drop in solar radiation seems more difficult to correlate [146]. The above-mentioned tests indicate that sometimes the PV panel's efficiency is higher than predicted by the manufacturer's correlation with incoming solar radiation (around noon) and sometimes is lower (late afternoon). On the average, the PV panel's performance meets or even surpasses the predictions of these correlations.

A clear dependence of the panel's efficiency on solar time can be seen by a plot the measured PV panel efficiency versus the sun's altitude angle of each measurement.

Following the methodology presented in [147], we calculate the solar altitude angle, α_S using the equation:

$$\sin \alpha_S = \cos \theta_z = \cos \varphi \cos \delta \cos\omega + \sin \varphi \sin \delta \qquad (4.3)$$

where **δ** is the declination angle ($-23.45^{o}<\delta<23.45^{o}$, positive declination is west of south), **ϕ** is the latitude (39.3604^{o}), **ω** is the hour angle (morning negative, afternoon positive). If we plot the measured PV panel efficiency versus the solar altitude angle, (α_S) for several days of experiments, we get the graph of Figure 4-26.

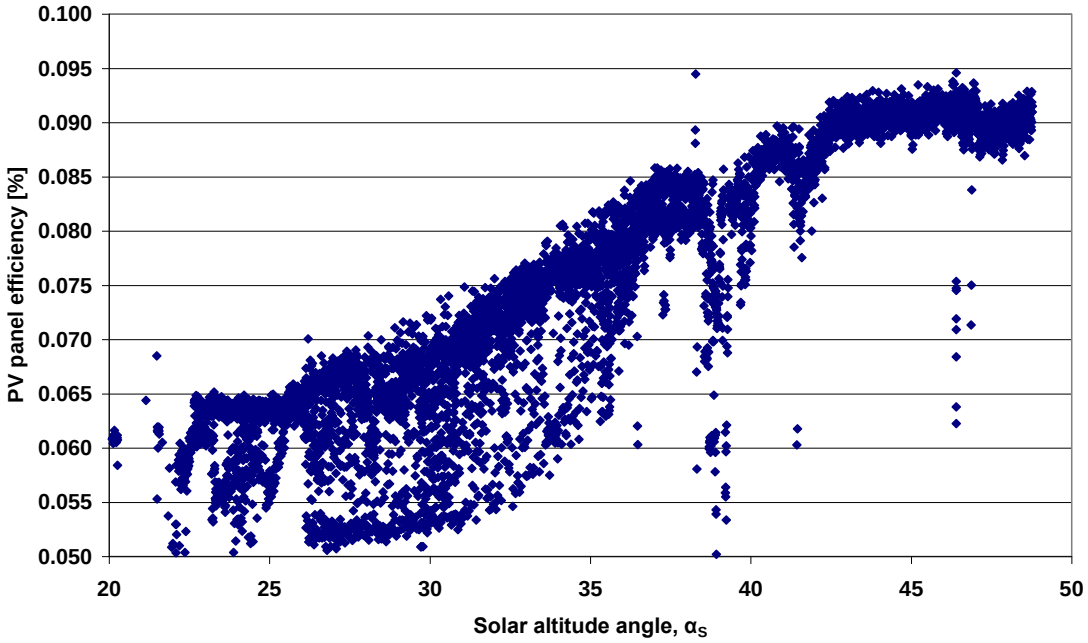

Figure 4-26 Measured PV panel efficiency versus the solar altitude angle for several days of recordings

Although the graph is noisy due to the inclusion of many measurement points with suboptimal control of the load, the trend is clearly observed. It seems that the difference in air mass associated with differences in solar altitude, may lead to a better correlation for the efficiency drop at low incoming solar radiation levels. But this is a specialized subject that needs further investigation [148] [149, 150].

As a final remark it should be mentioned that the actual efficiency values measured do not exceed 9%. This is due to the relatively low insolation values associated with the vertical placement of the PV panels in the specific BIPVT application. Incoming solar radiation at the vertical surface does not exceed 800 W/m^2, even at the more favorable conditions near the winter solstice. Updated efficiency values for the specific application and climate should further improve the accuracy of our building energy simulation work [71], [151], [152].

4.3 INDOOR FLOW VISUALIZATION MEASUREMENTS: TEST PROCEDURE

When air moves in a channel with low speed, flow sensors such as hot wires influence the fluid stream. Also, they provide only local information about air speed without information of the flow direction. On the other hand, most fluids (air, water, etc.) are transparent, thus their flow patterns are invisible without some special methods to make them visible. Flow visualization is a cheap method to make flow patterns visible. In the particle tracer method, particles, such as smoke, can be added to a flow to trace the fluid motion. We can illuminate the particles with a beam of laser light in order to visualize a slice of a complicated fluid flow pattern, assuming that the particles follow the streamlines of the flow. A detailed description of flow visualization with particles is described by Raffel et al. [153]

As a first step towards the better understanding of the air flow field inside the duct, flow visualization was performed in steady-state conditions, indoors [154]. A La Vision laser with a rotating mirror is employed to produce a plane light sheet (Figure 4-27). The characteristics of the Laser are P_o = 1.277 W, F = 10000 Hz and λ = 532 nm. The laser sheet crosses perpendicularly the backside of the device that is from plexiglass and lights up a vertical section of the channel (Figure 4-28).

Figure 4-27 The green 1.277 W laser with the rotating mirror, power supply -control unit

Two different positions are selected for the vertical channel section:

- A section through the centerline and
- A section along to the right-hand side, as viewed from the plexiglas side, at a distance of 200 mm from the frame.

Figure 4-29 shows a schematic of the flow visualization technique employed.

A smoke gun was employed to inject smoke at a selected point at the base of the channel. The smoke passes through the flow homogenization honeycomb structure and moves upwards with the flow, in parallel to the laser light sheet. A commercial video camera, (HDMi SONY HD, 24 fps) is placed in one of the two available holes (see Figure 4-30 and Figure 4-31), that have been cut through the left-hand aluminum frame. The camera produces high definition files, in .m2ts format.

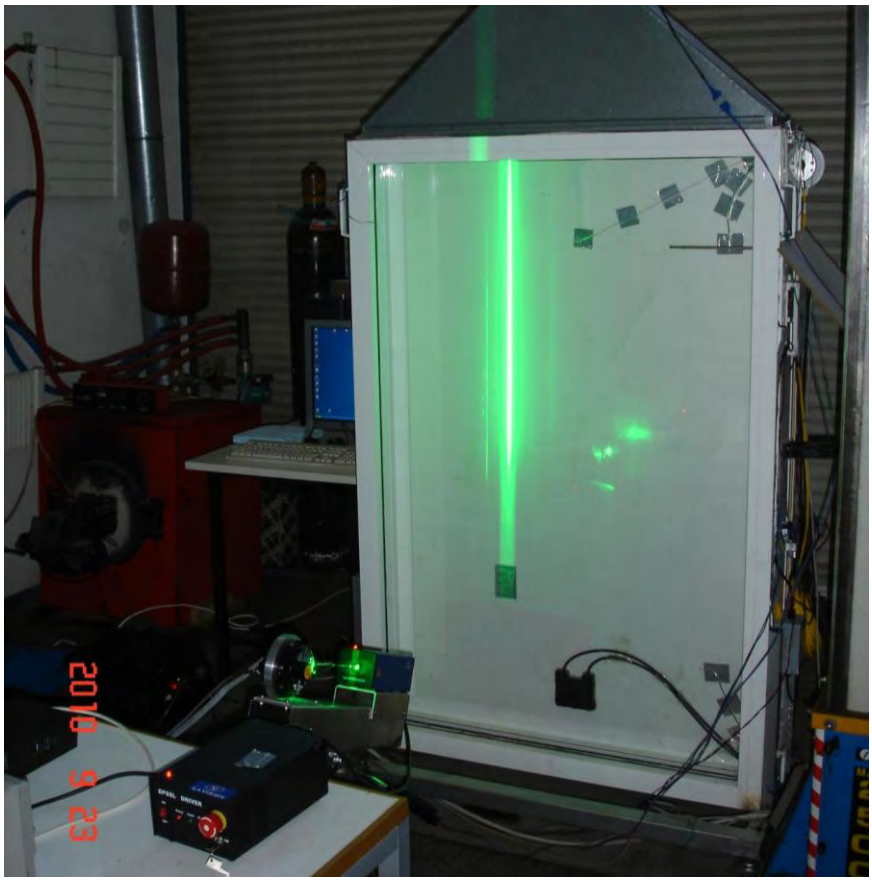

Figure 4-28 Laser device targeting to the test module.

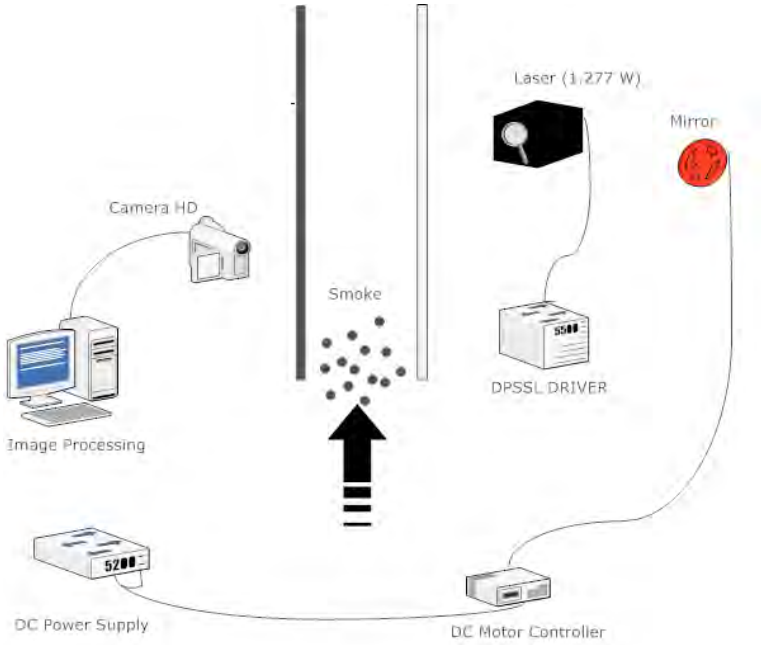

Figure 4-29 Schematic representation of the flow visualization layout.

Figure 4-30 Flow visualization: experimental layout. Video-camera placed in the upper position, seeing towards laser light sheet. The honey comb flow homogenization structure has been removed in this photo.

The following operation modes were studied in the frame of the indoor experiments:

- Mode 1: air flow field with buoyancy flow produced by heating up of the PV panel to its typical operation temperature.
- Mode 2: constant temperature air flow field with the low capacity (110m^3/h) fan.
- Mode 3: constant temperature air flow field with high capacity (190m^3/h) fan.

Figure 4-31 Flow visualization: experimental layout. Video-camera placed in the lower position

4.4 INDOOR FLOW VISUALIZATION MEASUREMENTS: RESULTS

In the following, the results of flow visualization experiments carried out according to the 3 different testing modes are summarized. For convenience, apart from the first, more detailed sequence of 24 clips presented in Figure 4-32, 5 frames are extracted each time from the video file (high definition, .m2ts). Subsequent frames shown in all figures beyond Figure 4-32, are spaced 3 frames (3/24 seconds) apart. Thus, the time duration of each 5-frame clip shown is 0.5 seconds.

All flow visualization videos are included and listed in ANNEX III.

4.4.1 COLD FLOW, LOW CAPACITY (110 m^3/h) FAN

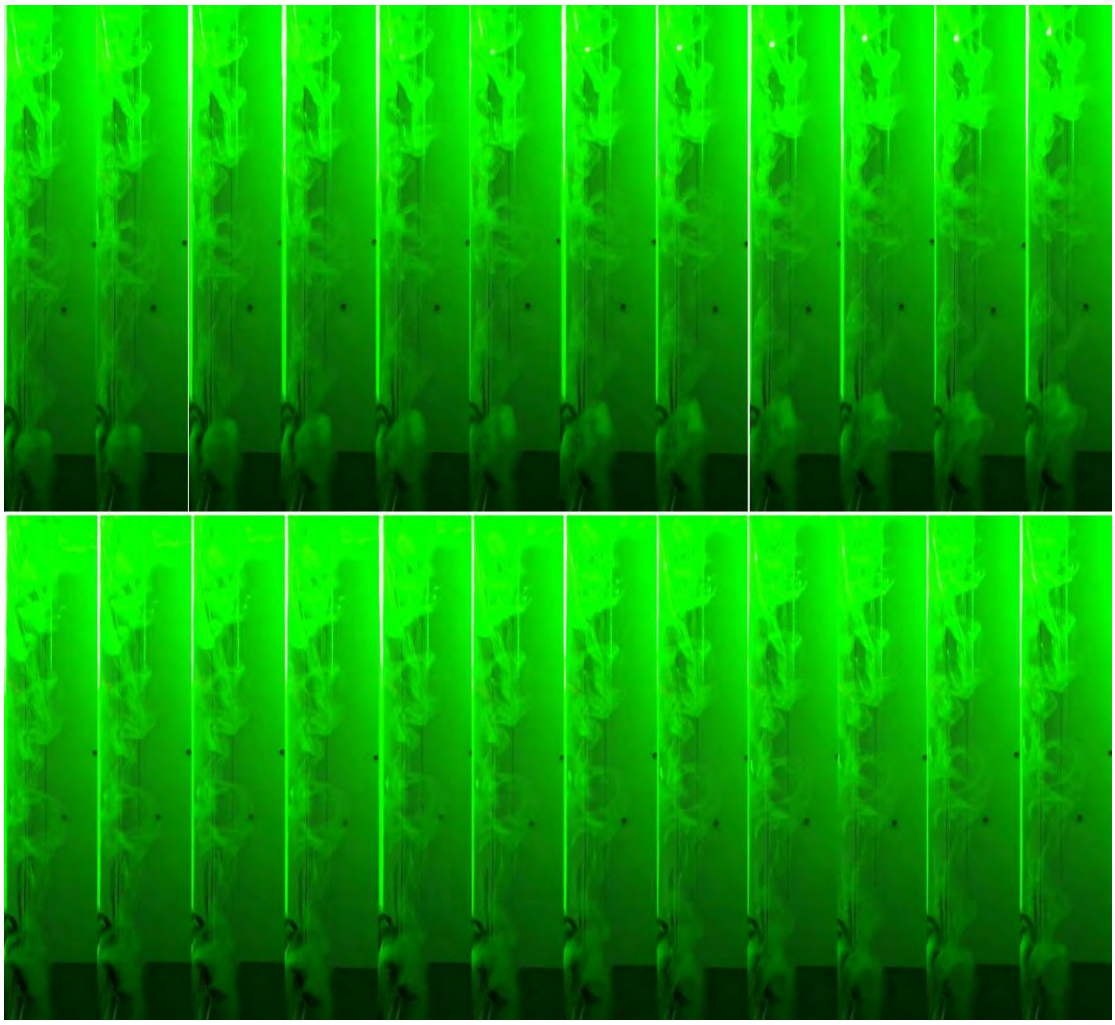

Figure 4-32 24 successive frames (duration 1 sec) of the cold flow visualization experiment with the low capacity fan. Starting frame at bottom left. End frame at top right. Camera in the lower position (Video 20604, ANNEX III).

This experiment is conducted indoors, with the low capacity fan installed on the outlet hood of the testing device. The 24 successive frames presented in Figure 4-32 have a total duration of 1 second. If we carefully look at the lower part of each clip, we first observe the laminar flow pattern produced by the honeycomb structure placed at the inlet of the test device. This pattern becomes unstable about 100 mm downstream the exit of the honeycomb structure. Various eddies of different length scales are produced, indicating that we are in the transition flow regime. The injection of smoke is intentionally limited to the left part of the cavity, which is close to the backsheet of the PV panel. The eddies are seen to move slowly upwards with relatively little rate of distortion, as expected since we are at low Re numbers.

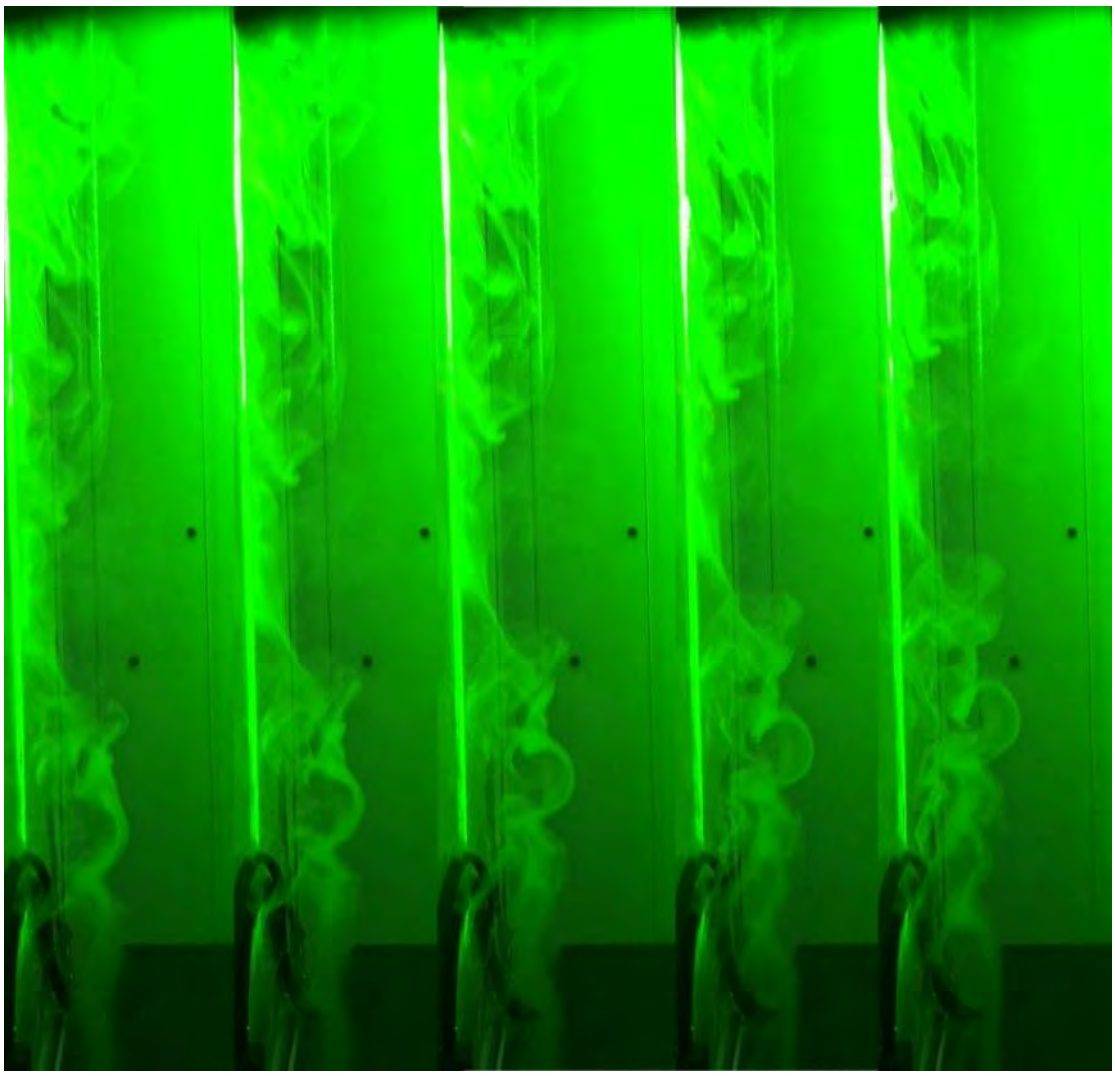

Figure 4-33 Forced convection, 110 m^3/h fan, camera in the lower position, laser light sheet close to the right-hand frame (add scale). (Video 20604, ANNEX III).

More detailed observations on the flow patterns are presented in the following figures.

An inspection of Figure 4-33 shows the propagation of characteristic flow patterns. A characteristic large scale motion may be seen in the form of a slow circulating eddy at the lower part of the channel. This eddy has a diameter of about 50 mm and in the course of the duration of the 5 frames (0.5 seconds) has moved about 100 mm in the vertical direction with the main flow.

This indicates a mean velocity of 0.10 m/ (0.5 s) = 0.2 m/s, which checks well with the hot wire anemometry measurements. In addition, the eddy has rotated about 90^o ($\pi/2$ rad) anti-clockwise during the same period, which amounts to π rad/s or about 0.5 Hz frequency of rotation.

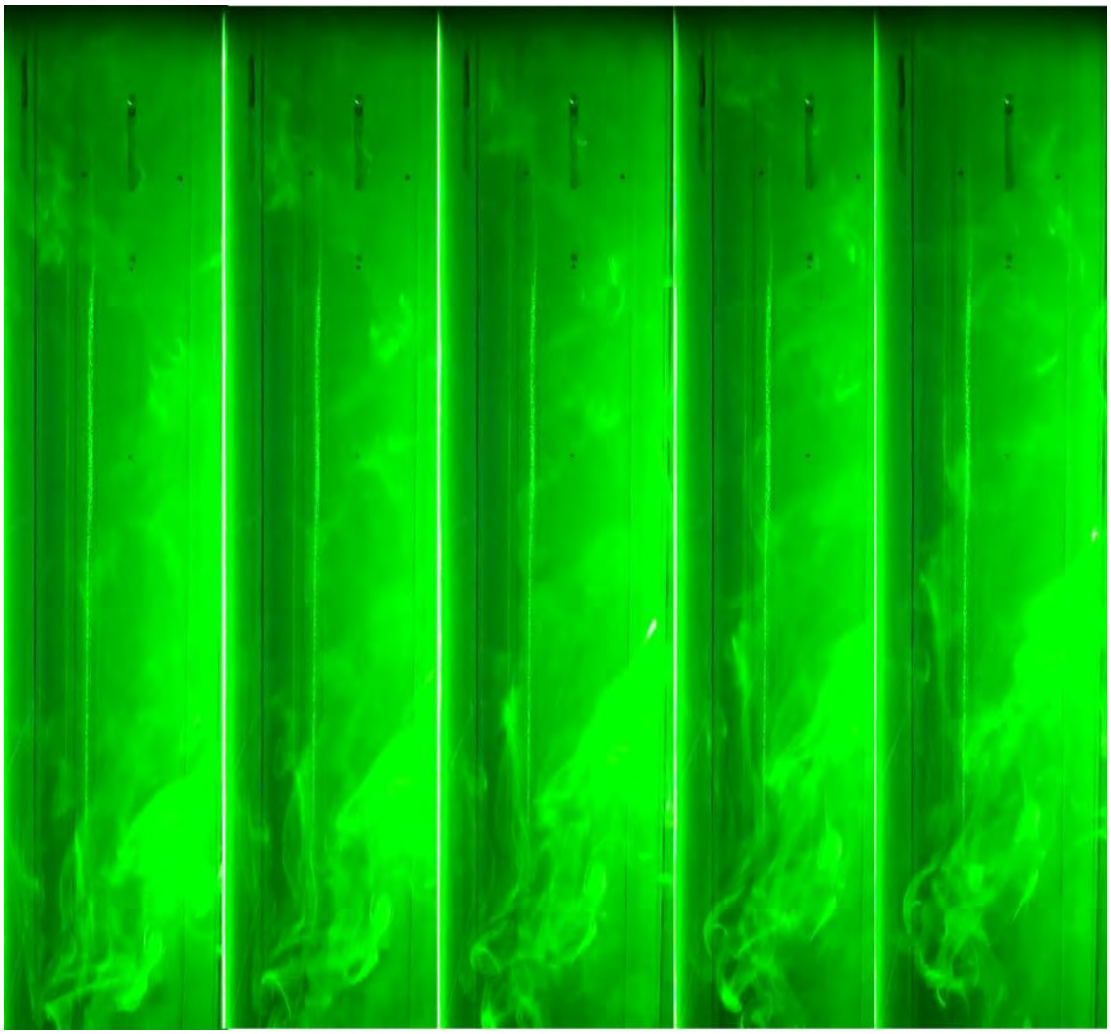

Figure 4-34 Forced convection, 110 m^3/h fan, camera in the upper position, laser light sheet close to the right-hand frame (add scale), (Video 14818, ANNEX III).

It is interesting to see what is happening in the upper part of the channel. This is shown in a characteristic series of clips in Figure 4-34.

The characteristic flow patterns that have been observed to follow the flow in a vertical direction in Figure 4-33, are now observed to detach from the PV panel and move towards the plexiglass side of the channel. This could be due to a certain degree of influence from entrance effects that, combined with the low velocities of the bulk flow produce 2-D or 3-D flow patterns.

4.4.2 COLD FLOW, HIGH CAPACITY (190 m^3/h) FAN

The experiments presented below are conducted indoors, at steady room temperature, with the high capacity fan installed to the top of the exhaust hood.

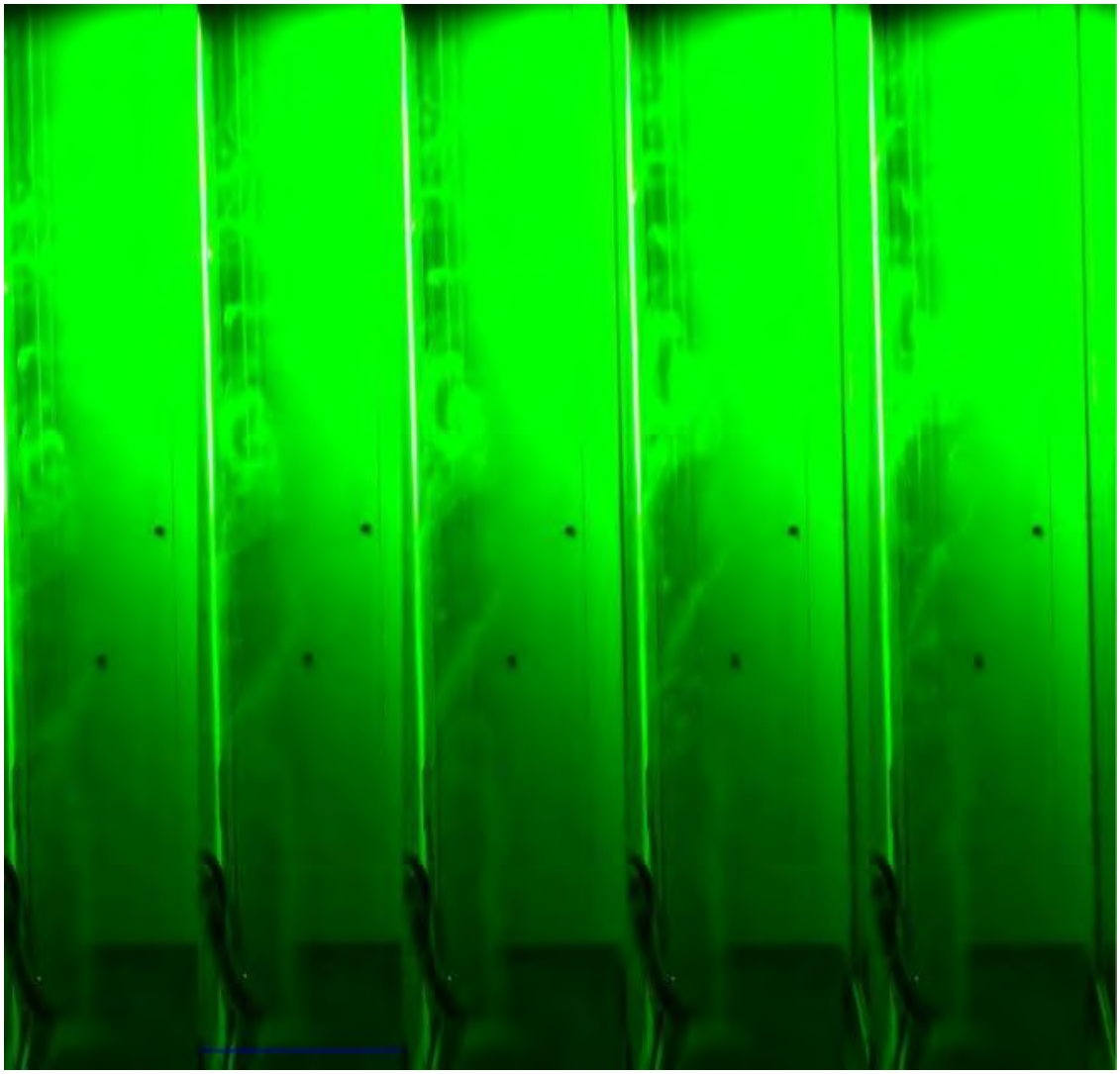

Figure 4-35 Forced convection, 190 m^3/h fan, camera in the lower position, laser light sheet close to the right-hand frame (Video 23224, ANNEX III).

An inspection of Figure 4-35 shows the propagation of characteristic flow patterns with the increased flow rate. An eddy with a diameter of about 40 mm seen in the middle of the first clip, after 5 frames (0.5 seconds) has moved about 180 mm vertically with the main flow.

This indicates a mean velocity of 0.18 m/ (0.5 s) = 0.36 m/s. In addition, the eddy is seen to flatten and be compressed towards the PV panel wall during this period. The lateral deformation amounts to about out 0.5 Hz frequency of rotation.

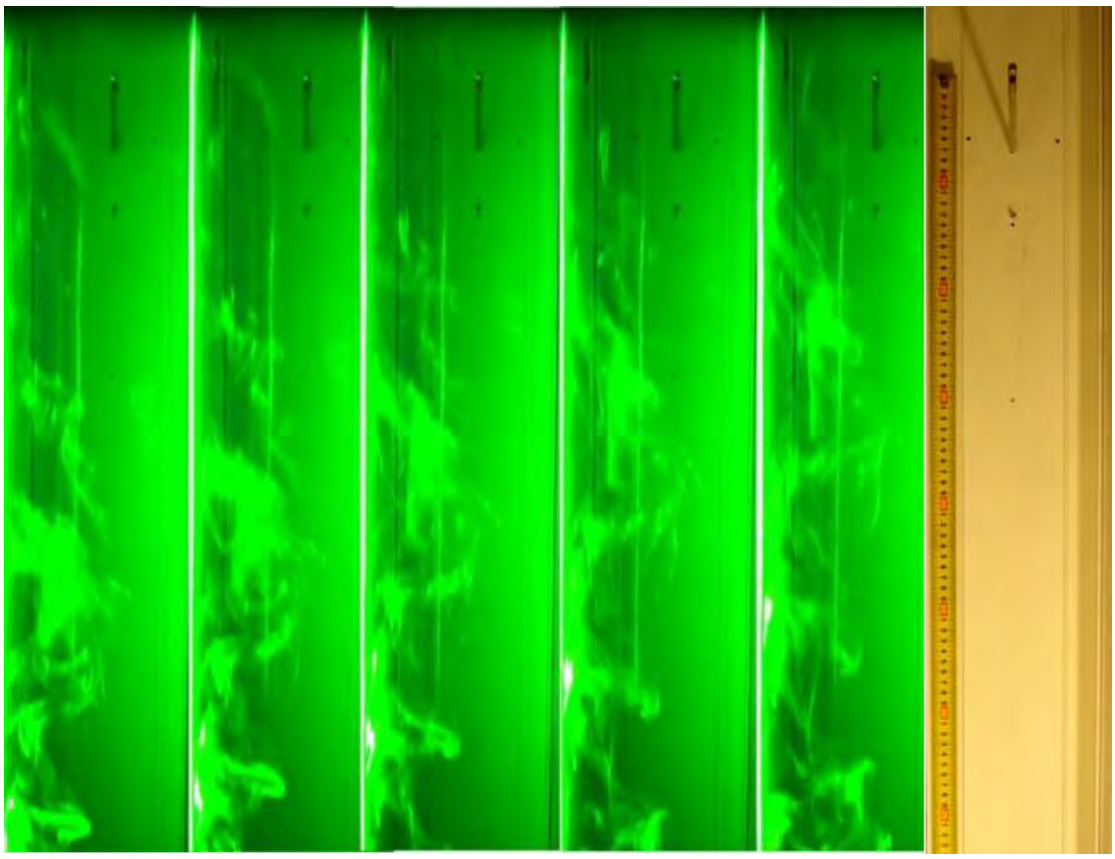

Figure 4-36 Forced convection, 190 m^3/h fan, camera in the upper position, laser light sheet close to the right-hand frame (scale shown by the measuring tape to the right), (Video 11314, ANNEX III)
It is interesting to see what is happening in the upper part of the channel with the higher capacity fan. This is shown in a characteristic series of clips in

Figure 4-36. A scale is given at the right hand side of the picture by means of a measuring tape fitted to the duct lengthwise.

The characteristic flow patterns do not seem to detach very much from the PV panel. The higher velocities in the bulk flow should be responsible for this fact.

A characteristic protuberance seen in the lowest part of the first clip is seen to rotate clockwise along with its translational vertical motion. The observed rotation is about 180^o (π rad) clockwise, which amounts to 2π rad/s or about 1 Hz frequency of rotation.

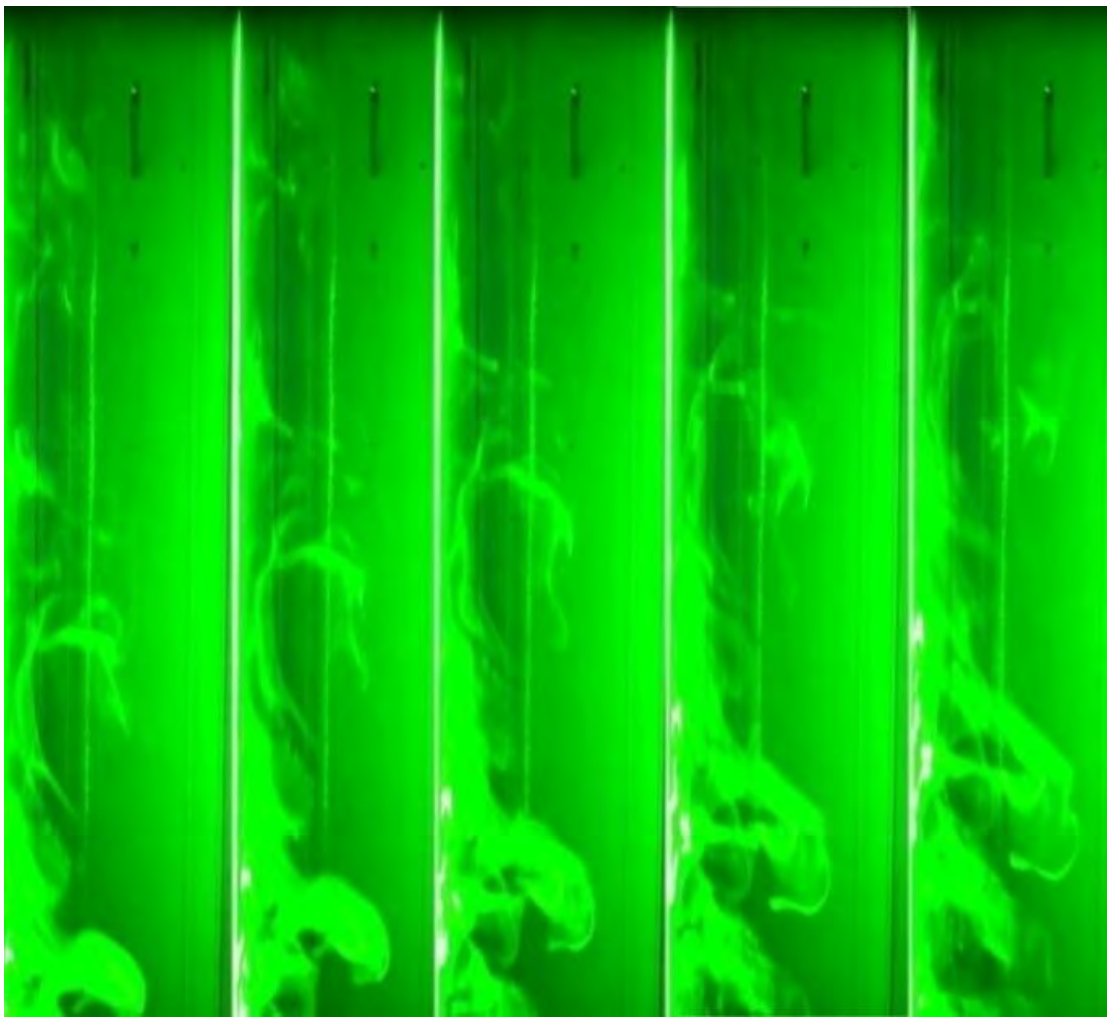

Figure 4-37 Forced convection, 190 m^3/h fan, camera in the upper position, laser light sheet close to the right-hand frame, (Video 111027, ANNEX III).
Another series of clips from the upper part of the channel is shown in

Figure 4-37. The velocity transducer employed in the outdoor experiments can be seen in the upper part of each clip.

A protuberance seen in the lowest part of the first clip is seen to rotate about 45^o clockwise, which amounts to about 0.25 Hz frequency of rotation.

As already mentioned in the comments to the previous set of clips, the characteristic flow patterns do not appear to significantly depart from the PV panel.

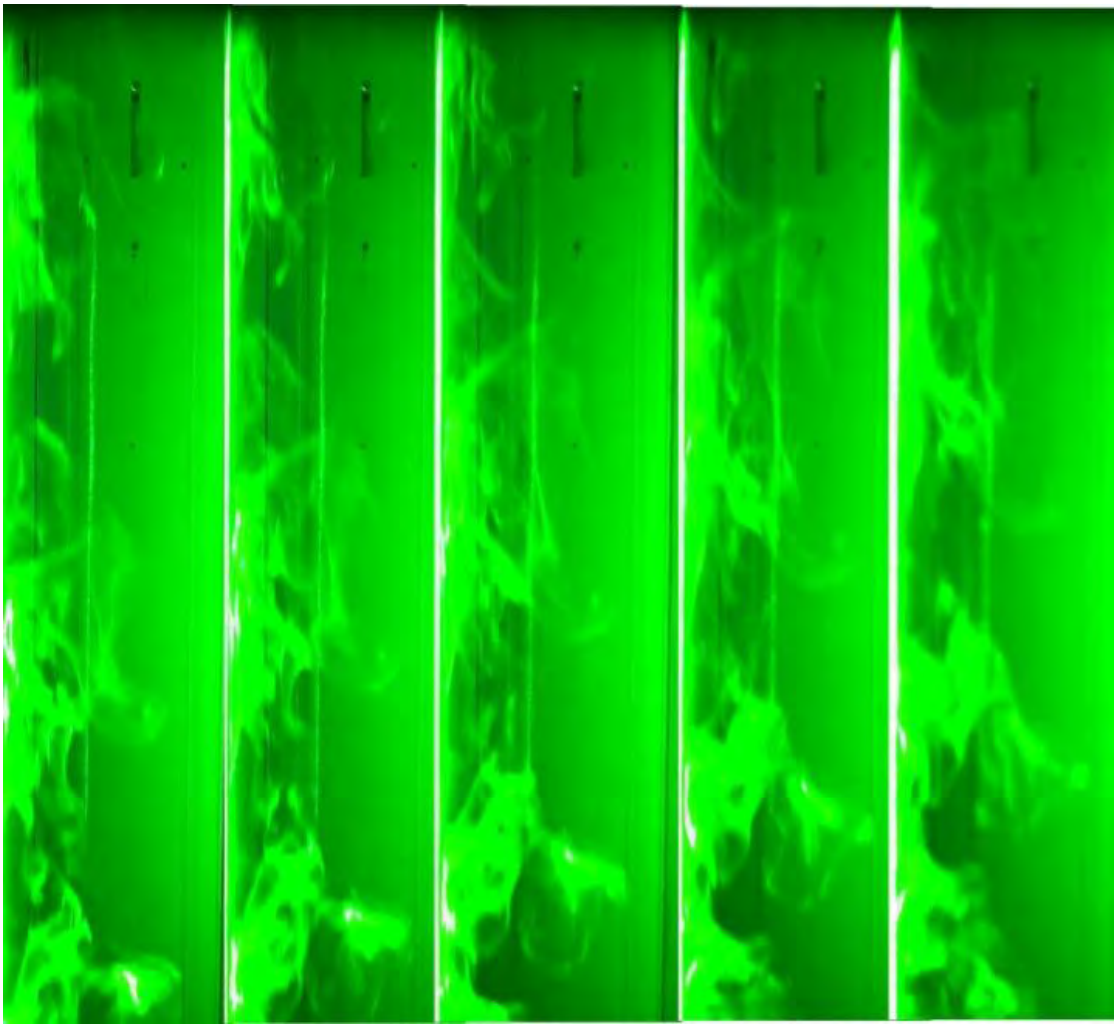

Figure 4-38 Forced convection, 190 m^3/h fan, camera in the upper position, laser light sheet close to the right-hand frame, (Video 11109, ANNEX III)

Again, very little rotation can be seen in eddies observed in Figure 4-38 that move vertically without significant distortion at this time scale.

Also, as already mentioned with the previous figures at the higher flowrates, the observed characteristic flow patterns do not appear to significantly depart from the PV panel towards the bulk flow.

The flow patterns are seen to be compressed towards the PV panel at the higher end of the duct, presumably due to the influence of the converging hood that lies beyond the upper part of the channel.

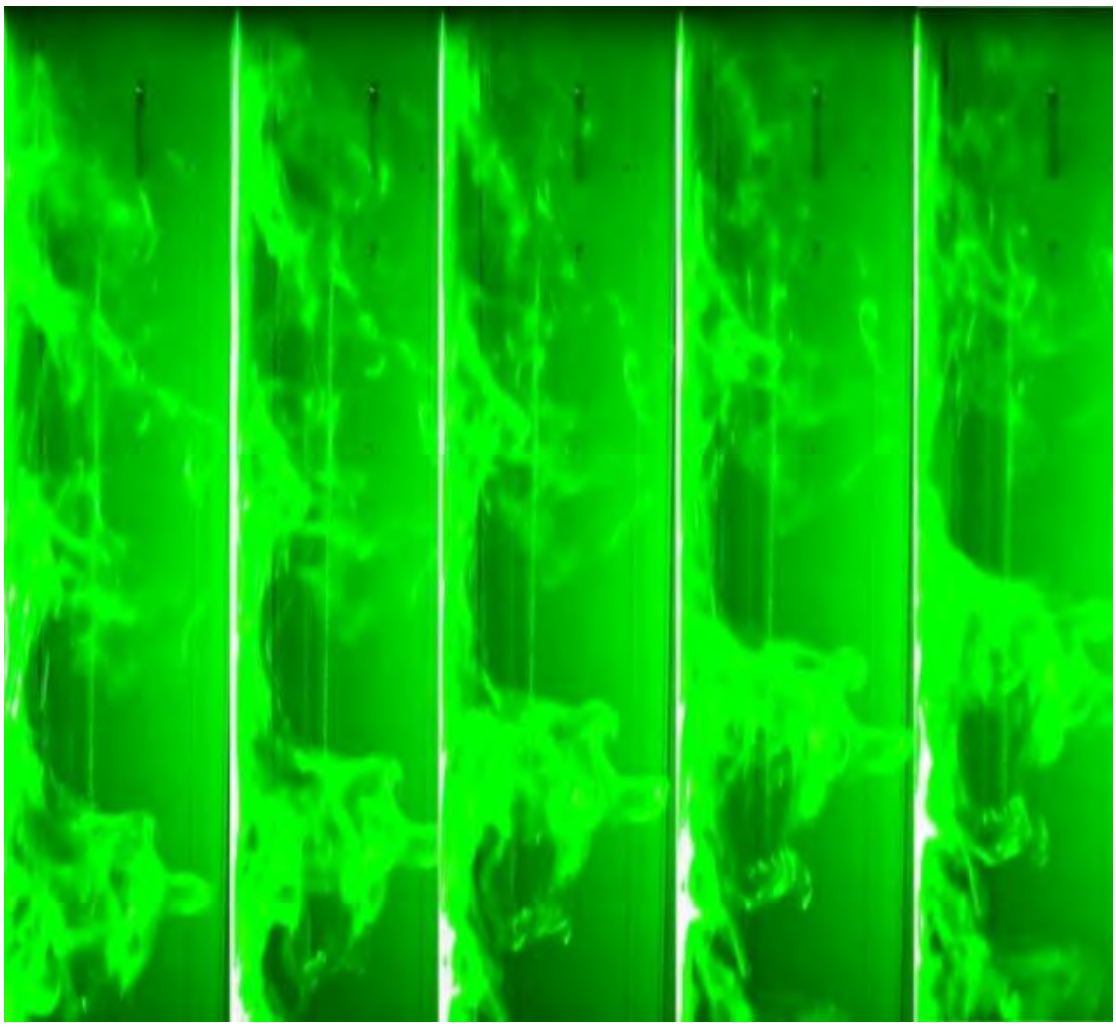

Figure 4-39 Forced convection, 190 m^3/h fan, camera in the upper position, laser light sheet close to the right-hand frame, (Video 11543, ANNEX III).

Analogous remarks may be done with the characteristic flow patterns observed in Figure 4-39 that move vertically without significant distortion at this time scale.

As already observed in the previous figures at the higher flowrate, the characteristic flow patterns do not significantly detach from the PV panel towards the bulk flow.

Further upwards they are seen to be compressed towards the PV panel, because of the influence of the converging hood that lies beyond the upper part of the channel.

Since the last figures correspond to the right-hand section (to the right part of the centerline), we conclude that the flow field does not significantly change in the y direction, that is, we approach the behavior predicted with the infinite width of the cavity.

4.4.3 BUOYANCY FLOW EXPERIMENT, HEATED PANEL, NO FAN

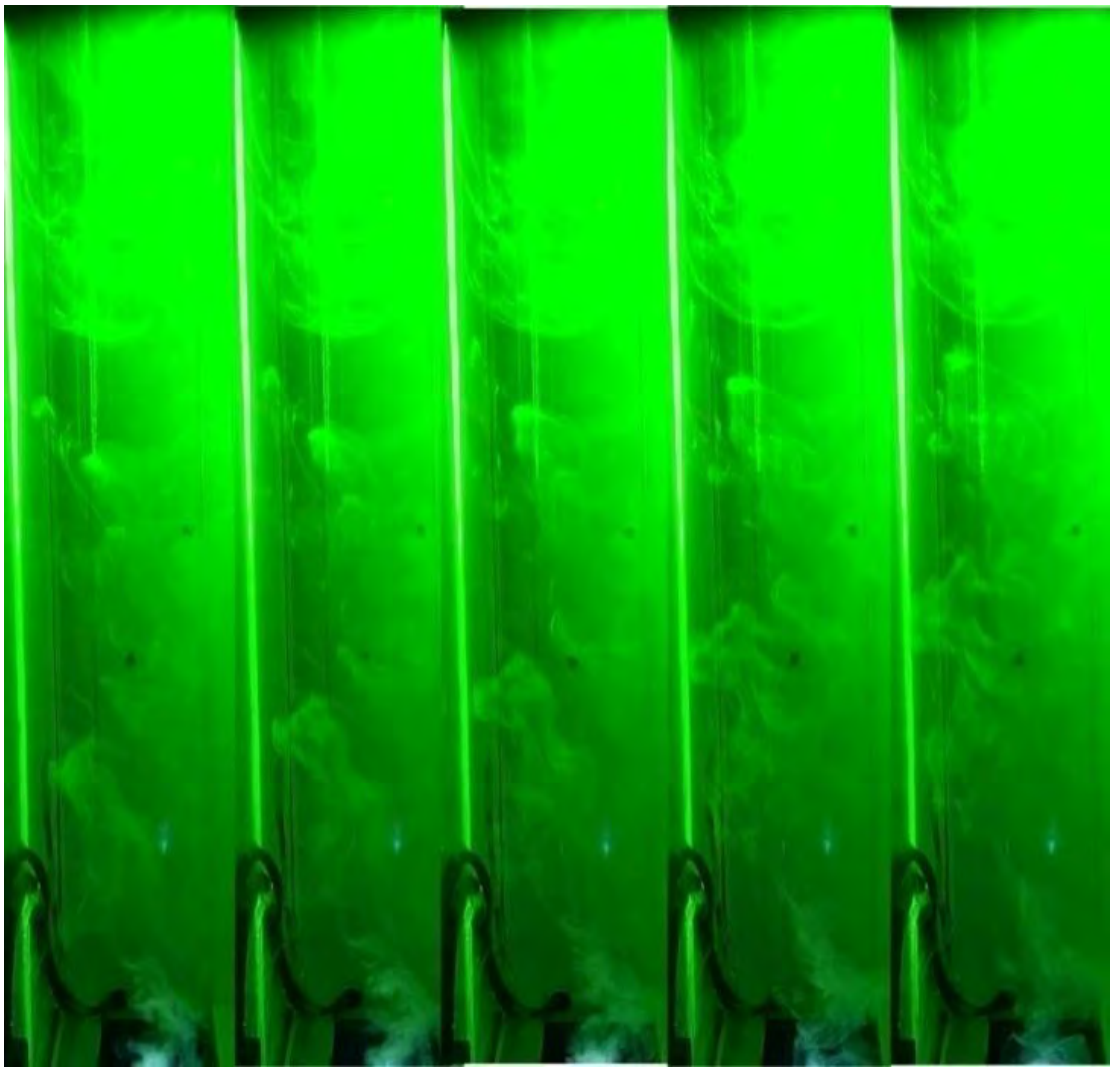

Figure 4-40 Free convection, camera in the lower position, laser light sheet close to the right-hand frame, the smoke gun's exit visible at lower part of figure (no honeycomb), (Video 22223, ANNEX III)

In this series of measurements, no fan is employed and the vertical air flow is produced by buoyancy, due to the heating of the PV panel (Figure 4-45). The flow homogenization honeycomb structure is removed in this series of experiments, in order to increase the draft.

The lower part of the channel is shown in the series of clips in Figure 4-40. Certain structures are visible that move vertically upwards following the main flow, at a velocity of about 0.1 m/s.

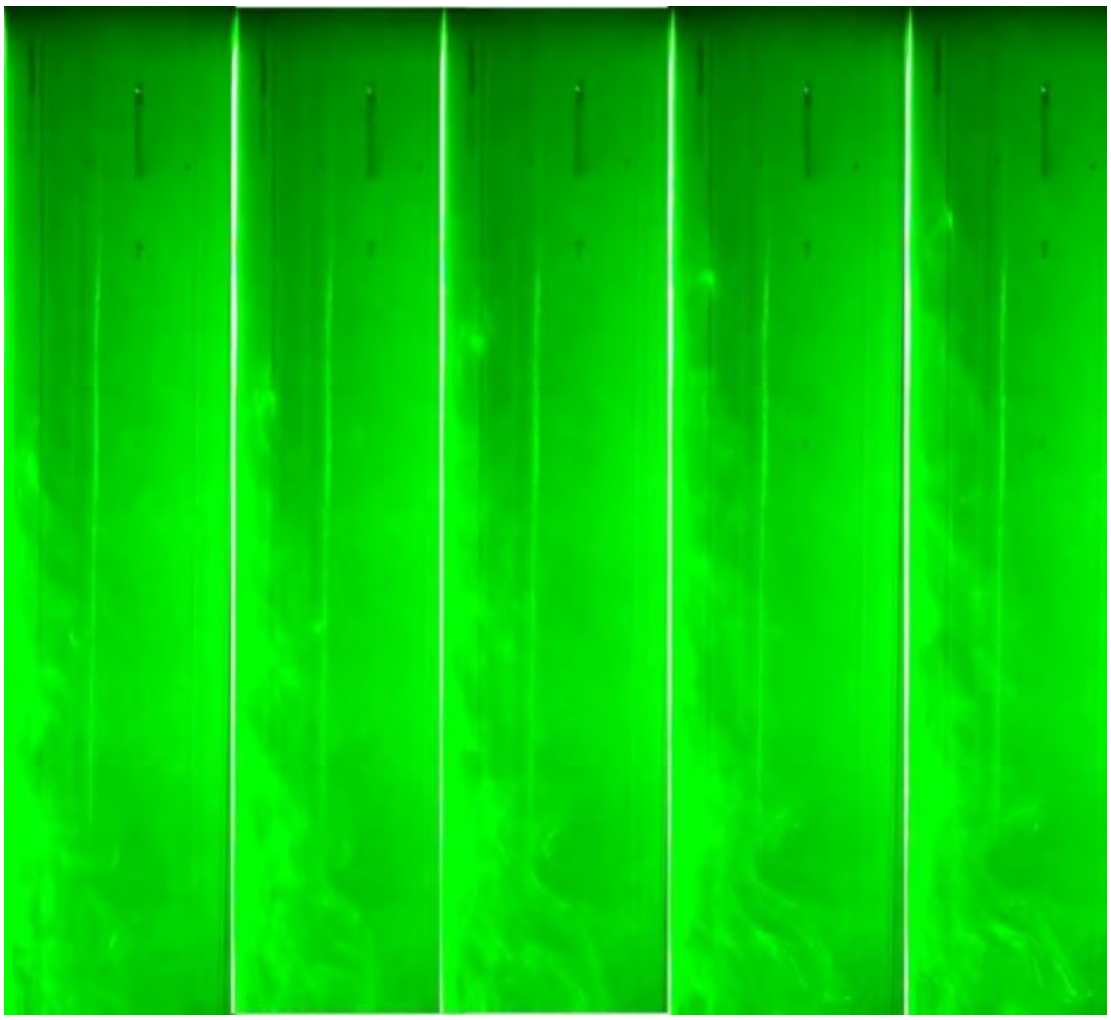

Figure 4-41 Free convection, camera in the upper position, laser light sheet close to the right-hand frame, (Video 13825. ANNEX III)

The same remarks can be done for the upper part of the channel (Figure 4-41). Again, the structures are moving vertically without visible distortion or tendency to detach from the PV wall. More quantitative details on the characteristics of the air flow field in the duct will be given in the next section, based on the results of hot-wire anemometry.

4.5 HOT WIRE ANEMOMETRY MEASUREMENTS: TEST PROCEDURE

Hot wire anemometers use a micron thickness wire, electrically heated up to some temperature above the ambient. Air flowing past the wire has a cooling effect on the wire. As the electrical resistance of most metals is dependent upon the temperature of the metal (platinum or tungsten is a popular choice), a relationship can be obtained between the resistance of the wire and the flow speed. Several ways of

implementing this exist, and hot-wire devices can be further classified as CCA (Constant-Current Anemometer), CVA (Constant-Voltage Anemometer) and CTA (Constant-Temperature Anemometer). The voltage output from these anemometers is thus the result of some sort of circuit within the device trying to maintain the specific variable (current, voltage or temperature) constant.

Hot-wire anemometers, while extremely delicate, have very high frequency-response and fine spatial resolution compared to other measurement methods, and as such are employed for the detailed study of turbulent flows. Commercially available hot-wire anemometers have a flat frequency response (<3dB) up to 17 kHz at the average velocity of 9.1 m/s, 30 kHz at 30.5 m/s, or 50 kHz at 91m/s.

4.5.1 Calibration of the Hot Wire

The calibration curve for the hot wire system employed in these measurements is shown in the following figure.

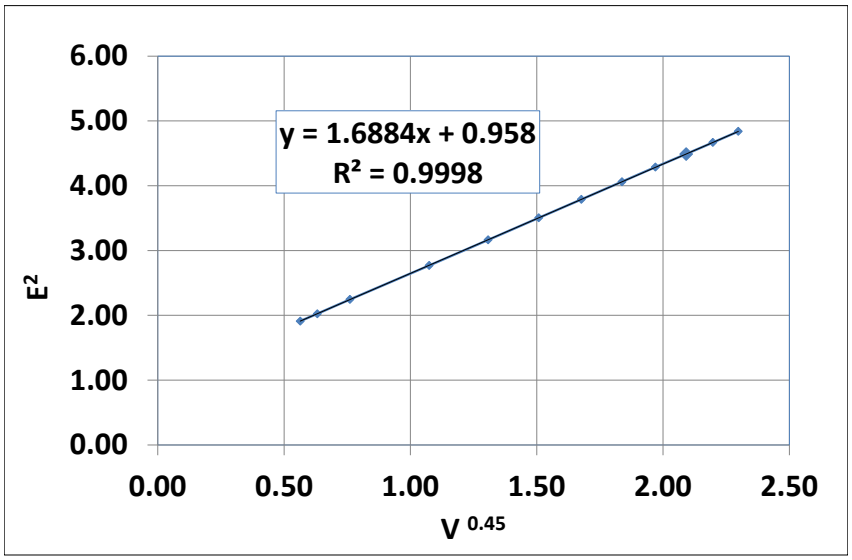

Figure 4-42 Calibration of the hot wire

4.5.2 Temperature Correction of Hot Wire measurements

Equation 4.2 is known as King's law. It concerns the wire itself, not the anemometer outputs. In order to retrieve King's law from anemometer outputs, all the resistances present in the circuits have to be taken into account, for example, the top bridge resistance in the arm containing the sensor in a CTA (constant temperature anemometer) circuit [155].

$$E^2 = A + VB^{0.45} \quad (4.4)$$

$$A = 0.39\frac{\pi l k_a}{\chi R_0} \qquad B = 0.51\frac{\pi l k_a}{\chi R_0}\left(\frac{\rho_a d}{\mu_\alpha}\right)^{0.50} \quad (4.5)$$

In King's law A and B are improperly called constants. Obviously they are not, they depend on the wire diameter and on the fluid temperature. If the temperature dependencies of the physical parameters (ρ, k, μ) are introduced in (eq. 4.3), one obtains

$$\frac{dA}{A} = 0.886\frac{dT_a}{T_a} \quad (4.6)$$

$$\frac{dB}{B} = (0.0886 - 0.50 - 0.38)\frac{dT_a}{T_a} = 0.006\frac{dT_a}{T_a} \quad (4.7)$$

Coefficient B therefore varies far less with temperature than coefficient A. This result is particularly interesting at large values of U when A can be neglected compared to $BV^{0.5}$. Uberoi and Corrsin confirmed these trends when experimenting on hot jets [156] . However, in our case, we have very low velocities and we need to take into account the temperature correction for A. To this end, we need to know the air temperature at each measurement point. We have measured these temperatures with a thermocouple. Thus, the value of A is corrected according to the above relation, based on the air temperatures measured by the thermocouple.

As a second step in the study of the air flow field inside the duct, a series of measurements was conducted with hot wire anemometry.

The experimental layout is presented in Figure 4-43 [154]. A X-Z-axis is employed to move a single component hot-wire probe (Dantec, Probe Type 55 P11) along the depth of the channel, through 4 holes drilled to the plexiglass, along the centerline at the distances shown in Figure 4-44 and Table 4-11. 28 measurement points are taken along the X-axis for each measurement hole, at the distances shown in the same figure. The technical data of the hot wire are presented in Table 4-10.

Table 4-10 Technical data of hot wire

Sensor material	Platinum - plated tungesten
Sensor dimension	5 μm dia, 1.25 mm long
Sensor resistance R20	3.5 W
Min velocity	0.05 m/s
Max velocity	500 m/s

Figure 4-43 Hot wire anemometry: experimental layout

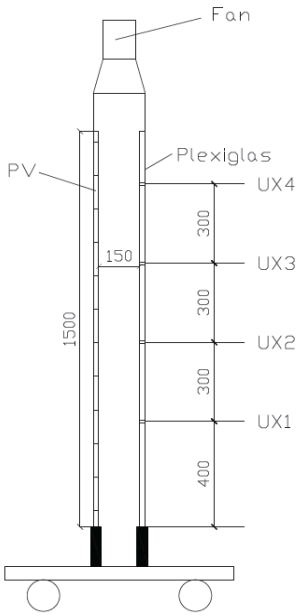

Figure 4-44 Positions of the 4 holes along the centerline of the channel, through which the hot wires were being inserted.

Table 4-11 Coordinates of the measurement points

Measurement	1	2	3	4	5	6	7	8				
mm	1,25	2,5	3,75	5	6,25	7,5	8,75	10,00				
Measurement	9	10	11	12	13	14	15	16	17	18	19	20
mm	20,00	30,00	40,00	50,00	60,0	70,00	80,00	90,00	100	110	120	130
Measurement	21	22	23	24	25	26	27	28				
mm	140	141,25	142,5	143,75	145	146,25	147,5	148,75				

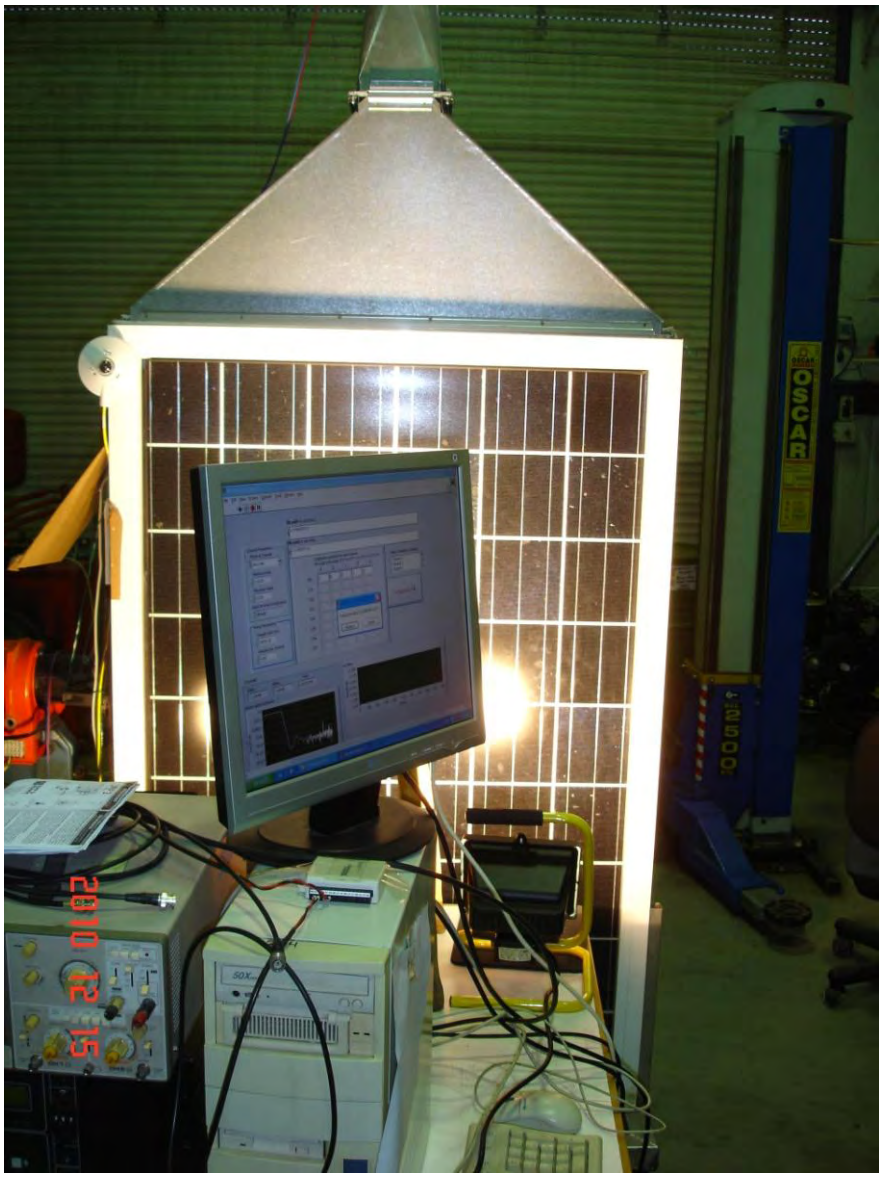

Figure 4-45 External heating of the panel, hot wire amplifier and data acquisition.

A single component, A.A. Lab Systems hot-wire Anemometry System with a bridge-type amplifier is employed to feed the hot wire and produce the measurement voltage that is fed to a NI 6012 data acquisition card (Figure 4-45). Measurements

are carried out at 3000 Hz acquisition rate. The above-mentioned, 3 operation modes were studied in the frame of these experiments.

In order to simulate the buoyancy flow in the device, external heating of the panel to the operation temperatures measured outdoors, is employed by means of halogen lamps as shown in Figure 4-45.

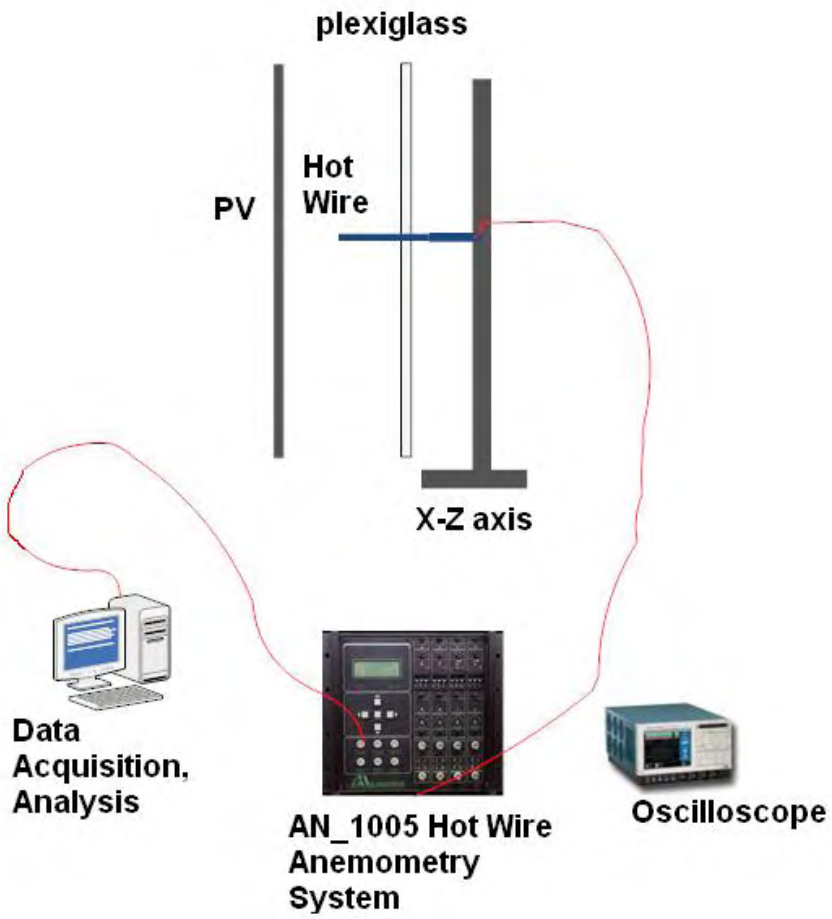

Figure 4-46 Schematic representation of the velocity measurements with hot wire anemometry

4.6 FLOW FIELD MEASUREMENT RESULTS BY HOT WIRE ANEMOMETRY

In this section we concentrate on the results of hot wire anemometry measurements of steady state flow inside the duct, for the three operation modes [154]. The results are statistically processed to deduce characteristic time and length scales for the turbulence.

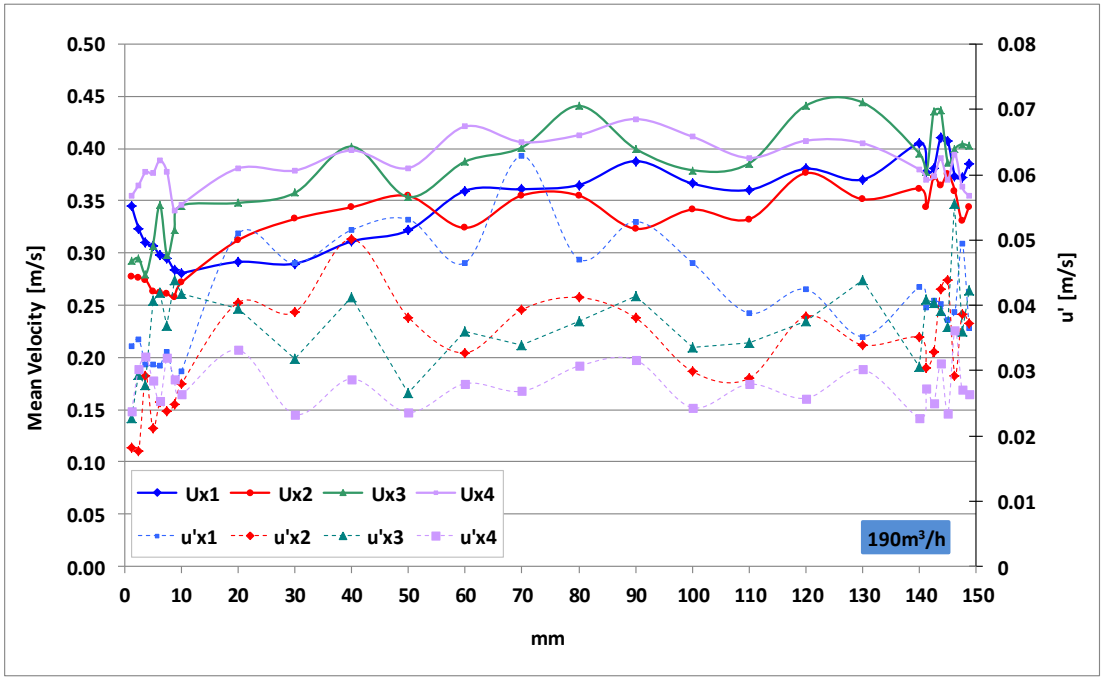

Figure 4-47 Cold flow experiment with the high capacity fan on: measurements of vertical component of air velocity along the depth of the cavity (x=150 is the back side of the PV panel), for 4 different vertical positions along the centerline (schematic in Figure 4-44).

Characteristic profiles of the vertical air velocity across the depth of the channel are presented in Figure 4.45 with the high capacity fan switched on (x=0 denotes the plexiglass wall, x=150 mm denotes the PV panel wall). The measurements are taken at 4 vertical positions along the centerline: Ux1, Ux2, Ux3 and Ux4 correspond to vertical positions at z = 400, 700, 1000, 1300 mm from the lower frame (Figure 4-44).

It is observed that the profiles are more or less flat across the channel depth at the centerline, and the air velocity at the specific points (along the centerline) is increased in the two upper levels, Ux3, Ux4. Obviously, the 3D evolution of the velocity field changes as we move towards the exit hood.

Furthermore, it is interesting to see the respective RMS velocity fluctuation levels, presented in the same figure. These velocities lie in the range of 0.022 m/s to 0.065 m/s, and they are decreasing as we move upwards, away from inlet. The Reynolds number for the mean flow is in the range of 4600-8000, thus the flow should be in the transition or turbulent regime in all cases. The turbulent nature of the flow has already been observed in certain flow visualization photographs, immediately downstream the flow homogenization honeycombs structures (Figure 4-32).

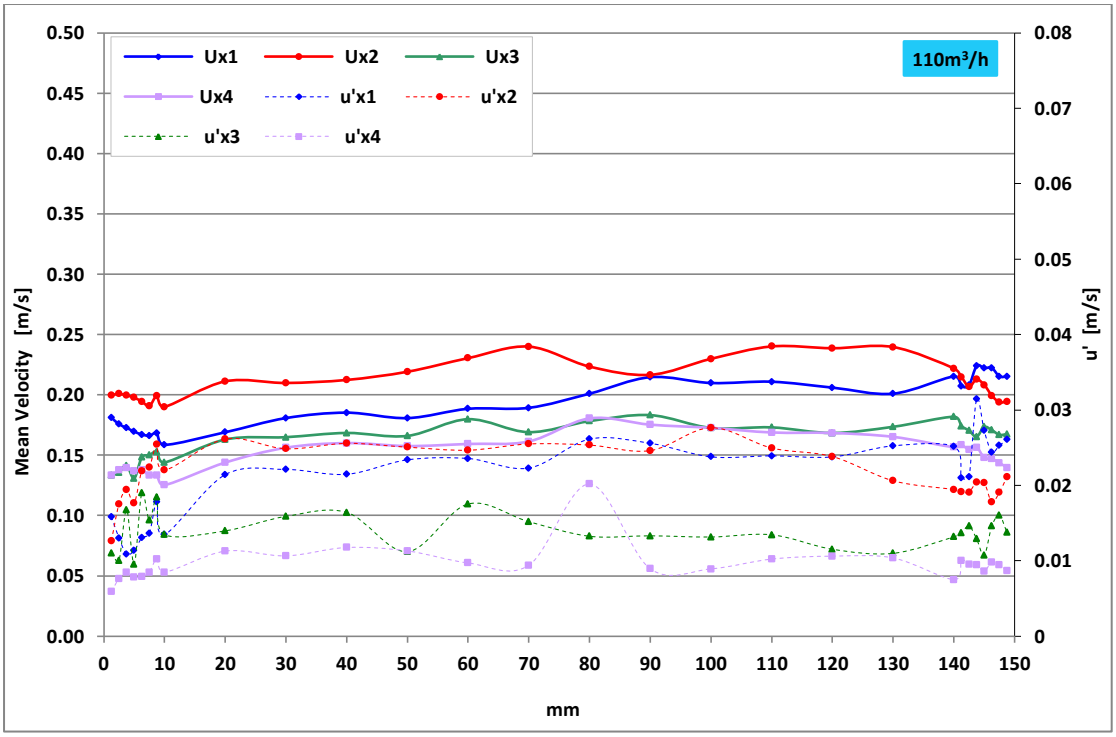

Figure 4-48 Cold flow experiment with the low capacity fan on: measurements of vertical component of air velocity along the depth of the cavity (x=150 is the back side of the PV panel), for 4 different vertical positions along the centerline (schematic in Figure 4-44)

Characteristic profiles of the vertical air velocity across the depth of the channel for the 4 previously mentioned vertical positions at z = 400, 700, 1000, 1300 mm from the lower frame are presented in Figure 4-48 with the low capacity fan switched on (x=0 denotes the plexiglas wall, x=150 mm denotes the PV panel wall).

Again, it is observed that the profiles are more or less flat across the channel depth at the centerline. However, in this case the air velocity slightly decreases in the two upper levels, Ux3, Ux4. Obviously, the 3D evolution of the velocity field is different with the low capacity fan. Furthermore, it is interesting to see the respective RMS velocity fluctuation levels, presented in the same figure. The RMS velocity fluctuations are reduced compared with the high capacity fan case. They lie in the range of 0.01 m/s to 0.04 m/s, and they are decreasing as we move upwards, away from inlet.

Finally, we examine the buoyancy flow case. Characteristic profiles of the vertical air velocity across the depth of the channel are presented in Figure 4.47 (x=0 denotes the plexiglass wall, x=150 mm denotes the PV panel wall). The measurements are taken at the same 4 vertical positions (Figure 4 44)

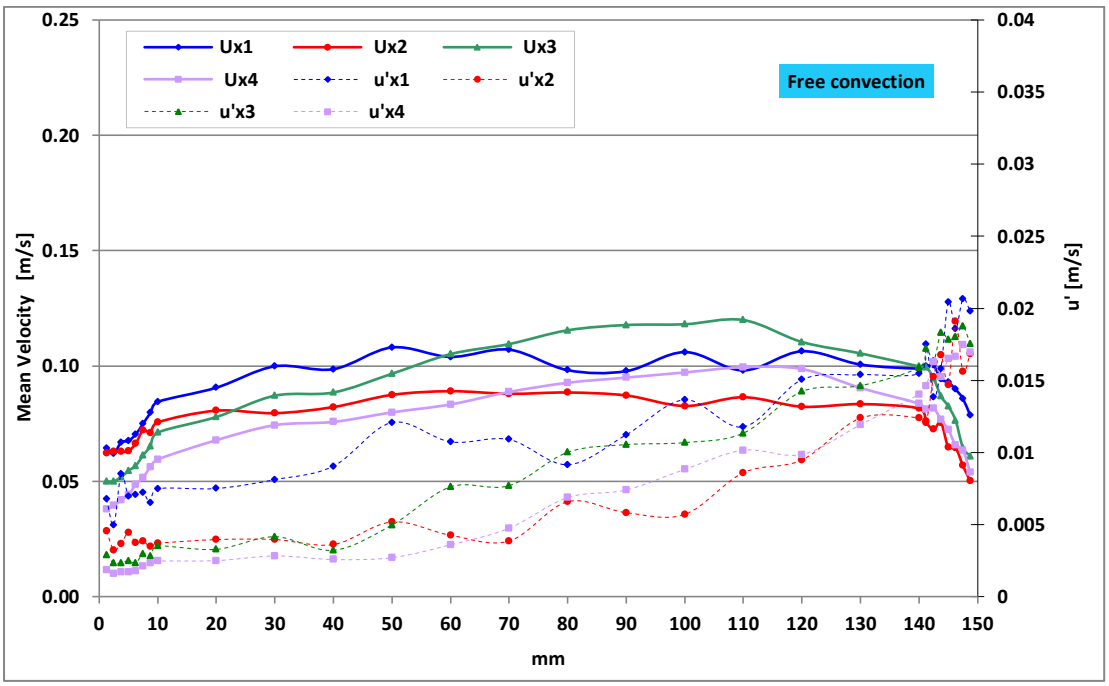

Figure 4-49 Buoyancy flow experiment (free convection): measurements of vertical component (z) of air velocity along the depth of the cavity (x=150 is the back side of the PV panel), for 4 different vertical positions along the centerline (schematic in Figure 4-44)

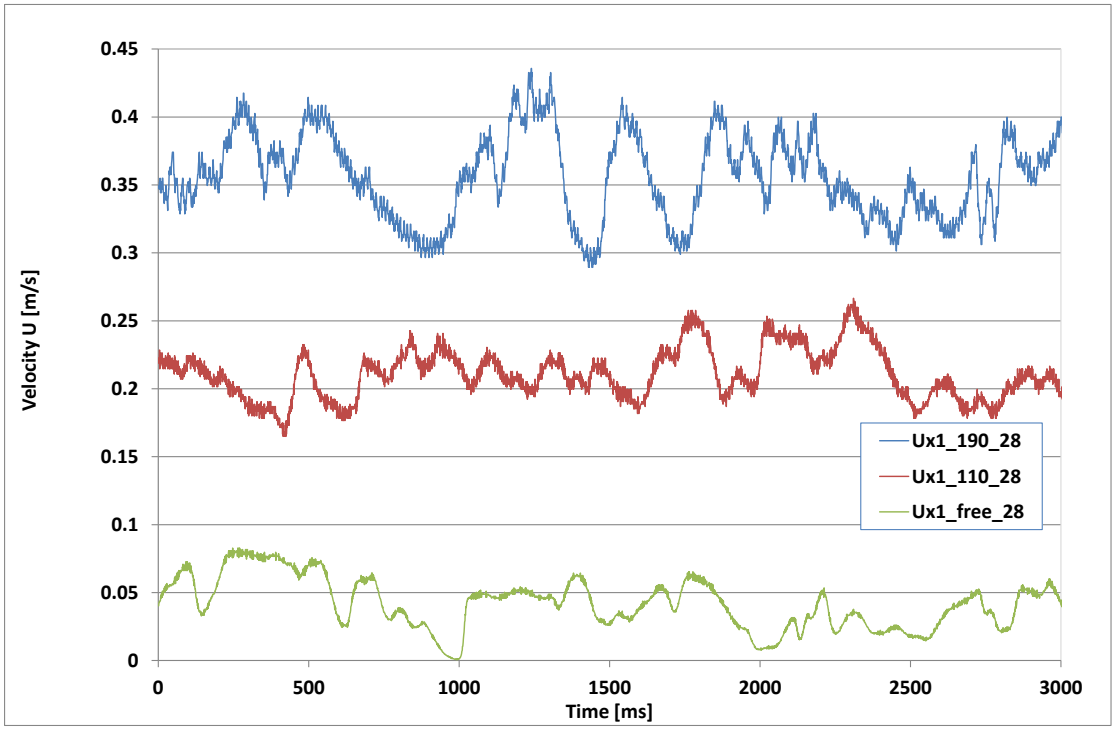

Figure 4-50 Characteristic time recordings of hot wire anemometry measurements. This case shows significant differences compared to the forced circulation cases. First it is observed that the vertical velocity components' levels are reduced, as expected.

Second, it is observed that the velocity profile at Z=400 mm from inlet is at a significantly higher level than the other 3 points further downstream. Also, the velocity profiles of the 3 upper level sections are no more flat: the air velocity is increasing as we move away from the PV panel. Obviously, the 3D evolution of the velocity field changes significantly as we move towards the exit hood. It is interesting to compare the respective RMS velocity fluctuation levels, presented in the same figure. They are lower than the previous case, as expected. They lie in the range of 0.0025 to 0.02 m/s, and they decrease as we move upwards from inlet. These velocity fluctuation levels show a similar profile but are significantly lower in magnitude than the fully turbulent ones (of the order of 0.1 m/s, nearly constant along the vertical centerline from y/H= 0.2 to 0.8) measured by Betts and Bokhari [82] in a tall differentially heated rectangular cavity (2.18 m high by 0.076 m wide by 0.52 m in depth).

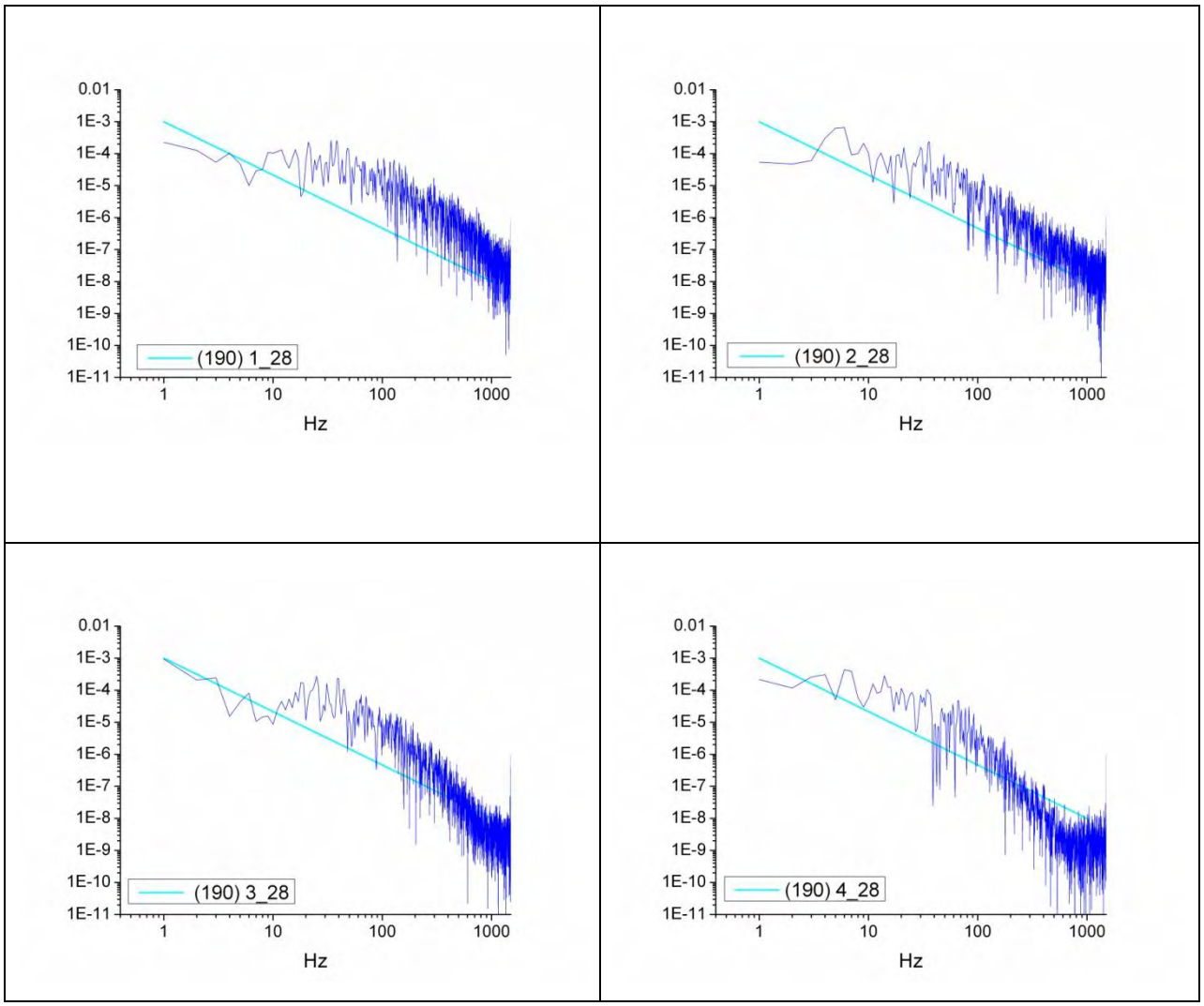

Figure 4-51 PSD spectrum, high capacity fan -190 m^3/h. Position nearest to the PV panel wall, for the 4 different vertical positions (UX1: z=400, UX2: z=700, UX3: z=1000, UX4: z=1300 mm from bottom), along the vertical centerline (x=148.75 mm).

Power Spectral Density (PSD) graphs produced by FFT analysis of the measured velocity time series give additional information on the RMS velocity fluctuation characteristics. A comparison of PSD spectra for a specific point in the channel (z = 700 mm), close to the PV panel wall (x=148.75 mm), for the 3 different modes of operation is presented in Figure 4-51, Figure 4-52, Figure 4-53.

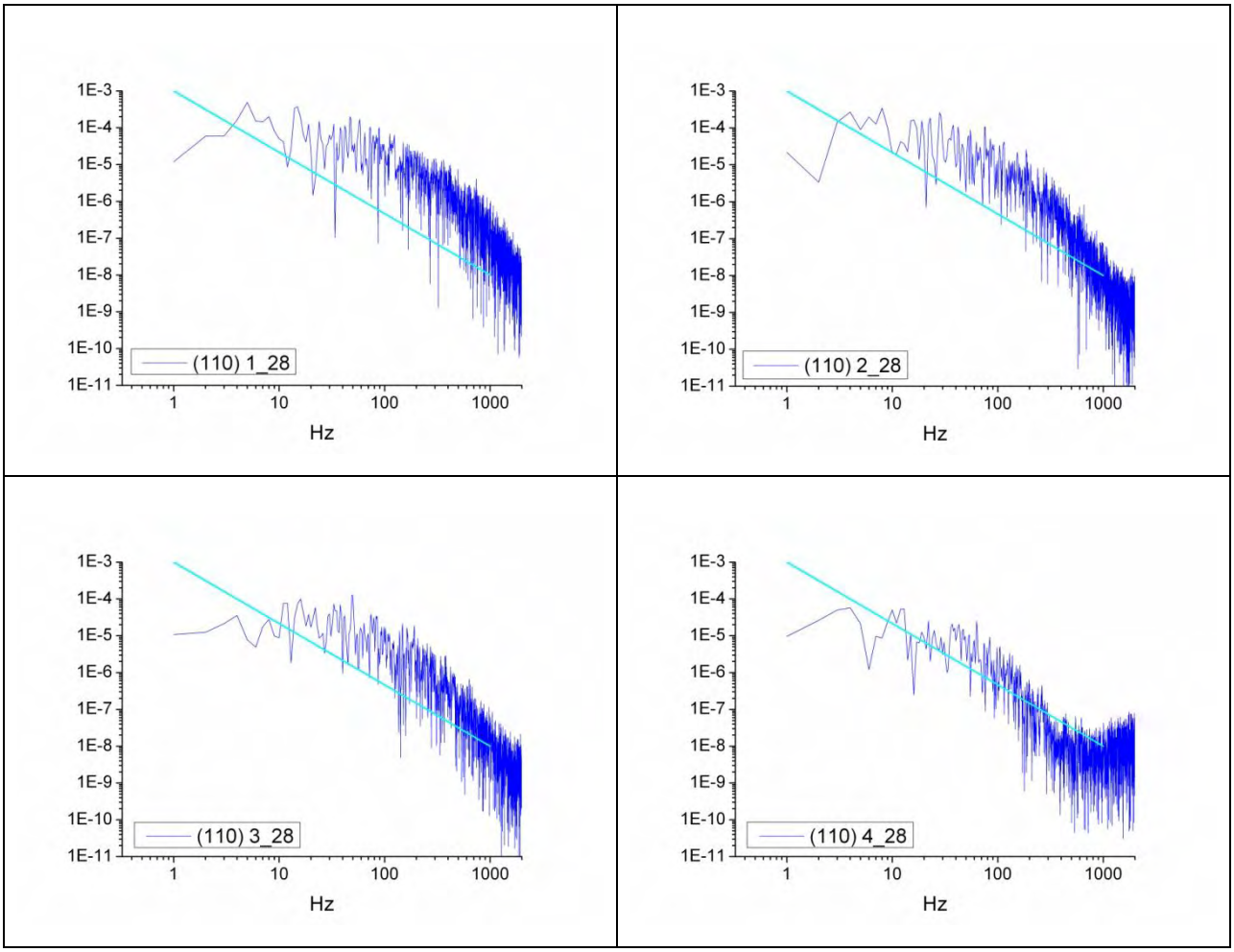

Figure 4-52 PSD spectrum, low capacity fan -110 m^3/h. Position nearest to the PV panel wall, for the 4 different vertical positions (UX1: z=400, UX2: z=700, UX3: z=1000, UX4: z=1300 mm from bottom), along the vertical centerline (x=148.75 mm).

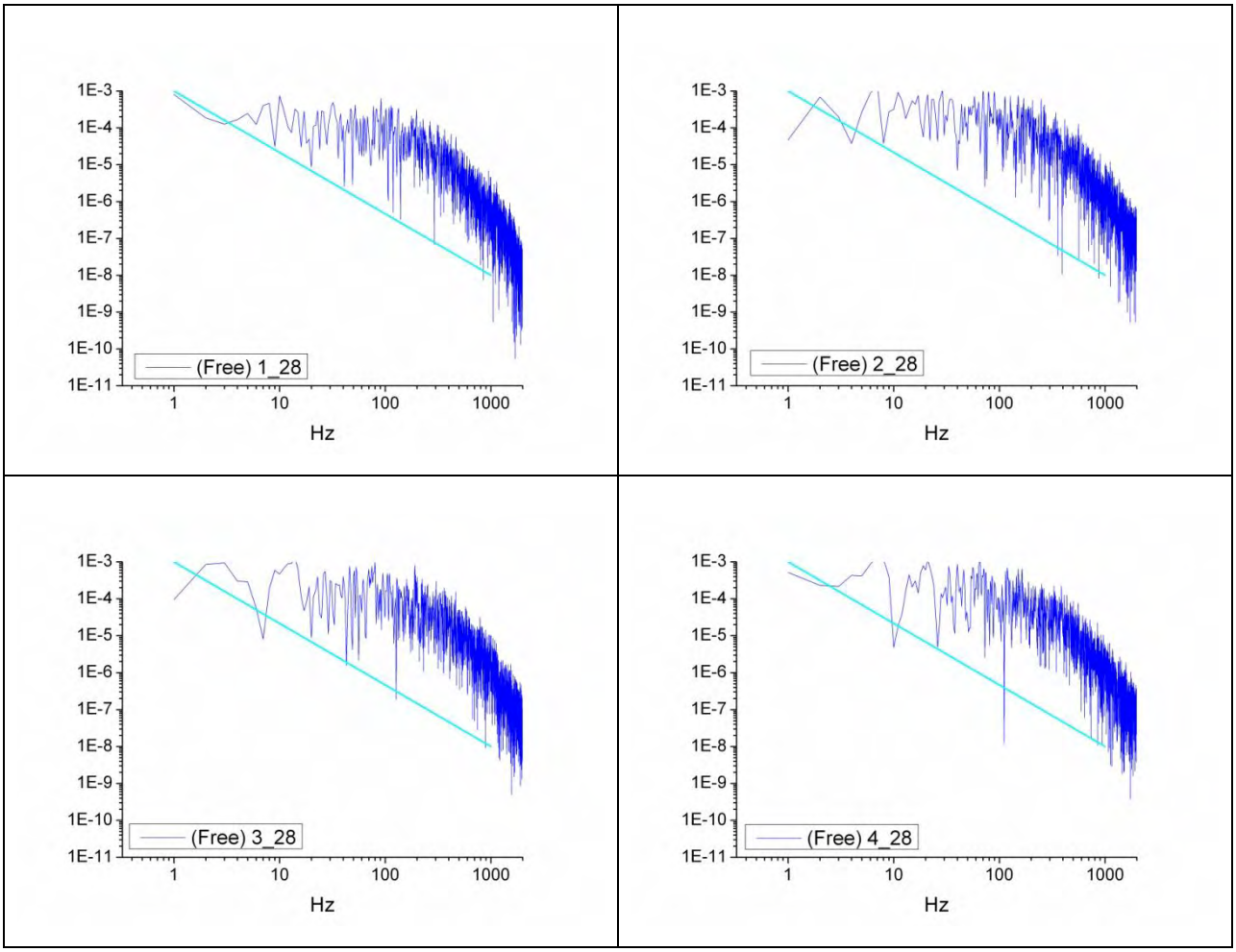

Figure 4-53 PSD spectrum, buoyancy flow experiment. Position nearest to the PV panel wall, for the 4 different vertical positions (UX1: z=400, UX2: z=700, UX3: z=1000, UX4: z=1300 mm from bottom), along the vertical centerline (x=148.75 mm).

The spectra are observed to have a lot of scatter. This could be partially due to the small sampling time, which is 30 s for the case of the high capacity fan (Figure 4-51).

However, the sampling time is increased to 60 s for the cases of low capacity fan (Figure 4-52) and buoyancy flow with heated PV panel (Figure 4-53) and the phenomenon persists. Obviously, flow instability is induced by the changing inlet conditions, due to the low Re numbers. These instabilities were significantly more enhanced when the testing device was placed outdoors. This is the reason that we did not perform hot wire anemometry measurements outdoors, as well as one of the two reasons that we could not succeed to conduct flow visualization experiments outdoors (the other one being the high light intensity under the sun).

In general, the PSD spectra obey the -5/3 law [155], which is an indication of the flow being on the turbulent regime.

4.7 HOT WIRE MEASUREMENTS PROCESSING

Furthermore, it is interesting to calculate a characteristic integral time scale for the velocity fluctuations, by means of an autocorrelation of the velocity time series. The results are shown in a series of figures. Two measurement points along the x-axis are studied: One closest to the PV panel wall (No.29, x=148.75 mm) and the other closest to the plexiglass cover (No.1, x = 1.25 mm). Under the reasonable assumption that the observed eddies are convected past the observation point without significant distortion and because of the weak turbulence, an integral length scale can be calculated based on each one of the above determined time scales, by means of the relation [157]:

$$\mathbf{l_I} = U\boldsymbol{\tau_I} \qquad \textbf{(4.8)}$$

In this type of flow where the large scale structures are convected, τ_i is a measure of the time it takes a large eddy to pass a point.

Integral time scales calculated for the free convection experiment with the heated PV panel are presented in **Figure 4-54** (close to the heated panel) and Figure 4-55 (close to the plexiglass cover). Each figure contains the integral time scale calculations for the 4 vertical positions (UX1: z=400, UX2: z=700, UX3: z=1000, UX4: z=1300 mm from the bottom of the panel), along the vertical centerline. The calculation is made with the MATLAB FFT routine (`autocorr`) and the integration with the `cumtrapz` routine. In the same way, integral time scales calculated for the high capacity fan cold flow experiment are presented in Figure 4-56 and Figure 4-57.

Finally, integral time scales calculated for the low capacity fan cold flow experiment are presented in Figure 4-58 and Figure 4-59. The calculated integral time is shown on each autocorrelation graph.

4.7.1 FREE CONVECTION EXPERIMENT (HEATED PV PANEL)

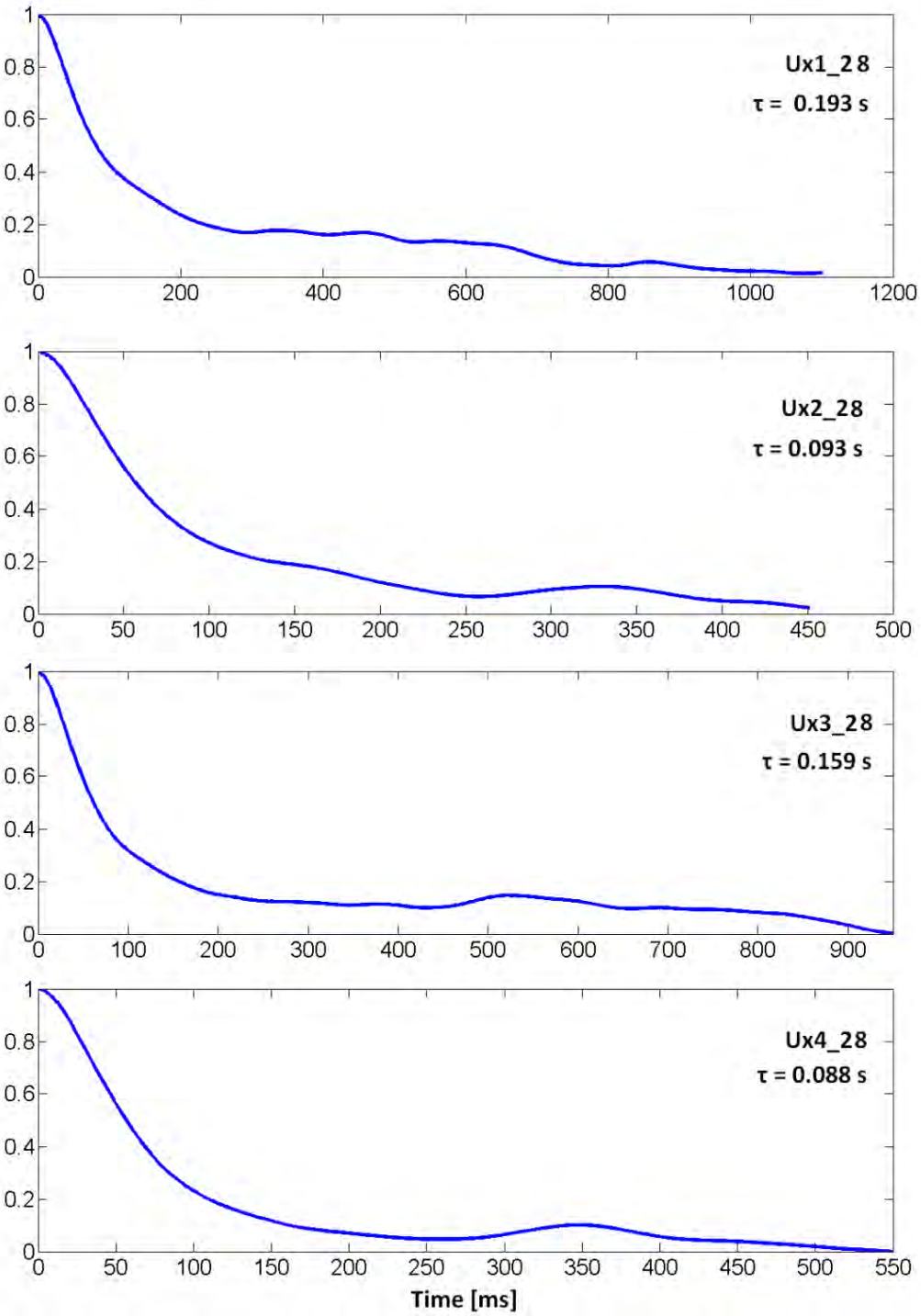

Figure 4-54 **Free convection experiment: Integral time scales computed by means of autocorrelation of velocity signals: Position nearest to the PV panel wall, for the 4 different vertical positions (UX1: z=400, UX2: z=700, UX3: z=1000, UX4: z=1300 mm from bottom), along the vertical centerline (=148.75 mm).**

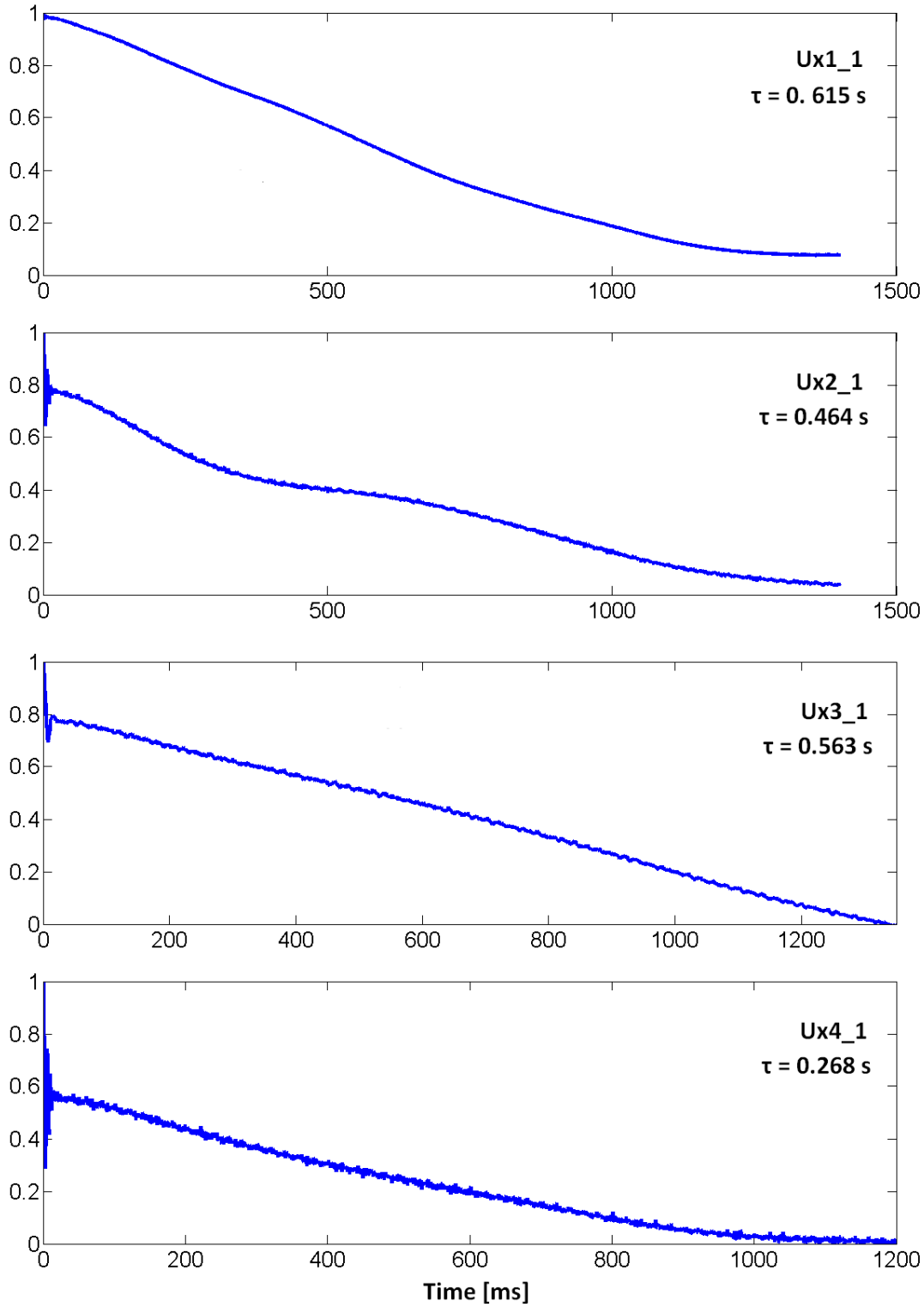

Figure 4-55 Free convection experiment: Integral time scales computed by means of autocorrelation of velocity signals: Position nearest to the plexiglass wall, for the 4 different vertical positions (UX1: z=400, UX2: z=700, UX3: z=1000, UX4: z=1300 mm from bottom), along the vertical centerline (x=1.25 mm).

4.7.2 HIGH CAPACITY FAN (COLD FLOW EXPERIMENT)

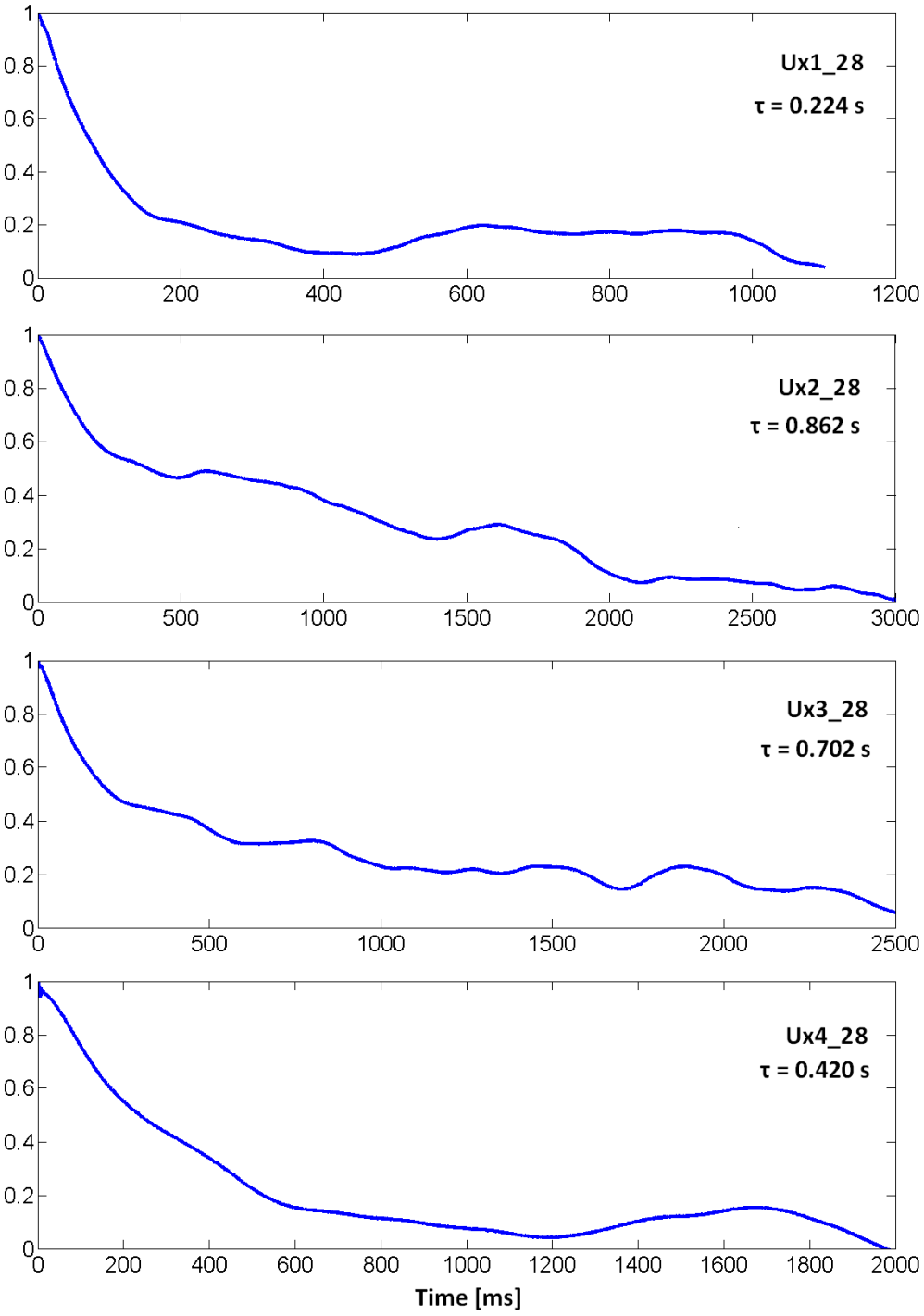

Figure 4-56 Cold flow experiment with the high capacity fan: Integral time scales computed by means of autocorrelation of velocity signals: Position nearest to the PV panel wall, for the 4 different vertical positions (UX1: z=400, UX2: z=700, UX3: z=1000, UX4: z=1300 mm from bottom), along the vertical centerline (x= 148.75 mm).

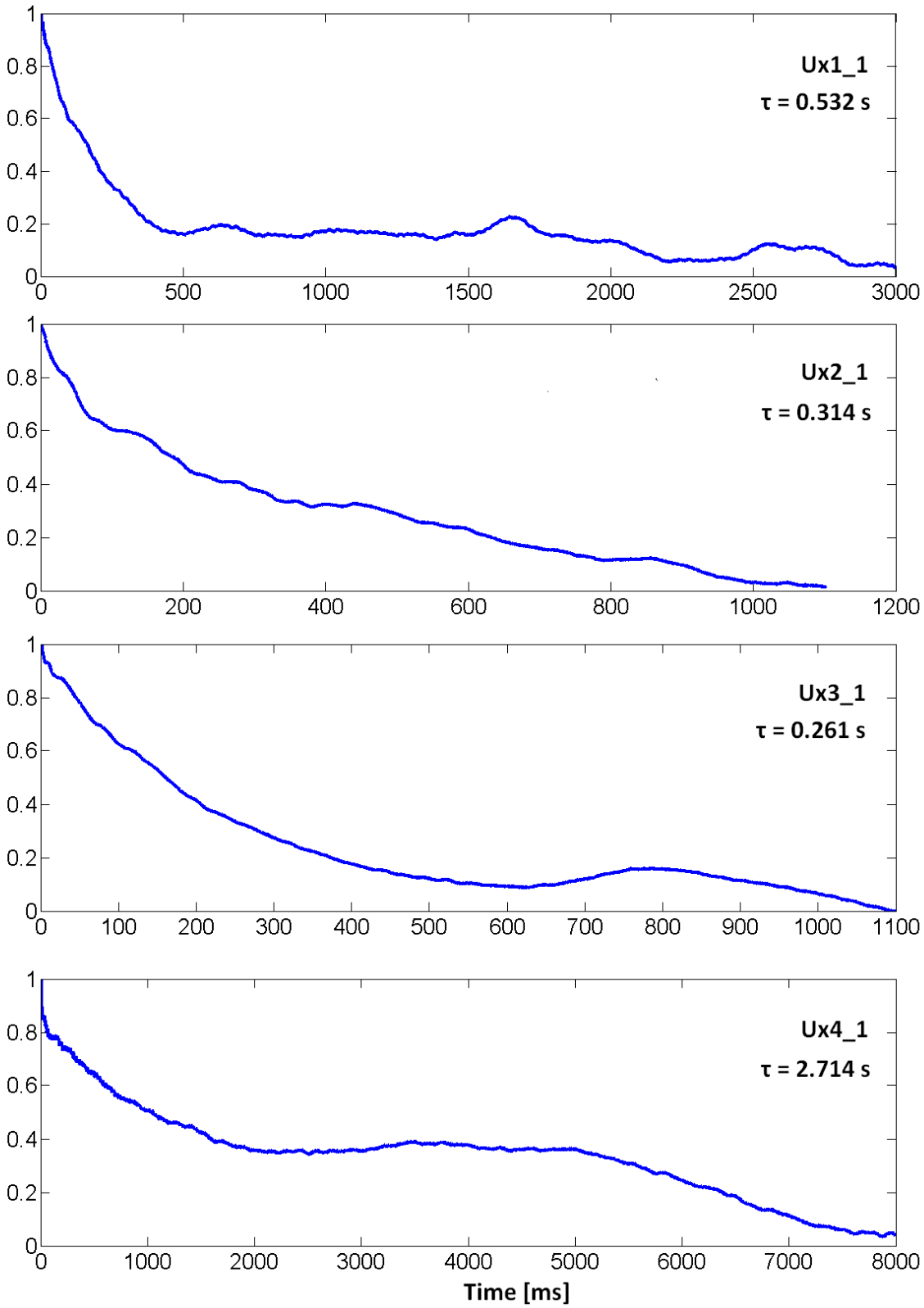

Figure 4-57 Cold flow experiment with the high capacity fan: Integral time scales computed by means of autocorrelation of velocity signals: Position nearest to the plexiglass wall, for the 4 different vertical positions (UX1: z=400, UX2: z=700, UX3: z=1000, UX4: z=1300 mm from bottom), along the vertical centerline (x=1.25 mm).

4.7.3 LOW CAPACITY FAN (COLD FLOW EXPERIMENT)

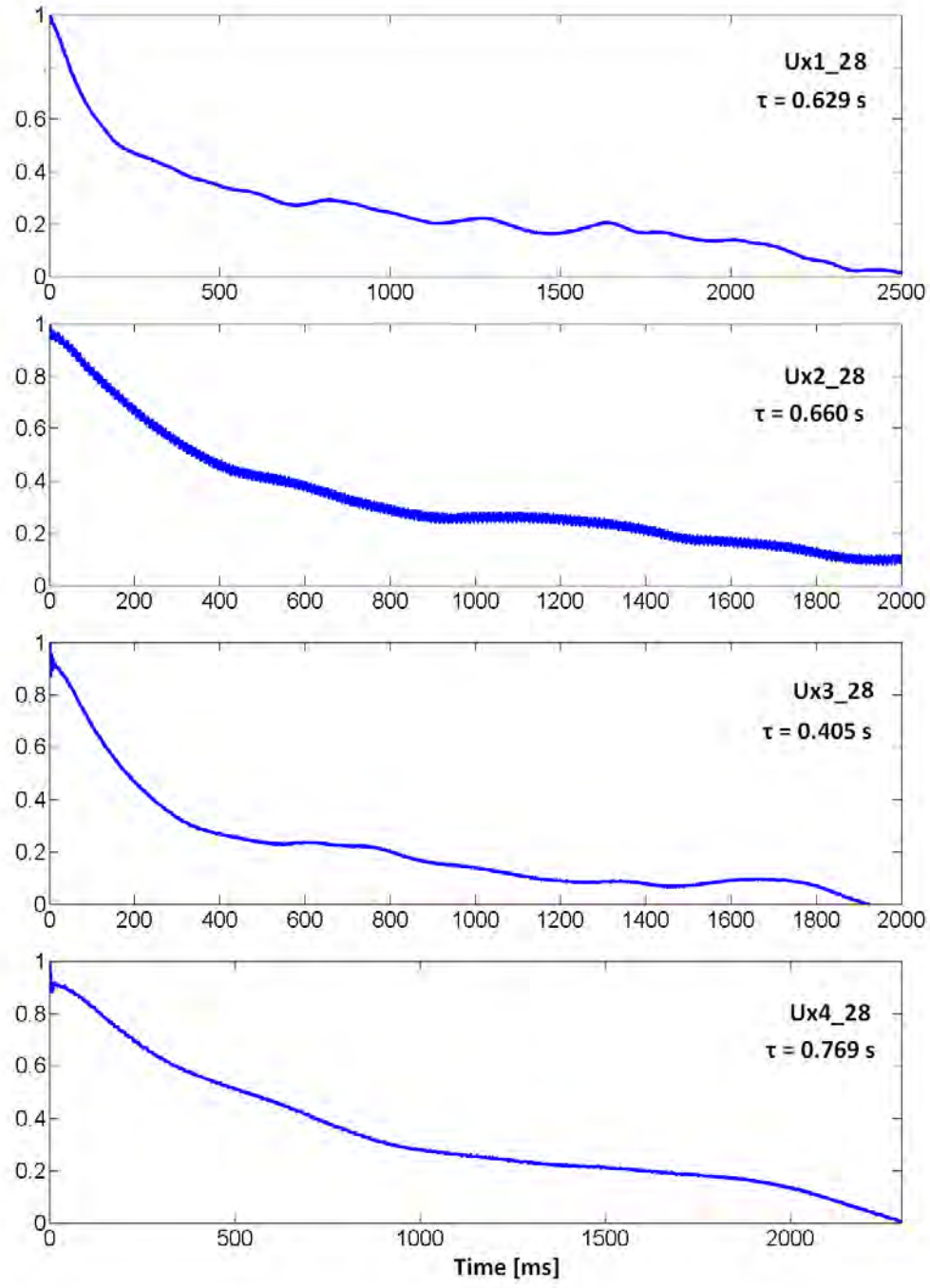

Figure 4-58 Cold flow experiment with the low capacity fan: Integral time scales computed by means of autocorrelation of velocity signals: Position nearest to the PV panel wall, for the 4 different vertical positions (UX1: z=400, UX2: z=700, UX3: z=1000, UX4: z=1300 mm from bottom), along the vertical centerline (x=148.75 mm).

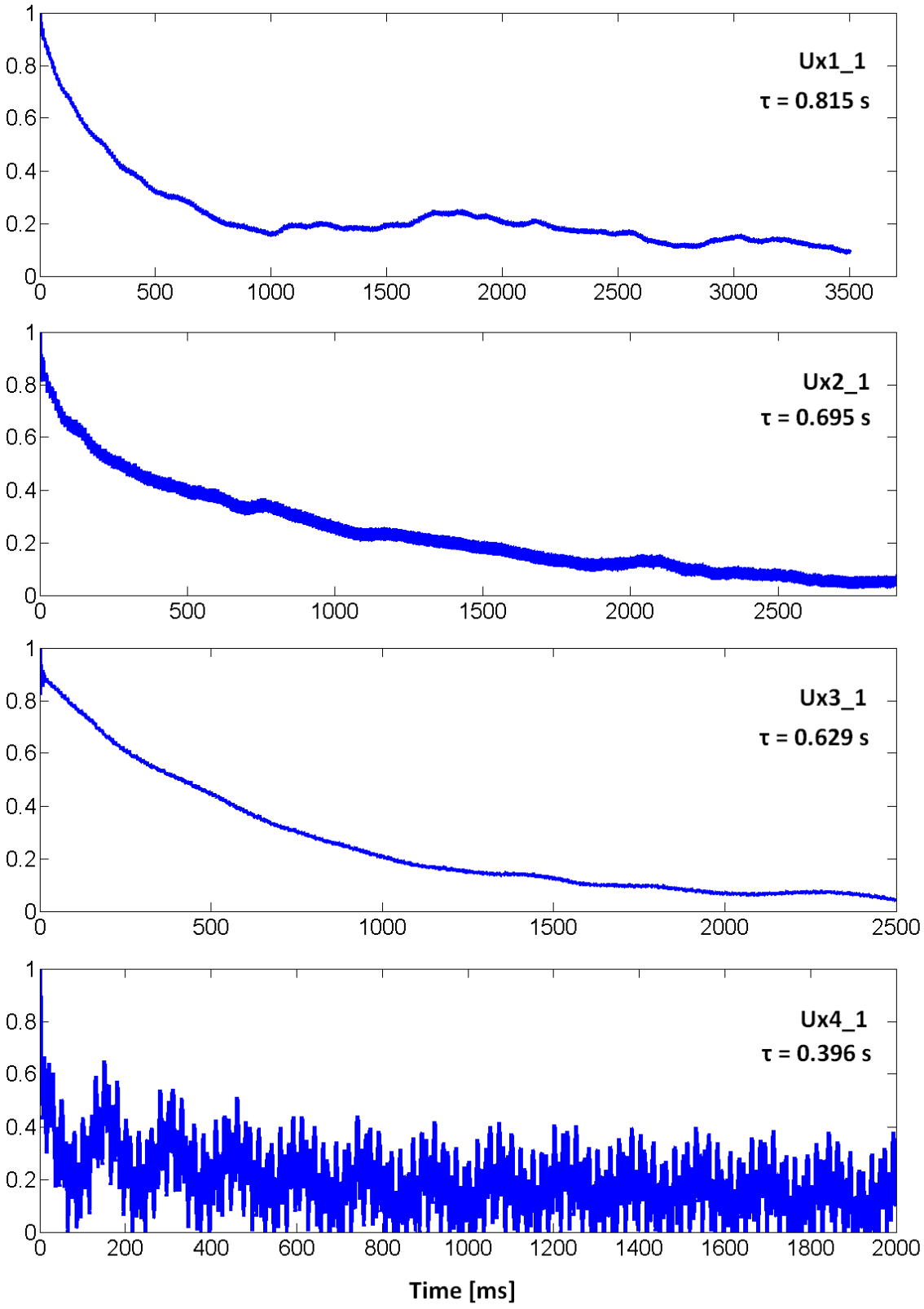

Figure 4-59 Cold flow experiment with the low capacity fan: Integral time scales computed by means of autocorrelation of velocity signals: Position nearest to the plexiglass wall, for the 4 different vertical positions (UX1: z=400, UX2: z=700, UX3: z=1000, UX4: z=1300 mm from bottom), along the vertical centerline (x=1.25 mm).

A summary of the results of autocorrelations is presented in the following graph:

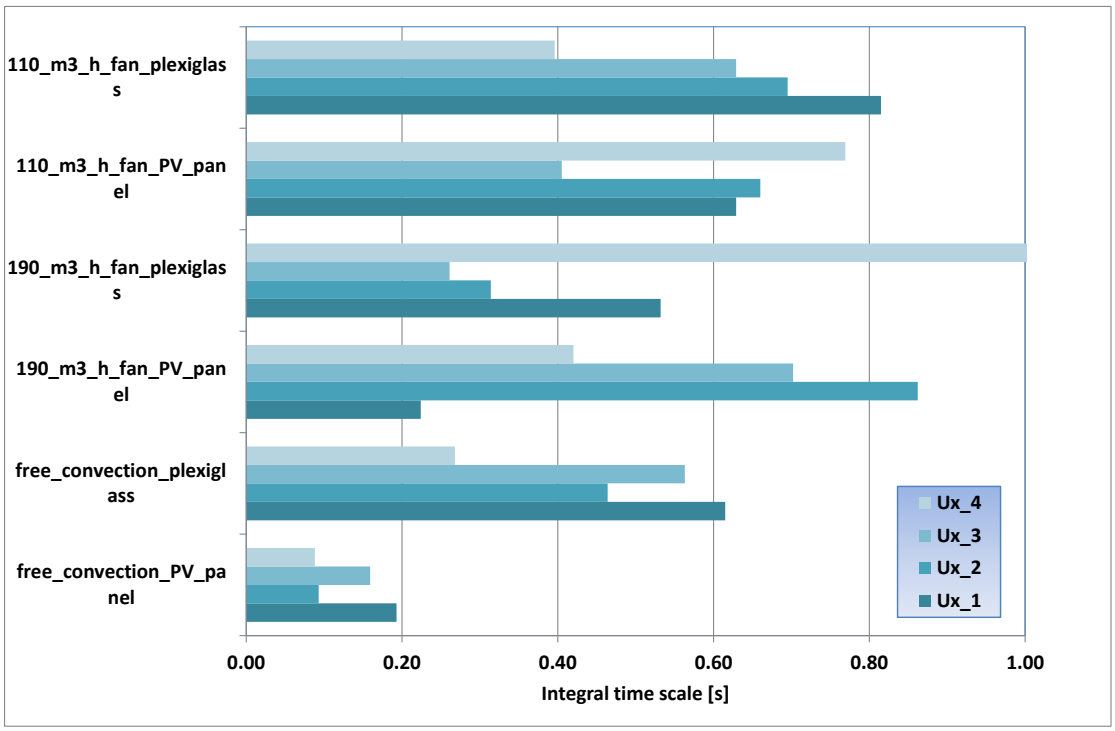

Figure 4-60 Summary of integral time scale computed by autocorrelation. for the 4 different vertical positions (UX1: z=400, UX2: z=700, UX3: z=1000, UX4: z=1300 mm from bottom) . Positions nearest to the plexiglass wall and nearest to the PV panel wall are shown.

In this figure, the ranges of integral time scale computed by autocorrelation are presented, starting from the low capacity fan case, followed by the high capacity fan case (cold flow experiments) and finally by the free convection case (heated PV panel). In each case, first the integral time scale ranges for the measurement point nearest to the plexiglass side is presented, followed by the measurement point nearest the PV panel. And for each one of these cases, the integral time scales for the 4 different vertical positions of the probe are shown, starting from the highest position (Ux4).

An important characteristic to be observed is the big variability of the results for each case, with the exception of the natural convection case and especially the points close to the heated PV panel, where we observe also the lowest integral time scales, of the order of 0.1-0.2 s.

An additional remark that should be made is that, as should be expected, the case with the higher capacity fan generally gives lower integral time scales than the one with the lower capacity fan.

4.7.4 SUMMARY OF CALCULATION OF INTEGRAL TIME SCALES

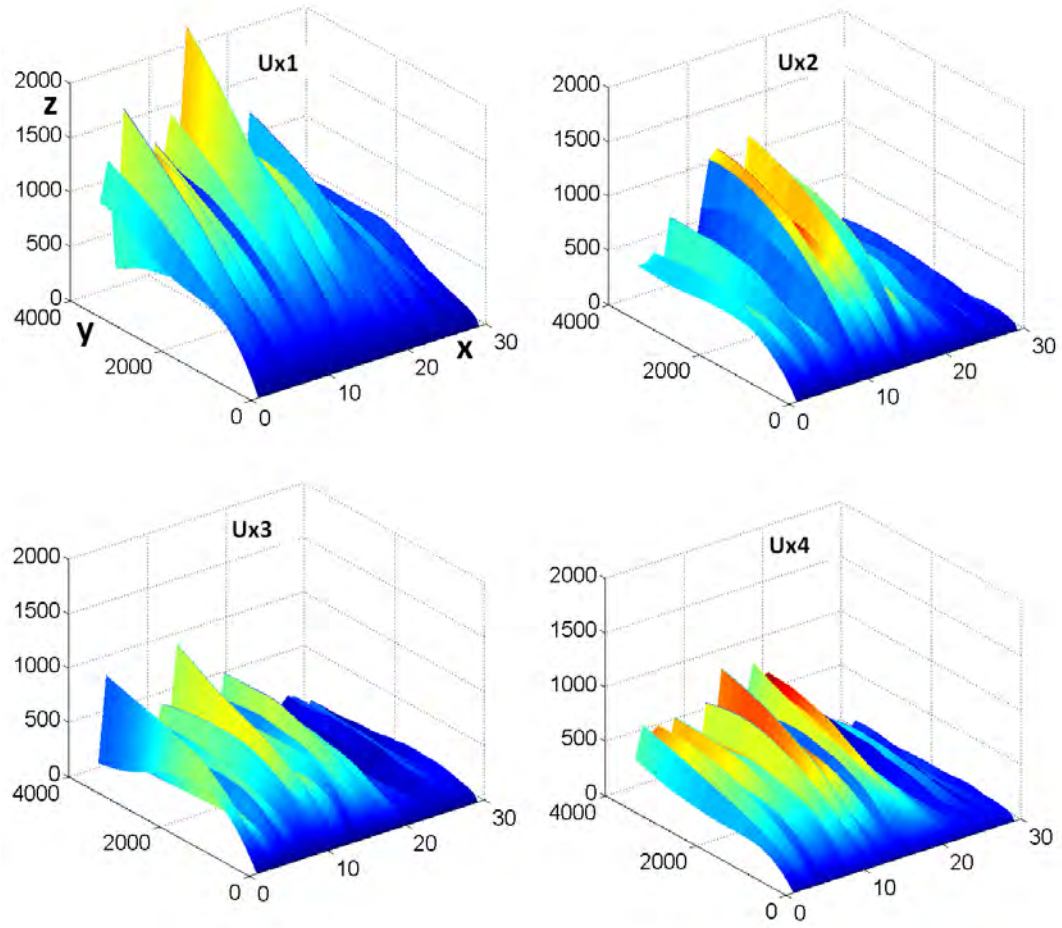

Figure 4-61 Buoyancy flow experiment (free convection): calculation of integral time scales of air velocity measured along the depth of the cavity (x=150 is the back side of the PV panel), for 4 different vertical positions along the centerline (schematic in Figure 4-44), Axis X: measurement points. Axis Y: Autocorrelation time shift [ms]. Axis Z: Integral time scale [ms]

A summary of all integral time calculations for all 29 points along the x direction, for the 4 different vertical positions along the centerline of the channel, are presented in Figure 4-61 for the free convection experiment with the heated PV panel.

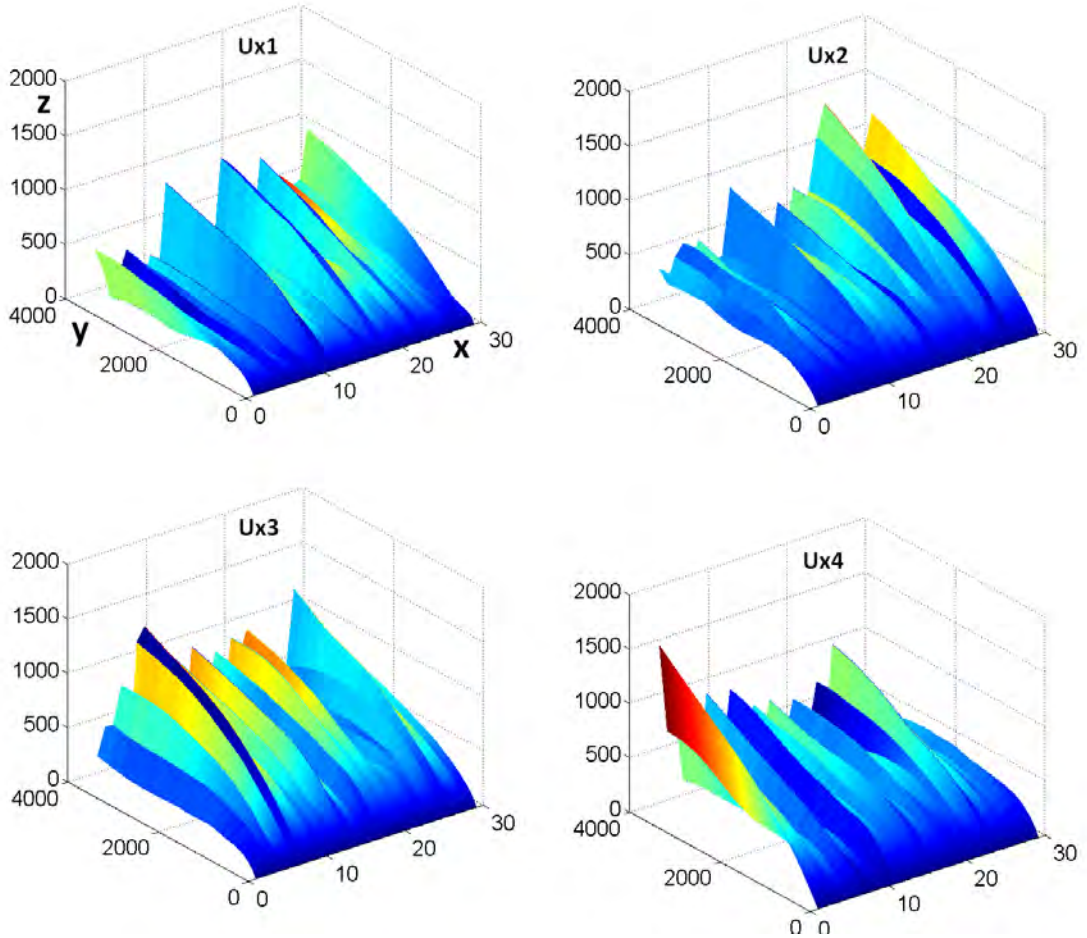

Figure 4-62 Cold flow experiment (high capacity fan): calculation of integral time scales of air velocity measured along the depth of the cavity (x=150 is the back side of the PV panel), for 4 different vertical positions along the centerline (schematic in Figure 4-44), Axis X: measurement points. Axis Y: Autocorrelation time shift [ms]. Axis Z: Integral time scale [ms]

A summary of all integral time calculations for all 29 points along the x direction, for the 4 different vertical positions along the centerline of the channel, are presented in Figure 4-62 for the cold flow experiment with the high capacity fan.

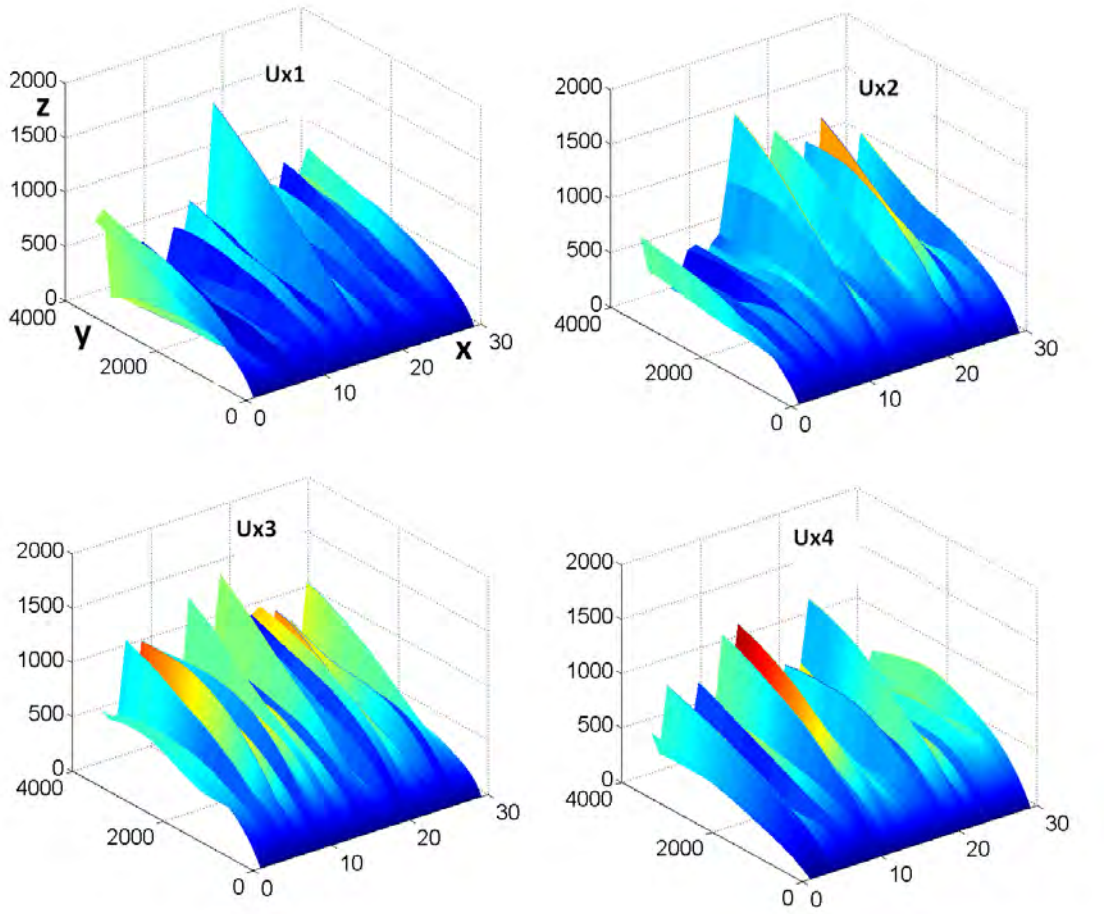

Figure 4-63 Cold flow experiment (low capacity fan): calculation of integral time scales of air velocity measured along the depth of the cavity (x=150 is the back side of the PV panel), for 4 different vertical positions along the centerline (schematic in Figure 4-44), Axis X: measurement points. Axis Y: Autocorrelation time shift [ms]. Axis Z: Integral time scale [ms]

A summary of all integral time calculations for all 29 points along the x direction, for the 4 different vertical positions along the centerline of the channel, are presented in Figure 4-63 for the cold flow experiment with the low capacity fan. As a general remark, the unstable flow characteristics observed with the FFT graphs are also apparent in these figures. On the average, integral time scales of the order of 500 ms are observed with the heated panel, natural convection mode, which results in integral length scales of the order of 25 mm close to the wall, according to eq. 4-8. This matches with the average diameter of eddies observed in the flow visualization.

More information on the flow and heat transfer characteristics of the flow can be extracted by calculating the Kolmogorov time and length scales for characteristic measurement points. The dynamical behavior of the smallest eddies is determined entirely by the rate at which they are fed energy, ε, and the size of the kinematic

viscosity v. The small eddies are where the mechanical energy is converted to heat, although the rate of conversion is determined by the large scales. A Kolmogorov length and time scale can be estimated by means of the following relations:

$$\mathbf{l_K} = (\frac{\nu^3}{\varepsilon})^{0.25} \quad \textbf{(4.9)}$$

$$\boldsymbol{\tau_K} = (\frac{\nu}{\varepsilon})^{0.5} \quad \textbf{(4.10)}$$

The dissipation rate, ε can be approximated by means of the following relation [158]: If u is a turbulent velocity scale, the root mean square fluctuating velocity (typical of the most energetic eddies), and l is a length scale of the most energetic eddies, then it is an experimental fact that:

$$\boldsymbol{\varepsilon} = \frac{u^3}{l} \quad \textbf{(4.11)}$$

where u denotes a turbulent velocity scale (see for example Figure 4-47,

Figure 4-49) and l denotes a characteristic large length scale (the mean diameter of the most energetic eddies). If we assume the characteristic length scale to be 1/6th of the depth of the channel, that is, 25mm, (which is equal to the integral length scale estimated above), and u=0.02 m/s for the natural convection case, then ε=0.001 and for v=1.82 E-5 m^2/s (kinematic viscosity of air at 50^{o}C), we get the following typical value for the Kolmogorov length scale: l_K=1.8 mm. The results are briefly presented in the following table.

Table 4-12 Calculation of kolmogorov length scale

length scale	l	0.025	m
turbulent velocity scale	u	0.02	m/s
dissipation (energy consumed/ unit mass of flow)	ε	0.00108	W/kg
kinematic viscosity	v	1.82E-05	m^2/s
Kolmogorov microscale	η	0.0018	m

Smaller scales cannot exist because the viscous transport smears them out. In most flows the Kolmogorov microscale η is a few tenths of a millimeter. In our case it is significantly higher, because we are in the transition regime and turbulent dissipation is at low levels. Based on this result, if we try to enhance the heat transfer surface by means of fins, the minimum free distance between fins must exceed 1.8 mm.

4.8 VELOCITY FIELD ALONG THE WIDTH OF THE PANEL

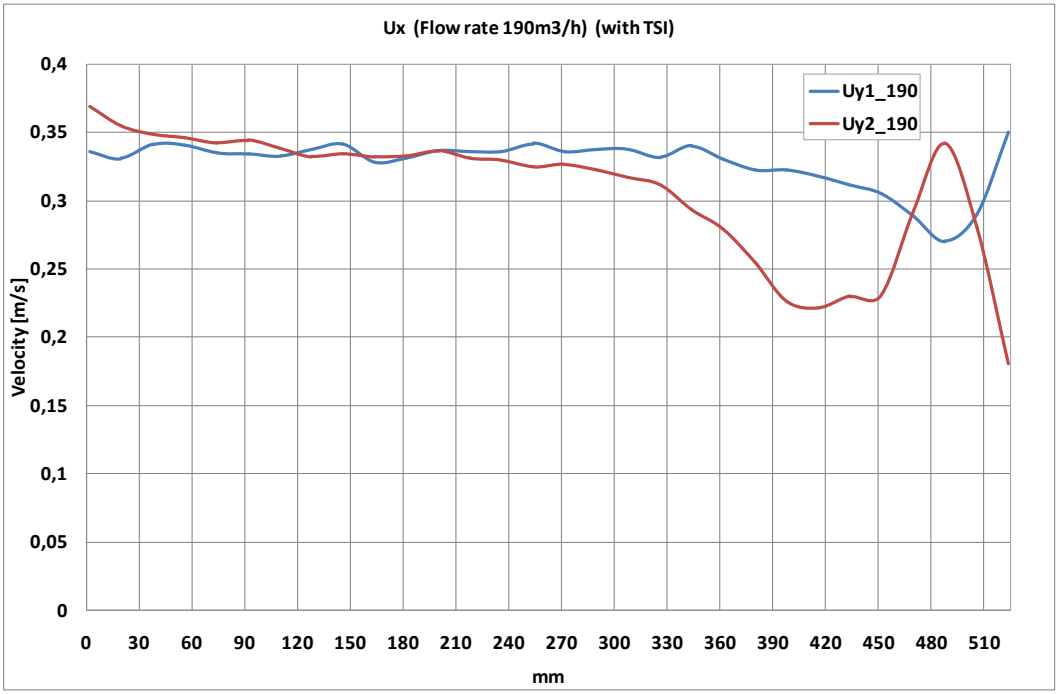

Figure 4-64 Cold flow experiment with the high capacity fan on: measurements of vertical component (z) of air velocity along the width of the cavity (y=510 mm is the middle of the panel width), for 2 different vertical positions.

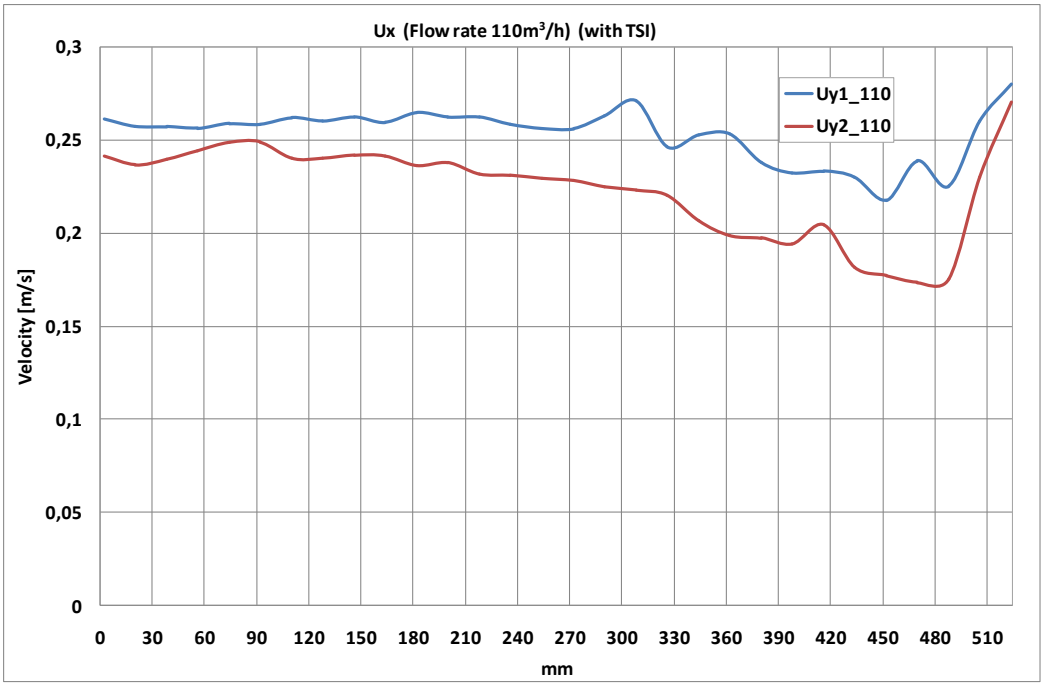

Figure 4-65 Cold flow experiment with the low capacity fan on: measurements of vertical component (z) of air velocity along the width of the cavity (y=510 mm is the middle of the panel width), for 2 different vertical positions.

A small decrease in local air velocity is observed, along with an increase in convection coefficient, with the shift to forced convection following switching on the fan. Thus, the installation of the specific capacity fan does not seem to increase the air flow through the cavity under the specific insolation and weather conditions.

4.9 Discussion of Results: Outdoor and Indoor Experiments

4.9.1 Solar radiation levels and efficiency of the solar panel.

The basic testing device was subjected to outdoor measurements during several hours for a number of days in summer and autumn 2010. Three operating modes are tested: natural convection (no fan), and forced convection cooling by means of two different capacity axial fans with 110 and 190 m^3/h nominal flow rate.

The transient electrical and thermal behavior of the testing collector device was recorded outdoors, for several hours during a number of days in summer and autumn.

The validation experiments enhance our understanding of the concept's operation and provide data for the fine tuning of the respective sub models in the building energy simulation. A certain degree of variation in PV conversion efficiency was recorded and explained, which stays in general agreement with the manufacturer's data.

It became apparent that a better understanding of the flow field inside the cavity is necessary. Further investigation of the air flow and turbulence field was carried out by means of indoor flow visualization measurements and hot wire anemometry measurements.

Three modes of indoor operation were tested: Mode 1 was buoyancy flow with externally heated panel to reach normal operating temperature. Mode 2 and 3 (lower and higher capacity fan) were tested at room temperature.

4.9.2 Flow visualization experiments

The device was subjected to flow visualization experiments aiming at better understanding of the flow field in the 3 modes mentioned above.

Some preliminary image analysis indicates low turbulence levels and a significant effect of flow entrance conditions on the flow field. An inspection of characteristic series of clips shows the propagation of characteristic turbulent flow patterns. A characteristic large scale motion may be seen in the form of slow circulating eddies at the lower part of the channel that initially adhere to the heated PV panel and further downstream detach and move towards the bulk flow. The important role of the heated PV panel in the evolution of turbulent flow patterns was observed. Also, a complex 3-D flow field with significant variations in air velocity from the centerline to the PV panel and plexiglass walls was observed.

It became apparent that measurements of the mean velocity field and turbulence levels in the same modes would further enhance our understanding of the heat transfer behavior.

4.9.3 INDOOR HOT WIRE ANEMOMETRY MEASUREMENTS

Velocity profiles were recorded at the centerline, along the depth of the cavity, for 4 different vertical positions. Average velocities of the order of 0.10 m/s with respective turbulent velocities of 0.01 m/s were recorded for the buoyancy flow (mode 1). Higher average velocities of the order of 0.2 – 0.35 m/s (lower and higher capacity fans, respectively) and turbulent velocities of 0.015-0.03 m/s were recorded in the cold flow experiments.

The hot wire anemometry data were analyzed by means of FFT and autocorrelation. Integral time scales as low as 500 ms were calculated for the buoyancy flow case, which corresponds to an integral length scale of about 0.025 m. A Kolmogorov length scale of the order of 0.0018 m was calculated for the same case.

The experimental velocity profiles along the channel indicate the developing character of the flow.

Turbulent kinetic energy profiles clearly show that a (not fully developed) turbulent flow is attained near the outlet.

It was decided to attempt a better understanding of the 3D flow field and heat transfer rates, by means of CFD computations for the above-mentioned modes of operation that would be validated against the hot wire anemometry measurements.

CHAPTER

5

5 CFD SIMULATIONS

The design optimization of the proposed concept may be supported by CFD modeling of the basic building block, which was already experimentally assessed as reported in chapter 4. The CFD simulations undertaken in this study were performed with ANSYS CFX. Existing measurements are employed for CFD results validation. Once validated, the model can be employed for the preliminary assessment of design improvements in the form of the PV backsheet surface modifications, changes in the geometry of the cavity, type of fans etc.

Use of advanced Computational fluid dynamics (CFD) enables simulation of the behavior of systems, processes and equipment involving flow of gases and liquids, heat and mass transfer, chemical reactions and related physical phenomena. ANSYS CFX is a high-performance, general purpose CFD software that has been applied to solve wide-ranging fluid flow problems for over 20 years[159]. At the heart of ANSYS CFX is its advanced finite volume solver, the key element that enables to achieve reliable and accurate solutions. The modern, highly parallelized solver is the foundation for an abundant choice of physical models to simulate virtually any type of phenomena related to fluid flow: laminar to turbulent (including transition), incompressible to fully compressible, subsonic to transonic and supersonic, isothermal or with heat transfer by convection and/or radiation, non-reacting to combusting, stationary and/or rotating devices, single fluids and mixtures of fluids in one or more phases (incl. free surfaces) and much more. The solver and its many physical models are wrapped in a modern, intuitive, and flexible GUI user friendly environment, with extensive capabilities for customizing and automating using session files, scripting, and a powerful expression language.

5.1 SELECTION OF TURBULENCE MODEL

As already presented in chapter 4.1 (flow visualization), the flow inside the duct is turbulent, at relatively low Re numbers. That is, small perturbations are slowly evolving to larger vortices that move with the main direction of the flow without significant dissipation.

Two-equation turbulence models are very widely used in CFD, as they offer a good compromise between numerical effort and computational accuracy. Both velocity and length scale are solved using separate transport equations (hence the term 'two-equation').

In our case, we may choose between the *k-ε* and the *k-ω* two-equation models [160], both of which use the gradient diffusion hypothesis to correlate the Reynolds stresses to the mean velocity gradients and turbulent viscosity. The turbulent viscosity is modeled as the product of a turbulent velocity and turbulent length scale.

In two-equation models, the turbulence velocity scale is computed from the turbulent kinetic energy, which is provided from the solution of its transport equation. The turbulent length scale is estimated from two properties of the turbulence field, usually the turbulent kinetic energy and its dissipation rate. The dissipation rate of the turbulent kinetic energy is provided from the solution of its transport equation.

***k-ε* model:**

The *k-ε* model is one of the most widely used turbulence models. It is a two equation model that means, it includes two extra transport equations to represent the turbulent properties of the flow. This allows a two equation model to account for history effects like convection and diffusion of the turbulent energy.

The first transported variable is the turbulent kinetic energy, *k*. The second transported variable is the turbulent dissipation, *ε*. It is the variable that determines the scale of the turbulence, whereas the first variable, *k*, determines the energy in the turbulence.

k is The turbulence kinetic energy k, is defined as the variance of the fluctuations in velocity. It has dimensions of (L^2 T^{-2}), and *ε* is the turbulence eddy dissipation rate (the rate at which the velocity fluctuations dissipate), and has dimensions of *k* per unit time (L^2 T^{-3}).

The *k-ω* Model:

One of the advantages of the *k-ω* formulation is the near wall treatment for low-Reynolds number computations. The model does not involve the complex non-linear damping functions required for the *k-ε* model and is therefore more accurate and robust. A low-Reynolds *k-ε* model would typically require a near wall resolution of $y^+<0.2$, while a low-Reynolds number *k-ω* model would require at least $y^+<2$. In industrial flows, even $y^+<2$ cannot be guaranteed in most applications and for this reason, a new near wall treatment was developed for the *k-ω* model. It allows for smooth shift from a low-Reynolds number form to a wall function formulation.

The Shear Stress Transport (SST) Model:

The SST *k-ω* turbulence model [161] is two-equation an improvement over the *k-ω* eddy-viscosity model which has become very popular. The shear stress transport (SST) formulation combines the best of two worlds. The use of a *k-ω* formulation in the inner parts of the boundary layer makes the model directly usable all the way down to the wall through the viscous sub - layer, hence the SST *k-ω* model can be used as a Low-Re turbulence model without any extra damping functions. The SST formulation also switches to a *k-ε* model in the free-stream and thereby avoids the common *k-ω* problem that the model is too sensitive to the inlet free-stream turbulence properties. Investigators who use the SST k-ω model often merit it for its good behavior in adverse pressure gradients and separating flow. The SST k-ω model does produce a bit too large turbulence levels in regions with large normal strain, like stagnation regions and regions with strong acceleration. This tendency is much less pronounced than with a normal k-ε model though.

Since we are trying to model the vorticities which make up turbulence, it is important to have a mesh and numerical scheme accurate enough to capture this. We tested running at steady state and we found difficulties with convergence. We also run transient and we noticed small perturbations at low Re. We tested with a k-ε based model with inadequate results, except for the natural convection case. Low performance of this model is expected since the k-ε model is known to not handle low k well. Finally, we shifted to the *k-ω* (inc SST) based model, which is known to handle small k well. Indeed, this gave improved results, although it was necessary to refine the mesh. Finer meshes have reduced numerical dissipation and therefore capture more flow features. This means a simulation on a coarse grid with a turbulence model may be steady, but with grid refinement becomes unsteady. This was not "detected" by CFX, it is just a fact that the numerical dissipation has reduced sufficiently that the transient features are not damped out.

The computation is made to check with our test rig's results. All the cases that were studied are based on 3D simulations. Three different computational cases are examined.

This computation will supply the data for the subsequent building energy simulation (next chapter). With aid of TRNSYS software the overall power output is optimized (energy and economic wire) in transient conditions employing data from TMY

5.2 SOLID MODEL

The solid model of the testing device of chapter 4 has been designed in AutoCad.

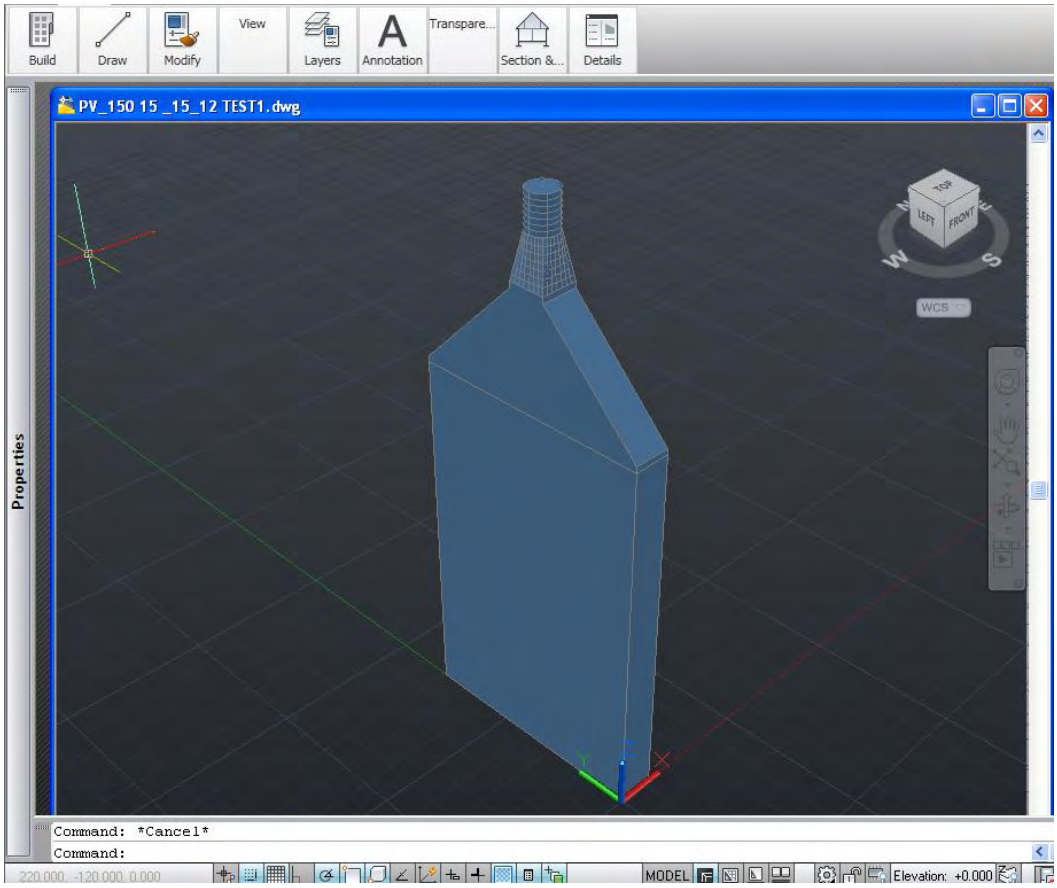

Figure 5-1 Solid model of the test rig's channel

Then the solid model has been inserted in ANSYS ICEM CFD –AI*ENVIROMENT to create the mesh for the CFD simulation.

After the initial checks, it was decided to refine the mesh near the PV panel and the plexiglass layer.

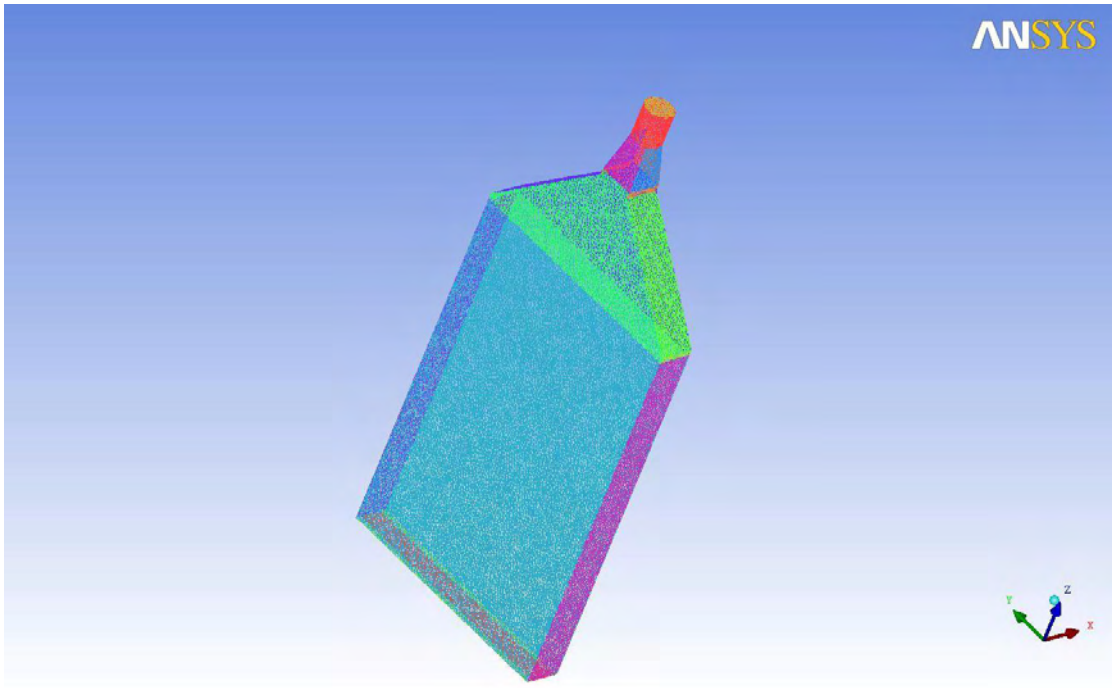

Figure 5-2 The mesh generated with ICEM CFX

The parameters of mesh are:

Global Mesh Size

Global Element Scale factor : Scale factor 3

Global Element Seed Size: Max Element: 3

Volume Meshing Parameters

Mesh Type : Tetra/Mixed

Mesh method: Robus

Table 5-1 Information of Total Elements

Total Elements	Total Nodes	TRI_3	TETRA_4	LINE_2
1.20E+06	2.03E+05	4.46E+04	1.15E+06	1.37E+03

5.3 PREPROCESSING

After generating the mesh, we begin CFX-Pre processor to define the simulation, in CFX-Pre we select the physical model to be used the CFD simulation.

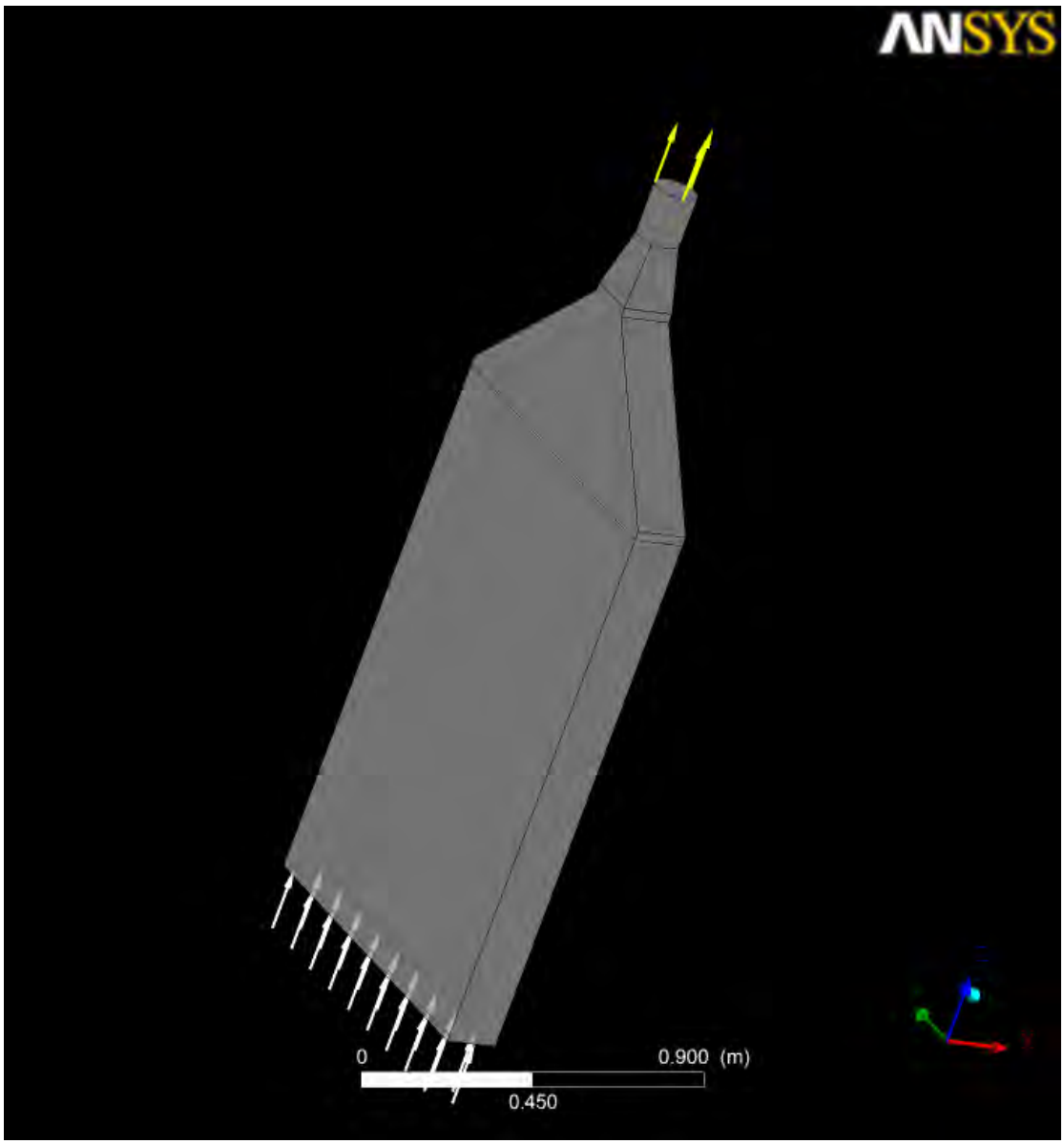

Figure 5-3 Inlet and outlet of the ambient air in the gap

5.4 CFD SIMULATIONS RESULTS

5.4.1 CFX RESULTS CASE 2 (110 M^3/H FAN)

Table 5-2 Simulation details

Name	Location	Type	Materials	Models
110m^3/h	BODY	Fluid	Air Ideal Gas	Heat Transfer Model = Isothermal Fluid Temperature = 18.0 [^{o}C] Turbulence Option = k-ω Turbulence Wall Function= Automatic Buoyancy Turbulence=Production and Dissipation

Table 5-3 Boundary Physics of the test rig for 1st case

Domain	Name	Location	Type	Settings
110m^3/h	Inlet	Inlet	Inlet	Flow Regime = Subsonic Mass&Momentum=StaticPressure Relative Pressure = 0 [Pa] Flow Direction = Zero Gradient Turbulence Option=Zero Gradient
110m^3/h	Outlet	Outlet	Outlet	Flow Regime = Subsonic Mass And Momentum = Average Static Pressure Relative Pressure = -5[Pa]
110m^3/h	PV	PV	Wall	Mass &Momentum = No Slip Wall Wall Roughness = Rough Wall Roughness Height 1.5 [micron]
110m^3/h	Plexiglas	Plexiglas	Wall	Mass &Momentum = No Slip Wall Wall Roughness = Rough Wall Roughness Height = 1.50 [micron]
110m^3/h	Round, Transaction	round	Wall	Mass&Momentum = No Slip Wall Wall Roughness = Rough Wall Roughness Height = 150 [micron]
110m^3/h	Aluminum	Aluminum	Wall	Mass&Momentum = No Slip Wall Wall Roughness = Rough Wall Roughness Height = 1.5 [micron]
110m^3/h	Inlet sheet	Inlet sheet	Wall	Mass And Momentum = No Slip Wall Wall Roughness = Rough Wall Roughness Height = 150 [micron]

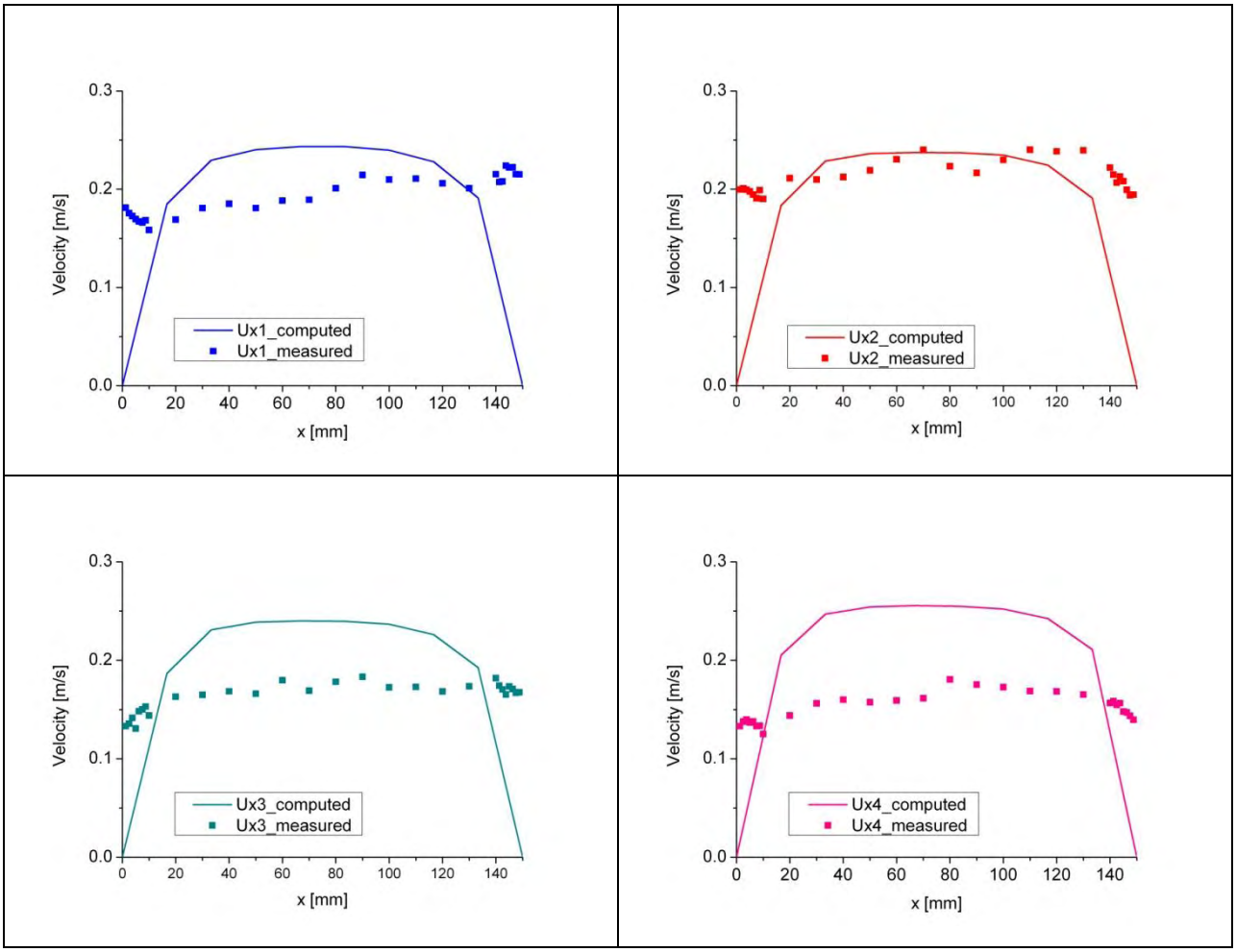

Figure 5-4 Velocity profiles measured and predicted by the CFX simulation (110m^3/h)

The velocity profiles predicted by the CFX simulation have a tendency to resemble more to laminar flow profiles [162]. On the other hand, the measured velocity profiles are flat and resemble more to turbulent profiles. It should be mentioned here that the turbulence models employed in the simulations with this type of codes are more apt to predict significant turbulence levels, i.e. Re of the order of 10^5 and above, whereas in our case we are one order of magnitude lower in Re.

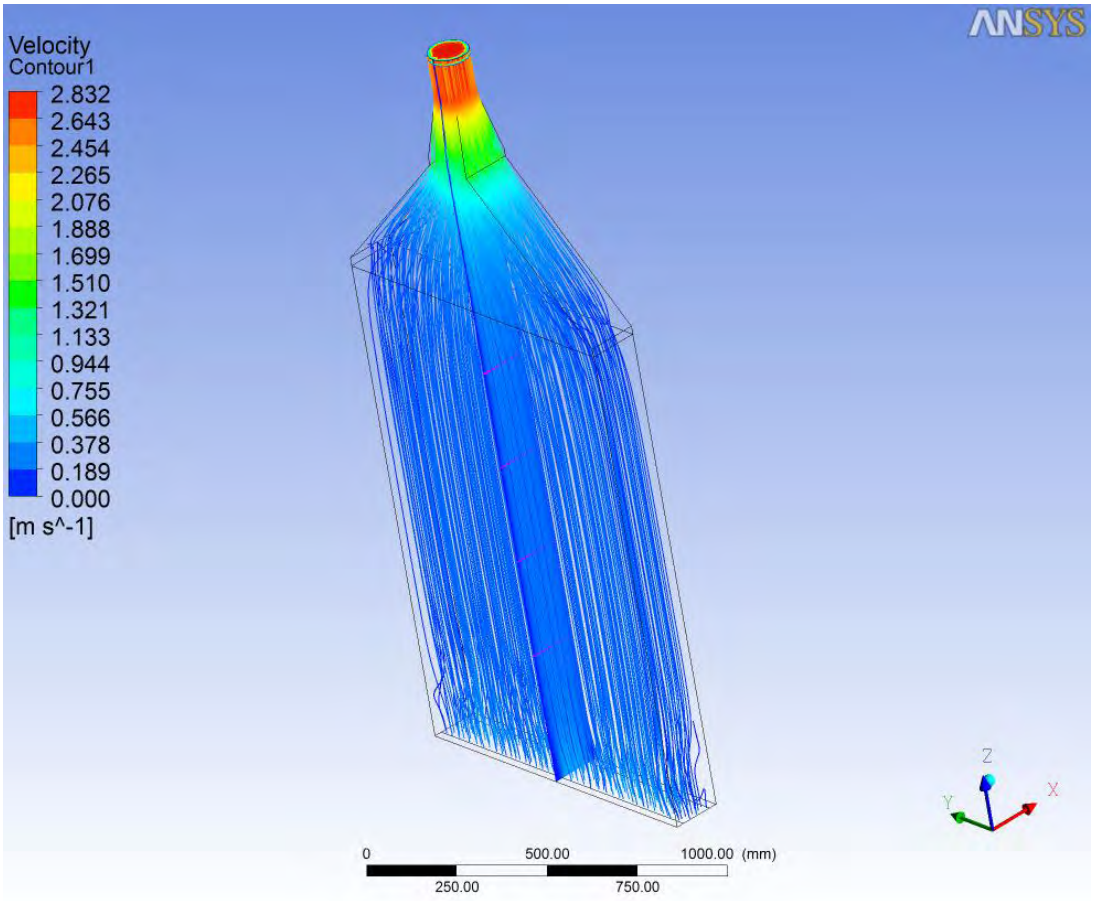

Figure 5-5 Streamlines

5.4.2 CFX RESULTS CASE 3 (190m^3/h)

Table 5-4 Simulation details for 2nd case

Name	Location	Type	Materials	Models
190m^3/h	BODY	Fluid	Air Ideal Gas	Heat Transfer Model = Isothermal Fluid Temperature = 16.0 [^{o}C] Turbulence Option = k-ω Turbulence Wall Functions = Automatic Buoyancy Turbulence =Production and Dissipation

Table 5-5 Boundary Physics of the test rig for 2nd case

Domain	Name	Location	Type	Settings
190m^3/h	Inlet	Inlet	Inlet	Flow Regime = Subsonic Mass And Momentum = Static Pressure Relative Pressure = 0 [Pa] Flow Direction = Zero Gradient Turbulence Option = Zero Gradient
190m^3/h	Outlet	Outlet	Outlet	Flow Regime = Subsonic Mass And Momentum = Average Static Pressure Relative Pressure = -15[Pa]
190m^3/h	PV	PV	Wall	Mass And Momentum = No Slip Wall Wall Roughness = Rough Wall Roughness Height 1.5 [micron]
190m^3/h	Plexiglas	Plexiglas	Wall	Mass And Momentum = No Slip Wall Wall Roughness = Rough Wall Roughness Height = 1.50 [micron]
190m^3/h	Round, Transaction	round	Wall	Mass And Momentum = No Slip Wall Wall Roughness = Rough Wall Roughness Height = 150 [micron]
190m^3/h	Aluminum	Aluminum	Wall	Mass And Momentum = No Slip Wall Wall Roughness = Rough Wall Roughness Height = 1.5 [micron]
190m^3/h	Inlet sheet	Inlet sheet	Wall	Mass And Momentum = No Slip Wall Wall Roughness = Rough Wall Roughness Height = 150 [micron]

The velocity profiles predicted by the CFX simulation are somewhat better matching the measurements than those for the low capacity fan case (**Figure 5-6**). This is expected since the Re number range here is higher and we are more close to the turbulent flow regime.

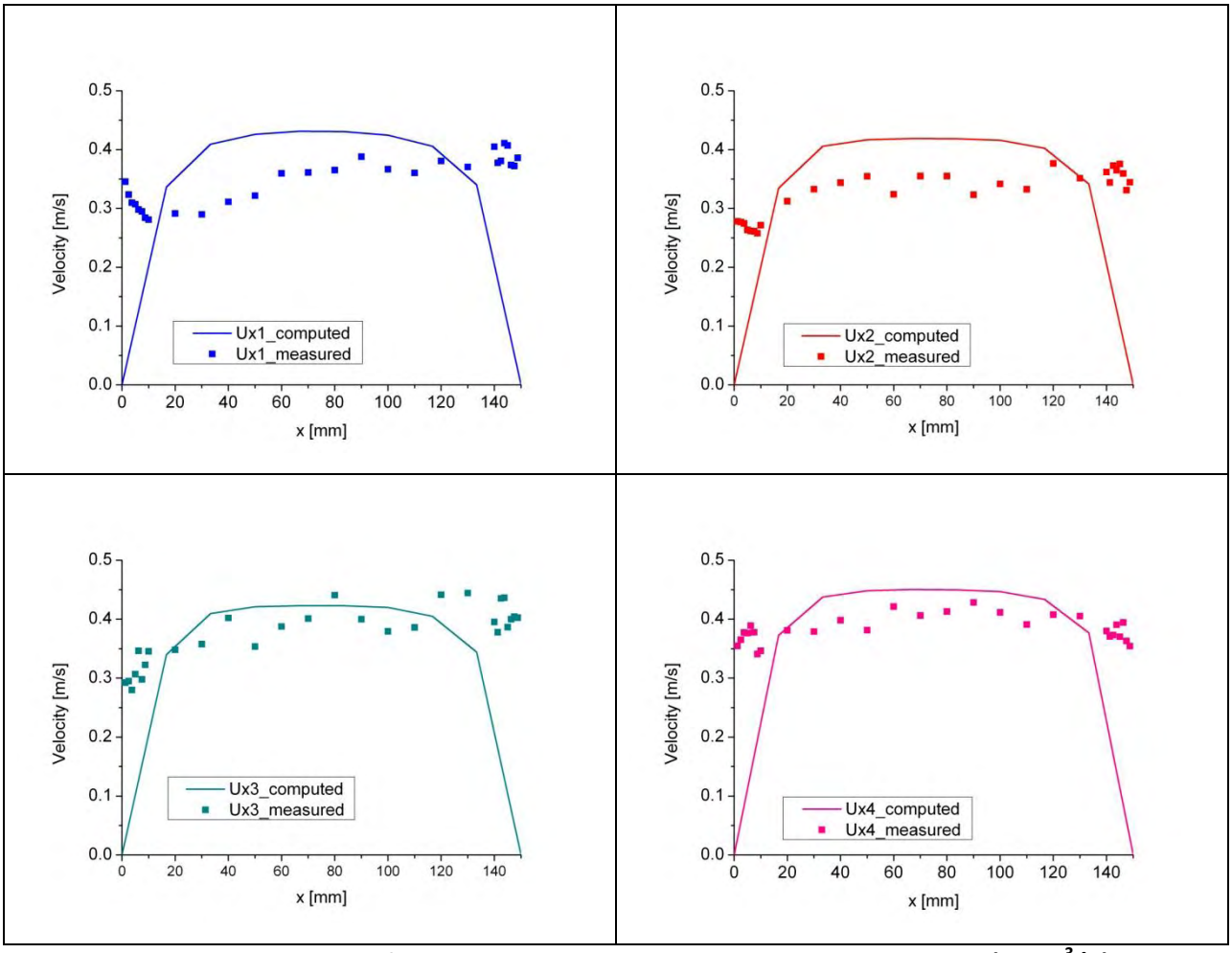

Figure 5-6 Velocity profiles measured and predicted by the CFX simulation (190m^3/h)

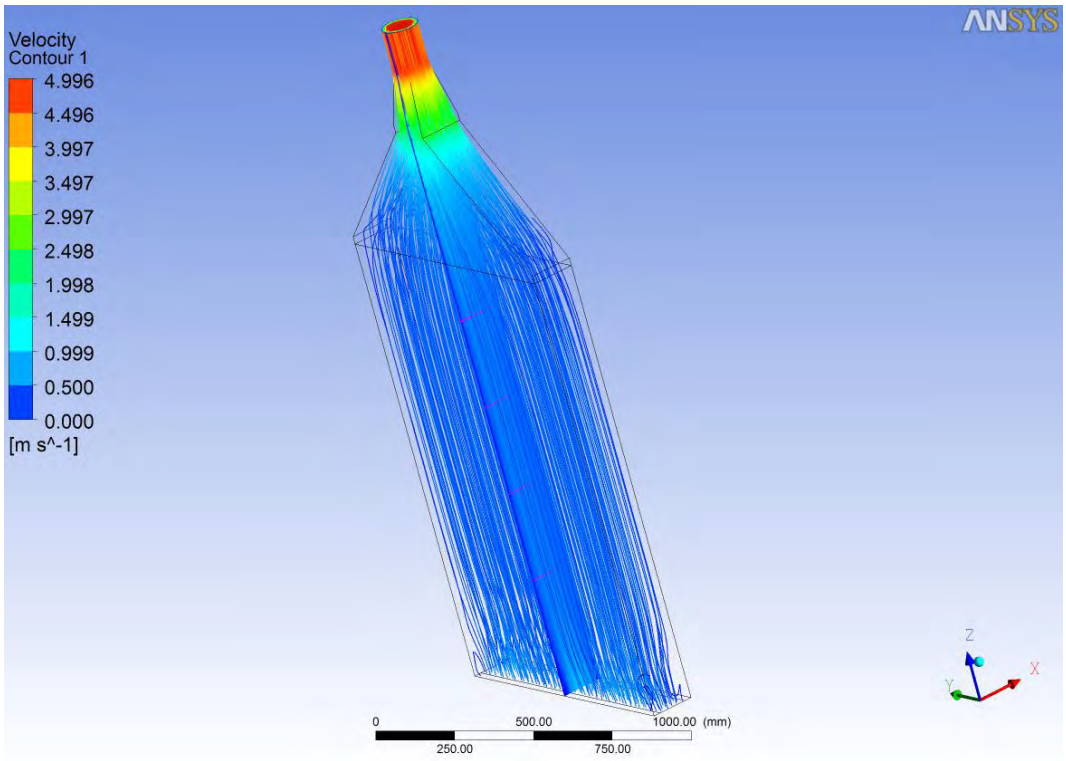

Figure 5-7 Streamlines

5.4.3 CFX RESULTS CASE 1 NATURAL CONVECTION

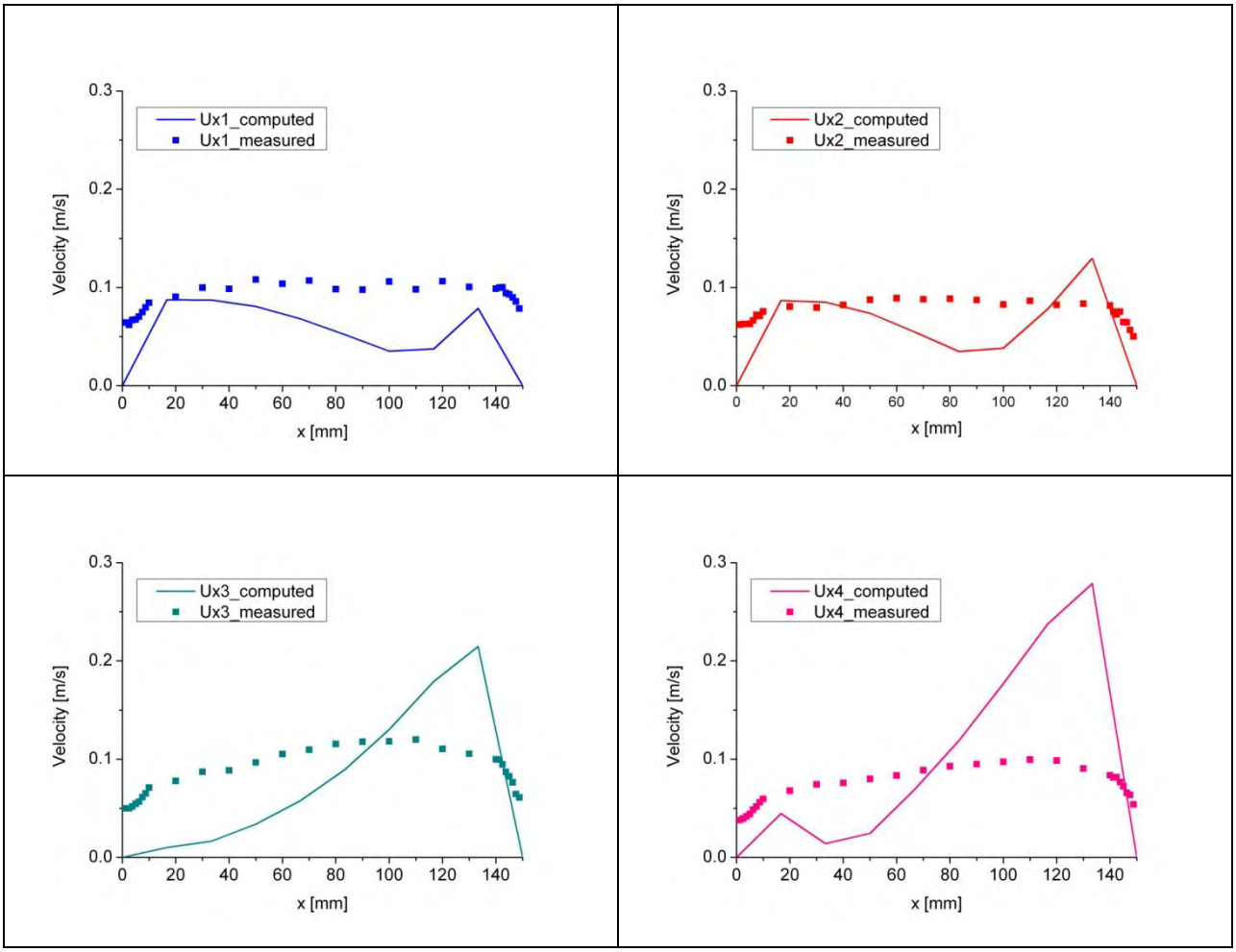

Figure 5-8 Velocity Profiles measured and predicted by the CFX simulation (natural convection mode)

The velocity profiles on the centerline predicted by the simulation for the natural convection mode, in the 4 different vertical (z) locations specified in the previous chapter, are shown in Figure 5-8. The matching of simulation and experimental results is of significantly lower quality than with the previous cases. This should be expected by the fact that the velocities and Re numbers are significantly lower here and the simulation of buoyancy flows is more demanding. The predicted velocity profile is highly asymmetrical and the convergence of the code is of lower quality than the previous cases. This should be expected from the unsteady character of the buoyancy flow, also observed in the measurements. Nevertheless, the vertical velocities are predicted to the correct order of magnitude, in the range of 0.05 to 0.2 m/s. The predicted velocity profiles along the y direction are also asymmetric about the center of the cross section. To better explain the predicted behavior, a 3D view of the flow field is presented in the next figure.

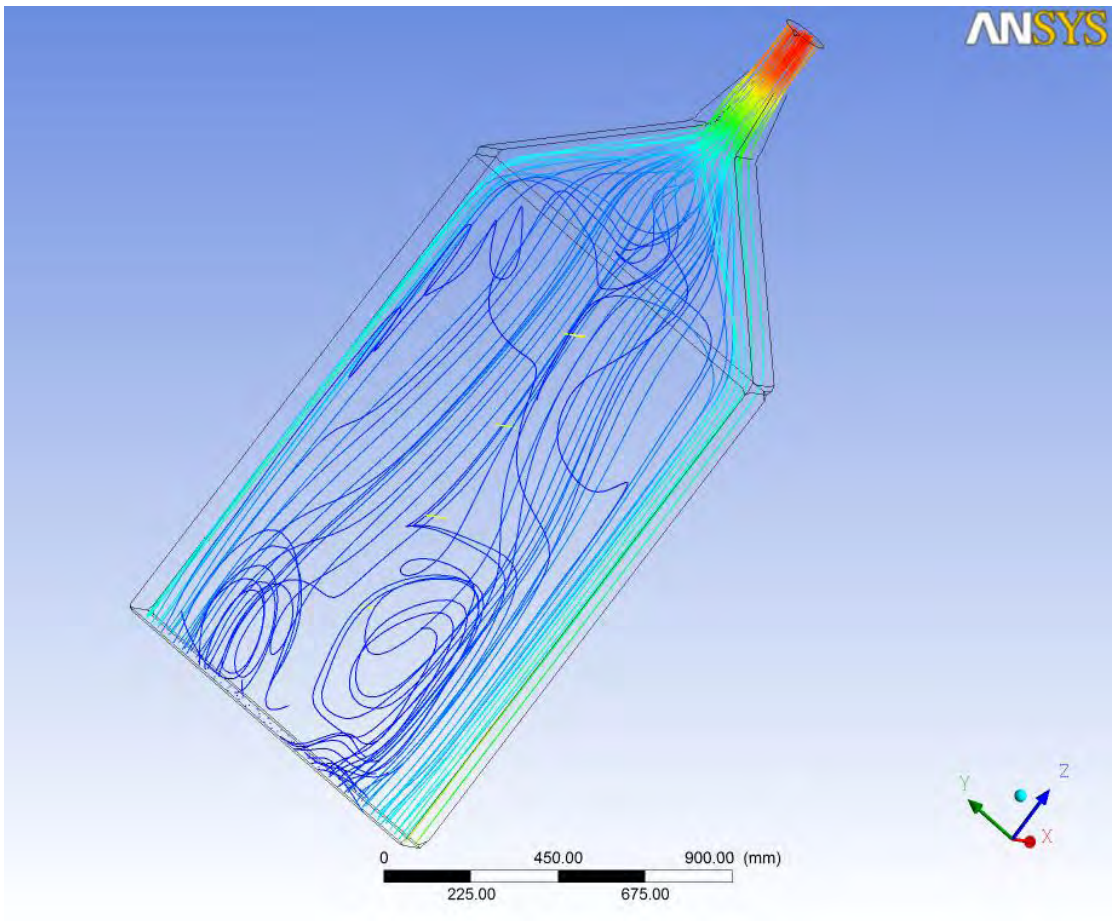

Figure 5-9 Stream Lines

Table 5-6 Simulation details for 3rd case (Free convection)

Name	Location	Type	Materials	Models
Free Convection	BODY	Fluid	Air Ideal Gas	Heat Transfer Model = Thermal Energy Turbulence Option= k epsilon; Turbulent Wall Functions = Scalable Buoyancy Turbulence =Production and Dissipation Turbulence Schmidt Number=1 Dissipation Coefficient =5 Buoyancy Model = Buoyant Domain Motion = Stationary

Table 5-7 Boundary Physics of the test rig for 3rd case (Free convection)

Domain	Name	Location	Type	Settings
Free Convection	Inlet	Inlet	Inlet	Flow Regime = Subsonic Mass&Momentum = Static Pressure Relative Pressure = 0 [Pa] Flow Direction = Normal to Boundary Condition Turbulence = High (Intensity = 10 %) Heat Transfer = Static Temperature Static Temperature = 18.4 [^{o}C]
Free Convection	Outlet	Outlet	Outlet	Flow Regime = Subsonic Mass&Momentum=Average Static Press Relative Pressure = -5 [Pa] Pressure Profile Blend = 0.05 Pressure Averaging = Average Over Whole Outlet
Free Convection	PV	PV	Wall	Mass And Momentum = No Slip Wall Wall Roughness = Rough Wall Roughness Height 1.5 [micron] Heat Transfer = Temperature Fixed Temperature = 43.15 [^{o}C]
Free Convection	Plexiglas	Plexiglas	Wall	Mass And Momentum = No Slip Wall Wall Roughness = Rough Wall Roughness Height = 1.50 [micron] Heat Transfer = Temperature Fixed Temperature = 22 [^{o}C]
Free Convection	Round, Transaction	round	Wall	Mass And Momentum = No Slip Wall Wall Roughness = Rough Wall Roughness Height = 150 [micron] Heat Transfer = Adiabatic
Free Convection	Aluminum	Aluminum	Wall	Mass And Momentum = No Slip Wall Wall Roughness = Rough Wall Roughness Height = 1.5 [micron] Heat Transfer = Temperature Fixed Temperature = 22 [^{o}C]
Free Convection	Inlet sheet	Inlet sheet	Wall	Mass And Momentum = No Slip Wall Wall Roughness = Rough Wall Roughness Height = 150 [micron] Heat Transfer = Temperature Fixed Temperature = 22 [^{o}C]

Comparisons between CFD simulation and hot wire anemometry measurements for the three test cases examined are summarized as follows:

- Buoyancy flow case: average prediction

- Lower capacity fan case: good prediction
- Higher capacity fan case: good prediction

The following Table summarizes the computational cases examined by the CFD and the respective experimental cases employed for validation. It must be mentioned that the computational cases with ID 4, 5 and 6 are steady state computations, however they are validated based on transient outdoor experiments of section 4.2. Of course, the validation in this case is only approximate.

Table 5-8 Computational cases examined with the respective validation experiments

ID	No fan	Lower capacity fan	Higher capacity fan	Heated PV panel	Outdoor/ Indoor	
1	+			+	Indoor	Sec. 4.7.1
2		+			Indoor	Sec. 4.7.3
3			+		Indoor	Sec. 4.7.2
4	+			+	Outdoor	Sec. 4.2.2
5		+		+	Outdoor	Sec. 4.2.2
6			+	+	Outdoor	Sec. 4.2.2

Having established an acceptable degree of validation for the CFD computation cases, we now exploit the results towards the extraction of improved accuracy heat transfer coefficients. This is described in the next section.

Table 5-9 Velocity and Volumetric flow rate at outlet for the Computational cases

ID	Velocity at outlet [m/s]	Volumetric flow rate at outlet[m3/h]
1	2.68	118.2
2	2.63	116.1
3	4.70	207.6
4	3.03	133.9
5	3.15	139.1
6	5.13	226.3

5.5 CALCULATION OF LOCAL NU AND CONVECTION COEFFICIENTS FROM CFD RESULTS

Accurate knowledge of the heat transfer coefficients between the backsheet of the PV modules and the air flowing in the cavity is essential to the computation of both

the electrical performance of the modules and the thermal energy gains of the cavity.

As already discussed in chapter 2, there exist numerous correlations for the estimation of convection coefficients in the duct, both for the case of buoyancy flow (natural convection), as well as for the case of forced circulation of air in the cavity by use of fans (forced convection).

A comparison of the results of several correlations, for the range of Ra and Re numbers of interest in our case, is presented in Figure 5-10 (natural convection) and Figure 5-11 (forced convection).

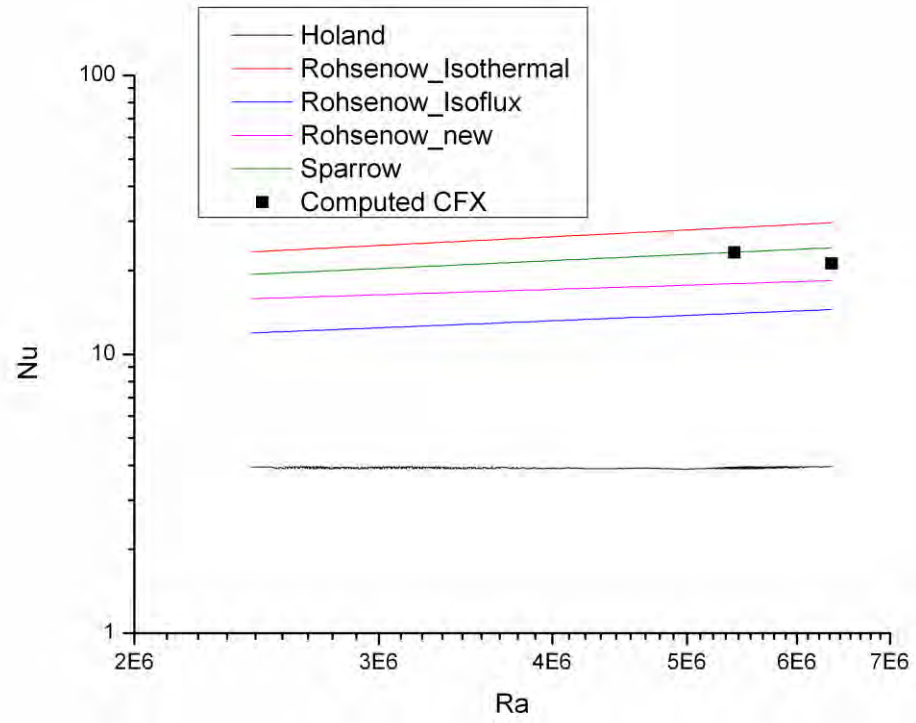

Figure 5-10 Natural convection: Comparison of the values of Nu determined by the measurements to those predicted by several well-known correlations from the literature.

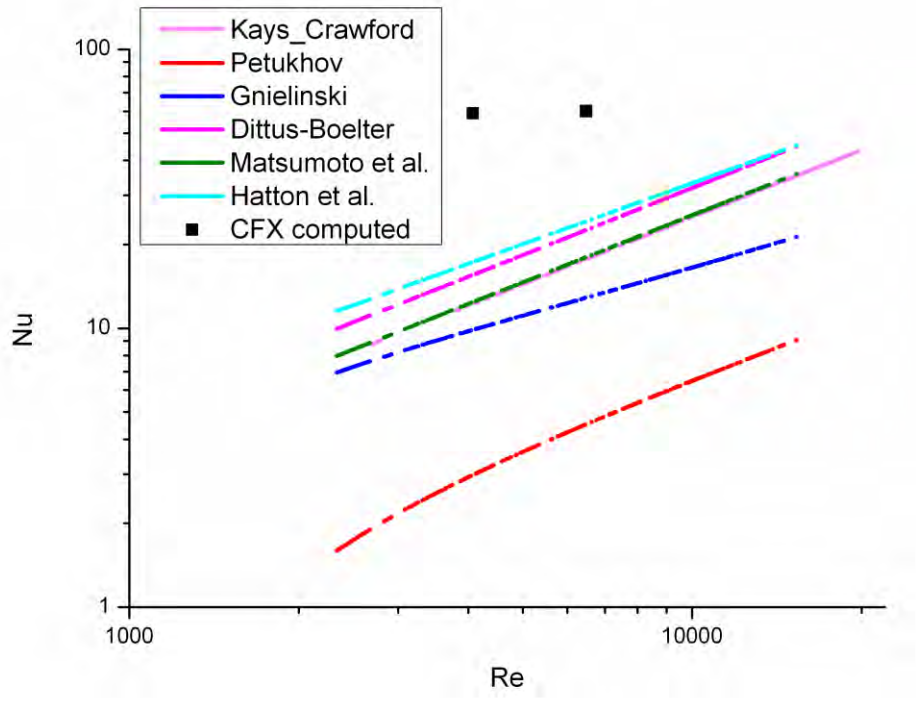

Figure 5-11 Forced convection: Comparison of the values of Nu determined by the measurements to those predicted by several well-known correlations from the literature.

It may be observed at a first glance that the range of Nu numbers predicted is extended, indicating an insufficient knowledge of the flow and heat transfer behavior of ducts in the transition flow regime which is associated with the specific geometry and flow rates.

For this reason, an important part of this thesis (Part A) was devoted to the better understanding of the flow and heat transfer inside the specific type of cavity. On the other hand, if we focus to the lower part of the Re numbers range and to air flows, better agreement among measured data and expressions is observed. In [90], heat transfer coefficients were measured for the unribbed rectangular channel and compared with correlations reported in the literature. Typically, the local distributions obtained are characterized by a gradual decay along the streamwise coordinate until a quasi-constant value (corresponding to the fully developed conditions) is reached. This value, recast in dimensionless form, compares well with the Nu number for a fully developed channel flow with asymmetric heating expressed by the equations (Figure 5-11)

$$Nu = 0.019\ Re^{0.8} Pr^{0.5}$$

$$Nu = 0.041\ Re^{0.727}$$

respectively taken from [89] and from numerical data presented in [163] for air (Pr=0.7). The measured heat transfer coefficients are in good agreement with the above correlations, despite the fact that, for the heated plate without ribs, the thermal boundary condition is not well controlled. Indeed, the finite thickness of the heated plate does not ensure the complete absence of thermal conduction along the wall, a condition required to assume uniform heat flux conditions at the wall/ fluid interface. This problem is alleviated at higher Re numbers.

Now, the results of the validated CFD computations can be exploited in the determination of more accurate Nu and convection coefficient for the specific cavity flow. Starting from the natural convection case, Figure 5-12 presents the computed wall heat transfer coefficient at the backsheet of the PV module. An average value of the order of h=3.7 W/m^2K can be calculated, which amounts to Nu=21 (also indicated for comparison on Figure 5-10.

The same type of CFD computation can be made for the forced ventilation case. The results are shown in Figure 5.14 (lower capacity fan) and Figure 5-15 (higher capacity fan). The dotted pattern seen in these Figures should be attributed to numerical noise that is due to the imperfect convergence of the ANSYS runs (see residuals evolution in Figure 5.13).

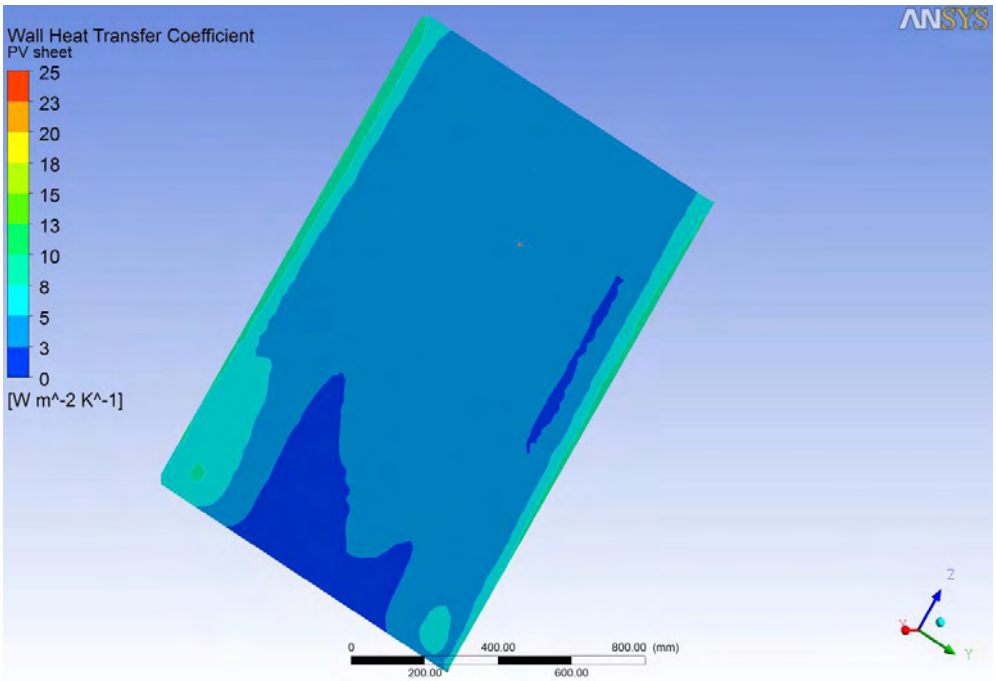

Figure 5-12 Wall heat transfer coefficient for the natural convection case

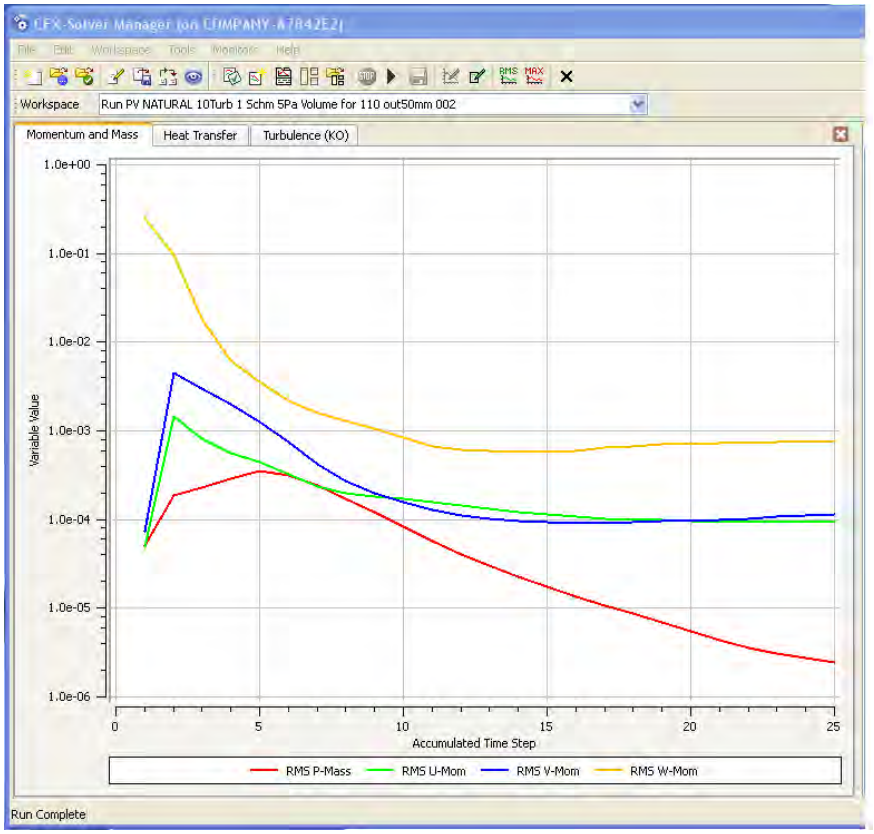

Figure 5-13 Evolution of residuals in Ansys-Cfx run for the lower capacity fan case (Fig.5-14)

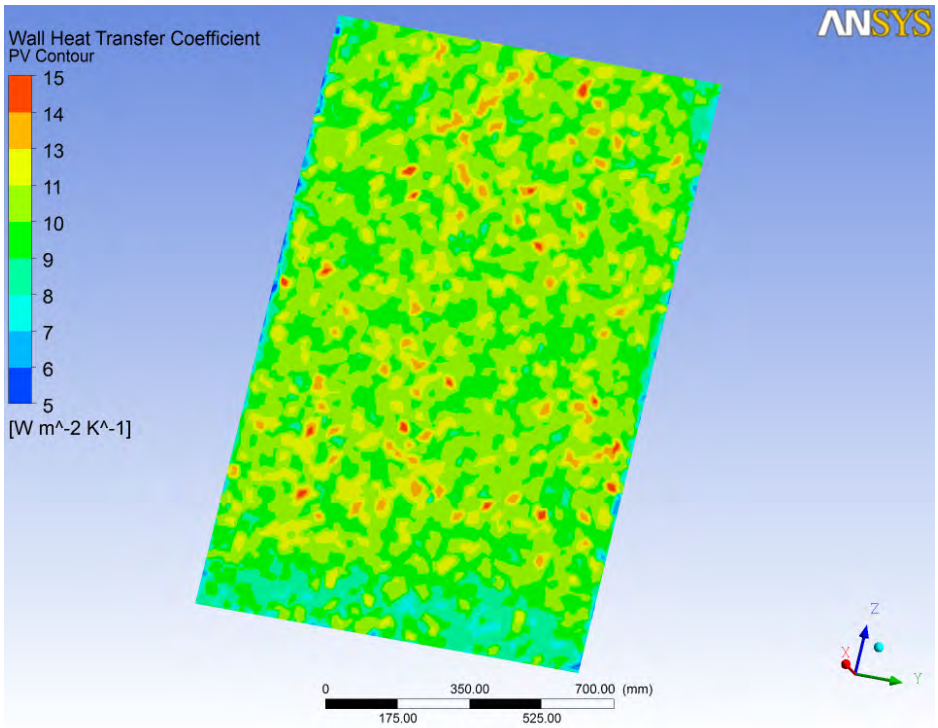

Figure 5-14 Wall heat transfer coefficient for the forced convection case by ANSYS-CFX (lower capacity fan)

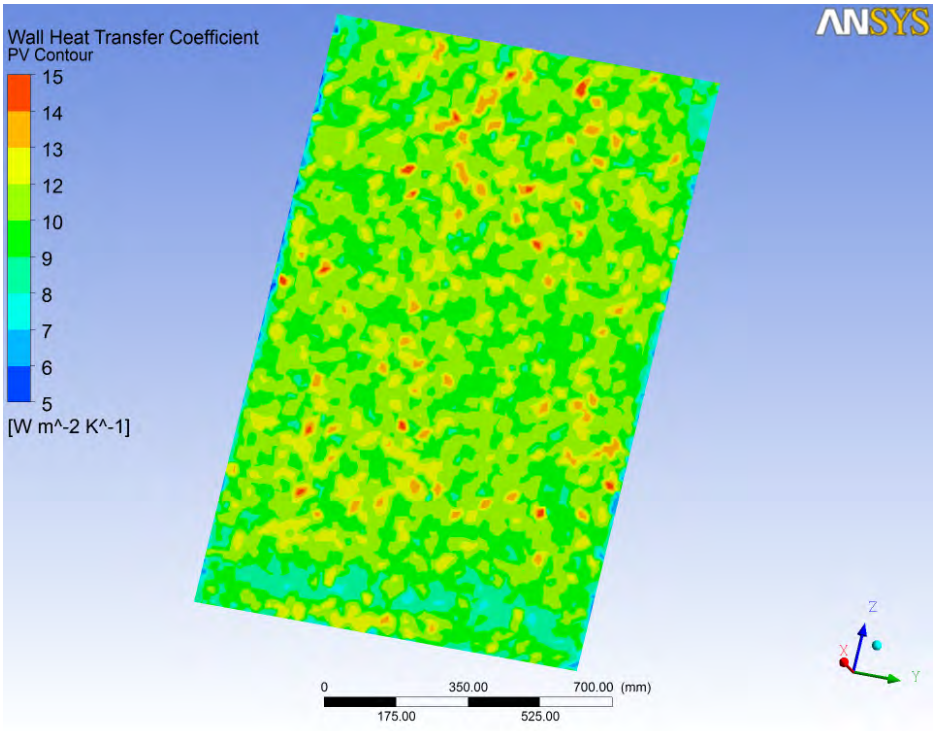

Figure 5-15 Wall heat transfer coefficient for the forced convection case by ANSYS-CFX (higher capacity fan)

Table 5-10 summarizes the range of variation of Re number in the cavity, in the 3 modes of operation (no fan, lower capacity fan, higher capacity fan).

Table 5-10 Comparison of local Re and Ra number ranges in the 3 modes

OUTDOOR EXPERIMENTS						
Mode	Re		Ra		Pr	Nu
	min	max	min	max		
Mode1	580	9700	2.43E+06	6.36E+06	0.71	23
Mode 2	2330	18400	-	-	0.71	59
Mode 3	2600	22000	-	-	0.71	60

INDOOR EXPERIMENTS						
Mode	Re		Ra		Pr	Nu
	min	max	min	max		
Mode1	600	2400	3.25E+06	5.63E+06	0.71	21
Mode 2	2268	4352	-	-	0.71	-
Mode 3	4637	7955	-	-	0.71	-

A comparison of the respective, computed average values of convection coefficients in the 3 PV cooling modes is presented in Table 5-11.

Table 5-11 Comparison of average values of wall heat transfer coefficients (3 cases)

	ID	Wall Heat transfer coefficient [W/m^{2}K]
Natural INDOORS	1	3.7
110 In	2	Isothermal experiment
190 In	3	Isothermal experiment
Natural OUTDOORS	4	4.1
110 Out	5	10.4
190 Out	6	10.6

One computation is made for the indoor test with heated PV panel (Figure 5-12), which results to an average value of 3.7 W/m^{2}K. The same computation for the respective outdoor test (different panel temperatures and air inlet conditions) gives h=4.1 W/m^{2}K. Significantly higher convection coefficients than those predicted by the routine forced convection correlations, are found for the outdoor tests with the low or the high capacity fan (10.4 and 10.6 W/m^{2}K respectively). The improved heat transfer coefficients are employed in the improvement of the respective correlations in the building energy simulation (next chapter).

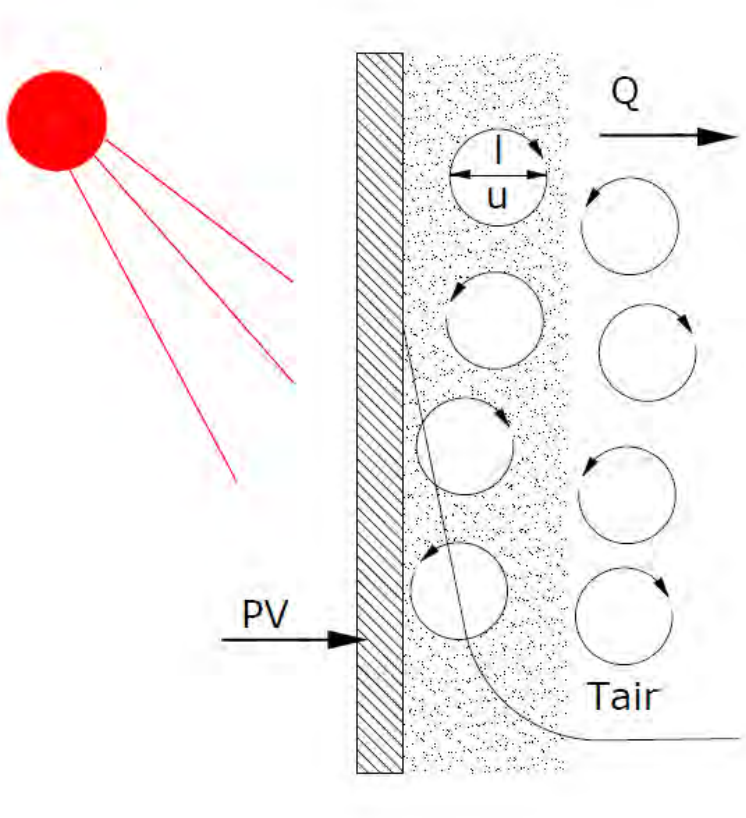

Figure 5-16 Correlation of thermometric diffusivity to velocity fluctuations (adapted from [164]).

In principle, it would also be feasible to extract rough estimations for the effect of the flow field on the value of the convection coefficient. To this end we may rely on the concept of thermometric diffusivity, as related to the most energetic eddy circumferential velocity (Figure 5-16).

The heat transfer rate from the PV backsheet to the heated air can be expressed as follows, by means of a thermometric diffusivity concept:

$$\gamma_{conv} = \rho\, c_p\, K_{conv} \approx \rho\, c_p\, u'\, l \quad (5.1)$$

$$Q_{conv} = A_{conv}\, \gamma_{conv} \left(\frac{\partial T}{\partial x}\right)_{conv} \quad (5.2)$$

On the other hand, we may simplify the calculation of the partial derivative as follows:

$$\left(\frac{\partial T}{\partial x}\right)_{conv} \cong \frac{T_{PV} - T_{air}}{l} \quad (5.3)$$

And thus we arrive at the following relation for the convective heat transfer rate:

$$Q_{dot} = A_{conv}\ \rho\, c_p\, u'\, l\, \frac{T_{PV} - T_{air}}{l} \cong A_{conv}\ \rho\, c_p\, u'\ \ T_{PV} - T_{air} \quad (5.4)$$

Thus we arrive at the following relation for estimating the convection coefficient as function of a characteristic turbulent velocity and a Stanton number:

$$h = St\, \rho\, c_p\, u' \quad (5.5)$$

This relation may be employed in cross-checking the results of Table 5.11 by taking into account the respective velocity fluctuation levels from Figures 4.45, 4.46 and 4.47 and making the assumptions of an indicative Stanton number St=0.25 for all three sets of indoor measurement cases.

The results are presented in Figure 5-17. As expected, the matching of indoor and outdoor measurement results is good for the free convection case, since the boundary conditions are similar (heated panel). On the other hand, the estimation of convection coefficients for the 110 m^3/h fan case falls well below the estimations from the CFD computations for the respective outdoor experiment. This is expected since the indoor experiment is a cold flow experiment that does not take into account the free convection from the heated panel. On the other hand, the estimation for the 190 m^3/h fan case matches well the respective estimations from

the CFD computations for the outdoor experiment. It seems that in higher Re numbers the phenomenon of forced convection prevails over the free convection.

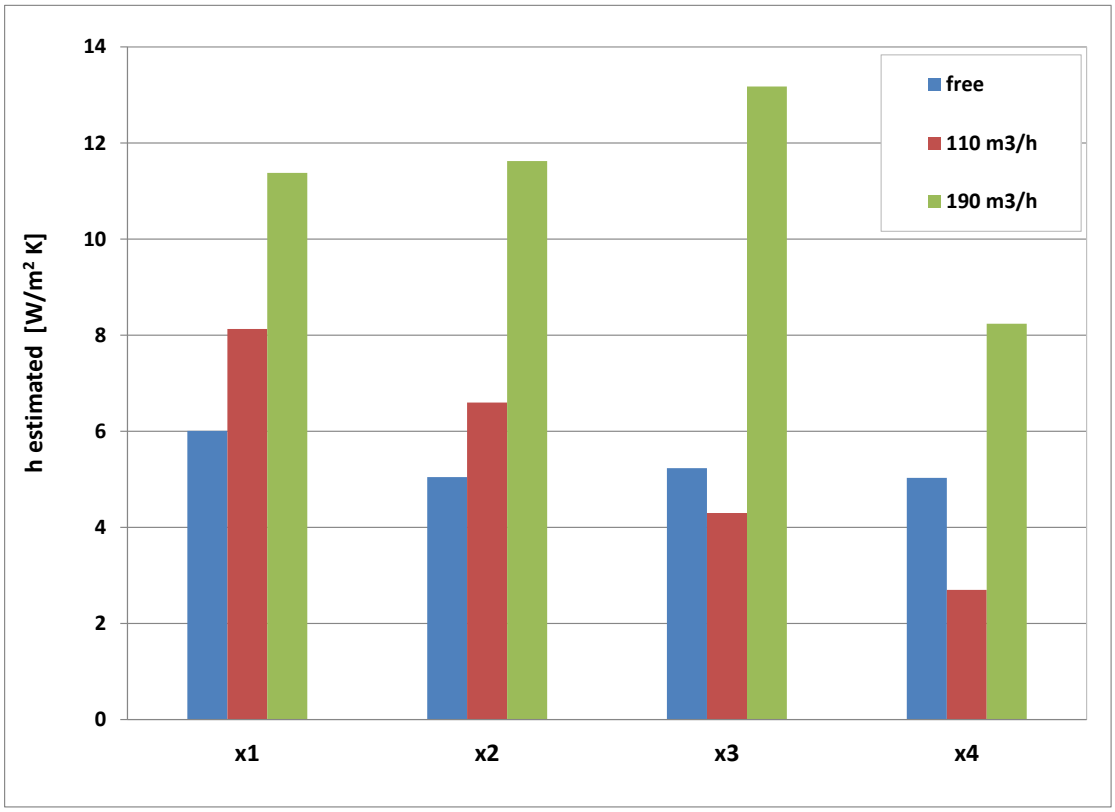

Figure 5-17 Estimation of local convection coefficients based on the hot wire anemometry measurements of velocity fluctuations. Assumption: Stanton number = 0.25 for all cases.

The results of this section led to the improvements of the heat transfer correlations to be employed in the TRNSYS simulations that are reported in the next chapter. Especially the correlations for the forced convection cases need to be significantly improved, to produce higher Nu number values that lump the influence of buoyancy forces that are also present in this complex flow situation.

5.6 Discussion of CFD results and estimation of heat transfer coefficients

The device was modeled in ANSYS CFX and 3D computations of the steady state flow field were produced, simulating the 3 modes of indoor hot wire anemometry experiments. The k-ω turbulence model was found more successful in matching the flow fields seen in the flow visualization. Specific improvements were made to the CFD computation boundary conditions in order to better predict the transient flow

regime. A moderately dense mesh of 1,200,000 tetrahedral elements and 203,000 nodes was applied to model the cavity.

The main findings are discussed below:

The numerical method along with the $k–\varepsilon$ and $k-\omega$ turbulence models considered in this study are capable of predicting average heat transfer and induced flow rate.

The value and distribution of turbulent kinetic energy at the inlet significantly affect the predicted heat transfer and induced flow rate considerably.

Correlating equations are developed for average Nusselt and Reynolds numbers from the experimental and numerical results in terms of dimensionless parameters.

Flow behavior in the forced convection mode (isothermal option of heat transfer model): The CFD computation predicts in a satisfactory way the flow field measured by the hot wire anemometry and the flow behavior observed in the flow visualization experiments. This happens despite the fact that we are in the transition flow regime, with relatively low Reynolds numbers prevailing. The boundary condition applied for the hood exit is a fixed pressure boundary condition: -15 Pa for the high capacity fan and -5 Pa for the low capacity fan respectively.

Flow behavior in the buoyancy flow mode (thermal energy option in the heat transfer model): The CFD computation is in good agreement with the hot wire anemometry results. The characteristic flow profile in the central vertical section across the depth of the channel with the two vertical velocity peaks observed in the hot wire anemometry measurements is correctly predicted.

Once tuned based on the indoor measurements, the CFD model was employed in the simulation of outdoor measurements. The results were validated against the results of the outdoor measurements. Thus, it was pointed out that the Nu calculation based on the CFD results is reliable.

The improved Nu and the respective wall heat transfer coefficient correlations are employed in the TRNSYS building energy simulation of the concept in the next chapter.

Moreover, the successful validation of the CFD computation is very important for the further optimization of the concept. Suggested improvements in the form of changes in the surface roughness or finned design of the backsheet of the PV panel may be assessed in advance by CFD computations.

Part B: Study of the building energy performance of the concept

CHAPTER

6

6 BUILDING ENERGY SIMULATION OF THE BIPV CONCEPT[2]

6.1 TRNSYS AS A BUILDING ENERGY SIMULATION SOFTWARE

TRNSYS is a transient systems simulation program with a modular structure that was designed to solve complex energy system problems by breaking the problem down into a series of smaller components. TRNSYS components (referred to as "Types") may be as simple as a pump or pipe, or as complicated as a multi-zone building model. The components are configured and assembled using a fully integrated visual interface known as the TRNSYS Simulation Studio, and building input data are entered through a dedicated visual interface. In the simulation studio, the user specifies the components that constitute the system and the manner in which they are connected. The simulation engine solves then the resulting set of algebraic and differential equations. In addition to a detailed multizone building model, the TRNSYS library includes components for solar thermal and photovoltaic systems, low energy buildings and HVAC systems, renewable energy systems, cogeneration, fuel cells, etc. The modular nature of TRNSYS facilitates the addition of new mathematical models to the program. In addition to the ability to develop new components in any programming language, the program allows to directly embed components implemented using other software (e.g. Matlab/Simulink, Excel/VBA, and EES). The TRNSYS library, written in Fortran source code, includes many of the

[2] A part of this chapter has been published as: Zogou O, Stapountzis H. Energy analysis of an improved concept of integrated PV panels in an office building in central Greece. Applied Energy. 2011;88:853-66.

components commonly found in energy systems, as well as component routines to handle input of weather data or other time-dependent forcing functions and output of simulation results. The software is well suited to detailed analyses of any system whose behaviour is dependent on the passage of time and has become reference software for researchers and engineers around the world. Main applications include: solar systems (solar thermal and photovoltaic systems), low energy buildings and HVAC systems, renewable energy systems, cogeneration, fuel cells. TRNSYS is one of the listed simulation programs in the recent European Standards on solar thermal systems (ENV-12977-2) and has passed the Building Energy Simulation Test (BESTEST) [165],[137]. The level of detail of TRNSYS' building model, known as "Type 56", is compliant with the requirements of ANSI/ASHRAE Standard 140-2001. The level of detail of Type 56 also meets the general technical requirements of the European Directive on the Energy Performance of Buildings [166]. During the last two decades, TRNSYS is widely employed in building energy systems simulations [11, 12, 28-30]. There exist systematic studies comparing the performance of this software against experimental results, as well as comparing the results of TRNSYS to other industry standards for building energy simulation [15, 31].

6.2 COMBINED PV/THERMAL SOLAR COLLECTOR MODEL

A sub model for the behavior of an integrated PV façade already exists in the TRNSYS environment. It has been developed by TESS [94]. The energy balance of the specific BIPVT concept is presented in Figure 2-10.

$$\mathbf{Q_{absorbed} + Power_{PV} = Q_u + Q_{loss,top,conv} + Q_{loss,top,rad} + Q_{loss,back}} \quad \textbf{(6.1)}$$

Where:

$Q_{absorbed}$ rate at which energy is absorbed by the collector (not including the energy absorbed and converted to electricity)

$Q_{loss,top,conv}$ rate at which energy is lost to the ambient through convection off the cover

$Ql_{oss,top,rad}$ rate at which energy is lost to the sky through radiation off the cover

$Q_{loss,back}$ rate at which energy is lost to the zone through the back of the collector

Q_u net rate at which energy is added to the flow stream by the collector

$$\mathbf{Q_{loss,top,conv} = h_{conv.top}\, Area(T_{PV} - T_{amb})} \quad \textbf{(6.2)}$$

$$\mathbf{Q_{loss,top,rad} = h_{rad.top}\, Area(T_{PV} - T_{sky})} \quad \textbf{(6.3)}$$

$$\mathbf{Q_{loss,back} = h_{conv.back}\, Area(T_2 - T_3)} \quad \textbf{(6.4)}$$

$$\mathbf{Q_{absorbed}} = \mathbf{Area}\ \alpha_{PV}\ G_T(1 - n_{PV}) \quad \textbf{(6.5)}$$

$$\mathbf{Power_{PV}} = \mathbf{Area}\ \alpha_{PV}\ G_T n_{PV} \quad \textbf{(6.6)}$$

Where:

G_T total incident solar radiation on the collector surface

$h_{conv,top}$ convective heat transfer coefficient from the top of the cover surface to the ambient air

α_{PV} absorptance of the PV surface

n_{PV} efficiency of the PV cells as a function of the cell temperature and the incident radiation

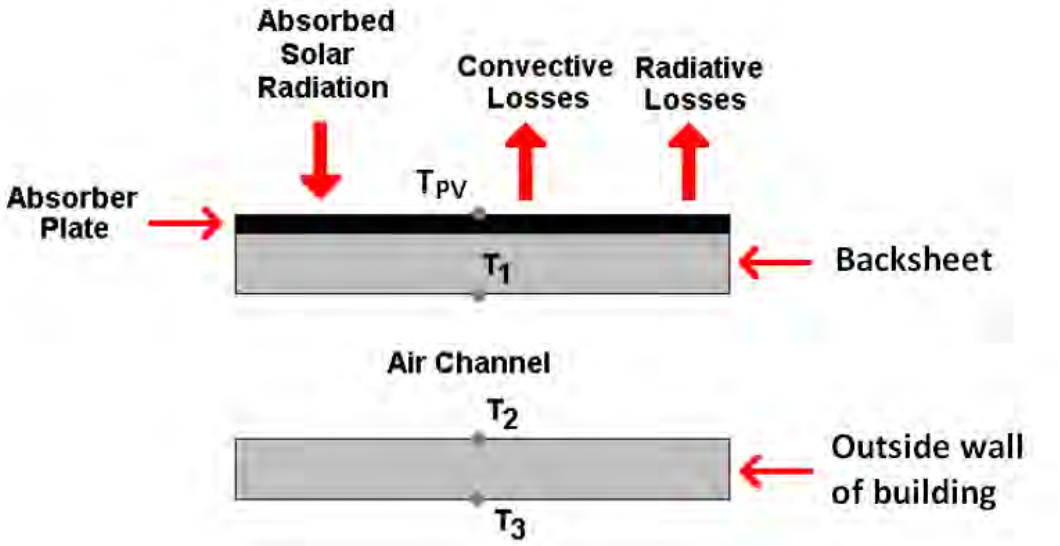

$$S = h_{conv,top}\ T_{PV} - T_{amb}\ + h_{rad,top}\ T_{PV} - T_{sky}\ + \frac{T_{PV} - T_1}{R_2} \quad (6.7)$$

Figure 6-1 Energy balance components on the PV module

Where :

S the absorbed solar radiation minus the electricity production of PV cells.

R_2 is the resistance to heat transfer from the surface of the PV cells to upper surface of the channel.

$$h_{rad,top} = \varepsilon_{PV}\ T_{PV} + T_{sky}\ \ T_{PV}^2 + T_{sky}^2 \quad \textbf{(6.8)}$$

Where :

$h_{rad,top}$ radiative heat transfer coefficient from the top of the cover surface to the sky

ε_{PV} absorptance of the PV surface

For the fluid convection correlations we have three special cases:

(i) No forced air flow through the channel Re = 0 and the Nusselt number is based on free convection on the relationship of Hollands et al [95, 167], equation (2.20).

(ii) The air flow through the channel is laminar (Reynolds number <2300).

Then a constant surface temperature heat transfer correlation is utilized: Nu = 3.66.

(iii) The air flow through the channel is turbulent. (Reynolds number >2300) then a corrected version of the well-known Dittus-Boelter heat transfer correlation is utilized:

$$\mathbf{Nu = 0.023 * Re^{0.8} * Pr^{n}} \quad \textbf{(6.9)}$$

with n = 0.4 whenever the plate is warmer than the fluid and n = 0.3 when the plate is cooler than the fluid. In the corrected version, the constant of the above equation is doubled from 0.023 to 0.05, in order to take into account the increased Nu numbers reported from the measurements and computations of the previous chapter, that are due to the coexistence of natural convection along with the forced convection in the vertical channel.

Then the fluid convection coefficient h can be calculated:

$$\mathbf{h = \frac{Nu * k}{D_h}} \quad \textbf{(6.10)}$$

An existing model in the TESS package, namely, Type 568: Un-glazed Building Integrated Photovoltaic System (Interfaces with Type56) has been employed as a basis for the BIPV system simulation.

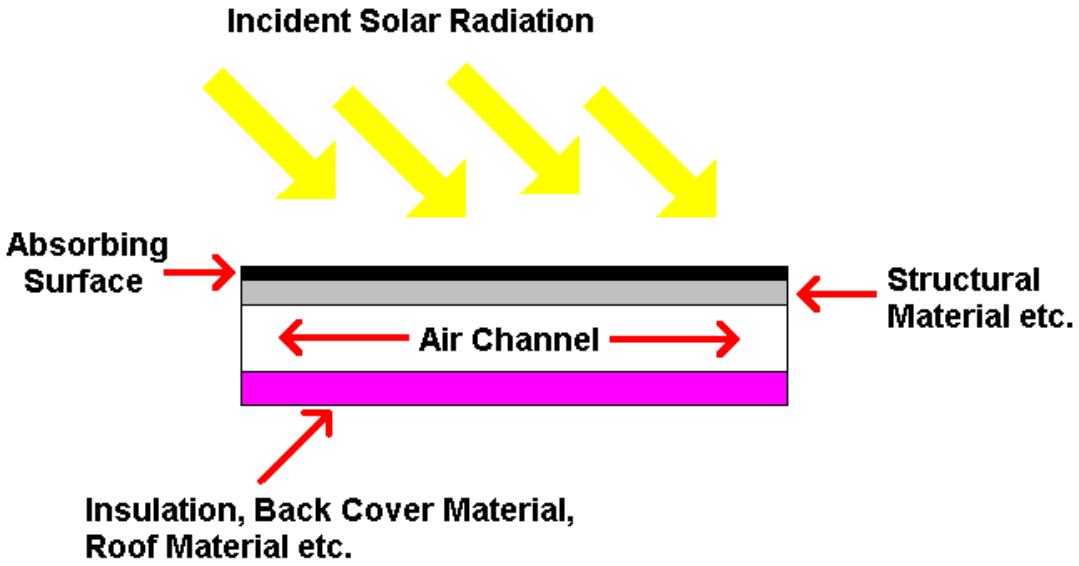

Figure 6-2 PV/T Schematic of Type 568 and Type 569 of TESS library

This component is intended to model an un-glazed solar collector that has the dual purpose of creating power from embedded photovoltaic (PV) cells and providing heat to an air stream passing beneath the absorbing PV surface. The waste heat rejected to the air stream is useful for two reasons;

- it cools the PV cells allowing higher power conversion efficiencies and
- it provides a source of heat for many possible low-grade temperature applications including heating of room air.

Type 568 is intended to operate with detailed building models that can provide the temperature of the back surface of the collector (zone air/collector back interface) given the mean surface temperature of the lower flow channel. The Type 56, multi-zone building model, in TRNSYS is one of these detailed zone models. Instructions for connecting this model to a Type 56 building can be found later in this document.

The thermal model of this collector relies on algorithms supplied in “Solar Engineering of Thermal Processes” Duffie and Beckman [147] and the fluid convection calculations provided by “Introduction to Heat Transfer” by Incropera and Dewitt [168] .

As explained in section 5.5, the improved understanding of the heat transfer behavior inside the cavity that resulted from the experiments and computations of

Part A, led to an improvement in the heat transfer coefficient expressions for the specific case

6.3 DETAILS OF THE BUILDING ENERGY SIMULATION

A typical office building (see Figure 3-5) will be studied. Eight vertical bands of PV modules with the characteristics of Table 6-1 are installed on the south façade of the building, that is, a total of 48 PV modules with an area of about 72 $m^2$and a total rated power of 9.84 kW. An air flow rate of 110 m^3/h (133 kg/h) in the duct behind the modules is adequate to cover the ventilation needs. It needs to be tested if this flow rate sufficiently cools the PV panels. An increased air flow of 330 m^3/h (400 kg/h) is also comparatively assessed.

Table 6-1 The basic technical data for the PV modules (Kyocera KD 205GH)

DIMENSIONS		
LxWxD=990*1500*150 [mm]		
ELECTRICAL PERFORMANCE		
At 1000 W/m^2 (STC)	Unit	
Maximum Power	[W]	205
At 800 W/m^2 (NOCT)		
Maximum Power	[W]	145
NOCT	[^{o}C]	49
Temperature Coefficient of Voc	[V/^{o}C]	-1.20*10^{-1}
Temperature Coefficient of Isc	[A/^{o}C]	5.02*10^{-3}
Temperature Coefficient of Max Power	[W/^{o}C]	-9.43*10^{-1}
Reduction of Efficiency (from 1000W/m^2 to 200 W/m^2)	[141]	6
PV CELLS		
Number per module	54	
Cell Technology	Multicrystalline	
Cell shape	156*156 [mm]	

The reference building is located in Volos, Greece (latitude 39.390N, longitude 22.940E). The TMY employed in this study has been approximated based on the methodology presented in [169]. The monthly meteorological data of the Greek National Meteorological Agency pertaining to the city of Volos for the period 1956-1988, as well as the period 1996-2006 are presented in Figure 6-3.

The office building consists of a basement, ground level and three upper levels (floor area 162.75 m^2). Its rectangular shape is elongated along the E-W axis. Each level consists of seven zones, in order to better study the effect of orientation. For example, the first floor (see Figure 6-4) involves Zone_1.1, Zone_1.2, Zone_1.3, Zone_1.4, Zone_1.5, Zone_1.6 and Zone_1.7. The first number indicates the floor and the second the zone. Zone_1.7 consists of 4 offices and the reception room. Each floor has 10 offices (12.25m^2 each) and one reception room (40.25m^2). The characteristics of the building shell and windows are summarized in Table 6-2 and Table 6-3.

According to legislation, Greece is divided into four climatic zones. Each zone is subject to specific requirements for U-value (Table 6-4) and the energy consumption shall not exceed reference consumption according with the usage of the building.

The building materials and insulation thickness are assumed to follow the current Greek building standards and common practice. However, the wall behind the PV modules in the double façade is very well insulated with 10 cm polystyrol panel, in order to protect the interior of the building from overheating during the summer.

The following building operation schedule was assumed: Daily schedule 07:00 – 17:00 (Monday to Friday). The room thermostat controls zone temperature to 21^oC with a tolerance of ±1^oC for winter season and to 26^oC (tolerance of ±1^oC) for summer season.

Energy consumption for lighting is estimated at 15 W/m^2 plus 5 kWh/(m^2y) for parasitic control in accordance with PrEN 15193 [170]. Each office room (zones 1-6) is equipped with 1 personal computer and 1 printer and zone 7 (reception room) is equipped with 7 computers and 2 printers respectively with occupant density in accordance with prEN 13779 [171]. As regards the ventilation, 0.84 Air Changes per Hour (ACH) are assumed, a figure which surpasses the requirements of prEN 15251 [172] which correspond to 0.7 l/s m^2.

A flowchart summarizing the simulation model in the TRNSYS, release 16 environment is presented Figure 6-5. The way of interaction of the sub model for the heat transfer in the duct behind the modules discussed in the previous section is also shown in this figure.

The effect of installing PV panels to the south facing wall of the building is studied by performing simulations for the reference case and for three alternative building integrated photovoltaic configurations that are summarized in Table 6-5.

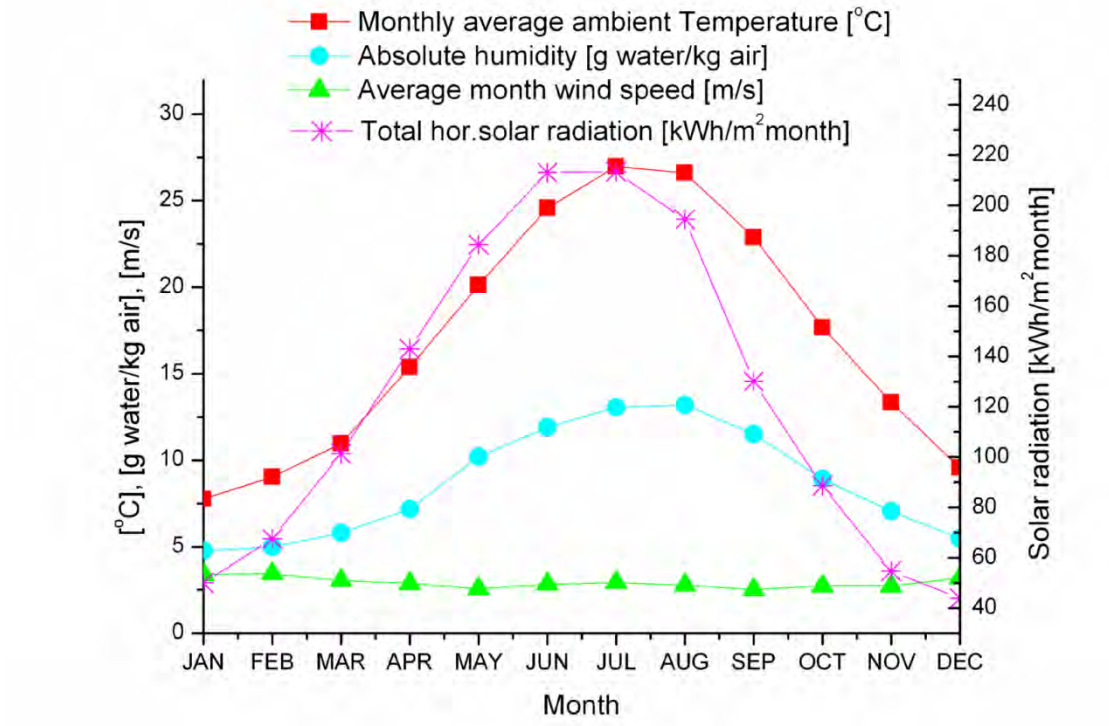

Figure 6-3 Characteristics of climatic conditions in the city of Volos

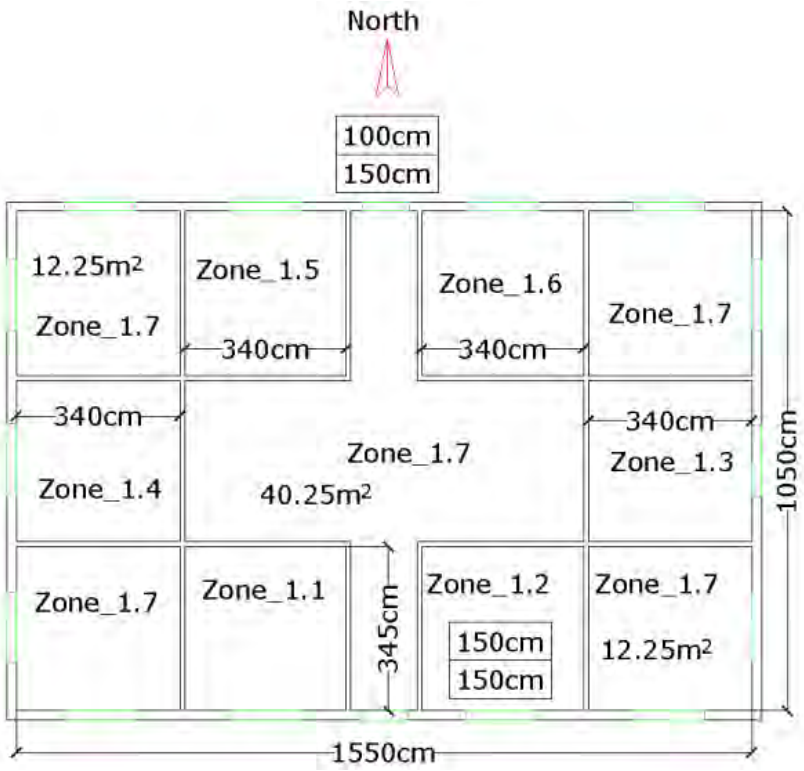

Figure 6-4 Typical (1st) floor layout of the building employed in the simulation.

Table 6-2 Insulation data for the building envelope

Building shell component	Total thickness [m]	U-value [W/m^{2}K]	Layers	Layer thickness
Floor, basement	0.325	0.692	Ceramic tiles	0.005
			Plaster	0.020
			Reinforced concrete B240	0.250
			Polystyrol insulation	0.050
Floor, office space	0.295	2.916	Ceramic tiles	0.005
			Plaster	0.020
			Reinforced concrete B240	0.250
			Plaster	0.020
Walls, outside building shell	0.290	0.497	Plaster	0.020
			Brick	0.090
			Polystyrol insulation	0.070
			Brick	0.090
			Plaster	0.020
Walls, behind PV panels	0.370	0.363	Plaster	0.020
			Brick	0.250
			Polystyrol insulation	0.100
Walls, inside	0.130	3.058	Plaster	0.020
			Brick	0.090
			Plaster	0.020
Roof	0.390	0.406	Plaster	0.020
			Reinforced concrete B240	0.250
			Polystyrol insulation	0.050
			Plaster	0.020
			Deck tiles	0.050
Frame, inside beams	0.290	2.952	Plaster	0.020
			Reinforced concrete B240	0.250
			Plaster	0.020
Frame, inside walls	0.24	3.182	Plaster	0.020
			Reinforced concrete B240	0.200
			Plaster	0.020
Frame, outside	0.315	0.500	Plaster	0.020
			Reinforced concrete B240	0.200
			Polystyrol insulation	0.075
			Plaster	0.020
Doors, inside	0.05	1.808	Processed wood chips	0.050

Table 6-3 Characteristics of window (including Aluminum frame)

Window type	Common double air
Glazing system	SOLAR E 4.LOF, 6 mm Air, Clear_4.LOF
U*	2.532
U**	3.850
g-value	0.477
τ_{sol}	0.380
Rsol	0.092

Table 6-4 U-Value for the four climatic zones

	Floor	Roof	Wall	Window
	$U_{F\,(}Wm^{-2}K^{-1}_{)}$	$U_{R\,(}Wm^{-2}K^{-1}_{)}$	$U_{W\,(}Wm^{-2}K^{-1}_{)}$	$U_{Win\,(}Wm^{-2}K^{-1}_{)}$
A climatic zone	≤ 1.20	≤ 0.50	≤ 0.60	≤ 3.20
B climatic zone	≤ 0.90	≤ 0.45	≤ 0.50	≤ 3.00
C climatic zone	≤ 0.75	≤ 0.40	≤ 0.45	≤ 2.80
D climatic zone	≤ 0.70	≤ 0.35	≤ 0.40	≤ 2.60

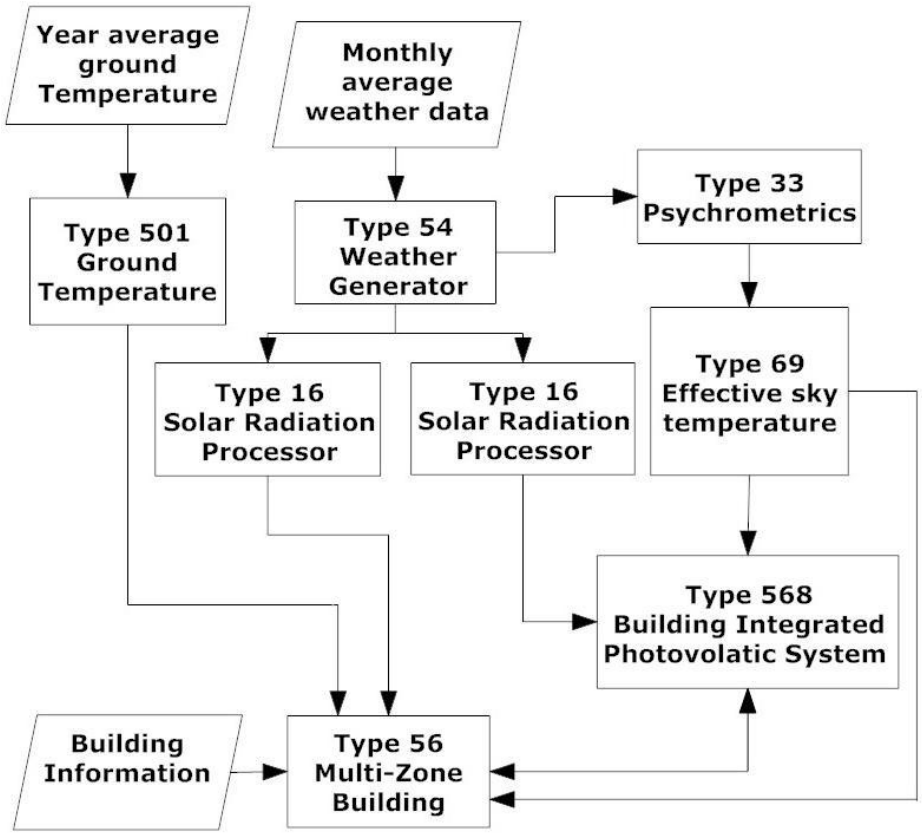

Figure 6-5 Diagram of building simulation in the TRNSYS environment.

Table 6-5 Simulation Cases

Reference case	Building without PV panels
Case 1	Building with PV panels in contact with the south facing walls (above the ground floor).
Case 2	Building with PV panels in south walls: double façade, with 0.15m air gap: air flow rate 133 kg/h
Case 3	Building with PV panels in the south walls: double façade with 0.15m air gap: air flow rate 400 kg/h
Case 2-1	Building with PV panels in south walls: double façade, with 0.15m air gap: air flow rate 133 kg/h and ***corrected convection coefficient h***
Case 3-1	Building with PV panels in the south walls: double façade with 0.15m air gap: air flow rate 400 kg/h and ***corrected convection coefficient h***

The transient behavior of the following system's performance variables are of interest in these simulations:

- Typical zone temperature
- Instantaneous zone heating and cooling loads
- backsheet temperature of modules
- electricity produced by the modules
- electricity consumed by the fans

6.4 SIMULATION RESULTS

6.4.1 TRANSIENT BEHAVIOR OF THE AIR IN THE DUCT AND PV EFFICIENCY

Comparative results of the hourly simulation of the reference case along with cases 1, 2 and 3 are presented in Figure 6-6 and Figure 6-9.

Figure 6-6 presents a comparison of the predicted backside panel temperature in the highest section of the duct, that is, behind the top PV module (3rd floor), for the case

[1-3] (see Table 6-5), during a typical week of the heating season. The predicted electricity generation from the PV panels with the limited cooling air flow rate (case 2) is also presented in the same figure. It may be observed in this figure that the PV backside temperature is lowest in case 3, where the flow rate is maximized. That is, case 3 is expected to result in the highest PV efficiency. However, since the duct system is also exploited to cover the space ventilation and part of the heating loads, case 2 is optimized for this objective. In the following, we examine if the case 2 design is a good compromise between these two design objectives.

A close inspection of Figure 6-6 indicates that with case 3 the backside of the highest PV panel has a maximum temperature reduction of 13 ^{o}C over case 1 (not cooled PV panels). If we inspect the respective results for the rest of the year, we observe a maximum temperature reduction of 19 ^{o}C [62].

Obviously, the cooling effect is more enhanced for the lower PV panels, as they are cooled by colder air. A yearly maximum of 20^{o}C in the temperature reduction of the lowest panels is observed over case 1. For comparison, the respective temperature reductions attained with the compromised case 2 over case 1, are about 50% lower for the highest PV panels (see for example Figure 6-7). This is the penalty we must pay for the limiting of the PV cooling air flow rate that is necessary to cover the HVAC system's needs.

Following the improvement in the heat transfer coefficients correlation, additional TRNSYS simulations were carried out, to compute the effect to the backsheet temperature of the PV modules for case 2-1 and case 3-1.

It should be mentioned that the electricity consumption of the air circulation fans is not included in the simulation. This was decided based on a rough calculation, as follows: There exist 8 vertical sheets of PV panels in the modeled building. One fan is needed for each one of the cavities formed behind the modules. Since the required flowrate is of the order of 180 m^3/h (see calculations in chapter 3) and the necessary pressure head does not exceed 100 Pa (because of the favourable chimney effect in the cavity behind the heated panels), the theoretical power required would be of the order of 5W for each one of the 8 fans. If we count on common efficiency values for this class of AC shaded pole induction motors (see Table 6-6) that do not exceed 30% and a fan flow efficiency of the order of 80% then the required power consumption for each fan would be 20 W, that is, a total of 160 W electricity consumption should be included in the system's energy balance. This value could be halved to about 80W if we employed highly efficient split phase or permanent split capacitor electric

motors (see Table 6-6). This figure can be neglected if compared to the average electricity produced by the PV panels which is in the range of kW (Figure 6-6).

Table 6-6 Comparative Efficiency of small AC motors (adapted from [173]).

Power range	Efficiency [ ] Shaded-pole motor	Efficiency [ ] Split phase motor	Efficiency [ ] PSC motor
1W	0.1	-	-
10 W	0.22-0.30	0.40-0.50	0.35-0.45
50 W	0.30-0.35	0.50-0.60	0.45-0.55
100 W	0.32-0.40	0.60-0.70	0.60-0.70

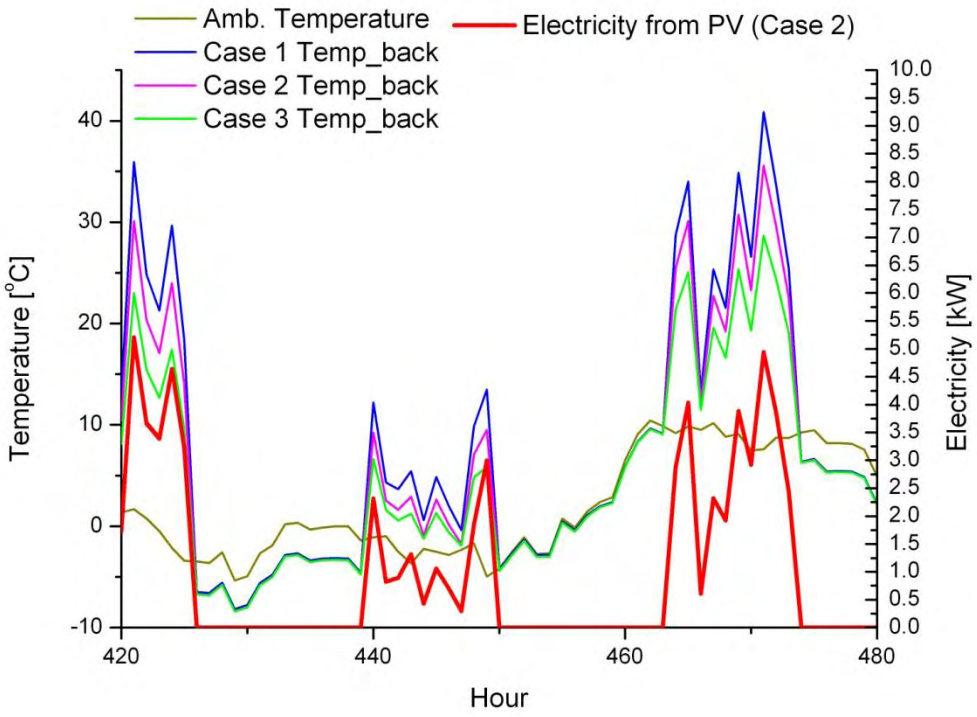

Figure 6-6 Typical variation of the backsheet temperature of the highest PV panels during the heating season and electricity production for case 2

The corrected predictions of hourly backsheet temperatures of the highest PV panels (Figure 3-5) during the coldest week in winter season are presented in Figure 6-7 for case 2-1 and 3-1 (corrected) versus case 2 and case 3. For case 2, the maximum temperature correction was only 1 ^{o}C and for case 3 it reached 4 ^{o}C (see Figure 6-7 and Figure 6-8). The maximum corrections in temperature are observed during the winter season, when the air enters the cavity with the lowest temperatures.

According to the improved simulation, a yearly maximum of 10^{o}C temperature reduction of the lowest panels of case 2-1 was computed over case 1. The respective

prediction for case 3-1 over case 1 is a reduction of 23°C in the temperature of the lowest panels. Obviously, the air flow past the PV panels significantly reduces their temperature.

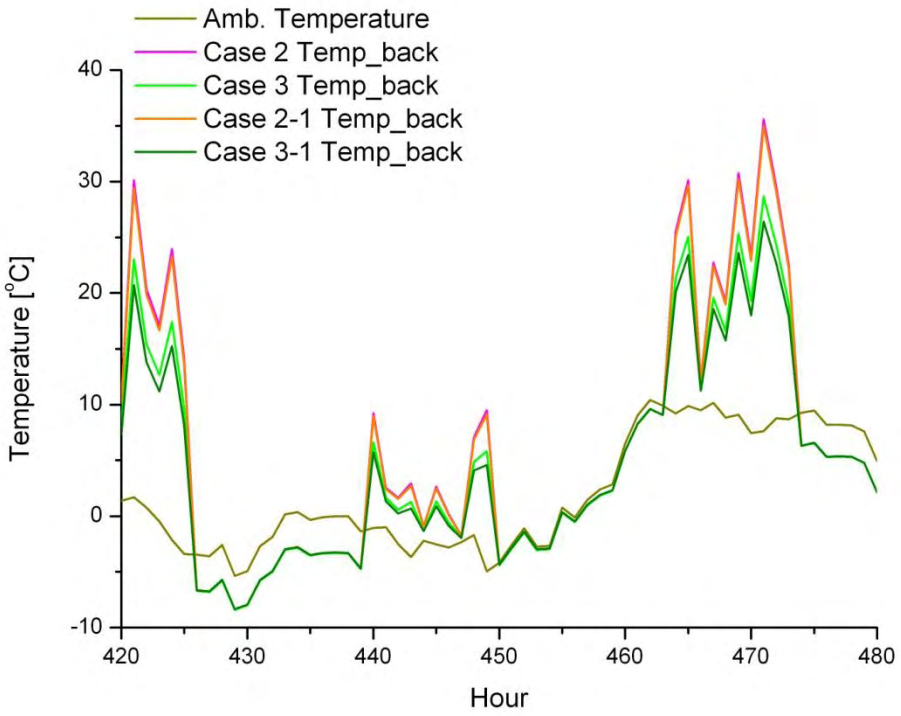

Figure 6-7 Typical variation of the backsheet temperature of the highest PV panels during the heating for case 2-1 and 3-1 with corrected convection coefficient.

Figure 6-9 presents a comparison of the predicted zone temperatures with cases 1, 2 and 3, against the reference case (Table 6 5), during the same (coldest) week of winter (-5 °C lowest ambient air temperature).

When PV panels are installed, (cases 1-3), the air zone temperature drops at a slower rate after the heating is shut-off. This is explained by the additional insulation layer introduced by the PV panels and the air space in-between. It is known that for a single air space, the minimum heat conductance is typically reached with an air space of 0.6 to 2.0 cm. Once the boundary layer regime has been reached, further increase in air space thickness results to little or no decrease in conductance as mentioned in [49].

One can observe that in all 3 cases with a PV façade, the zone temperature without heating is about the same. That is, the existence of the air duct with air flowing in it, does not significantly affect the building shell losses. This can be explained because of the high insulation placed on the inside of the duct.

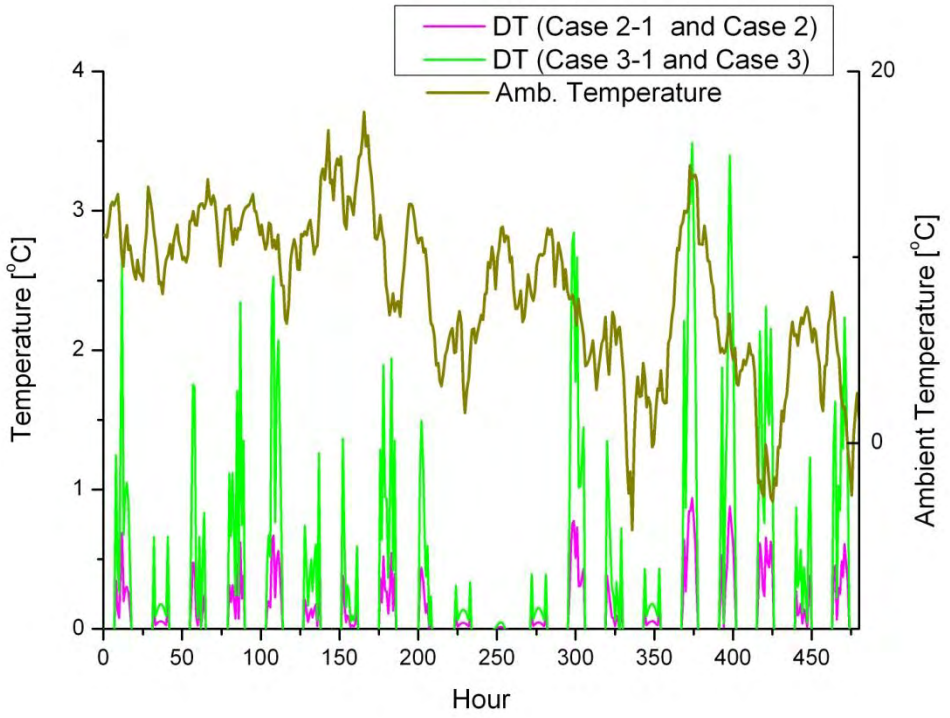

Figure 6-8 Corrections in the predicted hourly temperature variations by the use of the improved heat transfer correlations (cases 2 and 3).

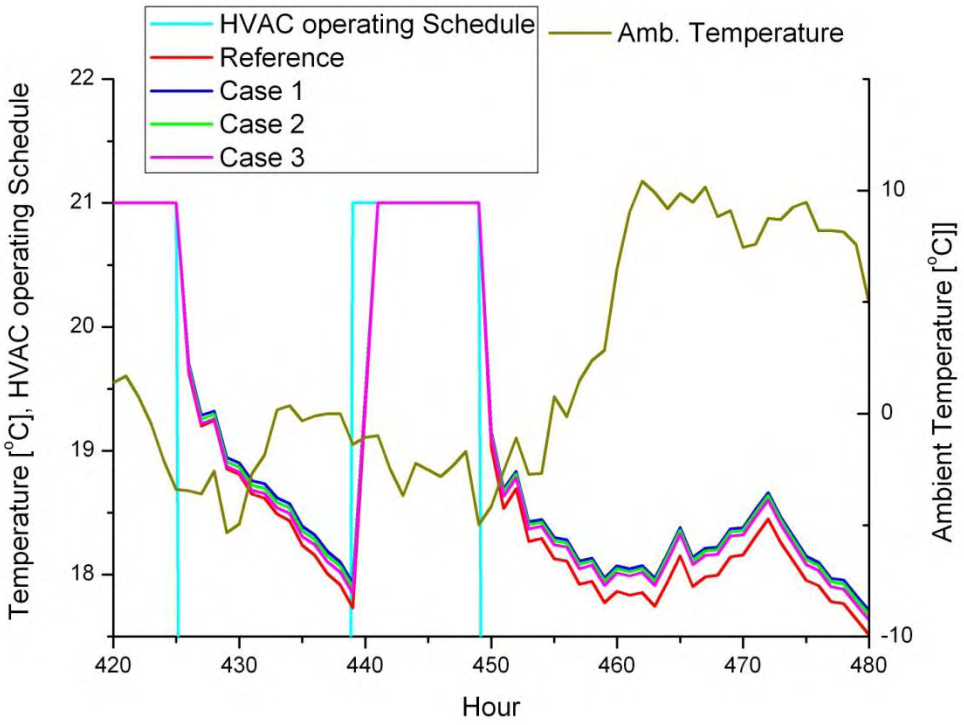

Figure 6-9 Effect of 3 different modes of installation of the BIPV panels to the variation of zone 3.1 temperature during the winter season

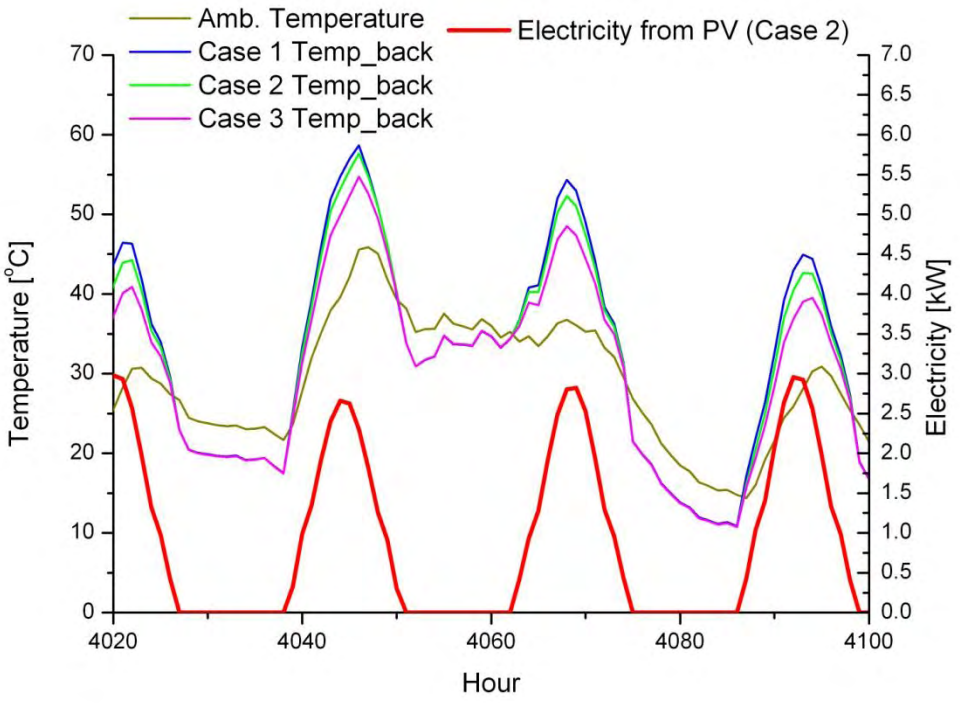

Figure 6-10 Typical variation of the backsheet temperature of the highest PV panels and electricity production during the cooling season (case 2)

Figure 6-10 gives some insight in the behavior of the system during the cooling season (the hottest week of the summer). A comparison of the predicted backside panel temperature in the highest section of the duct, that is, behind the top PV module (3rd floor) for the four cases is presented. The predicted electricity generation from the PV panels (case 2) is also presented in the same figure. Again, the PV backside temperature is significantly reduced between case 1 (not cooled) and case 3 (highest flow rate). As regards case 2, with the limited flow rate, its cooling effect is significantly reduced whenever the ambient temperature levels exceed 40 ^{o}C. Obviously, the cooling effect significantly improves the PV panels' efficiency during the summer, especially with the higher flow rate of case 3. As can be seen in Figure 6-11, the temperature difference for case 3-1 and case 3 is higher than the case with the limited flow rate, like in winter season.

As regards the zone temperatures, the same observations apply as with the heating season. The additional insulating effect of the double façade is favorable to the building's thermal behavior. Moreover, the existence of the vertical ducts behind the PV panels in cases 2-1 and 3-1, allows for alternative night cooling strategies that can significantly reduce the cooling energy requirements of the building.

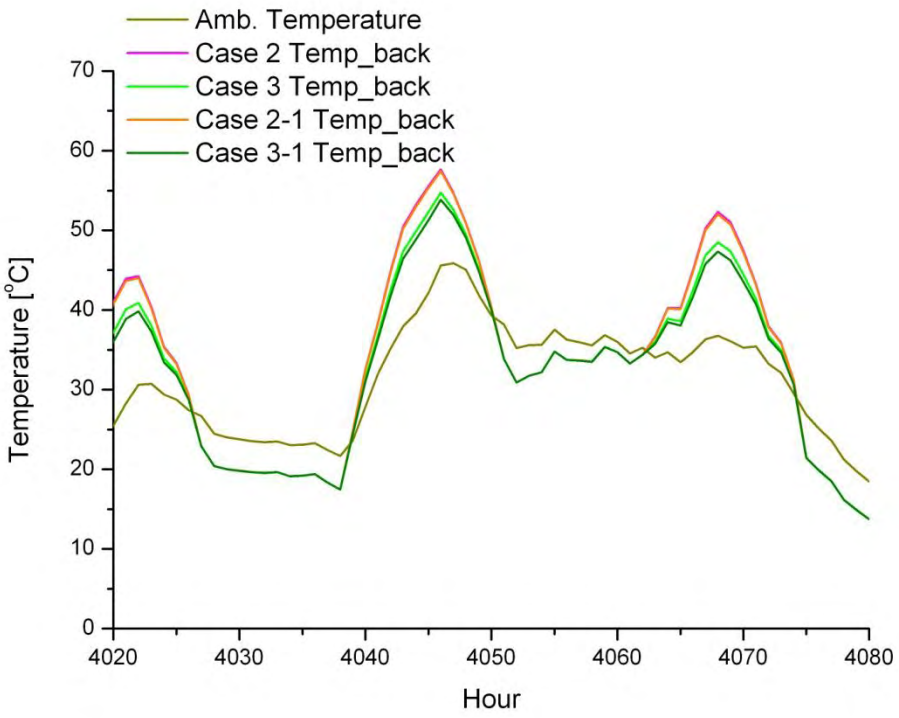

Figure 6-11 Variation of the backsheet temperature of the highest PV panels during the cooling season (case 2-1)

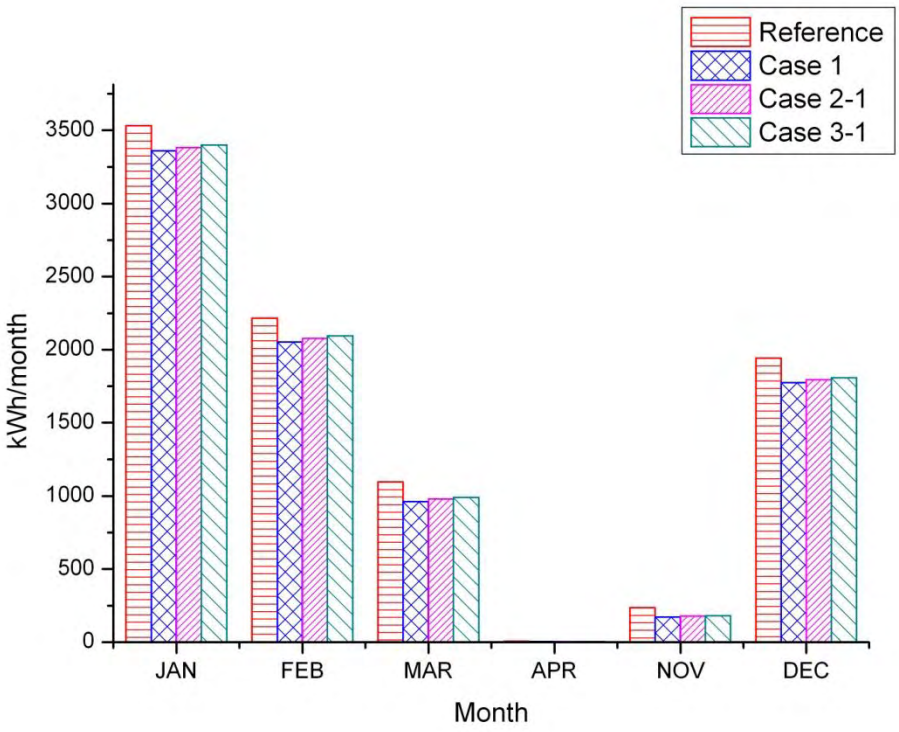

Figure 6-12 Variation of the monthly heating load of the building

The overall effect on the heating and cooling loads is comparatively presented for the four cases in Figure 6-12 and **Figure** 6-13 respectively.

The installation of PV modules slightly reduces the heating load for case [1, 2-1, 3-1] compared to the reference case. On the one hand, the PV panels and air layer offer extra insulation, but on the other hand the same panels obstruct solar radiation (solar gains). In case 3-1 the heating load is increased, presumably due to the forced introduction of a higher flow rate of cold outdoor air in the vertical ducts between PV panels and buildings walls. This air flow cools the external wall.

The effect on the cooling load of the building is also of interest. The cooling load in case 1 and case 3-1 increases about 6% and 4%, respectively, compared to the reference building. In case 2-1 the increase is 5%. This should be attributed to the convection from the air flow in the ducts behind the PV panels [19]. But there exist also opportunities to gain from the process. During the day, the outdoor air driven through the ducts is heated to high temperatures and its enthalpy could be exploited for producing domestic hot water by means of a tank-type air to water heat exchanger or an air source heat pump water heater. The existence of the vertical ducts may be also exploited for night cooling of the building when the outside air temperature is lower than the inside air temperature.

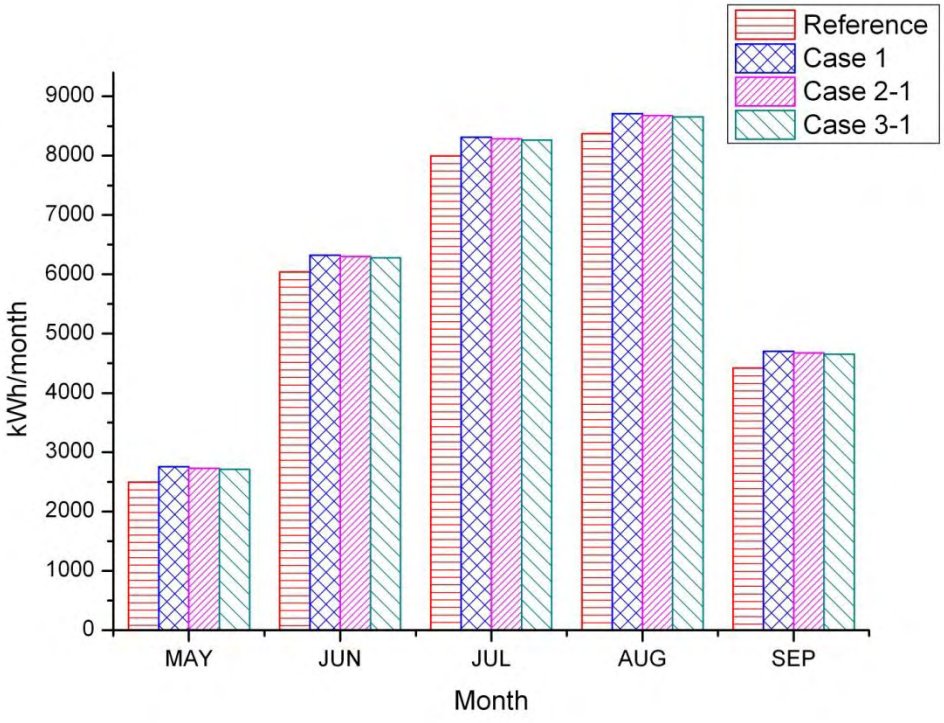

Figure 6-13 Variation of the monthly cooling load of the building

6.4.2 COMPARATIVE BUILDING ENERGY SIMULATION RESULTS

An overall PV electricity production balance is presented in Figure 6-14 and Figure 6-15. The results of this figure indicate that the air flow behind the PV panels certainly improves the electricity production during the summer months, because in summer the backside temperatures of the panels are high and the air flow significantly cools the panels.

For case 2-1 the yearly electricity production is predicted to be 2 % higher than case 1 (not cooled PV panels). For case 3-1, which has an improved cooling effect, the electricity produced is 4% higher than the base case 1 [65]. According to these calculations, it may be necessary to increase (say, double) the duct air flow rates during the summer, to improve the cooling of the PV panels. This problem is due to the increased ambient temperature during the summer period in low latitude countries, which limits the PV cooling potential by ambient air that is already at 40^{o}C or even higher.

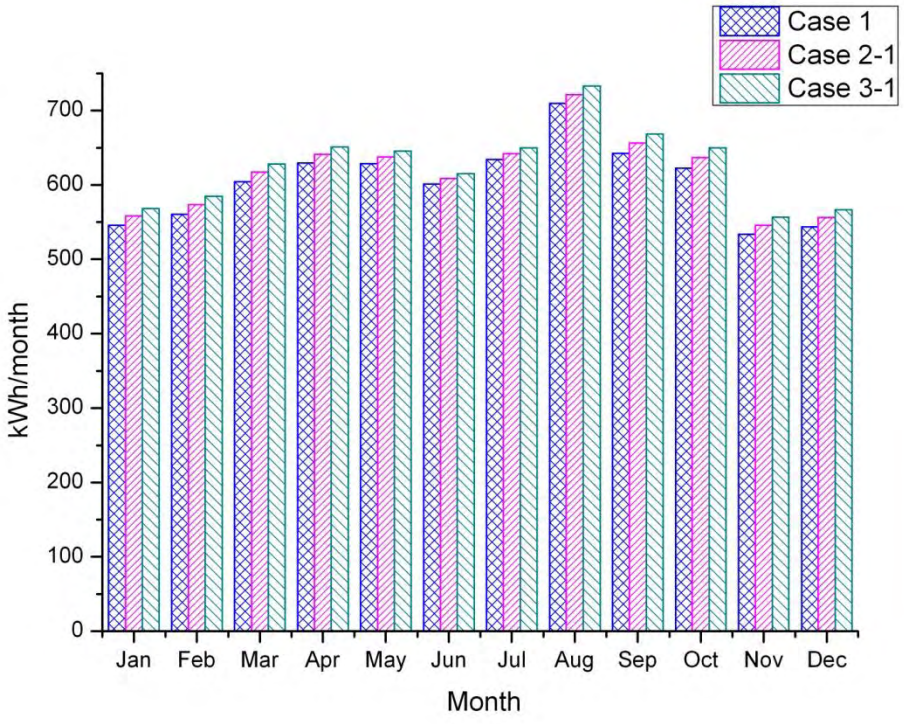

Figure 6-14 Monthly electricity production from the PV panel arrays

The monthly energy balances for case 2-1, including electricity, air enthalpy gains in the duct, heating and cooling loads, are presented in Figure 6-16. During the heating season, according to the overall computation balances, the ventilation air heated in the duct can supply as much as 36% of the total heating load (3000 kWh out of the total heating load of 8400 kWh).

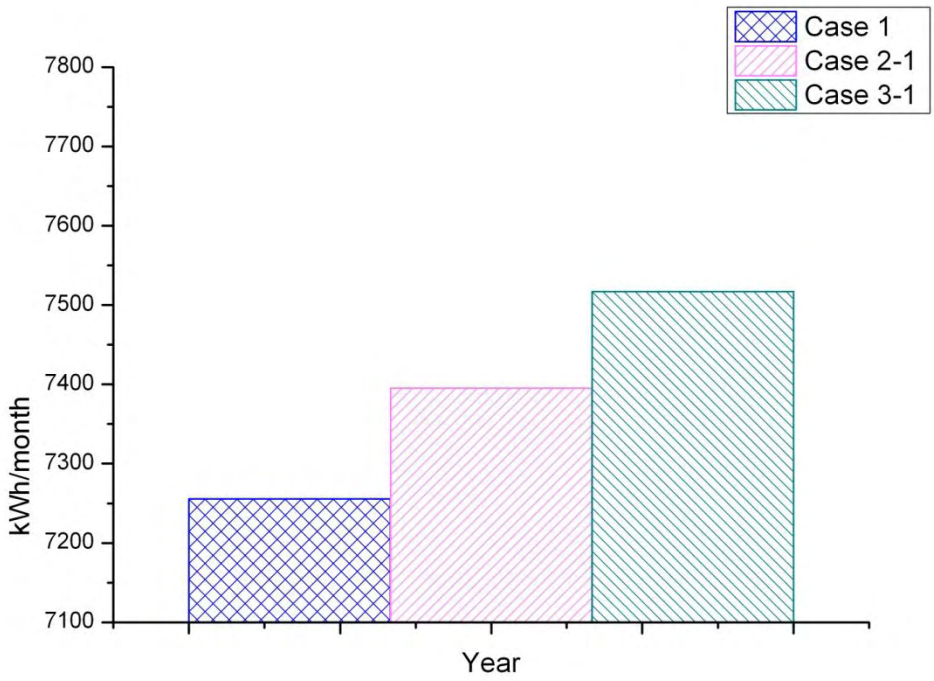

Figure 6-15 Annual Electricity production for cases [1 - 3.1]

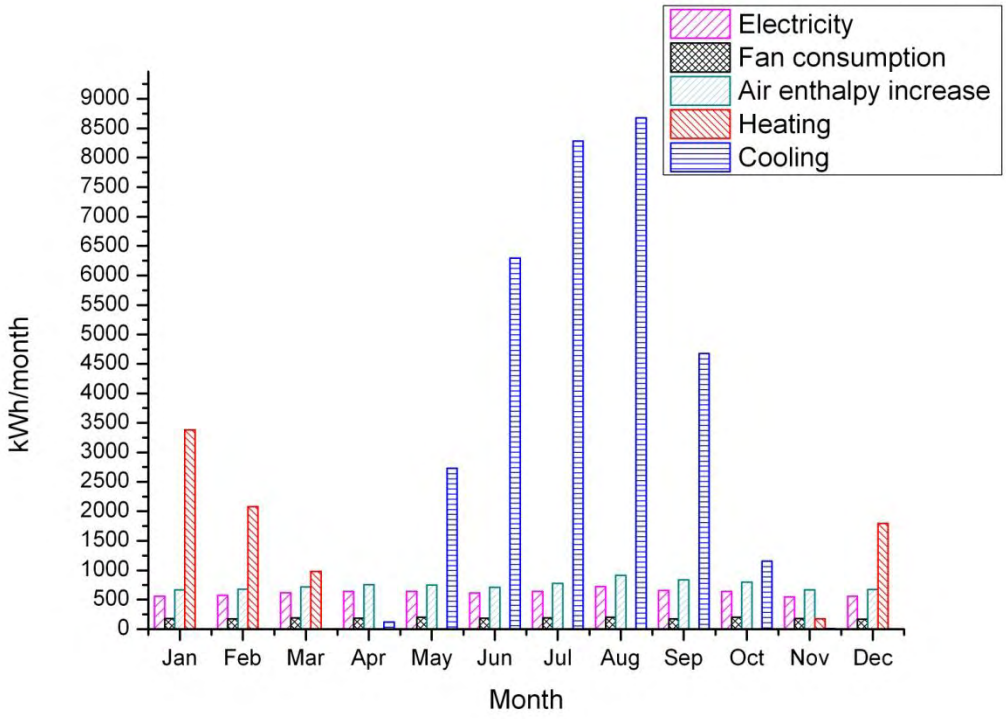

Figure 6-16 Monthly energy balances for case 2.1 (electrical – vs- thermal kWh)

The monthly cooling load, also shown in Figure 6-16, is high, because the south-facing walls of the building are not shaded (shading coefficients for the opaque and

transparent surfaces of the building are assumed to be equal to 1) and the internal gains of the office building are significant (occupants-lights-equipment).

During the year, the electricity production exceeds the fan electricity consumption. Also, a significant air enthalpy increase of 4800 kWh is calculated. The ventilation of the rooms during summer is effected by direct outdoor air, bypassing the duct at each level. The hot air produced from the duct during the summer would be a good candidate for production of space cooling. The expected efficiency in this case would be low (a COP less than 0.2 is estimated, although Mei et al. report on a desiccant cooling machine, installed in the Mataro Library, with a COP of 0.518 [174]). Florides et al. describes the advantages and disadvantages of low energy cooling techniques [134]. Unfortunately, due to the small size and height of the system, the air temperature does not exceed 60^{o}C (Figure 6-17). A workable approach would be to employ the hot air produced from the duct during the summer, to produce domestic hot water, by using an air-to-water heat exchanger.

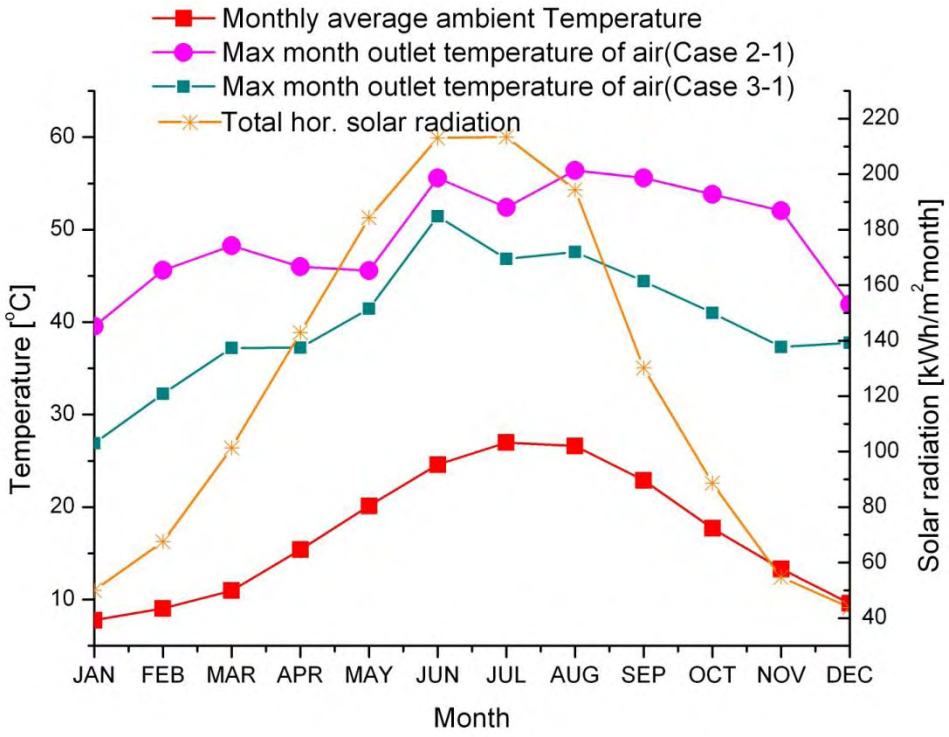

Figure 6-17 Monthly variation of maximum exit air temperature

The optimization problem should also take into account the electricity consumption of the fans. It must be kept in mind that the fans are working to cover the ventilation needs of the building during the working hours. They are working at a varying capacity, according to the building's ventilation needs, including night cooling in the summer. The exploitation of buoyancy effects saves a lot of electricity consumption

for the fans. It can be seen that during the year the fan consumption (see Figure 6-16) is always lower than the electricity production.

6.4.3 HVAC SYSTEM DESIGN IMPLICATIONS (CASE 2-1)

The HVAC system must meet a sensible heating load of 58 kW. As regards the necessary outdoor air, this is calculated to 1640 m^3/h based on the minimum requirements of prEN 15251) [172]. Out of this quantity, about 880 m^3/h are preheated in the ducts behind the PV arrays during the heating season. The sizing of the supply air duct is based on the above-mentioned sensible heating load and the temperature difference between 40^{o}C (maximum air supply temperature) and 21^{o}C (return duct air temperature). This results to a total air flow of about 9000 m^3/h for the winter season. Thus, the outdoor air represents 18% of the total air supply of the HVAC equipment in winter. The outdoor air is preheated in the ducts behind the PV modules. The maximum outlet temperature for January is 39.5^{o}C (see Figure 6-17). Thus, for January, which is the coldest month of the year, the energy saving is about 15% (510 kWh). During the months November and April, 100% of the heating loads are covered by the air heated in the duct. The total energy saving is about 36% [175]. The monthly energy balance for the winter season is presented in Figure 6-18.

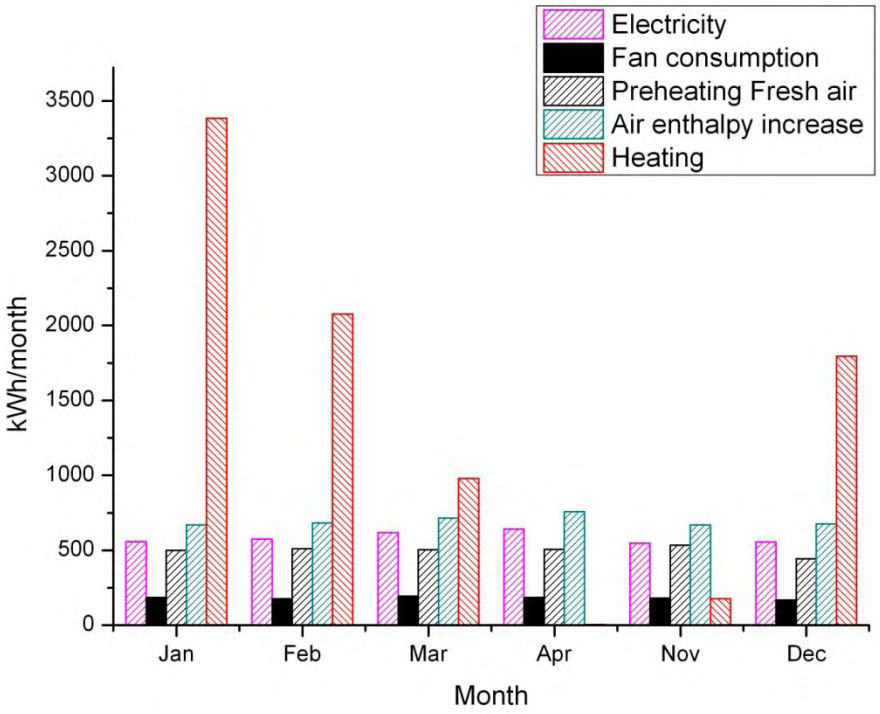

Figure 6-18 Monthly energy balance for winter season

The economic viability of the specific BIPVT concept could be enhanced if one takes into account the increase in energy rating of the building, due to the incorporation of the BIPVT system. To assess this effect, the primary energy consumption for heating, cooling and lighting, as calculated according to the methodology of EN 13790 is presented in Table 6-7. The primary energy conversion factors to transform natural gas and electricity consumption were selected as 1.05 and 2.9 respectively [176].

Table 6-7 Energy consumption and energy use for the 3 alternative cases

	Reference	Case 1	Case 2.1	Case 3.1
	kWh/m^{2}y			
Heating	14	12.8	13.0	13.1
Cooling	45	47.3	47.1	46.9
Lighting	48	48.1	48.1	48.1
Electricity production		11.2	11.4	11.6
Heat from air stream			3.3	
Sum	107	97.0	93.4	96.5
Energy needs				
Natural gas (heating)	14	12.8	9.64	13.02
Electricity (cooling, lighting)	93	84.2	83.80	83.46
Final energy (including system losses)				
Natural gas (heating)	16	14.1	10.60	14.32
Electricity (cooling, lighting)	93	84.2	83.80	83.46
Primary Energy				
Natural gas (heating)	17	15.5	11.66	15.75
Electricity(cooling, lighting)	270	252.7	256.7	255.6
Sum	296	268	265	271

Table 6-8 Building rating categories

Rating	Limits
A^+	**$EP \leq 0.50R_R$**
A	**$0.33\ R_R < ER \leq 0.50\ R_R$**
B^+	**$0.50\ R_R < ER \leq 0.75\ R_R$**
B	**$0.75\ R_R < ER \leq 1.00\ R_R$**
C	**$1.00\ R_R < ER \leq 1.41\ R_R$**

From the above Table 6-7 we see that in terms of primary energy consumption, a fuel saving of about 40% and electricity saving of 10% can be attained. Thus, if we install a total of 70 m^2 of PV modules in the building, we can move half way towards the next class (that is, B^+ - see

Table 6-8) in the grading scheme of the building's energy certificate [2] [166].

The yearly electrical efficiency with respect to the incident radiation for the heating season is predicted to be 10.5% and the thermal efficiency 13%, respectively, provided that all the hot air is exploited in space heating in winter and hot water in the summer. If we focus only on the hot air exploited in space heating during winter, the system's thermal efficiency drops to 4.2%. Of course, there exist hidden additional winter gains due to the heating of the south-facing walls of the building. Study and optimization of the overall system efficiency with respect to the thermal inertia of the walls and the type and placement of the insulation is a demanding task for the HVAC research engineer.

The above results are in agreement with Charalambous et al.[1], Tiwari [66] and Chow et al. [177] which report on standard types of by PV/T collectors, and with Agrawal and Tiwari [68] reporting on a rooftop PV/T collector.

We can further increase system's efficiency during winter, if we utilize the warm air in the ducts during the hours and days when the HVAC is off, to maintain the inside air temperature of certain building zones at acceptable levels and reduce the Monday morning startup loads.

During the summer season, in order to make the system more productive, we can employ the air ducts for night ventilation to decrease the indoor temperature levels. An initial economic analysis can be based on the computed system's energy performance data. Finally, the PV installation costs could be reduced by introducing a standardized system of fitting the PV arrays in a pre-fabricated frame, as applied today in the case of expensive ceramic tiles.

6.4.4 USE OF FINS TO ENHANCE BACKSHEET HEAT TRANSFER

In the following, the feasibility of backsheet cooling enhancement by means of the use of a finned backsheet cover with improved material is assessed. More specifically, an attempt is made to increase the heat transfer rate from the backsheet to the cooling air flow, by means of fins and modification of the backsheet material by use of metal fibers in the plastic.

The fins are assumed not to disturb the buoyancy flow. In this calculation, pin fins of parabolic profile are selected [178], with a circular base of 2 mm diameter and a length of 4mm. The distance between fins is 2mm, due to the results of the

turbulence measurements and calculations of chapter 4 (length scale of the smallest eddies of the order of 1.8 mm).

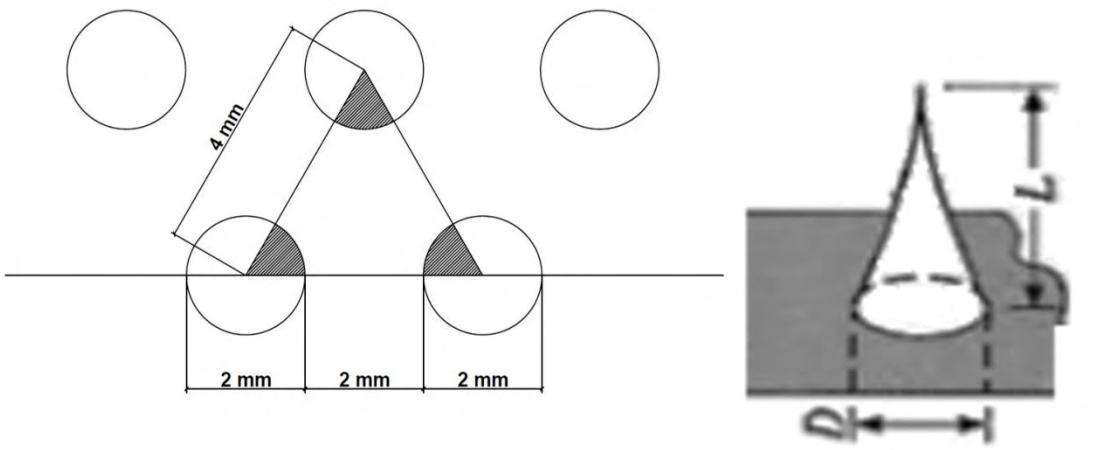

Figure 6-19 Proposed pin fins' arrangement (parabolic fin profile)

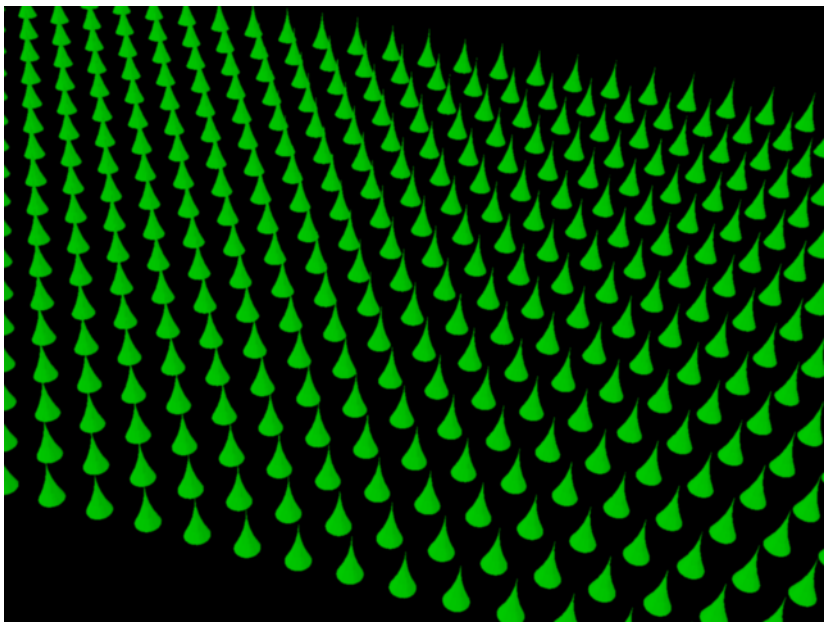

Figure 6-20 View of the improved backsheet surface (cooling air side)

The fin array is designed according to the pattern shown in Figure 6-19 and Figure 6-20. An equilateral triangular staggered arrangement is selected, with a 2 mm free distance between fins, both horizontally and diagonally.

According to [178] Table 3.5, the following expression is valid for the pin fin's efficiency n_f:

$$n_f = \frac{2}{\left(\frac{4}{9} mL^{\,2}+1\right)^{1/2}+1} \quad \textbf{(6.11)}$$

Where the characteristic number m for the specific fin type is given by the relation:

$$\mathbf{m} = \sqrt{\frac{4h_R}{D\lambda_R}} \quad \textbf{(6.12)}$$

Where

λ_R thermal conductivity of fin [W/m K]

h_R convection coefficient of fin [W/m^2 K]

Assuming a thermal conductivity of the backsheet equal to 0.2 W/mK, a fin base diameter of D=2 mm, and a convection coefficient of 10.5 W/m^{2}K, the dimensionless number m is of the order of 300.

And the heat transfer area of each fin is given by the relation:

$$A_f = \frac{\pi L^3}{8D}\left(C_3 C_4 - \frac{L}{2D}\ln\left(\frac{2DC_4}{l} + C_3\right)\right) \quad \textbf{(6.13)}$$

Where

$C_3 = 1 + 2(D/L)^2$

$C_4 = 1 + 2(D/L)^{2\ 1/2}$

$V = (\pi/20)D^2L$

Based on the above relations, we can make a comparison of the heat transfer rate from the finned backsheet surface to that from the normal (unfinned) surface. The comparison will be made for the basic triangular module of the finned surface (see figure).

Heat transfer rate from surface without fins:

$$Q = A\,h\,(t_w - t_a) \quad \textbf{(6.14)}$$

Where A is the surface area of the equilateral triangle of Figure 6-19 with a 4 mm - base.

The heat transfer rate from the finned surface is the sum of two parts:

Heat transfer rate from pin fins:

$$\boldsymbol{Q_{fins} = \frac{3}{6}A_{fin}h\,(t_{base} - t_a)\eta_f} \quad \textbf{(6.15)}$$

Where η_f is the pin fins' efficiency and A_{fin} the fin's surface area (equations above).

Heat transfer from the unfinned part:

$$\boldsymbol{A_{fins\,no} = A_{total} - \frac{3}{6}A_{fin}} \quad \textbf{(6.16)}$$

$$\boldsymbol{Q_{fins\,no} = A_{fins\,no}h\,(t_w - t_a)\eta_f} \quad \textbf{(6.17)}$$

Finally, we arrive at the expression for the total heat transfer rate from the finned surface:

$$\boldsymbol{Q_{total} = Q_{fins\,no} + Q_{fins}} \quad \textbf{(6.18)}$$

As a result, the total heat transfer from the finned surface can be readily doubled compared to the reference heat transfer rate from the level (unfinned) surface (Table 6-9).

This is an indicative calculation, aiming to assess the capacity of different backsheet design versions. However, a search in the specialized literature reveals similar trends. For example, Cavallero and Tanda [90] in their liquid crystal thermography measurements in smaller rectangular channels with somewhat higher Re numbers (8000-35000) report that average heat transfer coefficients for the ribbed surfaces turned out to be higher than those for the unribbed surface by a factor of up to 2 when the ribs were continuous, and by a factor of up to 3 when they were broken. The specific fin profile assumed in our calculation is indicative and is not considered optimal from the manufacturing point of view. Truncated pin fins would be more favourable for the laminating process.

The extension of this simplified analysis to the analysis of rough fins of variable cross-section is straightforward [179]. In order to further improve fin efficiency, the backsheet material can be modified to increase its thermal conductivity.

Table 6-9 Calculation of extended heat transfer area from micro-fins

h	10.6	convection coefficient of fin	[W/m^2 K]
λ_R	0.2	thermal conductivity backsheet (fin)	[W/m K]
D	0.002	diameter fin	m
m	325	m (dimensionless fin number)	-
L	0.004	length fin	m
X	0.002	distance fins	m
c3	1.5	C3	
c4	1.118	C4	
V	2.51E-09	fin volume	m^3
Af	1.58E-05	heat transfer area fin	m^2
nf	0.86	fin efficiency	
A	5.36E-06	module area no fins	m^2
A_{fins}	7.91E-06	module area fins	m^2
A_{module}	6.93E-06	module area total	m^2
$A_{fins\ no}$	1.33E-05		m^2
	1.91	module area multiplication with the fins	

In the following, the effect of doubling the heat transfer rate from the backsheet to the cooling air flow on the building energy performance is indicatively assessed by means of comparative building energy simulation runs. It should be obvious by the above analysis that a significantly higher increase in heat transfer rate from the backsheet to the cooling air is possible by further improvement in the design of the backsheet, which has not yet been given the attention it deserves.

Table 6-10 Simulation Cases

Reference case	Building without PV panels
Case 1	Building with PV panels in contact with the south facing walls (above the ground floor).
Case 2-1	Building with PV panels in south walls: double façade, with 0.15m air gap: air flow rate 133 kg/h and ***corrected convection coefficient h***
Case 3-1	Building with PV panels in the south walls: double façade with 0.15m air gap: air flow rate 400 kg/h and ***corrected convection coefficient h***
Case 2-2	Building with PV panels in south walls: double façade, with 0.15m air gap: air flow rate 133 kg/h and ***doubled heat transfer area***
Case 3-2	Building with PV panels in the south walls: double façade with 0.15m air gap: air flow rate 400 kg/h and ***doubled heat transfer area***

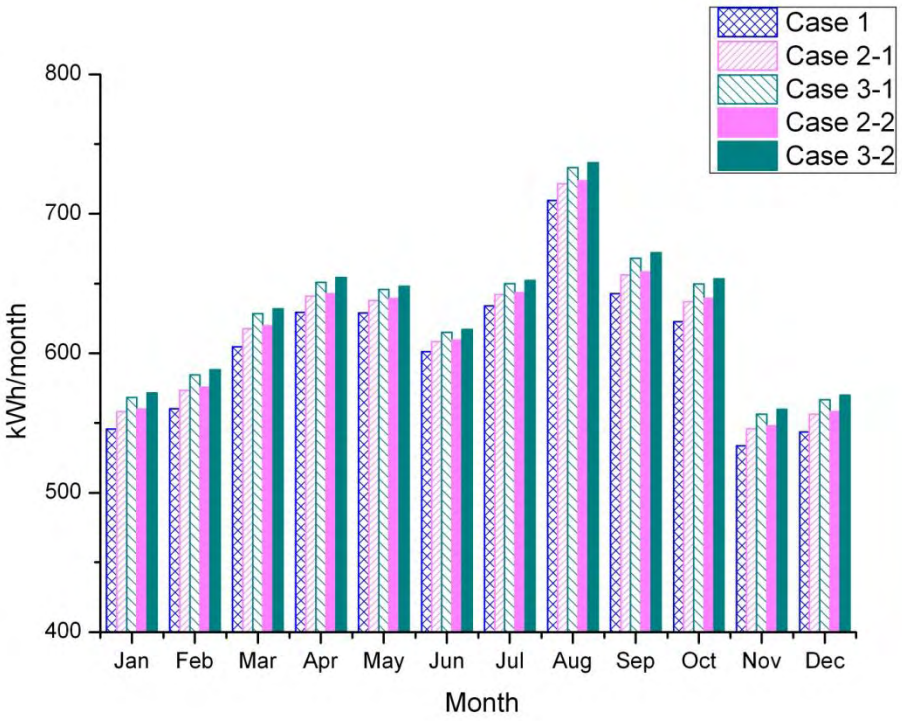

Figure 6-21 Comparative evolution of monthly electricity production from the PV panel arrays, for the simulation cases of Table 6-10.

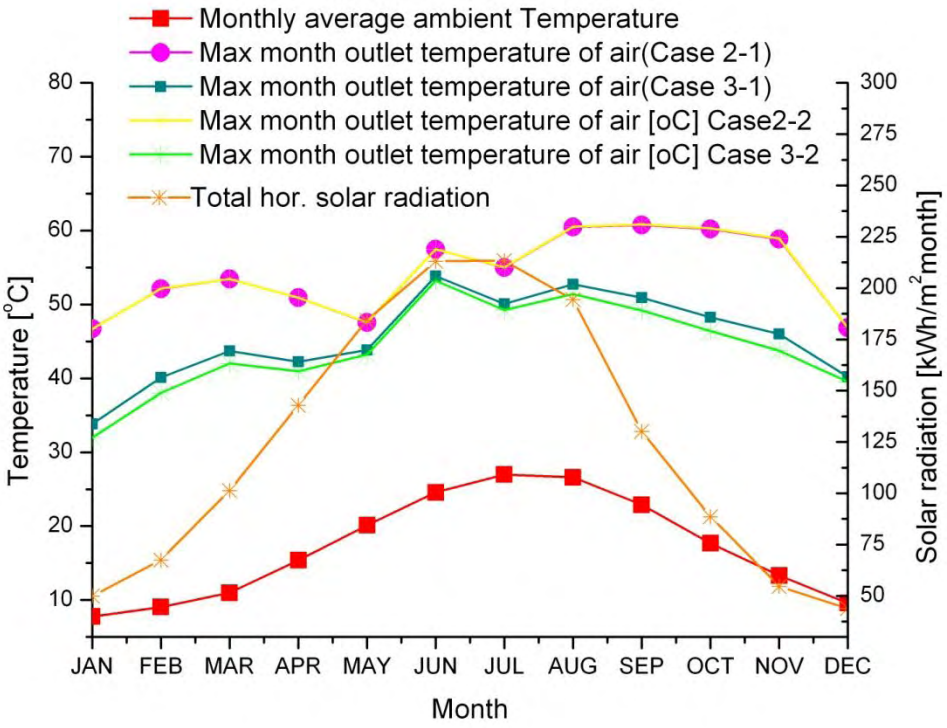

Figure 6-22 Comparative average monthly variation of maximum exit air temperature for cases 2-1, 2-2, 3-1, 3-2.

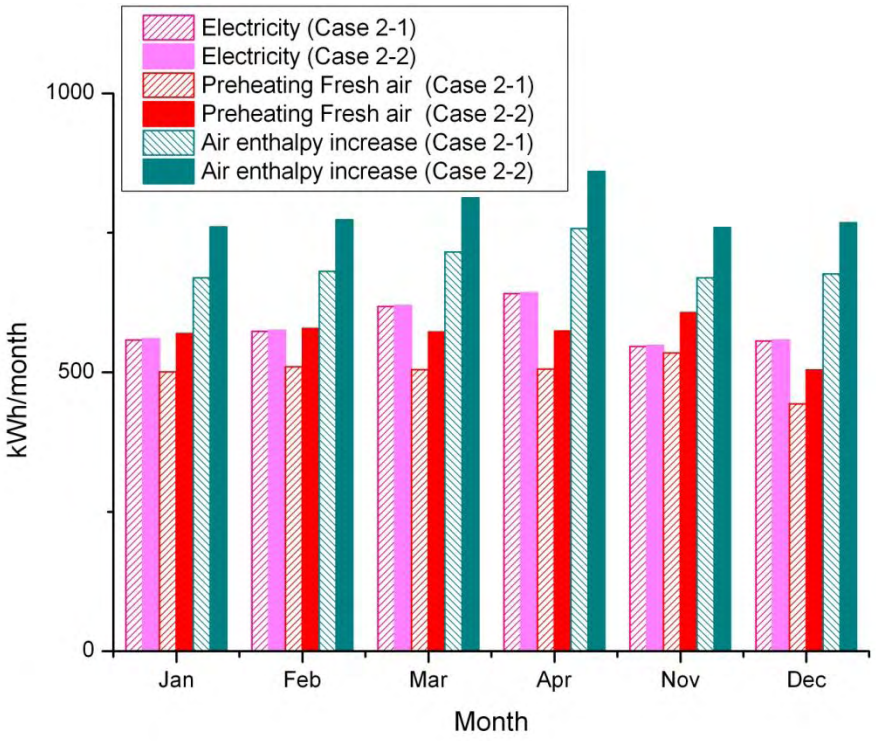

Figure 6-23 Comparative monthly energy balances for winter season: Cases 2-1, 2-2.

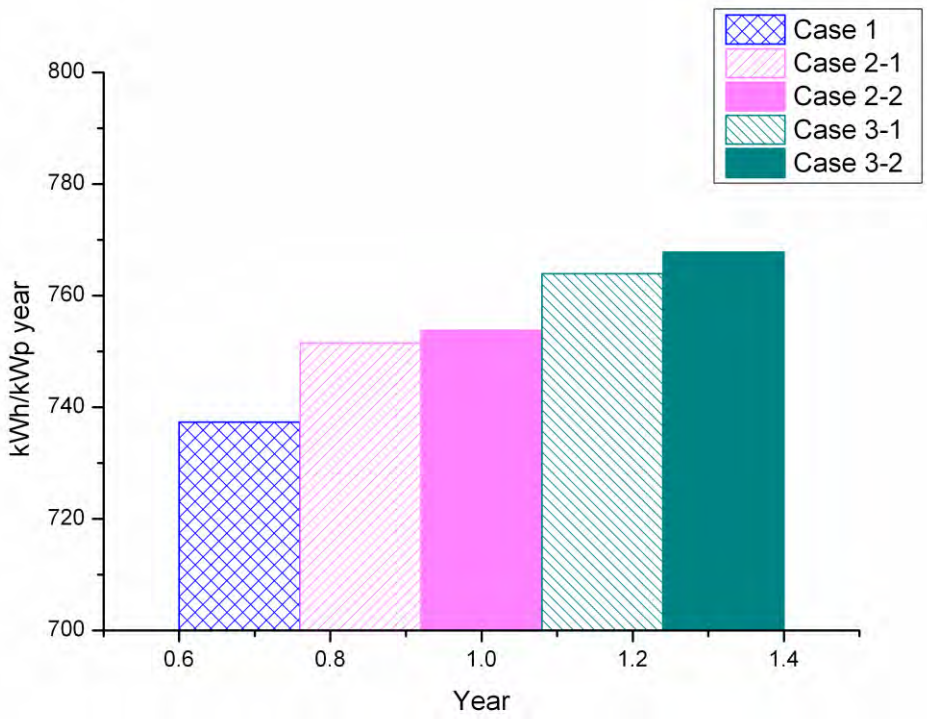

Figure 6-24 Comparative annual electricity production for the 5 cases of Table 6-10. For comparison, annual electricity production for roof-mounted PV panels is 1200 kWh/kWp.

The monthly energy balances for case 2-1 and case 2-2 including electricity, air enthalpy gains in the duct, and the gains from preheating fresh air for winter season, are presented in Figure 6-16 and Figure 6-23. During the heating season, according to the overall computation balances, the ventilation air heated in the duct for the case 2-2 can supply as much as 40% of the total heating load (3400 kWh out of the total heating load of 8400 kWh). This leads to a decrease in heating fuel consumption of about 13% for the winter season, without exploiting the excess air enthalpy, compared with case 2-1. For case 2-2, which has an improved cooling effect, the electricity produced is 0.5% higher than case 2-1.

6.5 DISCUSSION OF RESULTS

The BIPV concept proposed in the frame of this thesis was studied by means of TRNSYS building energy simulation. The results of the flow and heat transfer investigations of Part A of this thesis are employed in the determination of more accurate Nusselt number correlations for the specific BIPV design concept.

These correlations were employed to improve the respective sub model of the TRNSYS simulation.

The overall effect on the energy performance of the modules is studied by means of the electricity produced by the PV panels, the heating energy gains and their overall effects on the energy rating of the building.

As regards the electricity production, the optimized installation of the modules with increased cooling effect results in an average annual production of 770 kWh/ kWp, whereas the respective production from uncooled PV panels mounted flash the south facing wall is calculated to be 735 kWh_e/ kW_p. For comparison, the average annual electricity production from roof mounted PV panels in the same location is calculated to be of the order of 1200 kWh_e/ kW_p. However, the vertical panels' arrangement in the double façade results in additional annual building energy savings, in the form of space heating during winter amounting 310 kWh_{th}/ kW_p and a further 210 kWh_{th}/ kW_p savings in service water heating energy consumption. Moreover, the above improvements may lead to improvement in building energy rating by one step, which results in further benefits for the building's owner. The air gap that is formed behind the modules can be additionally exploited for night cooling during summer. Furthermore, the selection of flow rate and duct dimensions is critical to the performance of the PV façade.

According to the building energy simulation, significant improvements in the thermal gains of the building can be succeeded by an improved design of the backsheet (enhancing heat transfer by micro-fins, modified backsheet material etc). It should be noted that up to now, the design of the backsheet has not received the attention it deserves by the photovoltaic design engineers and manufacturers. The new approach suggested here refers to the re-design, or a novel design of the backsheet, to simultaneously fulfill two kinds of objectives:

1. The usual objectives required by the PV backsheet (that is, water and air proof sealing of the PV, durability etc) and
2. The objective of rejecting heat and cooling the PV modules at an increased rate, due to improved design of the layers to reduce heat resistance, and the design of the external layer in the form of finned or micro-finned surface.

According to the proposed procedure, the new design of backsheet would be integrated in the manufacturing process and thus applied in the series production of PV modules, not as add-on on existing PV panels.

Now, the results of this chapter may be reliably employed to perform the economic analysis of the next chapter.

CHAPTER

7

7 ECONOMIC ANALYSIS OF THE BUILDING ENERGY PERFORMANCE

An economic analysis of the building application of the specific BIPV concept is carried out in this chapter. The building studied in chapter 7 is employed as an example in this analysis. Two levels of complexity are applied: We begin with a simplified analysis based on the assumption of a rough estimate of the annual PV electricity production per installed 1000 Wp, (1 kW peak electric power produced), as well as the annual heating and hot water energy gains. As a second step, a more detailed analysis which employs the TRNSYS simulation and the respective economic analysis module, to integrate over a Typical Meteorological Year for the specific location and calculate the evolution of present value of the investment during the 25 years of the installations' lifetime.

Aim of this analysis is to get more refined results that will allow a profitability comparison among the following 3 alternative investments:

(i) Installation of 9800 kWp of PV modules on the roof of the building (Roof mounted).

(ii) Installation of 9800 kWp of standard PV modules as a double façade, as studied in the frame of this thesis (Case 2-1).

(iv) Installation of 9800 kWp of the same PV modules, with improved backsheet design according to the suggestions of section 7.5.4 as a double façade (Case 2-2).

7.1 SIMPLIFIED ANALYSIS

The basic assumptions and results for the simplified analysis are listed below. The same assumptions are made for the detailed analysis of the next section.

Table 7-1 Basic assumptions of the simplified economic analysis

Credit conditions		
Interest rate	8.55	%
Payback period	10	years
Gratis period	0	years
Capital market conditions		
Interest rate for fixed deposit	3.5	%
Inflation rate without Energy price increase	3	%
Inflation rate including Energy price increase	4	%
Photovoltaic installation conditions		
Power of PV-installation	9800	W
Time duration of power warranty	20	years
Power guaranteed in last year covered by warranty	80	%
Total price for PV-installation (incl. VAT, Transport, Montage, Network connection costs, etc.)	35000	EUR
Yearly maintenance costs (incl. rental of electricity meter)	250	EUR
Annual insurance costs	150	EUR
Tax rates		
VAT	23	%
Income tax rate	free	%

For the energy savings for heating and domestic hot water we assumed that the price of natural gas is 0.06 Euro/kWh and the price increases 3% per year. As we can see from Table 7-2 the first year of operation the profit of the BIPV system is 32 % lower, but the 20th year, as the electricity production reduces and the price of natural gas increases the profit is only 26 % lower than the roof mounted PV.

Table 7-2 Assumptions related to the energy production of the PV panels (simplified economic analysis)

Production conditions			
Subsidies for the period from 1 to 20 years		0.55	EUR/kWh
Actual average consumer price for 1 kWh		0.1	EUR/kWh
Regional estimated electricity and heating energy production			
	Roof mounted	Case 2-1	Case 2-2
	kWh	kWh	kWh
Annual electricity production per installed 1000 Wp	1200	750	760
Estimated heating energy gains per installed 1000 Wp	0	310	340
Estimated hot water production gains per installed 1000 Wp	0	210	230
	EUR	EUR	EUR
Electricity sales, 1st Year	6494	4059	4070
Electricity sales, 20th Year	5260	3288	3296
Energy savings (heating and hot water) 1st Year	0	340	380
Energy savings (heating and hot water) 20th Year	0	596	670

7.2 DETAILED ANALYSIS BY USE OF THE TRNSYS ECONOMIC ANALYSIS MODULE

In this section, a detailed economic analysis is performed. Aim of this analysis is to get more refined results that will allow a profitability comparison among the above 3 alternative investments.

The economic comparison is made by means of comparing the evolution of the present value of the 3 alternative investments during the next 25 years (Figure 7.1). The full details of the analysis are reported in Annex VII.

According to the comparative results presented in Figure 7.1, the roof- mounted photovoltaic installation remains the most economically profitable. As regards the standard reference case 2-1 (standard PV panels incorporated in a BIPV system), its present value of investment stays consistently lower than the roof-mounted solution. On the other hand, the suggested improvements in the backsheet design lead to a small increase in profitability of the investment.

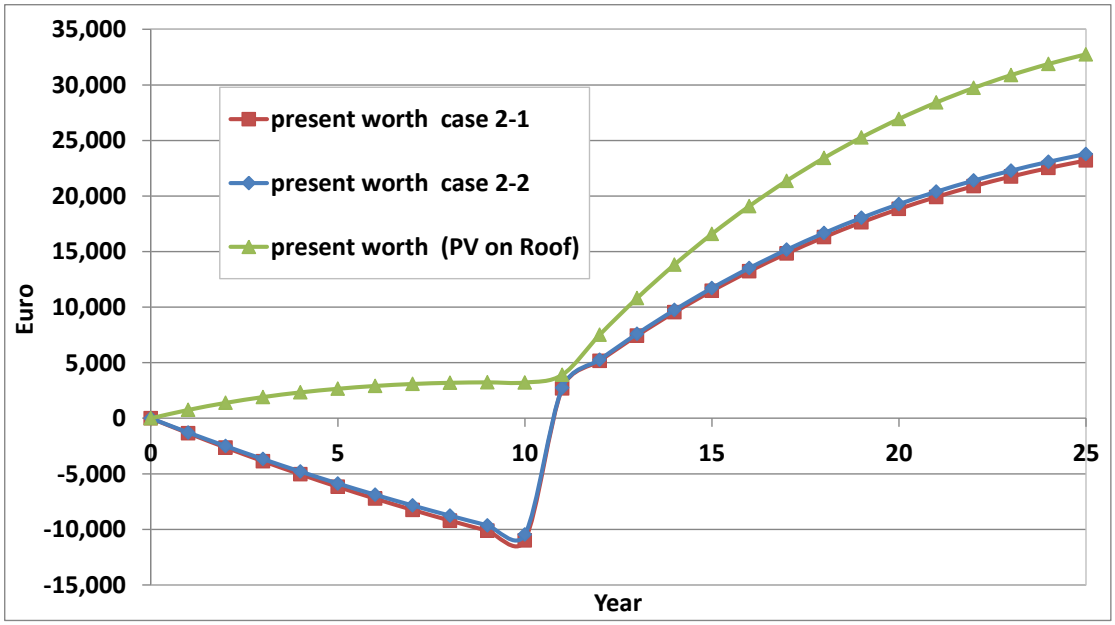

Figure 7-1 Comparative evolution of present value of investment during the next 25 years.

Table 7-3 Return on investment for 20 and 25 years of operation

	Roof mounted	Case 2-1	Case 2-2
	(%)	(%)	(%)
Return on investment for 20 years of operation	27.07	8.95	9.74
Return on investment for 25 years of operation	30.85	12.32	13.15

The profitability of the three alternative cases is compared in Table 7-3, by means of the return on investment after 20 and 25 years. If the investors sell the electricity to the utility company at a rate of 0.55 Euro /kWh then the return on investment for 20 and 25 years of operation for Case 2-2 (BIPV with improved backsheet) correspond to 9.74 % and 13.15 % respectively.

This explains the necessity to subsidize the installation of PV modules.

Another way to compare the profitability of the tree alternative investments by means of the comparison of NPV for 20 and 25 years is presented in Figure 7-2.

The detailed economic analysis is based on the calculation of the net present value.

$$NPV = \frac{NCF}{(1+i)^t} - TCI$$

The calculation is made for a life span of 20 and 25 years.

The net present value (NPV) is calculated by subtracting the yearly payments to the bank from the net cash from the selling of the electricity minus operation and maintenance costs. The basic assumption as regards the financing and the same as these employed in the simplified analysis of the present section.

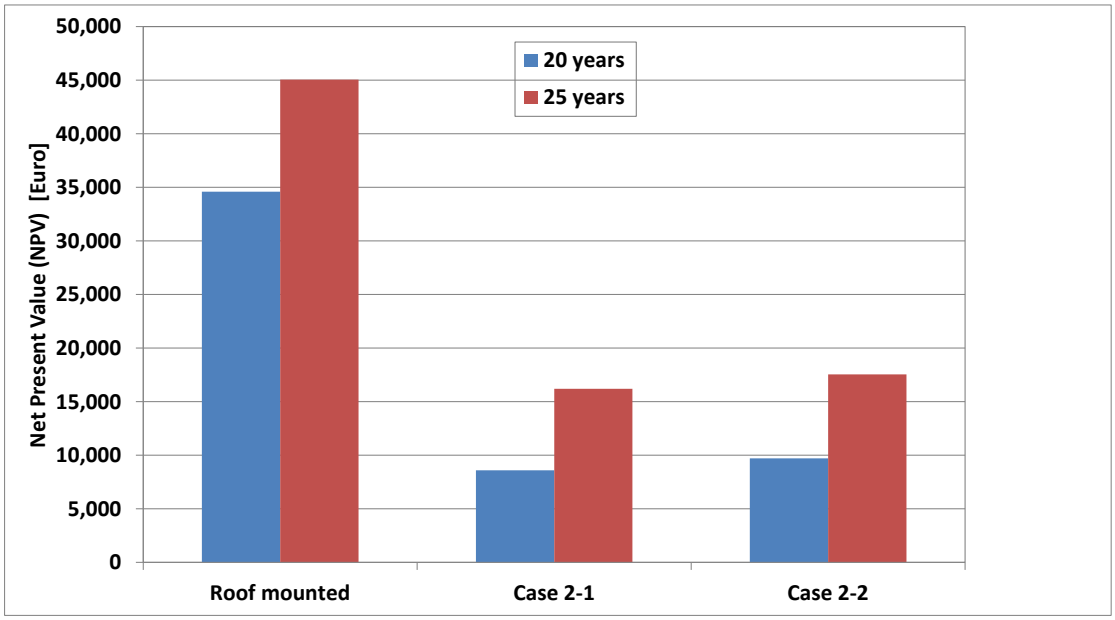

Figure 7-2 Net present value for 3 alternative investments

If the price of electricity was 0.3 Euro /kWh then even for the roof-mounted PV investment the NPV would be negative (-4669 Euro).

The situation may become more favourable for the PV installation investment if the electricity pricing varies with hour of day, with higher price for the peak load hours which roughly correspond to the maximum PV production hours. Such scenarios with variable electricity pricing can be readily tested with the TRNSYS hourly simulation.

7.3 Discussion of Building Energy Simulation and Economic Analysis Result

A building energy simulation of the proposed concept applied to a small office building is carried out in the TRNSYS simulation environment. The south-facing walls of the building are covered by double PV façades. The heat transfer coefficients for PV cooling are estimated based on the results of Part A.

The simulation is carried out with a time step of 1 hour, for one full Typical Meteorological Year in Volos.

The electrical energy produced is is 750 kWh per 1000 Wp of PV modules.

The heating energy produced during the year is 520 kWh per 1000 Wp of PV modules.

Out of these kWh, 60% is exploited in heating the building during the months November to April.

An economic analysis is carried out to assess the profitability of investing in the double PV façade system. The results indicate that the system is profitable under certain conditions. However, the roof-mounted case remains significantly more profitable.

CHAPTER

8

8 CONCLUSIONS

A new concept of integrating PV modules to the south-facing walls of a building is studied by means of experiment, CFD computations and building energy simulation. An air gap between the PV backsheet and the building wall is employed for circulating outdoor air to cool the modules, keeping their efficiency high. The heated air is exploited by the HVAC system during winter and service water system during the summer. Experimental data in real world operating conditions are critical to support the design optimization of the concept and layout.

- A basic building block of the proposed concept was designed and assembled for indoor and outdoor testing.
- Outdoor testing of the transient electrical and thermal behavior of the device was conducted for several hours during a number of days in summer and autumn. Three different modes of cooling were tested: natural convection and forced convection by use of two axial fans with different capacities.
- The results indicate a time constant of the order of 10 min for the panel temperature response and confirm the manufacturer's data as regards the effect of panel temperature on the photovoltaic efficiency. A further slight drop in PV efficiency was measured for late afternoon hours, presumably due to the increase in air mass.
- In general, the actual efficiency values measured do not exceed 9%. This is due to the relatively low insolation values associated with the vertical placement of the PV panels in the specific BIPVT application. Incoming solar radiation at the vertical surface does not exceed 800 W/m^2, even at the more favorable conditions near the winter solstice.
- A study of the flow field was necessary to further explain the observed behaviour. To this end, the testing device was subjected to indoor tests with

emulation of the above-mentioned modes of operation. Dynamic similarity of the indoor tests was checked by means of respective values of Re, Ra, Pr and Nu numbers' ranges. Indoor tests comprised flow visualization measurements and hot wire anemometry measurements.

- The flow visualization measurements reveal the transitional character of the flow and the main mechanism of eddy generation in the different modes of operation.
- Velocity profiles were recorded at the centerline, along the depth of the cavity, for 4 different vertical positions, by hot wire anemometry. Average velocities of the order of 0.10 m/s with respective turbulent velocities of 0.01 m/s were recorded for the buoyancy flow (mode 1). Higher average velocities of the order of 0.2 – 0.35 m/s (lower and higher capacity fans, respectively) and RMS velocity fluctuation levels of 0.015-0.03 m/s were recorded in the cold flow experiments. The measured velocity profiles along the channel indicate the developing character of the flow and a significant sensitivity to inlet boundary conditions.
- The hot wire anemometry data were analyzed by means of Power Spectral Density diagrams and autocorrelation. Integral time scales as low as 500 ms were calculated for the buoyancy flow case, which corresponds to an integral length scale of about 0.025 m. A Kolmogorov length scale of the order of 0.0018 m was calculated for the same case, by extension of experience from turbulent flows (although we cannot state that we are in the turbulent flow regime).
- Based on the analysis of the indoor test results, if we try to enhance the heat transfer surface by means of fins, the minimum free distance between fins must exceed 1.8 mm.
- CFD modeling was additionally applied to better understand the flow behavior of the basic testing device and the full scale BIPV system proposed. The CFD model was validated and tuned against the indoor tests in the three modes of operation. Once tuned, the CFD model was validated against the results of the outdoor tests in the three operation modes. The results improved our modeling of the flow and heat transfer inside the cavity and led to the determination of accurate wall heat transfer correlations that are necessary for the building energy simulations in Part B.
- The device was modeled in ANSYS CFX and 3D computations of the steady state flow field were produced, simulating the 3 modes of indoor hot wire anemometry experiments. The k-ω turbulence model was found more successful in matching the flow fields seen in the flow visualization. Specific improvements were made to the CFD computation boundary conditions in order to better predict the transient flow regime. A moderately dense mesh of 1,200,000 tetrahedral elements and 203,000 nodes was applied to model the cavity.

- Correlating equations are developed for average Nu/ Re or Nu/ Ra numbers from the experimental and numerical results in terms of dimensionless parameters. It was found that the existing correlations underestimated the Nu by a factor of 2.
- In Part B of this study, the overall effect on the energy performance of the modules is studied by means of building energy simulation. The electricity produced by the PV panels, the heating energy gains and their overall effects on the energy rating of the building are calculated.
- As regards the electricity production, the optimized installation of the modules with increased cooling effect results in an average annual production of 770 kWh/kWp, whereas the respective production from uncooled PV panels mounted flash the south facing wall is calculated to be 735 kWh_e/kW_p. For comparison, the average annual electricity production from roof mounted PV panels in the same location is calculated to be of the order of 1200 kWh_e/ kW_p. However, the vertical panels' arrangement in the double façade results in additional annual building energy savings, in the form of space heating during winter amounting 310 kWh_{th}/ kW_p and a further 210 kWh_{th}/ kW_p savings in service water heating energy consumption. Moreover, the above improvements may lead to improvement in building energy rating by one step, which results in further benefits for the building's owner.
- It was concluded that the selection of flow rate, duct dimensions and the heat transfer characteristics of the backsheet are critical to the performance of the PV facade. Also, different design versions must be adapted to different climatic conditions and orientation of the building.
- The profitability of the investment for a vertical placement of the modules in the proposed BIPV arrangement was compared to the standard rooftop installation by means of the return on investment after 20 and 25 years. As expected, the roof- mounted photovoltaic installation remains the most economically profitable. If the investors sell the electricity to the utility company at a rate of 0.55 Euro /kWh then the return on investment for 20 and 25 years of operation for the BIPV with improved backsheet corresponds to 8.95 % and 12.32 % respectively calculated for the vertical placement of the modules in the building. It is significantly lower than that for the roof top placement. The investment breaks even by the 11^{th} year of operation, only a little after the roof-mounted case. On the other hand, the suggested improvements in the backsheet design lead to a certain increase in profitability of the investment.
- The contribution of the proposed concept to the energy performance of a building could become significant provided that the building heating (and cooling) loads are minimized by adequate insulation and shading, as well as an energy efficient ventilation system design.

REFERENCES

1. Charalambous, P.G., et al., *Photovoltaic thermal (PV/T) collectors: A review.* Applied Thermal Engineering, 2007. **27**(2-3): p. 275-286.

2. NN, *Directive 2002/91/EC of the European Parliament and of the Council of 16 December 2002 on the energy performance of buildings*. 2002.

3. Delorme, D., *Lesson on Photovoltaic Cells*. 2004.

4. http://www.keiwa.co.jp/e/product/product_09.html.

5. de Dios, A.C., *Chemistry of the Environment (Greenhouse Effect), Lecture XXIII, Chem 002*

6. Antonio Luque and Steven Hegedus (Eds.), *Handbook of Photovoltaic Science and Engineering*. 2003: John Wiley & Sons Ltd.

7. Andreas Wagner, *Photovoltaic Engineering*. 1999, Berlin: Springer.

8. Goetzberger, A. and V.U. Hoffmann, *Photovoltaic Solar Energy Generation*. 2005: Springer.

9. California Energy Commssion, *A guide to photovoltaic (PV) system design and installation. Consultant Report 500-01-020, JUNE 2001*.

10. Van Dyke, E.E., et al., *Temperature dependence of performance of crystalline silicon photovoltaic modules.* S Afr J Sci, 2000: p. 96-198.

11. Hausler, T. and H. Rogass, *Latent heat storage on photovoltaic*, in *Sixteen European Photovoltaic Solar Energy Conference*. 2000: Glasgow, UK. p. 2265.

12. Radziemska, E., *Thermal performance of Si and GaAs based solar cells and modules: a review.* Progress in Energy and Combustion Science, 2003. **29**: p. 407-424.

13. Davis, M.W., A.H. Fanney, and B.P. Dougherty, *Prediction of building integrated photovoltaic cell temperatures.* Journal of Solar Energy Engineering, Transactions of the ASME, 2001. **123**(3): p. 200-210.

14. Bazilian, M.D., H. Kamalanathan, and D.K. Prasad, *Thermographic analysis of a building integrated photovoltaic system.* Renewable Energy, 2002. **26**(3): p. 449-461.

15. Van Helden, W.G.J., R.J.C. Van Zolingen, and H.A. Zondag, *PV thermal systems: PV panels supplying renewable electricity and heat.* Progress in Photovoltaics: Research and Applications, 2004. **12**: p. 415–426.

16. Anderson, T.N., et al., *Performance of a building integrated photovoltaic/thermal (BIPVT) solar collector.* Solar Energy, 2008.

17. Hagemann, I., *PV in buildings – The influence of PV on the design and planning process of a building* Renewable Energy, 1996. **8**(1-4): p. 467-470.

18. DIN-4701, *Regeln fuer die Berechnung des Waermebedarfs von Gebaeuden*. 2002.

19. Gratia, E. and A. De Herde, *Optimal operation of a south double-skin facade.* Energy and Buildings, 2004. **36**(1): p. 41-60.

20. DIN-4108-Bl.4, *Wärmeschutz und Energie-Einsparung in Gebäuden Teil 4: Wärme- und feuchteschutztechnische Bemessungswerte*. 2002.

21. Pappas, A. and Z. Zhai, *Numerical investigation on thermal performance and correlations of double skin façade with buoyancy-driven airflow.* Energy and Buildings, 2008. **40**(4): p. 466-475.

22. Wilk H, *OKA-House of the Future*, in *IEA SHCP Task 19* 1997.

23. European Photovoltaic Industry Association, http://www.epia.org.

24. Hynes K, et al. *Energy analysis of PV cladding systems*. in *13th Euro. Conf. Photovoltaic Solar Energy Conversion* (1995.

25. Luque, A. and S. Hegedus, *Handbook of Photovoltaic Science and Engineering*. 2003: John Wiley & Sons Ltd,.

26. Hagemann, I. and J. Leppänen. in *Proc. 14th Euro. Conf. Photovoltaic Solar Energy Conversion*. (1997.

27. Prasad, D. and M. Snow, *Designing with solar power: a source book for building integrated photovoltaics(BIPV)*. 2005: Earthscan Ltd.

28. Saelens D., *Energy Performance Assessments of Single Storey Multiple-Skin Facades. PhD thesis, Laboratory for Building Physics*. 2002, Department of Civil Engineering, Catholic University of Leuven Belgium http://www.kuleuven.ac.be/bwf/common/data/PhD_2002_Saelens.pdf.

29. Poirazis, H., *Double Skin Façades for Office Buildings Literature Review*, Division of Energy and Building Design Department of Construction and

Architecture Lund Institute of Technology Lund University, 2004, EBD-R--04/3.

30. Fux, V., *Thermal simulation of ventilated PV-Facades*. 2006, Loughborough Univercity.

31. Uuttu, S., *Study of Current Structures in Double-Skin Facades.*, in *Structural Engineering and Building Physics. Department of Civil and Environmental Engineering*. 2001 Helsinki University of Technology (HUT),Finland.

32. Gertis, K., *Are new facade developements rational? - Part 2: Double glazed facades.* Bauphysik 1999. **21**(2): p. 54-66.

33. Lang, W., *Typologische Klassifizierung von Doppelfassaden und experimentelle Untersuchung von dort eingebauten Lamellensystemen aus Holz zur Steuerung des Energiehaushaltes hoher Hduser unter Beriicksichtigung der Nutzung von Solarenergie (Classification of double glazed facades and experimental investigations of integrated lamella-systems for the energy regulation of high buildings by consideration of solar energy).* . 2000, Dissertation TU München.

34. Zöllner, A., *Experimentelle und theoretische Untersuchungen des kombinierten Warmetransports in Doppelfassaden. (Experimental and theoretical examinations of the combined heat transfer in double facades)*. 2001, Dissertation TU München.

35. Lee, K., *Untersuchung zur Einsatzmoglichkeit von Doppelfassaden bei hohen Verwaltungsgebauden mit Glasfassaden im extrem gemabigten Klimagebiet Application of double facades in high administration buildings with glazing facades in extremely moderate climate)*. 2002, Dissertation TU Berlin.

36. Oesterle E, L.R.-D., Lutz M, Heusler M,, *Double Skin Facades – Integrated Planning*. 2001, Munich, Germany: Prestel Verlag.

37. Lee, E., et al., *High-Performance Commercial Building Façades. Building Technologies Program,*. 2002, Environmental Energy Technologies Division, Ernest Orlando Lawrence Berkeley National Laboratory (LBNL), University of California, Berkeley, USA (LBNL – 50502).

38. Zöllner, A., E.R.F. Winter, and R. Viskanta, *Experimental studies of combined heat transfer in turbulent mixed convection fluid flows in double-skin-façades.* International Journal of Heat and Mass Transfer, 2002. **45**(22): p. 4401-4408.

39. Gratia, E. and A. De Herde, *Natural ventilation in a double-skin facade.* Energy and Buildings, 2004. **36**(2): p. 137-146.

40. Hien, W.N., et al., *Effects of double glazed facade on energy consumption, thermal comfort and condensation for a typical office building in Singapore.* Energy and Buildings, 2005. **37**(6): p. 563-572.

41. Balocco Carla, *A non-dimensional analysis of a ventilated double façade energy performance.* Energy and Buildings, 2004. **36**(1): p. 35-40.

42. Yilmaz, Z. and F. Cetintas, *Double skin facade's effects on heat losses of office buildings in Istanbul.* Energy and Buildings, 2005. **37**(7): p. 691-697.

43. Hamza, N., *Double versus single skin facades in hot arid areas.* Energy and Buildings, 2008. **40**(3): p. 240-248.

44. Höseggen, R., B.J. Wachenfeldt, and S.O. Hanssen, *Building simulation as an assisting tool in decision making. Case study: With or without a double-skin facade?* Energy and Buildings, 2008. **40**(5): p. 821-827.

45. ESRU, *ESP-r: a building and plant energy simulation environment, User Guide, Version 9 Series, ESRU Publication, University of Strathclyde, Glasgow, UK*. 1999.

46. Manz, H., *Numerical simulation of heat transfer by natural convection in cavities of façade elements.* Energy and Buildings, 2003. **35**(3): p. 305-311.

47. Manz, H. and T. Frank, *Thermal simulation of buildings with double-skin faηades.* Energy and Buildings, 2005. **37**(11): p. 1114-1121.

48. Batchelor, G.K., *Heat transfer by free convection across a closed cavity between vertical boundaries at different temperatures* Quarterly Applied Mathematics, 1953. **12**: p. 209-233.

49. Selkowitz, S.E., *Thermal performance of insulating window systems.* ASHRAE Transactions, December 1978. **85, Part 2, Paper DE-79-5 #5**.

50. Benemann, J., C. Oussama, and E. Schaar-Grabriel, *Building integrated PV modules.* Energy Material and Solar Cells, 2001. **67**: p. 345-354.

51. Chow, T.T., J.W. Hand, and P.A. Strachan, *Building-integrated photovoltaic and thermal applications in a subtropical hotel building.* Applied Thermal Engineering, 2003. **23**(16): p. 2035-2049.

52. Eicker, U., et al., *Facades and summer performance of buildings.* Energy and Buildings, 2008. **40**: p. 600-611.

53. Seng, L.Y., G. Lalchand, and G.M. Sow Lin, *Economical, environmental and technical analysis of building integrated photovoltaic systems in Malaysia.* Energy Policy, 2008. **36**(6): p. 2130-2142.

54. Gan, G., *Effect of air gap on the performance of building-integrated photovoltaics.* Energy, 2009. **34**(7): p. 913-921.

55. Sandberg, M. and B. Moshfeghb, *Buoyancy-induced air flow in photovoltaic facades Effect of geometry of the air gap and location of solar cell modules* Building and Environment, 2002. **37**: p. 211-218.

56. Manz, H., *Total solar energy transmittance of glass double facades with free convection.* Energy and Buildings, 2004. **36**(2): p. 127-136.

57. Fossa, M., C. Ménézo, and E. Leonardi, *Experimental natural convection on vertical surfaces for building integrated photovoltaic (BIPV) applications.* Experimental Thermal and Fluid Science, 2008. **32**(4): p. 980-990.

58. Sarhaddi, F., et al., *An improved thermal and electrical model for a solar photovoltaic thermal (PV/T) air collector.* Applied Energy, 2010. **87**(7): p. 2328-2339.

59. Infield, D., L. Mei, and U. Eicker, *Thermal performance estimation for ventilated PV facades.* Solar Energy, 2004. **76**(1-3): p. 93-98.

60. Balocco Carla, *A simple model to stydy ventilated facedes energy performance.* Energy and Buildings, 2002. **34**: p. 469-475.

61. Mei, L., et al., *Thermal modelling of a building with an integrated ventilated PV façade.* Energy and Buildings, 2003. **35**(6): p. 605-617.

62. Manz, H., A. Schaelin, and H. Simmler, *Airflow patterns and thermal behavior of mechanically ventilated glass double facades.* Building and Environment, 2004. **39**(9): p. 1023-1033.

63. Liao, L., et al., *Numerical and experimental study of heat transfer in a BIPV-thermal system.* Journal of Solar Energy Engineering, Transactions of the ASME, 2007. **129**(4): p. 423-430.

64. Infield, D., et al., *A simplified approach to thermal performance calculation for building integrated mechanically ventilated PV facades.* Building and Environment, 2006. **41**(7): p. 893-901.

65. Yun, G.Y., M. McEvoy, and K. Steemers, *Design and overall energy performance of a ventilated photovoltaic facade.* Solar Energy, 2007. **81**(3): p. 383-394.

66. Solanki, S.C., S. Dubey, and A. Tiwari, *Indoor simulation and testing of photovoltaic thermal (PV/T) air collectors.* Applied Energy, 2009. **86**(11): p. 2421-2428.

67. Joshi, A.S., et al., *Performance evaluation of a hybrid photovoltaic thermal (PV/T) (glass-to-glass) system.* International Journal of Thermal Sciences, 2009. **48**(1): p. 154-164.

68. Agrawal, B. and G.N. Tiwari, *Optimizing the energy and exergy of building integrated photovoltaic thermal (BIPVT) systems under cold climatic conditions.* Applied Energy, 2010. **87**(2): p. 417-426.

69. Skoplaki, E. and J.A. Palyvos, *Operating temperature of photovoltaic modules: A survey of pertinent correlations.* Renewable Energy, 2009. **34**(1): p. 23-29.

70. Clarke, J.A., et al., *Photovoltaic-integrated building facades.* Renewable Energy, 1996. **8**(1-4): p. 475-479.

71. Zogou, O. and H. Stapountzis, *Energy analysis of an improved concept of integrated PV panels in an office building in central Greece.* Applied Energy, 2011. **88**: p. 853-866.

72. Versteegh, T.A.M. and F.T.M. Nieuwstadt, *A direct numerical simulation of natural convection between two infinite vertical differentially heated walls scaling laws and wall functions.* International Journal of Heat and Mass Transfer, 1999. **42**(19): p. 3673-3693.

73. Versteegh, T.A.M. and F.T.M. Nieuwstadt, *Turbulent budgets of natural convection in an infinite, differentially heated, vertical channel.* International Journal of Heat and Fluid Flow, 1998. **19**(2): p. 135-149.

74. Mansour, N.N., J. Kim, and P. Moin, *Reynolds-stress and dissipation rate budget in a turbulent channel flow. .* J. Fluid Mech., 1988. **194**: p. 15-44.

75. Versteegh, T.A.M., *Natural Convection in an Infinite, Differentially Heated, Vertical Channel*, in *Ph.D. Thesis, Delft University of Technology*. 1998.

76. Dafa'Alla, A.A. and P.L. Betts, *Experimental study of turbulent natural convection in a tall cavity.* Exp. Heat Transfer, 1996. **9**: p. 165-194.

77. George, W.K. and S.P. Capp, *A theory for natural convection turbulent boundary layers next to heated vertical surfaces.* International Journal of Heat and Mass Transfer, 1979. **22**(6): p. 813-826.

78. Elder, J.W., *Turbulent free convection in a vertical slot.* J. Fluid Mech., 1965. **23**: p. 99-111.

79. Elder, J.W., *Numerical experiments with free convection in a vertical slot* J. Fluid Mech. , 1966. **24**: p. 823-843.

80. Vest, C.M. and V.S. Arpaci, *Stability of natural convection in a vertical slot.* J. Fluid Mech. , 1969(36): p. 1-15.

81. Chait, A. and S.A. Korpela, *The secondary flow and its stability for natural convection in a tall vertical enclosure.* J. Fluid Mech., 1989. **200** p. 189-216.

82. Betts, P.L. and I.H. Bokhari, *Experiments on turbulent natural convection in an enclosed tall cavity.* International Journal of Heat and Fluid Flow 2000. **21**: p. 675-683.

83. Fedorov, A.G. and R. Viskanda, *Turbulent natural convection heat transfer in an asymmetrically heated, vertical parallel-plate channel.* Int. J. Heat Mass Transfer, 1997. **40**(16): p. 3849-3860.

84. Shiri, A. and W.K. George. *Turbulent natural convection in a differentially heated vertical channel*. in *Proceedings of 2008 ASME Summer Heat Transfer Conference*. August 10-14, 2008,. Jacksonville, Florida USA,.

85. Tieszen, S., et al., *Modeling of natural convection heat transfer.* Center for Turbulence Research, Proceedings of the Summer Program 1998, 1998.

86. Di Piazza, I.D. and M. Ciofalo, *Low-Prandtl number natural convection in volumetrically heated rectangular enclosures I. Slender cavity, AR = 4.* International Journal of Heat and Mass Transfer, 2000. **43**(17): p. 3027-3051.

87. Van Doormaal, J.P. and G.D. Raithby, *ENHANCEMENTS OF THE SIMPLE METHOD FOR PREDICTING INCOMPRESSIBLE FLUID FLOWS.* Numerical heat transfer, 1984. **7**(2): p. 147-163.

88. Albets-Chico, X., A. Oliva, and C.D. Pérez-Segarra, *Numerical Experiments in Turbulent Natural Convection Using Two-Equation Eddy-Viscosity Models.* ASME Transactions, Journal of Heat Transfer, 2008. **130**(July 2008): p. 1-11.

89. Matsumoto, R., S. Kikkawa, and M. Senda, *Effect of pin fin arrangement on endwall heat transfer.* JSME Int. J. Series B, 1997. **40**: p. 142-151.

90. Cavallero, D. and G. Tanda, *An experimental investigation of forced convection heat transfer in channels with rib turbulators by means of liquid crystal thermography.* Experimental Thermal and Fluid Science, 2002. **26**(2-4): p. 115-121.

91. VDI and G.V.u. Chemieingenieurwesen, *Waermeatlas - Berechnungsblaettern fuer den Waermeuebergang*. 9 ed. 2002, Berlin, Heidelberg: Springer Verlag.

92. ASHRAE HANDBOOK, *Fundamentals*. 2009: American Society of Heating, Refrigerating, and Air-Conditioning Engineers.

93. Duffie, J.A. and W. A.Beckman, *Solar Engineering of thermal Processes*. 2 ed. 1980, New York: John Wiley & Sons.

94. NN, *T.E.S.S. Component Libraries for TRNSYS, version 2.0. User's Manual*. 2004, Madison WI: http://www.tess-inc.com/services/software.

95. Hollands K. G. T., et al., *Free Convection Heat Transfer Across Inclined Air Layers.* J. Heat Transfer, 1976. **98,189**.

96. Ayyaswamy, P.S. and I. Catton, *The Boundary-layer regime for natural convection in a differentially heated, tilted rectangular cavity.* J. Heat Transfer, 1973. **95**: p. 543-545.

97. Bar-Cohen, A. and W.M. Rohsenow, *Thermally optimum spacing of vertical, natural convection cooled, parallel plates.* Journal of Heat Transfer, 1984. **106**(1): p. 116-123.

98. Rohsenow, W.M., J.P. Hartnett, and Y.I. Cho, *Handbook of Heat Transfer*. 1998, New York: McGraw-Hill.

99. Sparrow, E.M. and L.F.A. Azevedo, *Vertical-channel natural convection spanning between the fully-developed limit and the single-plate boundary-layer limit.* International Journal of Heat and Mass Transfer, 1985. **28**(10): p. 1847-1857.

100. Sparrow, E.M., G.M. Chrysler, and L.F. Azevedo, *Observed Flow Reversals and Measured-Predicted Nusselt Numbers for Natural Convection in a One-Sided Heated Vertical Channel.* Journal of Heat Transfer, 1984. **106**(2): p. 325-332.

101. Shah, R.K. and A.L. London, *Laminar Flow Forced Convection in Ducts*. 1978, New York: Academic Press.

102. Heaton, H.S., W.C. Reynolds, and Kays W.M., *Heat Transfer in Annular Passages. Simultaneous Development of Velocity and Temperature Fields in Laminar Flow.* Int. J. Heat and Mass Transfer, 1264. **7**: p. 763.

103. Mercer, W.E., Pearce W.M., and J.E. Hitchcock, *Laminar Forced Convection in the Entrance Region Between Parallel Plates.* Trans. ASME, J. Heat Transfer, 1967. **89**: p. 251.

104. Petukhov, B.S., *In: T.F. Irvine and J.P. Hartnett, Eds., Advances in Heat Transfer, Vol. 6,*. 1970, Academic Press: New York.

105. Kakaç, S., R.K. Shah, and W. Aung, *Handbook of Single-Phase Convective Heat Transfer.* Wiley-Interscience, 1987.

106. Hatton A.P., James D.D., and Swire H.W., *Combined forced and natural convection with low-speed air flow over horizontal cylinders* J. Fluid Mech, 1970. **42**: p. 17-31.

107. Fedorov A.G. and Viskanda R., *Turbulent natural convection heat transfer in an asymmetrically heated, vertical parallel-plate channel.* Int. J. Heat Mass Transfer, 1997. **40**(16): p. 3849-3860.

108. Yilmaz, T. and S.M. Fraser, *Turbulent natural convection in a vertical parallel-plate channel with asymmetric heating.* International Journal of Heat and Mass Transfer, 2007. **50**: p. 2612-2623.

109. Miyamoto, M., et al. *Turbulent free convection heat transfer from vertical parallel plates*. 1986.

110. Fraser, S.M., A. Gilchrist, and T. Yilmaz. *Natural convection LDA measurements*. in *Laser Anemometry Advances and Applications, ASME,* . 1991. New York.

111. La Pica, A., G. Rodonò, and R. Volpes, *An experimental investigation on natural convection of air in a vertical channel.* International Journal of Heat and Mass Transfer, 1993. **36**(3): p. 611-616.

112. Kays W.M. and London A.L., *Compact Heat Exchangers*. 1964, New York: McGraw_Hill.

113. Dittus, F.W. and L.M.K. Boelter. Vol. 2. 1930, University of California, Berkley, Publications of Engineering, Vol 2, p.443,. 443.

114. http://www.cppsolar.com/web.

115. Barber, G.D., et al. *New Barrier Coating Materials for PV Module Backsheets*. in *29th IEEE PV Specialists Conference, New Orleans, Louisiana, May 20-24, 2002*. 2002.

116. Levy, S.B. and J. Cottrell, *Films and coatings for photovoltaic laminated module backsheet*, W.I.P. Organization, Editor. 2009: US.

117. Meyer, D.W., *Redundant electrical architecture for photovoltaic modules*, W.I.P. Organization, Editor. 2009, TENKSOLAR INC [US]: US.

118. Meyer, D.W., *Thin-film photovoltaic module*, U.P. Office, Editor. 2010, TENKSOLAR INC [US]: US.

119. Rummens, F., *Photovoltaic modules with polypropylene based backsheet*, W.I.P. Organization, Editor. 2011, RENOLIT BELGIUM N V [BE]: BE.

120. Sturzel, A., et al., *Photovoltaic module monochrome printing film, method for manufacturing same and use of same in the production of photovoltaic modules* E.P. Office, Editor. 2011, EMS PATENT AG [CH].

121. Burchill, M.T., et al., *Photovoltaic modules having a polyvinylidene fluoride*, U.P. Office, Editor. 2010, ARKEMA INC [US]: US.

122. Corfias-Zuccalli, C., et al., *Use of a polyethylene-based film in a photovoltaic module*, W.I.P. Organization, Editor. 2010, ARKEMA FRANCE [FR]: FR.

123. Gee, J.M., M. Aboudi, and F. Bagh, *Low-concentration flat profile photovoltaic modules*, W.I.P. Organization, Editor. 2010, APPLIED MATERIALS INC [US]: US.

124. Ge-Jiaxin, J., et al., *Thermoformable photovoltaic backsheet*, W.I.P. Organization, Editor. 2010, ARKEMA FRANCE [FR]: FR.

125. Ge-Jiaxin, J., et al., *Acrylic photovoltaic module backsheet*, W.I.P. Organization, Editor. 2010, ARKEMA FRANCE [FR]: FR.

126. Hanoka, J., *Frameless photovoltaic module*, W.I.P. Organization, Editor. 2007, EVERGREEN SOLAR INC [US]: US.

127. Stefani, F., A. Russo, and G. Aiazzi, *A progress for manufacturing photovoltaic panels*, W.I.P. Organization, Editor. 2010, SYSTEM PHOTONICS S P A [IT]: IT.

128. Temchenko, M., et al., *Heat dissipating protective sheets and encapsulant for photovoltaic modules*, W.I.P. Organization, Editor. 2010, MADICO INC [US]: US.

129. Tsuzuki, A., et al., *Backsheet for photovoltaic module, backside laminate for photovoltaic module, and photovoltaic module*, U.P. Office, Editor. 2010: JP.

130. Vogt, M., et al., *Polyamide-grafted polymers, photovoltaic modules with a backsheet film comprising a polyamide-grafted polymer and manufacturing process and use thereof* W.I.P. Organization, Editor. 2010, ARKEMA FRANCE [FR]; ETIMEX SOLAR GMBH [DE];: FR, DE.

131. Zhiyong, X., D. Cunningham, and J. Wohlgemuth, *Photovoltaic device with a polymeric mat and method of making the same*, W.I.P. Organization, Editor. 2010, BP CORP NORTH AMERICA INC [US]: US.

132. http://us.firstpvm.com/product.asp?ClassID=29.

133. http://www.coveme.com/Applications/20/29.

134. Florides, G.A., et al., *Review of solar and low energy cooling technologies for buildings.* Renewable and Sustainable Energy Reviews, 2002. **6**: p. 557–572.

135. TERREAL FAÇADE, *http://www.terrealfacade.com/*.

136. SIS Solar Ventures LTD., *http://www.sissolarventures.com/*.

137. Neymark, J., et al., *Applying the building energy simulation test (BESTEST) diagnostic method to verification of space conditioning equipment models used in whole-building energy simulation programs.* Energy and Buildings 2002. **34**: p. 917–931.

138. Himmler, R. *Energy Efficient Non-Residential Buildings: Examples and Experiences in Germany*. in *International Conference on Intelligent, Green and Energy-Efficient Building & New Technologies and Products Expo*. 2008. Beijing.

139. Zogou, O. and H. Stapountzis, *Experimental validation of an improved concept of building integrated PV panels.* Renewable Energy, 2011. **accepted for publication**.

140. Faranda, R. and S. Leva, *Energy comparison of MPPT techniques for PV Systems* WSEAS Transactions on Power Systems 2008. **3**(6): p. 446-455.

141. NN. *http://www.sissolarventures.com/*. 2007.

142. Dirmhirn, I., *Untersuchungen an Sternpyranometern.* Archiv fuer Meteorologie, Geophysik und Bioklimatologie Serie B, 1958. **9**(2): p. 124-148.

143. Umbertini, S. and U. Desideri, *Performance estimation and experimental measurements of a photovoltaic roof.* Renewable Energy, 2003. **28**: p. 1833-1850.

144. Huld, T., M. Suri, and E.D. Dunlop, *Geographical variation of the conversion efficiency of crystalline silicon photovoltaic modules in Europe.* Progress in Photovoltaics: Research and Applications, 2008. **16**(7): p. 595-607.

145. Piao, Z.G., et al. *Performance assessment of 3kW grid-connected PV systems in Korea*. in *INTELEC, International Telecommunications Energy Conference (Proceedings)*. 2009.

146. Fanney, A.H., B.P. Dougherty, and M.W. Davis, *Measured Performance of Building Integrated Photovoltaic Panels.* ASME Transactions, Journal of Solar Energy Engineering, 2001. **123**: p. 187-193.

147. Duffie, J.A. and W.A. Beckman, *Solar Engineering Of Thermal Processes*. 1980, New York: John Wiley & Sons, Inc.

148. Perez-Lopez, J.J., F. Fabero, and F. Chenlo, *Experimental Solar Spectral Irradiance Until 2500 nm: Results and Influence on the PV Conversion of Different Materials.* Prog. Photovolt: Res. Appl., 2007. **15**: p. 303–315.

149. Ranganathan, R., et al., *Adaptive sun tracking algorithm for incident energy maximization and efficiency improvement of PV panels.* Renewable Energy, 2011. **36**(10): p. 2623-2626.

150. King, D.L., W.E. Boyson, and J.A. Kratochvil. *Analysis of factors influencing the annual energy production of photovoltaic systems*. 2002.

151. Alonso García, M.C. and J.L. Balenzategui, *Estimation of photovoltaic module yearly temperature and performance based on Nominal Operation Cell Temperature calculations.* Renewable Energy, 2004. **29**(12): p. 1997-2010.

152. Ross, R.G.J. and M.I. Smokler, *Flat-Plate Solar Array Project Final Report, Volume VI*, in *Engineering Sciences and Reliability*. 1986 p. 86-31.

153. Raffel, M., C. Willert, and J. Kompenhans, *Particle image velocimetry - a practical guide*. Second ed. 1998, Berlin, Heidelberg, New York, Barcelona, Budapest: Springer Verlag Berlin, Heidelberg, New York, Barcelona, Budapest.

154. Zogou, O. and H. Stapountzis, *Flow Visualization and Turbulence Measurements inside a PV/T Collector for Building Applications.* Applied Energy, 2011. **submitted for publication**.

155. Tropea, C., A.L. Yarin, and J.F. Foss, *Springer Handbook of Experimental Fluid Mechanics*. 2007: Springer-Verlag Berlin Heidelberg.

156. Uberoi M.S. and Corrsin S., *Spectra and diffusion in a round turbulent jet*, in *NACA Rep. 1040*. 1951.

157. Heywood, J.B., *Internal combustion engine fundamentals*. 1988, New York: McGraw-Hill.

158. Tennekes, H. and J.C. Lumley, *A First Course in Turbulence*. 1972, Cambridge, Mass.: The MIT Press.

159. http://www.ansys.com/Products/Simulation+Technology.

160. ANSYS CFX, *User Manual,*. 2009.

161. Menter F. R., *Two-Equation Eddy-Viscosity Turbulence Models for Engineering Applications.* AIAA Journal, 1994. **32**(8): p. 1598-1605.

162. Moran, M.J., et al., *Introduction to Thermal Systems Engineering: Thermodynamics, Fluid Mechanics and Heat Transfer*. 2003, New York: John Wiley & Sons, Inc.

163. Hatton, A.P., A. Quarmby, and I. Grundy, *Further calculations on the heat transfer with turbulent flow between parallel plates.* Int. J. Heat Mass Transfer, 1964. **7**: p. 817–823.

164. Lumley, J.L., *Engines: An Introduction*. 1999, New York: Cambridge University Press.

165. J. Neymark and R. Judkoff, *International Energy Agency Building Energy Simulation Test and Diagnostic Method for Heating, Ventilating, and Air-Conditioning Equipment Models (HVAC BESTEST) Volume 1: Cases E100-E200*. NREL/TP-550-30152 January 2002.

166. Greek_Republic, *Approval of Buildings' Energy Performance Regulation*. 2010, Ministerial Decision Δ6/Β/5825/9.4.2010.

167. Hollands, K.G.T., et al., *Free Convection Heat Transfer Across Inclined Air Layers.* J. Heat Transfer, 1976. **98,189**.

168. Frank P. Incropera, et al., *Introduction to Heat Transfer*. 5th ed. 2007, New York: JOHN WILEY & SONS.

169. Zogou, O. and A. Stamatelos, *Application of Building Energy Simulation in the Sizing and Design Optimization of an Office Building and its HVAC Equipment* in *Energy and Buildings: Efficiency, Air Quality, and Conservation*, J.B. Utrick, Editor. 2009, NOVA Publishers.

170. CEN, *CEN/TC 169 PrEN 15193: Energy performance of buildings - Energy requirements for lighting.* 2006-2007.

171. CEN, *CEN/TC 156, prEN 13779 -Ventilation for non-residential buildings - Performance requirements for ventilation and room-conditioning systems.* 2006-2007.

172. CEN, *CEN/TC 156, prEN 15251- Indoor environmental input parameters for design and assessment of energy performance of buildings addressing indoor air quality, thermal environment, lighting and acoustics.* 2006-2007.

173. Yeadon, W.H. and A.W. Yeadon, *Handbook of Small Electric Motors*. 2001, New York: McGraw Hill.

174. Mei, L., et al., *Cooling potential of ventilated PV facade and solar air heaters combined with a desiccant cooling machine.* Renewable Energy, 2006. **31**(8): p. 1265-1278.

175. Zogou, O. and H. Stapountzis. *Optimized Transient Response of Building Integrated PV panels*. in *Conference on the promotion of Distributed Renewable Energy Sources in the Mediterranean region*. 2009. December 11th - 12th, Nicosia, Cyprus.

176. CEN, *CEN/TC 169 PrEN 1536-1: Heating systems in buildings –method for calculation of system energy requirements and system efficiencies – part 1: General.* 2006-2008.

177. Chow, T.T., et al., *Annual performance of building-integrated photovoltaic/water-heating system for warm climate application.* Applied Energy, 2009. **86**(5): p. 689-696.

178. Incropera, F., et al., *Fundamentals of Heat and Mass Transfer*. Sixth ed. 2006, New York: JOHN WILEY & SONS.

179. Díez, L.I., et al., *Thermal analysis of rough micro-fins of variable cross-section by the power series method.* International Journal of Thermal Sciences, 2010. **49**(1): p. 23-35.

180. Cooper P. I., *The absortion of radiation in solar stills.* Solar Energy, 1969. **12**: p. 333-346.

181. http://www.pveducation.org.

182. http://energyworksus.com.

183. NN, *CEN/TC 89/WG 4 N 249: Energy performance of buildings – Calculation of energy use for space heating and cooling*. 2004.

ANNEX I : DEFINITIONS (SOLAR ANGLES)

The following definitions are employed.

Air Mass m. The ratio of the mass of the atmosphere through which beam radiation passes to the mass it would pass through if the sun were at the zenith (i.e.. directly overhead). Thus at sea level, ***m =*** 1 when the sun is at the zenith, and ***m =*** 2 for a zenith angle θ_Z of 60°. For zenith angles from 0° to 70° at sea level, to a close approximation,

$$m = I/\cos \theta_Z \qquad \textbf{(eq. 1)}$$

Beam Radiation. The solar radiation received from the sun without having been scattered by the atmosphere. (Beam radiation is often referred to as direct solar radiation)

Diffuse Radiation. The solar radiation received from the sun after its direction has been changed by scattering by the atmosphere.

Total Solar Radiation. The sum of the beam and the diffuse solar radiation on a surface. (The most common measurements of solar radiation are total radiation on a horizontal surface, often referred to as global radiation on the surface.)

Irradiance*[W/m^2]** The rate at which radiant energy is incident on a surface, per unit area of surface. The symbol ***I is used for solar irradiance, with appropriate subscripts for beam, diffuse, or spectral radiation.

Solar Time. Time based on the apparent angular motion of the sun across the sky, with solar noon the time the sun crosses the meridian of the observer.

Solar time is the time used in all of the sun-angle relationships. It does not coincide with local clock time. It is necessary to convert standard time to solar time by applying two corrections. First, there is a constant correction for the difference in longitude between the observer's meridian (longitude) and the meridian on which the local standard time is based. The sun takes 4 minutes lo transverse 1° of longitude. The second correction is from the equation of time, which takes into account the perturbations in the earth's rate of rotation which affect the time the sun crosses the observer's meridian. The difference in minutes between solar time and standard time is

$$\textbf{Solar time} - \textbf{standard time} = 4\,(\textbf{Lst} - \textbf{Lloc}) + \textbf{E} \quad \textbf{(eq. 2)}$$

Where $L_{st}$is the standard meridian for the local time zone and L_{loc} is the longitude of the location. The Local Standard Time Meridian (LSTM) is a reference meridian used for a particular time zone and is similar to the Prime Meridian, which is used for Greenwich Mean Time.

The equation of time E (in minutes) is determined from Equation

$$E = 229.2\,(0.00075 + 0.001868\,cos\,B - 0.032077\,sin\,B - 0.014615\,cos2B - 0.04089\,sin2B) \quad \textbf{(eq. 3)}$$

Where

$$\mathbf{B} = (\mathbf{n} - \mathbf{1})\ 360/365 \quad \textbf{(eq. 4)}$$

n= day of the year. Thus 1≤ n ≤ 365

The corrections for equations of time and displacement from the standard meridian are in minutes. Time is usually specified in hours and minutes.

The geometric relationships between a plane of any particular orientation relative to the earth at any time (whether that plane is fixed or moving relative to the earth) and the incoming beam solar radiation, that is, the position of the sun relative to that plane, can be described in terms of several angles

The angles are as follows:

φ Latitude (Figure A. 1), the angular location north or south of the equator, north positive: -9O°≤ ϕ≤9O°.

δ Declination (Figure A. 1), the angular position of the sun at solar noon (i.e., when the sunis on the local meridian) with respect to the plane of the equator, north positive:-23.45° ≤ δ≤23.45°.

The declination δcan be found from the equation of Cooper (1969)[180]:

$$\delta = 23.45^0\,\sin(\tfrac{360}{365}\ \ 284 + n\ ) \quad \textbf{(eq. 5)}$$

n= day of the year

ϑz Zenith angle, the angle between the vertical and the line to the sun, the angle of incidence of beam radiation on a horizontal surface (Figure A. 2)

α_s Solar altitude angle (elevation angle), the angle between the horizontal and the line to the sun, i.e. the complement of the zenith angle. The sum of altitude angle and zenith angle equals 90^0.The maximum elevation angle occurs at solar noon and depends on the latitude and declination angle (Figure A. 2).

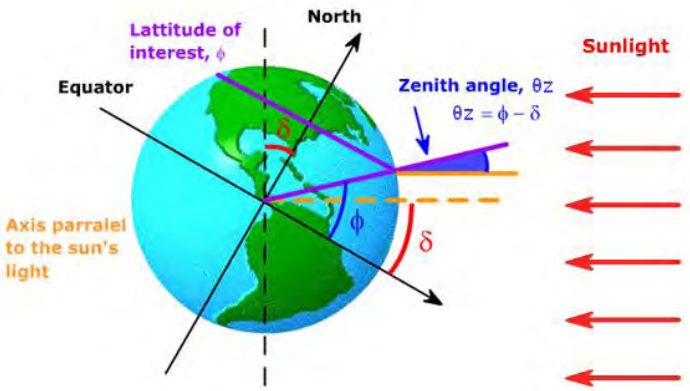

Figure A. 1 Latitude(*φ*), declination (*δ*) and zenith angle(*ϑz*), adapted from [181]

We calculate the solar altitude angle, α_S using the equation:

$$\sin \alpha_S = \cos \theta_z = \cos \varphi \cos \delta \cos\omega + \sin \varphi \sin \delta \quad \textbf{(eq. 6)}$$

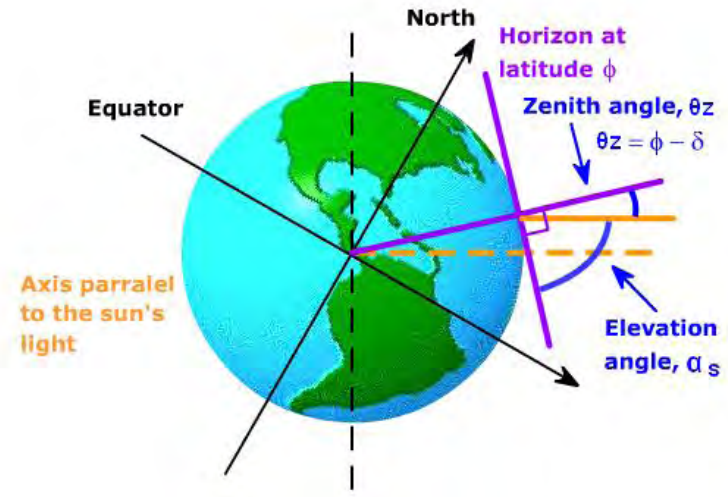

Figure A. 2 Zenith(*ϑz*)and Solar altitude (elevation)angle(*α_s*), adapted from[181]

y_s Solar azimuth angle, the angular displacement from south of the projectionof beam radiation on the horizontal plane ().

ω Hour angle, the angular displacement of the sun east or west of the local meridian due to rotation of the earth on its axis at 15° per hour, morning negative, afternoon positive.

ϑ Angle of incidence, the angle between the beam radiation on a surface and the normal to that surface. Additional angles are defined that describe the position of the sun in the sky:

β Slope, the angle between the plane of the surface in question and the horizontal $0 < \beta < 180°$. ($\beta > 90°$means that the surface has a downward facing component), (Figure A. 3).

γ Surface azimuth angle, the deviation of the projection on a horizontal plane of the normal to the surface from the local meridian, with zero due south, east negative, and west positive; $-180° < \gamma < 180°$ (Figure A. 3).

The geometrical position of the sun relative to a location is specified by an altitude angle $\alpha_s$and an azimuth angle $\gamma_s$ofa coordinate centered at the point of observation on earth.

In the Northern (Southern) Hemisphere, the solar azimuth is referenced to south (North) and is defined as positive towards the west, that is, in the evening, and negative towards the East, that is, in the morning.

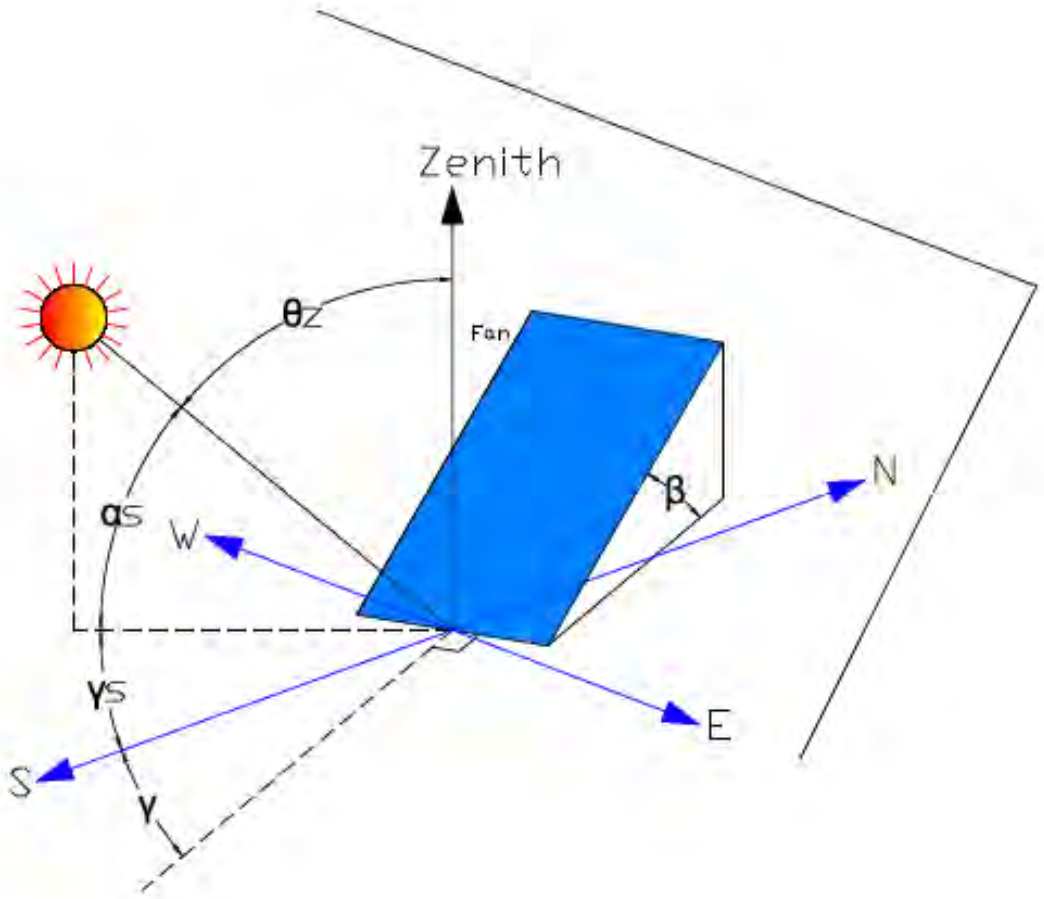

Figure A. 3 Zenith (θ_z), Solar altitude (α_s),Solar azimuth angle (γ_s), Slope (β), Surface azimuth (γ) for a tilted surface

ANNEX II: INCIDENT SOLAR RADIATION CALCULATIONS

The amount of solar radiation incident on a tilted surface is the component of solar radiation perpendicular to the surface (Figure A. 4). The following figure shows how to calculate the radiation incident on a titled surface (I_{module}) given either the solar radiation measured on the horizontal surface ($I_{horizontal}$) or the solar radiation measured perpendicular to the sun ($I_{incident}$). The equations relating I_{module}, $Ih_{orizontal}$ and $I_{incident}$ are:

$$\mathbf{I_{horizontal} = I_{incident} sin a_s} \quad \textbf{(eq. 7)}$$

$$\mathbf{I_{module} = I_{incident} sin(a_s + \beta)} \quad \textbf{(eq. 8)}$$

The elevation angle:

$$\mathbf{a_s = 90 - \varphi - \delta} \quad \textbf{(eq. 9)}$$

From these equations a relationship between S_{module} and $S_{horizontal}$ can be given as:

$$\mathbf{I_{module} = \frac{I_{horizontal}\ sin(a_s+\beta)}{sin\, a_s}} \quad \textbf{(eq. 10)}$$

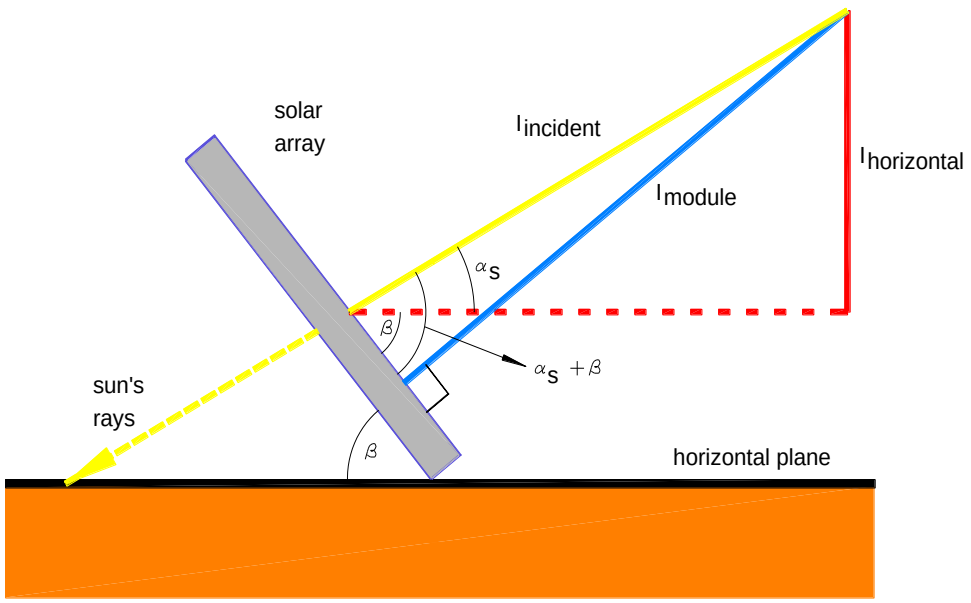

β IS THE TILT ANGLE OF THE MODULE MEASURED FROM THE HORIZONTAL. ADAPTED FROM [182]

Figure A. 4 Tilting the module to the incoming light reduces the module output.

An important parameter in the design of photovoltaic systems is the maximum elevation angle, that is, the maximum height of the sun in the sky at a particular time of the year. This maximum elevation angle occurs at solar noon and depends on the latitude and declination [183].

ANNEX III: FLOW VISUALIZATION VIDEOS

NAME	POSITION	FLOWRATE	
111027	UP	190m^3/h	honeycomb
11109	UP	190 m3/h	honeycomb
11314	UP	190 m3/h	honeycomb
11543	UP	190 m3/h	honeycomb
13825	***UP***	***Natural***	
14818	UP	110m^3/h	honeycomb
20604	Down	110m^3/h	honeycomb
20713	Down	110m^3/h	honeycomb
21505	Down	110m^3/h	honeycomb
22223	***Down***	***Natural***	
22441 (more left)	***Down***	***Natural***	
22808	Down	190 m3/h	honeycomb
23007	Down	190 m3/h	honeycomb
23224	Down	190 m3/h	honeycomb

ANNEX IV: HEAT TRANSFER COEFFICIENTS IN CFX

Fixed Temperature

The wall boundary is fixed at a specified ***Tw.*** The heat flux into the domain is calculated for laminar flows from the temperature gradient at the wall, and for turbulent flows by:

$$q_w = h_c \ T_w - T_{nw} \quad \textbf{(eq. 11)}$$

Where ***Tnw.***is the near wall temperature and hc involves the use of turbulent wall functions.

Wall Heat Transfer Coefficient (h_c) and Wall Adjacent Temperature (T_{nw}) From Ansys

These two variables are calculated as part of the convective heat transfer at a wall.

Laminar flow model:

- Wall Heat Transfer Coefficient, **hc**, is calculated by rearranging the expression for the convective heat flux in Equation 11.9 and setting the wall temperature as described above.
- Wall Adjacent Temperature, **Tnw** , is the average temperature in the element adjacent to the wall.

Turbulent flow model:

Wall Heat Transfer Coefficient is given by the thermal wall functions. The theory of thermal wall functions can be found at Heat Flux in the Near-Wall Region in the CFX-Solver Theory Guide. For turbulent flow without viscous work active, the Wall Adjacent Temperature is the conservative (solved for) temperature in the control volume adjacent to the wall. On the other hand, if viscous work is active, the Equation of Heat Flux in the CFX-Solver Theory Guide, can be rearranged as:

$$q_w = \frac{\tau_w c_p}{Pr_t U} \ T_w - T_f - \frac{Pr_t U^2}{2c_p} \quad \textbf{(eq. 12)}$$

Therefore, with viscous work active, the Wall Adjacent Temperature becomes:

$$T_{nw} = T_f + \frac{Pr_t U^2}{2c_p} \quad \textbf{(eq. 13)}$$

ANNEX V: MORE PSD SPECTRA FROM HOT-WIRE MEASUREMENTS

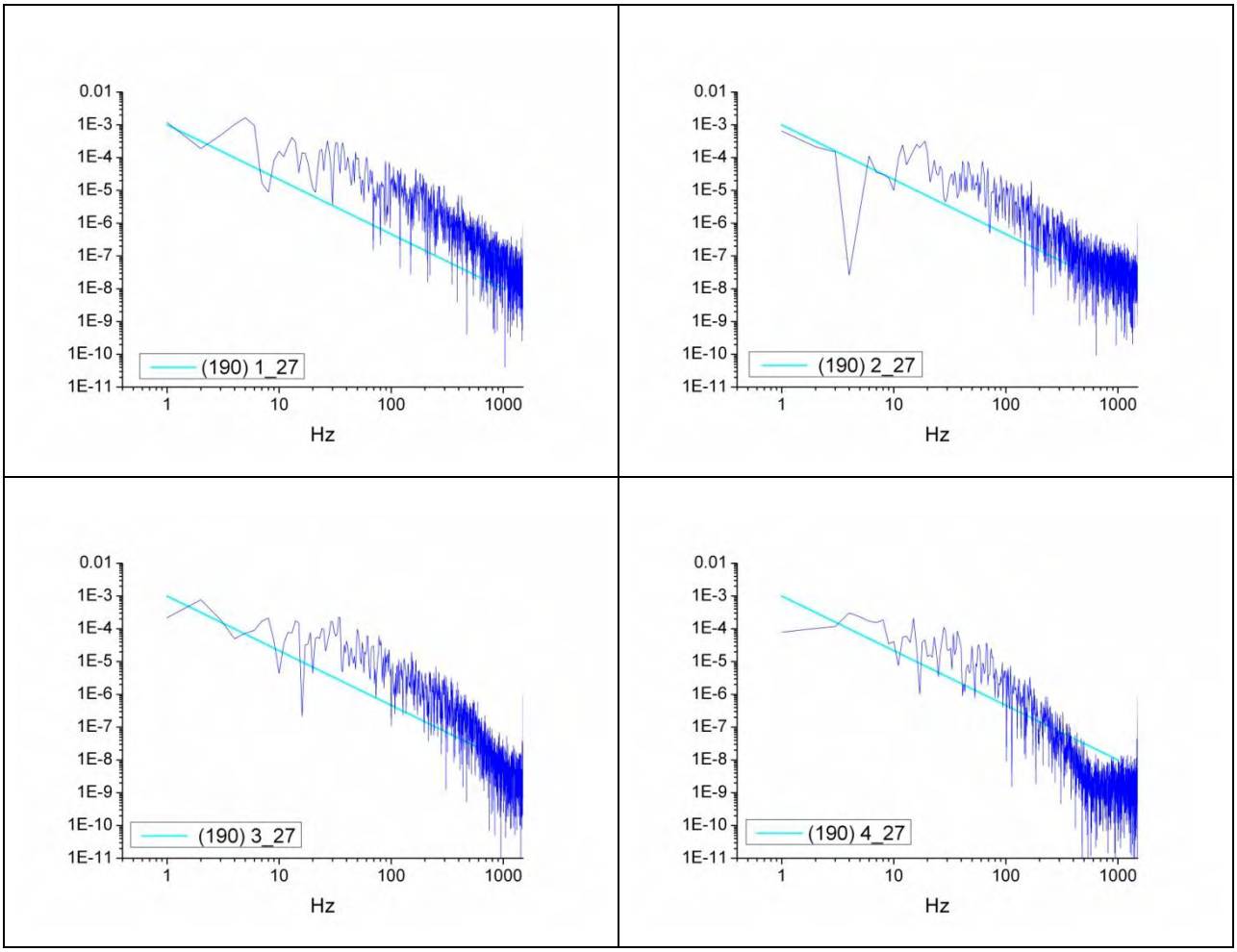

Figure A. 5 PSD spectrum, high capacity fan -190 m^3/h. Position nearest to the PV panel wall, for the 4 different vertical positions (UX1: z=400, UX2: z=700, UX3: z=1000, UX4: z=1300 mm from bottom), along the vertical centerline (x=147.50 mm).

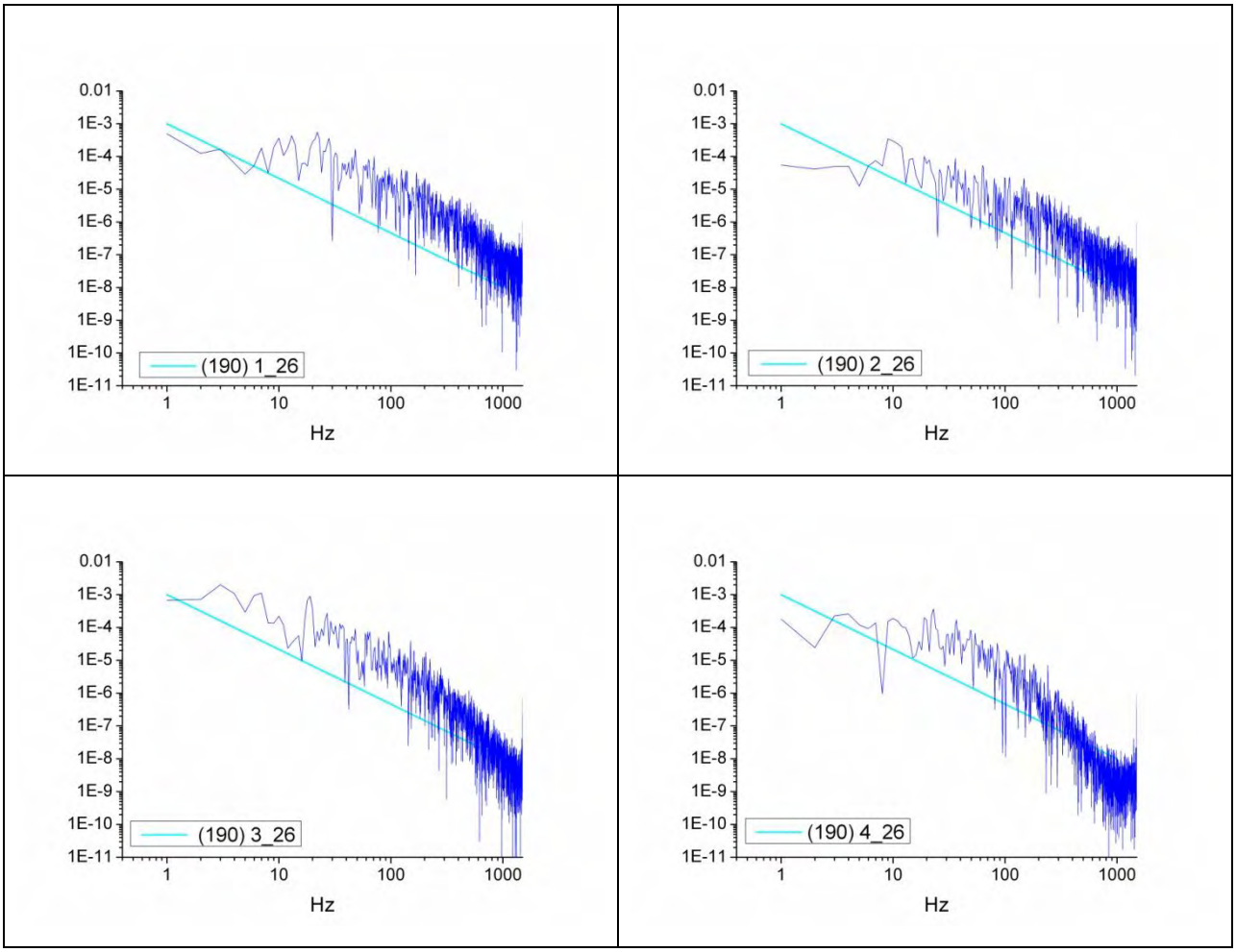

Figure A. 6 PSD spectrum, high capacity fan -190 m^3/h. Position nearest to the PV panel wall, for the 4 different vertical positions (UX1: z=400, UX2: z=700, UX3: z=1000, UX4: z=1300 mm from bottom), along the vertical centerline (x=146.250 mm).

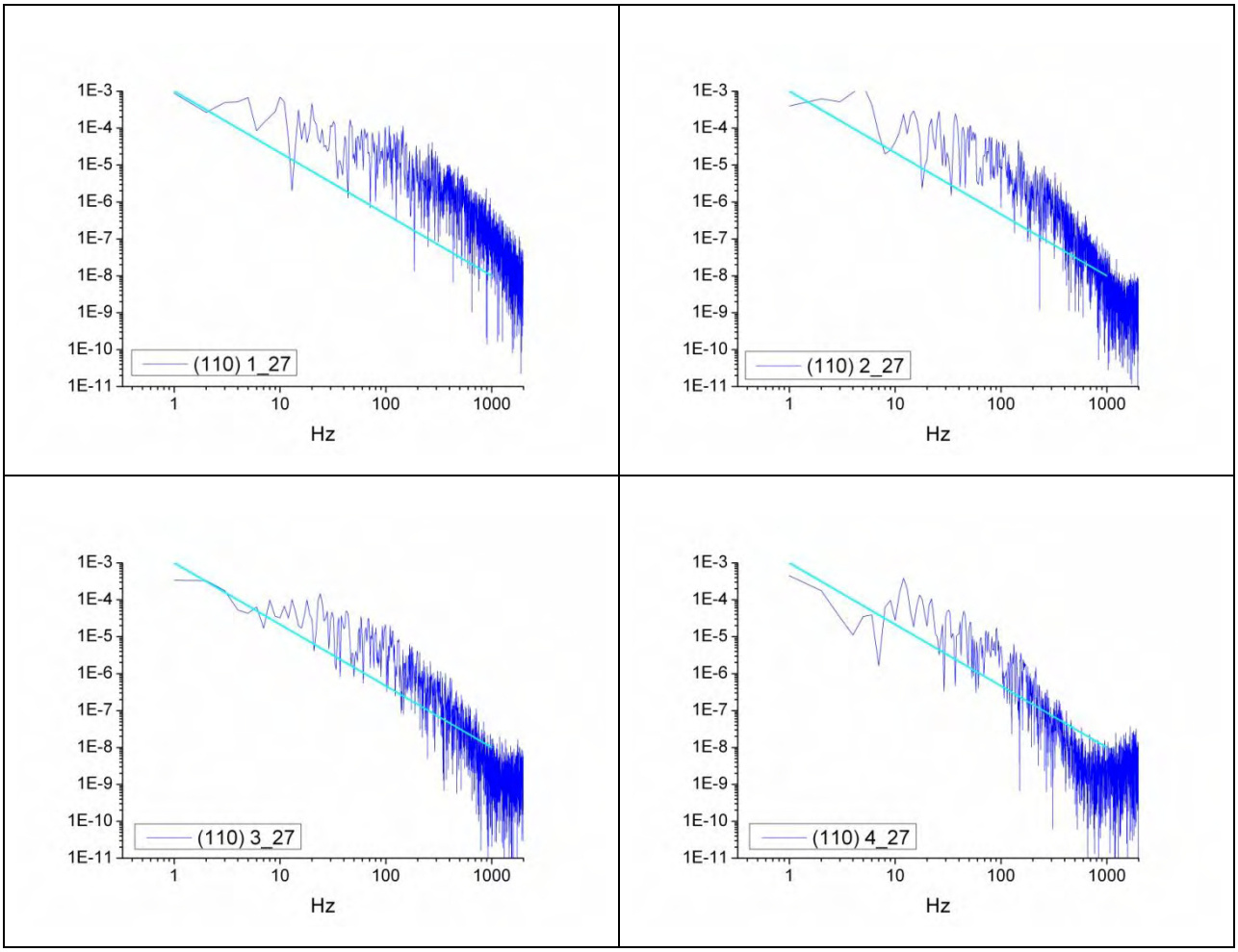

Figure A. 7 PSD spectrum, low capacity fan -110 m^3/h. Position nearest to the PV panel wall, for the 4 different vertical positions (UX1: z=400, UX2: z=700, UX3: z=1000, UX4: z=1300 mm from bottom), along the vertical centerline (x=147.50 mm).

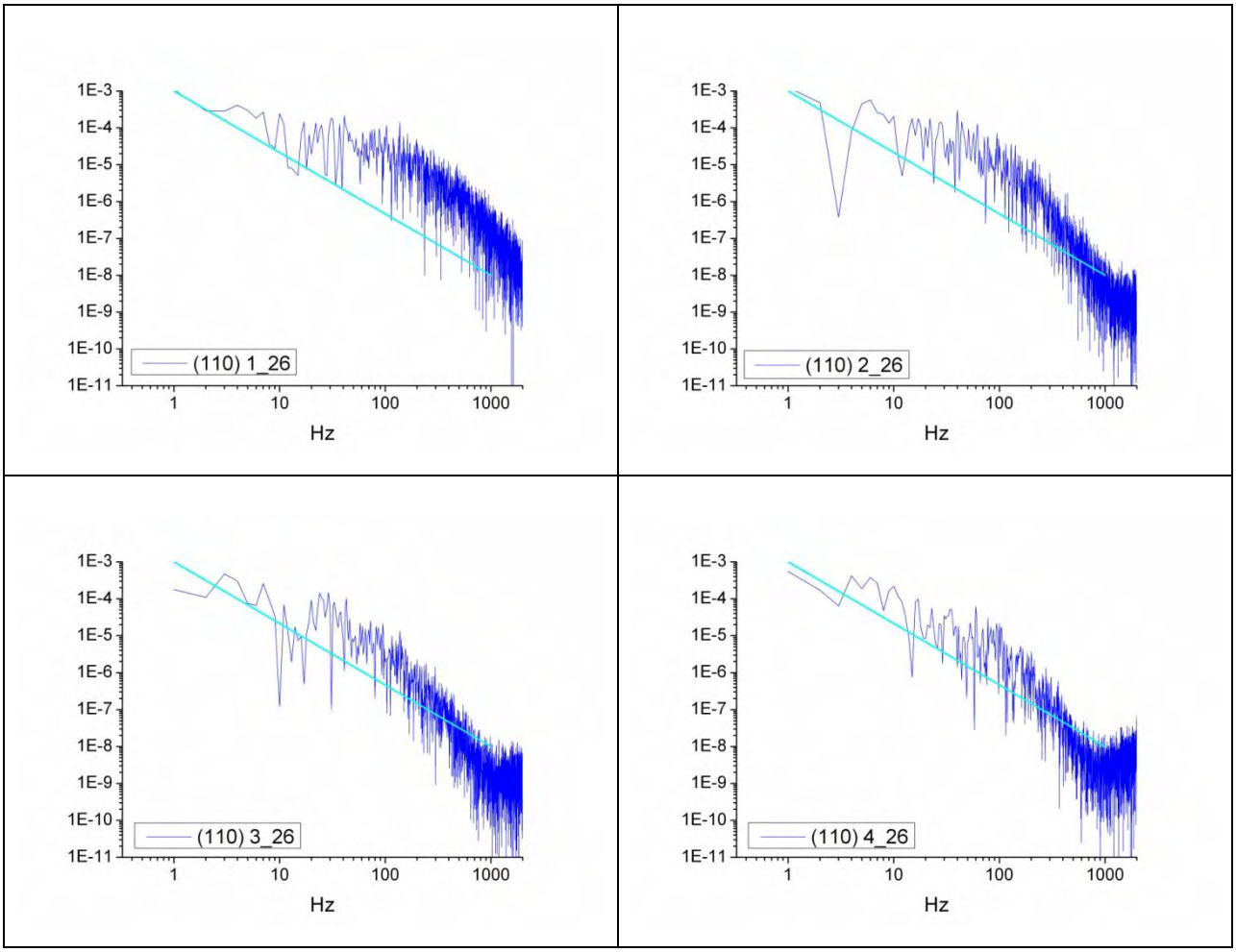

Figure A. 8 PSD spectrum, low capacity fan -110 m^3/h. Position nearest to the PV panel wall, for the 4 different vertical positions (UX1: z=400, UX2: z=700, UX3: z=1000, UX4: z=1300 mm from bottom), along the vertical centerline (x=146.25 mm).

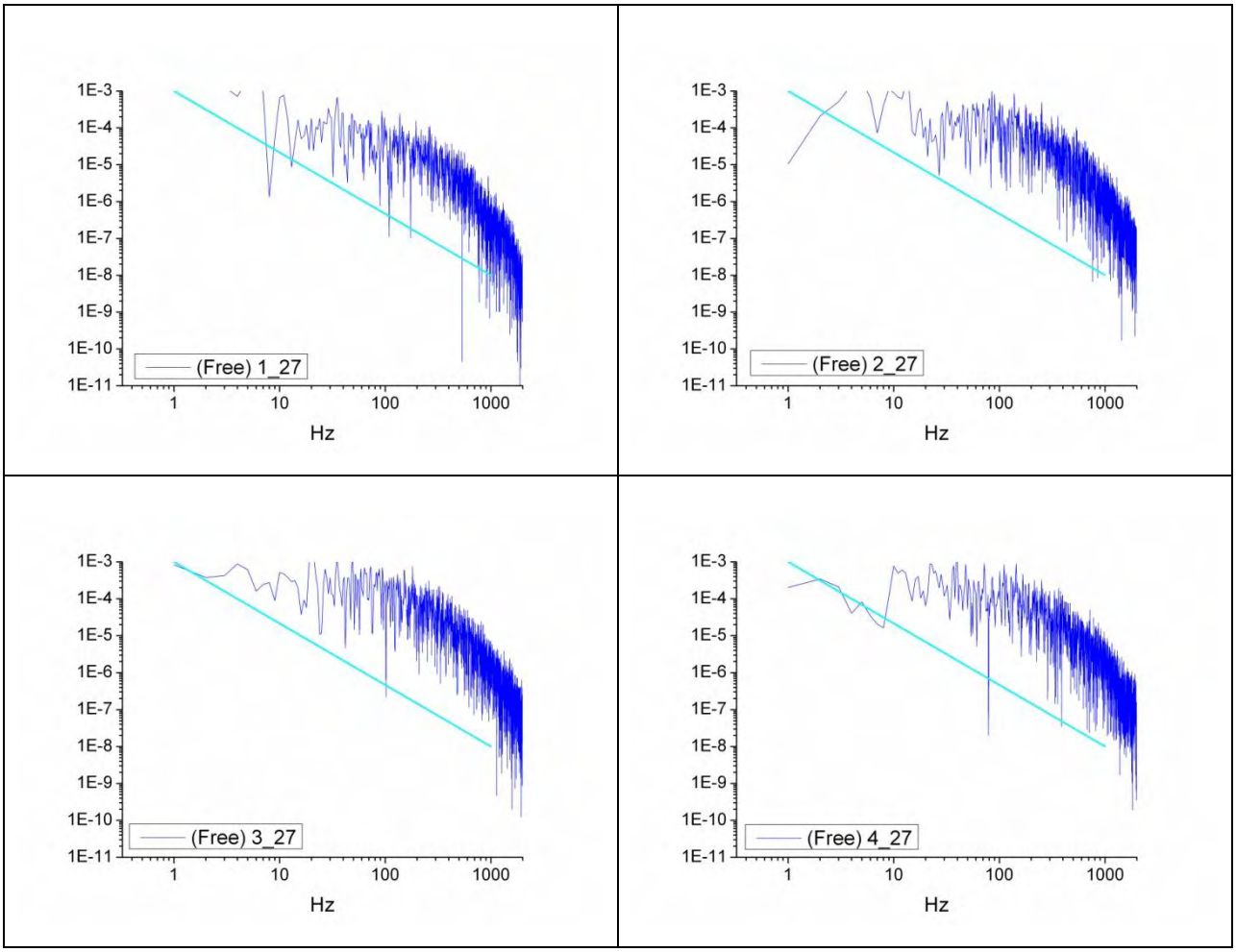

Figure A. 9 PSD spectrum, buoyancy flow experiment. Position nearest to the PV panel wall, for the 4 different vertical positions (UX1: z=400, UX2: z=700, UX3: z=1000, UX4: z=1300 mm from bottom), along the vertical centerline (x=147.50 mm).

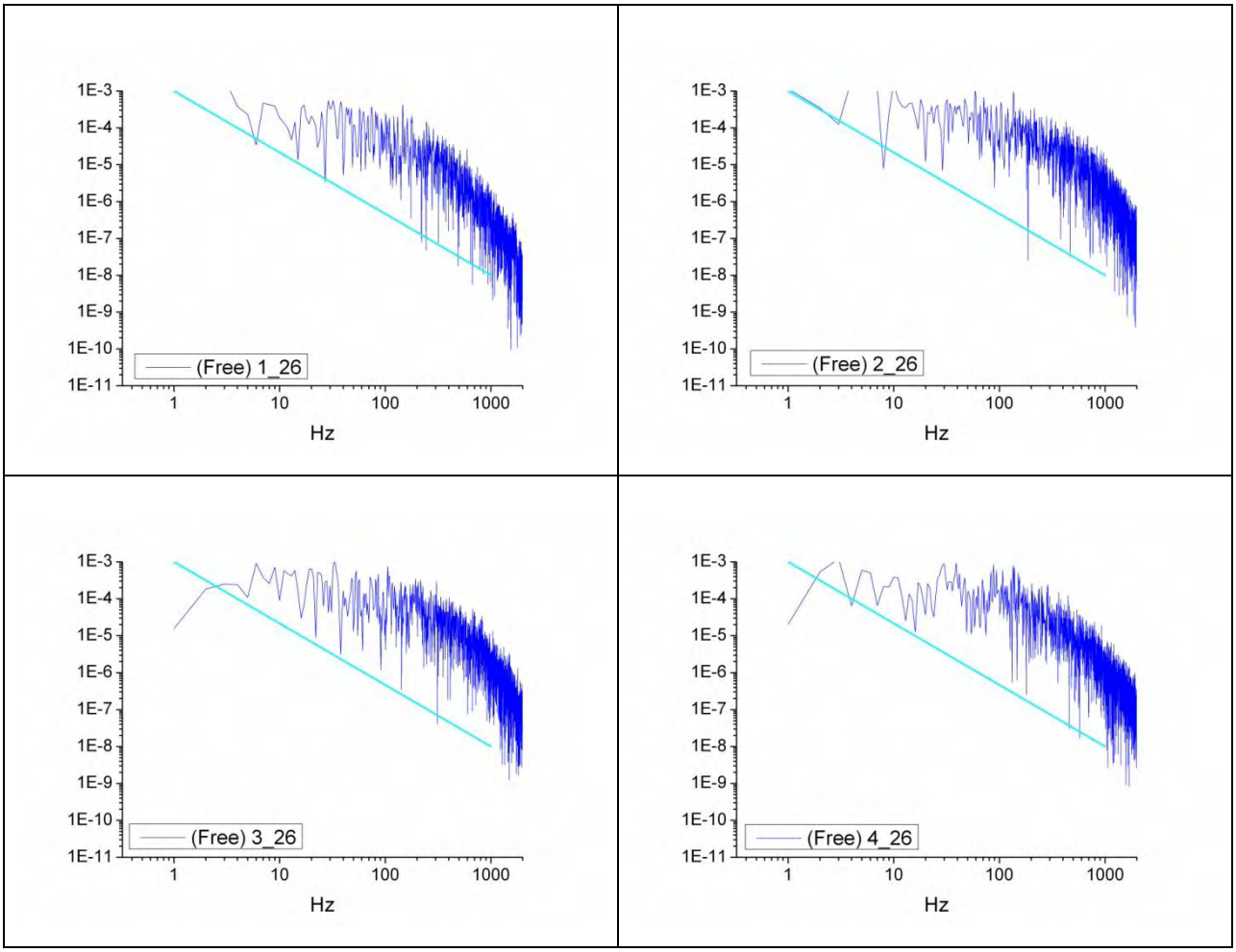

Figure A. 10 PSD spectrum, buoyancy flow experiment. Position nearest to the PV panel wall, for the 4 different vertical positions (UX1: z=400, UX2: z=700, UX3: z=1000, UX4: z=1300 mm from bottom), along the vertical centerline (x=146.25 mm).

ANNEX VI: LABVIEW CODE EMPLOYED IN THE MEASUREMENTS

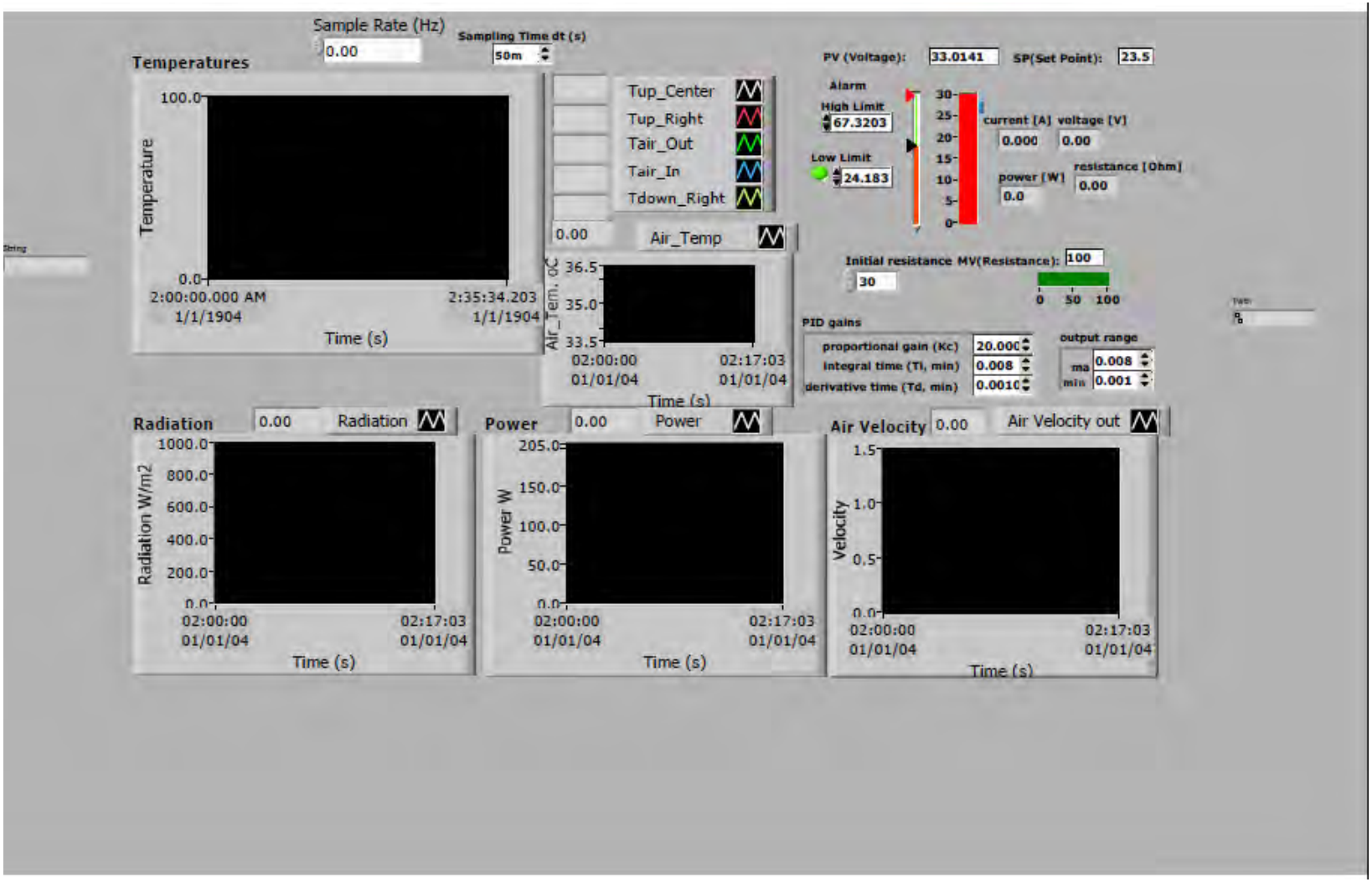

Figure A. 11 LabView Front Panel of the program employed in the measurements

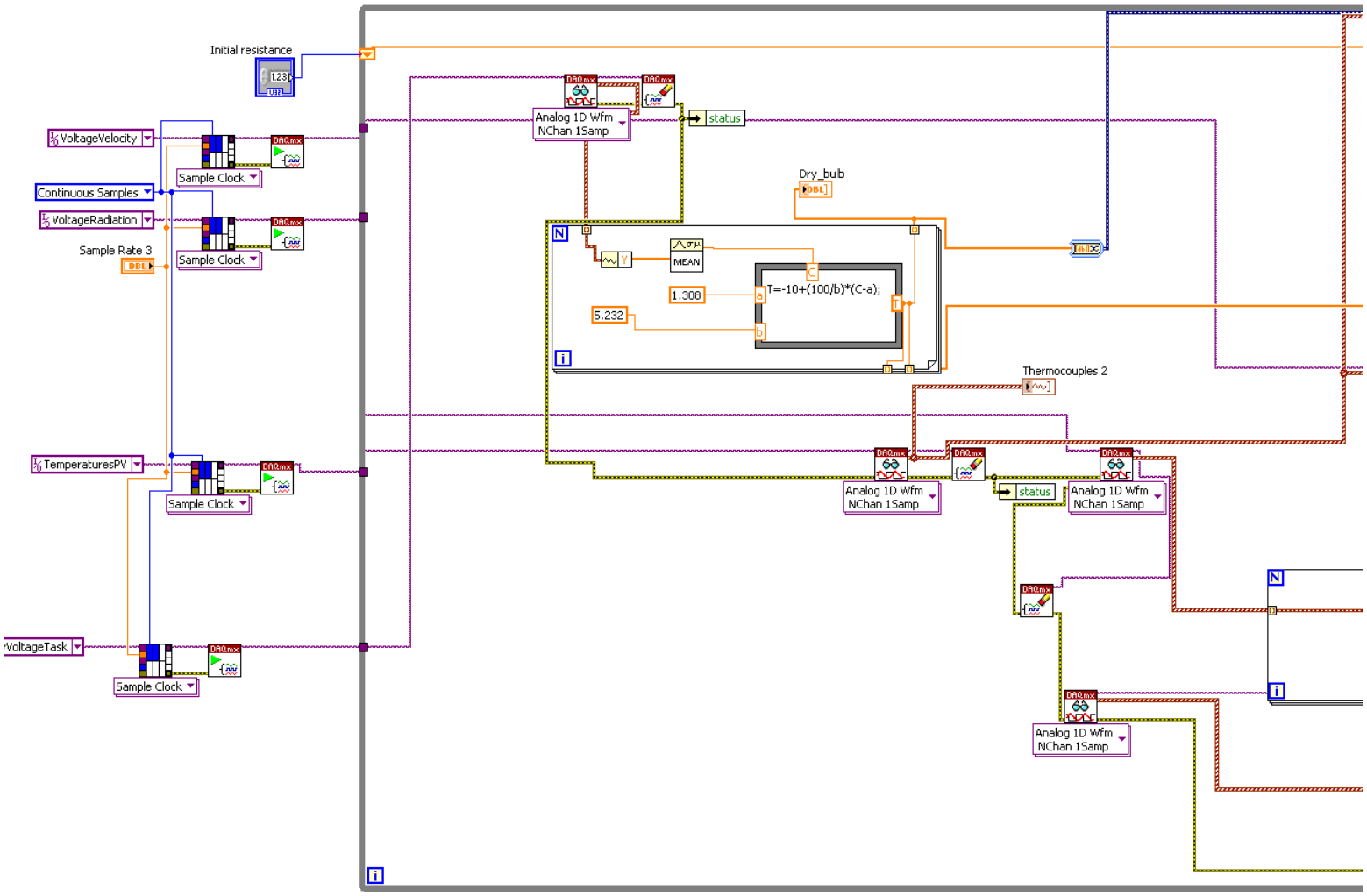

Figure A. 12 LabView Block Diagram of the program employed in the measurements

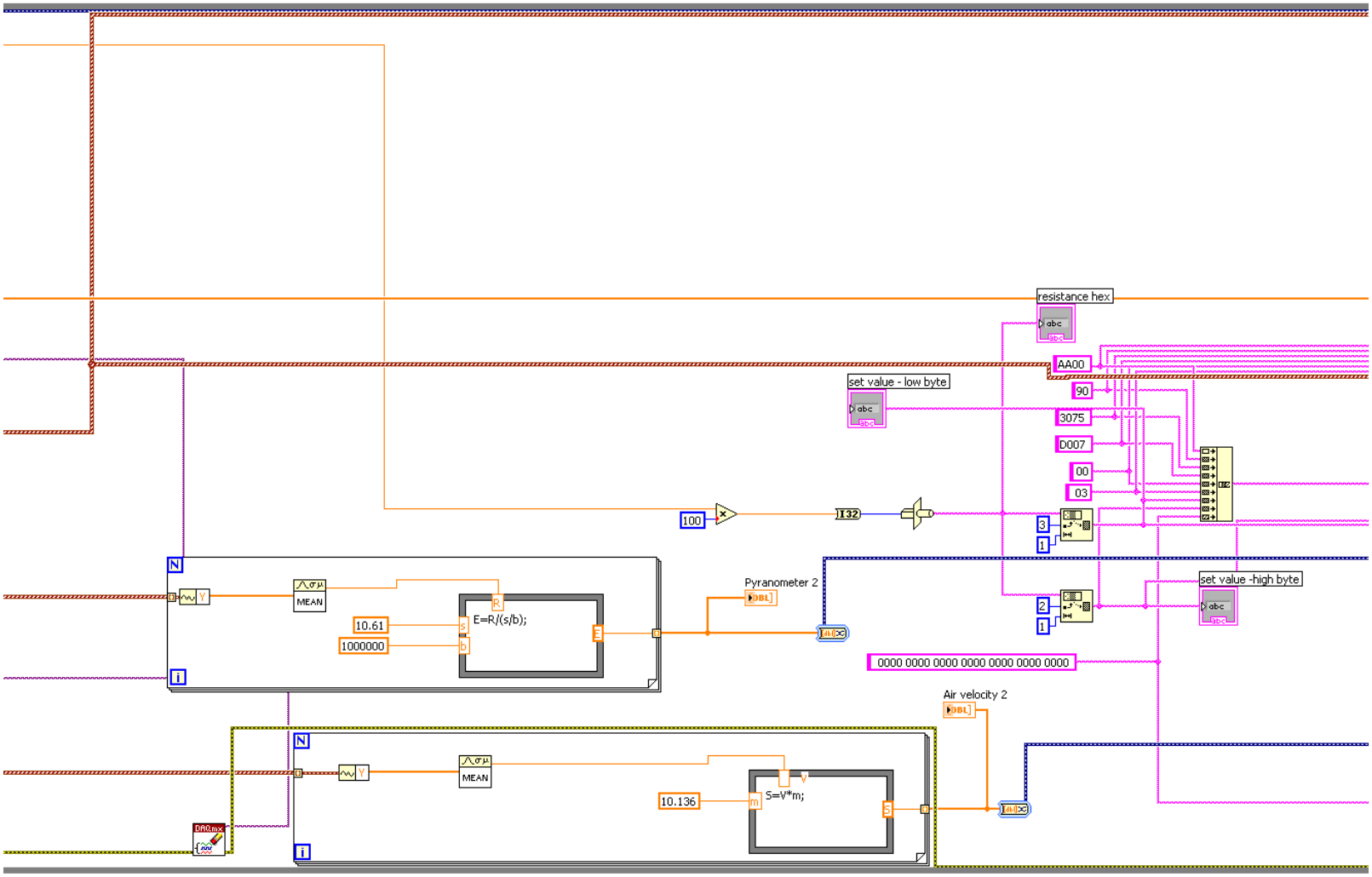

Figure A. 13 LabView Block Diagram of the program employed in the measurements

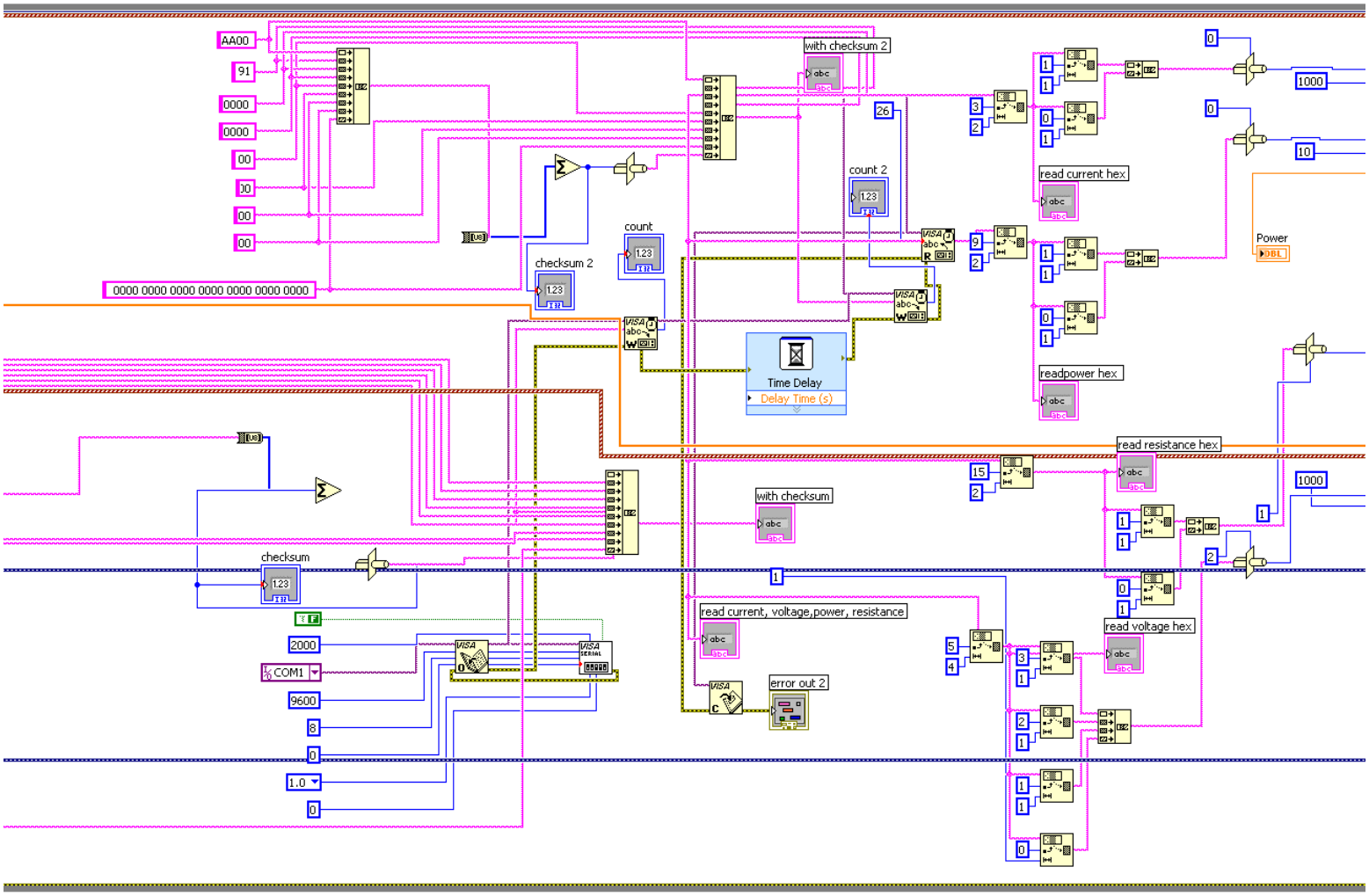

Figure A. 14 LabView Block Diagram of the program employed in the measurements

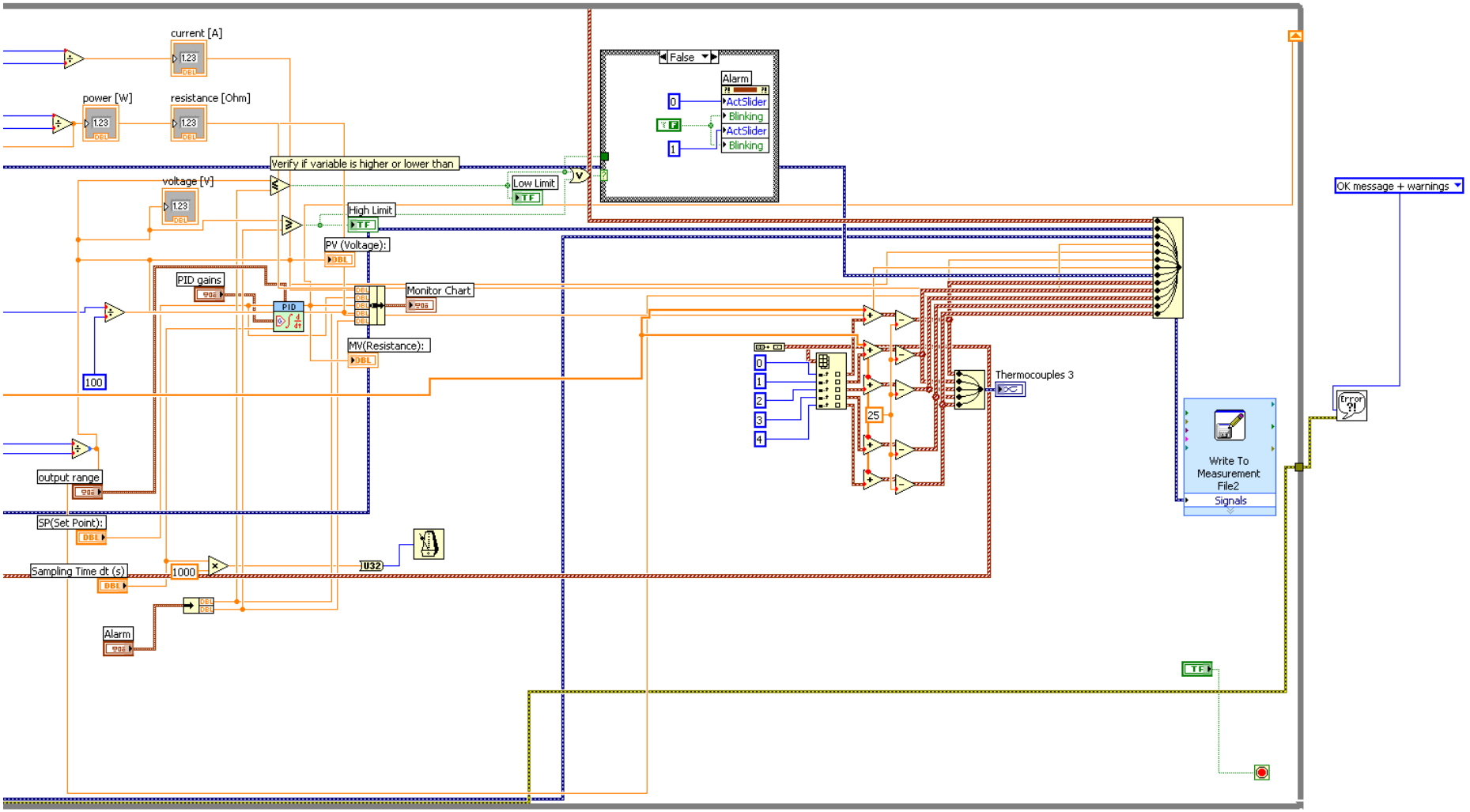

Figure A. 15 LabView Block Diagram of the program employed in the measurements

ANNEX VII: DETAILED ECONOMIC ANALYSIS DATA

Year	Date	Efficiency	Electricity sale	Heating Savings	Total income	Annual maintenance costs	Annual insurance costs	amorti-zation	loan interest	Loan Balance	depre-ciation	inte-rest	cash flow	inte-rest	Present Value	Present Value	Present Value	Rate of return
0	1/1/11	1.00								35000			0		23564	23564		
1	1/1/12	1.00	4059	340	4399	250	150	3699	2993	31301	1750	0	-2692	825	24389	21697		
2	1/1/13	0.98	4018	350	4369	250	150	4015	2676	27287	1750	-94	-5509	854	25243	19734		
3	1/1/14	0.97	3978	361	4339	258	150	4358	2333	22928	1750	-193	-8462	883	26126	17664		
4	1/1/15	0.96	3937	372	4309	265	150	4731	1960	18198	1750	-296	-11555	914	27041	15485		
5	1/1/16	0.95	3897	383	4279	273	150	5135	1556	13062	1750	-404	-14795	946	27987	13192		
6	1/1/17	0.94	3856	394	4250	281	133	5574	1117	7488	1750	-518	-18168	980	28966	10799		
7	1/1/18	0.93	3815	406	4221	290	130	6051	640	1437	1750	-636	-21693	1014	29980	8287		
8	1/1/19	0.92	3775	418	4193	299	128	6568	123	-5131	1750	-759	-25377	1049	31030	5653		
9	1/1/20	0.91	3734	431	4165	307	125	7130	-439	-12261	1750	-888	-29224	1086	32116	2892		
10	1/1/21	0.90	3694	444	4137	317	123	7739	-1048	-20000	1750	-1023	-33240	1124	33240	0		
Year	Date	Efficiency	Electricity sale	Heating Savings	Total income	Annual maintenance costs	Annual insurance costs	amorti-zation	loan interest	Loan Balance	depre-ciation	inte-rest	cash flow	inte-rest	Present Value	Present Value	Present Value	Rate of return
11	1/1/22	0.89	3653	457	4110	326		0	0	0	1750	0	3784			3784	3656	
12	1/1/23	0.88	3613	471	4083	336		0	0	0	1750	132	7663			7663	7154	
13	1/1/24	0.87	3572	485	4057	346		0	0	0	1750	268	11642			11642	10501	
14	1/1/25	0.86	3531	499	4031	356		0	0	0	1750	407	15724			15724	13703	
15	1/1/26	0.85	3491	514	4005	367		0	0	0	1750	550	19912			19912	16766	
16	1/1/27	0.84	3450	530	3980	378		0	0	0	1750	697	24211			24211	19696	
17	1/1/28	0.83	3410	546	3955	389		0	0	0	1750	847	28624			28624	22498	
18	1/1/29	0.82	3369	562	3931	401		0	0	0	1750	1002	33155			33155	25179	
19	1/1/30	0.81	3328	579	3907	413		0	0	0	1750	1160	37810			37810	27742	
20	1/1/31	0.80	3288	596	3884	426		0	0	0	1750	1323	42592			42592	30194	**2.16%**
Year	Date	Efficiency	Electricity sale	Heating Savings	Total income	Annual maintenance costs	Annual insurance costs	amorti-zation	loan interest	Loan Balance	depre-ciation	inte-rest	cash flow	inte-rest	Present Value	Present Value	Present Value	Rate of return
21	1/1/32	0.79	3247	614	3861	438		0	0	0	0	1491	47505			47505	32539	
22	1/1/33	0.78	3207	633	3839	452		0	0	0	0	1663	52555			52555	34780	
23	1/1/34	0.77	3166	651	3817	465		0	0	0	0	1839	57747			57747	36924	
24	1/1/36	0.76	3125	671	3796	479		0	0	0	0	2021	63086			63086	38973	
25	1/1/37	0.75	3085	691	3776	493		0	0	0	0	2208	68577			68577	40933	**5.31%**